The Mastcam-Z Radiometric Calibration Targets on NASA's Perseverance Rover: Derived Irradiance Time-Series, Dust Deposition, and Performance Over the First 670 Sols on Mars

Dissertation submitted for the title of
Doctor of Philosophy

PhD candidate:
Marco Merusi

Advisors:
Prof. Morten Bo Madsen
Dr. Kjartan Bergeron Kinch

Niels Bohr Institute
Faculty of Science
University of Copenhagen

This thesis has been submitted to the PhD School of The Faculty of Science,
University of Copenhagen

March 31st, 2023

Contents

Summary (in English)

NASA's Mars 2020 Perseverance Rover mission was launched from Cape Canaveral (FL) on July 30^{th}, 2020, and landed successfully within the crater Jezero, in the northern hemisphere of Mars, on February 18^{th}, 2021. The rover Perseverance is equipped with seven instruments, several technology experiments and cameras in order to study the martian geology and atmosphere, search for past life forms, characterize the environment in the scope of future human missions, and collect rock samples that will be sent back to Earth in the late 2020's. One of the scientific instruments in its payload is Mastcam-Z, a multispectral, stereoscopic pair of cameras capable of zoom, mounted on top of the rover's mast. The two CCD sensors have a Bayer pattern that can acquire broad-band Red/Green/Blue color images when imaging through a broad IR-cut filter. In addition, Mastcam-Z is provided with 12 narrow-band filters (six for each sensor, or "eye") spanning visible and near infrared wavelengths from 400 to 1022 nm. In the first 670 martian days (or "sols"), Mastcam-Z acquired more than 110 thousand images on Mars in colors and all the filters, for mosaics of landscapes, multispectral analysis of rocks and minerals, documentation of activities, video recording, and public outreach. The calibration of Mastcam-Z is an essential operation that converts the raw images to the unit of radiance, and then to reflectance. In particular, the generation of reflectance-calibrated images from radiance-calibrated images is the focus of this thesis and is realized through the calibration targets, a couple of passive physical devices mounted on the deck of the rover. The calibration targets consist of several color and grayscale ceramic patches whose reflectance is known from laboratory measurements at any illumination geometry and wavelength, and eight permanent strong magnets mounted underneath the patches. The observation of the calibration targets with Mastcam-Z allows an accurate derivation of the instantaneous local solar irradiance, which can be applied to all the other images to convert them from radiance to reflectance. Mastcam-Z captured more than 300 image sequences of its calibration targets over the first 670 sols, from which useful data were stored. The calibration is made through linear fits between the measured radiance and the reference reflectance of some small regions of one of the targets, and this method was selected as a result of several tests on images that were acquired before the launch of the rover. The solar irradiance is extracted as the slope of the fits. The calibration targets and our reflectance

calibration procedure proved to be accurate over the mission, and the time series of the derived irradiance was rather stable during the first 315 sols, after which the rover experienced the dust storm season which affected the irradiance but not our capability to perform calibration. I studied the effects of the deposition of the martian dust on the calibration target surfaces and its interaction with the sunlight. The layers of dust varied frequently on the surfaces, and most of it accumulated on the eight magnets, thus changing the reflectance spectra of the corresponding patches. In order to quantify the impact of the suspended dust, I computed the fraction of sunlight directly hitting the calibration targets and I found that it was roughly inversely correlated with the optical depth of the atmosphere. In addition, I analyzed the presence of a small offset in the linear fits employed for calibration, in an attempt to understand its origin, which was likely due to dust. Finally, I focused on an unexpected effect that affected one of the calibration target materials both visually and spectrally, that remained unsolved, and on some slight discrepancies occurring occasionally when the calibration targets are imaged when the Sun is very low on the horizon.

Resumé (in Danish)

NASAs Mars 2020 Perseverance Rover mission blev opsendt fra Cape Canaveral (Florida) den 30. juli 2020, og den landede sikkert i krateret Jezero på den nordlige halvkugle af Mars den 18. februar 2021. Perseverance-roveren er udstyret med adskillige instrumenter og flere teknologi-eksperimenter og kameraer for at studere Mars' geologi og atmosfære, lede efter spor af forgangne livsformer, karakterisere miljøet med henblik på fremtidige missioner med mennesker – og endelig for at indsamle klippe-prøver som vil blive sendt tilbage til Jorden sidst i 2020'erne. Gennem de første 670 Mars-dage ("sols") på Mars, tilbagelagde Perseverance mere end 14 km på overfladen og opnåede en række mål, som for eksempel teknologi-demonstrationen af helikopteren Ingenuity og udtagningen af 21 prøver af overfladen. Et af de videnskabelige instrumenter om bord er Mastcam-Z, et multispektralt, stereoskopisk par af kameraer udstyret med zoom og monteret højt på roverens mast. De to CCD-sensorer har et "Bayer"-mønster, som gør det muligt at optage bredbånds Rød/Grøn/Blå farvebilleder, når der optages gennem et bredt infrarødt afskæringsfilter. Herudover er Mastcam-Z udstyret med 12 smalle båndpasfiltre (seks for hver sensor, eller "øje"), som udspænder det synlige og nær-infrarøde bølgelængdeområde fra 400 til 1022 nm. Igennem de første 670 sols har Mastcam-Z optaget flere end 110.000 billeder fra Mars både i farve og igennem alle smalbånds-filtrene. Der er optaget billeder af landskaber, foretaget multispektrale analyser af klipper og mineraler, dokumenteret aktiviteter på overfladen, video-optagelser og billeder optaget med formidling for øje. Kalibrering af billeder fra Mastcam-Z er en vigtig aktivitet, hvorved de rå billeder konverteres først til enheden radians og siden til reflektans. Netop produktionen af reflektans-kalibrerede billeder fra radians-kalibrerede billeder er centralt for arbejdet beskrevet i denne afhandling og er blevet gennemført ved hjælp af et sæt af kalibrerings-targets, et par passive, men omhyggeligt designede fysiske objekter, som er monteret på roverens dæk. Disse kalibreringstargets består af adskillige farve og gråskalatonede keramiske elementer, hvis reflektans er kendt fra laboratoriemålinger i alle belysningsgeometrier og relevante bølgelængder. Otte kraftige permanente magneter er monteret under otte af de keramiske elementer. Observationer af disse kalibreringstargets med Mastcam-Z muliggør en præcis udledning af den øjeblikkelige lokale solindstråling, som kan anvendes for alle andre billeder for at konvertere disse fra radians- til reflektans-kalibrerede.

Mastcam-Z har optaget mere end 300 billed-sekvenser (billed-serier i forskellige båndpasfiltre) igennem de første 670 sols, hvorfra nyttig data er blevet ekstraheret og gemt. Kalibreringen er udført ved brug af lineære fits mellem den målte radians og referencer bestående af reflektansen af små områder af et af de to kalibreringstargets. Denne metode var valgt som et resultat af adskillige tests på billeder, som var optaget inden roveren blev opsendt. Solindstrålingen udtrækkes som hældningen af fittelinien i disse fits. Mastcam-Z kalibreringstargets og vores reflektans-kalibreringsprocedure har vist sig at forblive nøjagtig gennem missionens tidsforløb, og tidsserien af den udledte solindstråling var forholdsvis stabil gennem de første 315 sols. Herefter blev roveren udsat for en støvstormsperiode, som havde indflydelse på solindstrålingen, men ikke på vores mulighed for at udføre kalibreringsproceduren. Her har jeg studeret effekten af aflejring af Mars-støv på overfladerne på kalibreringstargets og vekselvirkningen af dette støvlag med det indgående sollys. Støvlaget ændrede sig ofte på overfladerne og det meste af det opsamledes netop over de otte indbyggede magneter, hvorved reflektans-spektrene af områderne lige over magneterne er blevet ændret væsentligt. For at kvantificere indflydelsen af det støv, der er i suspension i atmosfæren, har jeg beregnet den fraktion af sollys, som direkte rammer kalibreringstargets. Jeg fandt at denne fraktion var omvendt korrelleret med den optiske dybde af atmosfæren. Herudover har jeg analyseret tilstedeværelsen af en lille afskæring (et lille offset) i de lineære fits, som er blevet anvendt til kalibrering for herigennem at forsøge at forstå årsagen til dette offset, og fandt at det sandsynligvis skyldes tilstedeværelsen af støv. Endelig har jeg fokuseret på en uventet effekt, som viste sig både synligt og i spektral analyse for et af de keramiske reference-materialer, som blev brugt i roverens kalibreringstargets – og sluttelig har jeg undersøgt nogle relativt sjældent forekommende tilfælde, hvor billeder af kalibreringstargets er blevet optaget når Solen stod meget lavt over horisonten.

Publications

The list is updated to March 31st, 2023.

VAUGHAN, A. et al. (2022). Regolith of the crater floor units, Jezero crater, Mars: textures, composition and implications for provenance. *Journal of Geophysical Research-Planets*, Vol. **128**, Issue 3. DOI: 10.1029/2022JE007437

MERUSI, M. et al. (2022). The Mastcam-Z Radiometric Calibration Targets on NASA's Perseverance Rover: Derived Irradiance Time-Series, Dust Deposition, and Performance over the First 350 Sols on Mars. *Earth and Space Science*, Vol. **9**, Issue 12. DOI: 10.1029/2022EA002552

BELL, J. F. III et al. (2022). Geological, Multispectral, and Meteorological Imaging Results from the Mars 2020 Perseverance Rover in Jezero Crater. *Science Advances*, Vol. **8**, Issue 47. DOI: 10.1126/sciadv.abo4856

FARLEY, K. A. et al. (2022). Aqueously altered igneous rocks sampled on the floor of Jezero crater, Mars. *Science*, Vol. **377**, Issue 6614.
DOI: 10.1126/science.abo2196

HAYES, A. G. et al. (2021). Pre-Flight calibration of the Mars 2020 Rover Mastcam Zoom (Mastcam-Z) multispectral, stereoscopic imager. *Space Science Reviews*, Vol. **217**, Issue 2. DOI: 10.1007/s11214-021-00795-x

KINCH, K. M. et al. (2020). Radiometric calibration targets for the Mastcam-Z camera on the Mars 2020 Rover Mission. *Space Science Reviews*, Vol. **216**, Issue 8. DOI: 10.1007/s11214-020-00774-8

Reproductions from the literature

This thesis makes an extensive use of my peer-reviewed article, from which some parts have been transcribed with only minor changes or extensions. The article, with complete author list, is:
MERUSI, M., Kinch, K. B., Madsen, M. B., Bell, J. F., Maki, J. N., Hayes, A. G., Joseph, J., Johnson, J. R., Rice, M., Cloutis, E. A., Applin, D., Lemmon, M. T., Vaughan, A. F., Núñez, J. I., Jensen, E., Kristensen, J. Z., Paris, K., Cisneros, E., Kennedy, M. R. & Gasnault O. (2022). The Mastcam-Z Radiometric Calibration Targets on NASA's Perseverance Rover: Derived Irradiance Time-Series, Dust Deposition, and Performance over the First 350 Sols on Mars. *Earth and Space Science*, Vol. **9**, Issue 12. DOI: 10.1029/2022EA002552.
Such instances are listed as follows:

- The description of the calibration targets given in section 4.3 is reproduced from the first three paragraphs of section 2 of Merusi et al. (2022).
- The selection of the regions of interest of section 6.2 is reproduced from section 3.1 of Merusi et al. (2022).
- Section 6.4 is partially reproduced from the first three paragraphs of section 4.1 of Merusi et al. (2022).
- Section 6.4.2 is partially reproduced from the last two paragraphs of section 2 and the last paragraph of section 4.1 from Merusi et al. (2022).
- Section 6.5 of the thesis is partially reproduced from section 3.2 of Merusi et al. (2022).
- The captions of figures 7.1 and 7.3 are partially reproduced from those of figures 8a and 8b, respectively, from Merusi et al. (2022).
- The last paragraph of section 7.1 is partially transcribed from the last sentences of section 4.2 from Merusi et al. (2022).
- The description of dust displacement from landing to sol 350 described in section 7.2.1 is reproduced from the first paragraph of section 4.3.1 of Merusi et al. (2022).
- The description of the dust deposition on the magnet rings of section 7.2.2 is reproduced from the last paragraph of section 4.3.1 of Merusi et al. (2022).
- Section 7.2.3 is partially reproduced from section 4.3.2 of Merusi et al. (2022).

- The description of the two-term linear fits of section 7.3 is partially reproduced from section 4.4 of Merusi et al. (2022).
- The illustration of the yellowing effect of the AluWhite98 of section 7.4 is partially reproduced from section 4.5 of Merusi et al. (2022). In addition, the caption of figure 7.15 of the thesis is transcribed from that of figure 17 from the article.
- The descriptive captions of the example Radiometric Coefficient file in appendix A are reproduced from appendix A of Merusi et al. (2022).

Preface

This thesis is the culmination of my work as PhD fellow at the Niels Bohr Institute (University of Copenhagen), where I carried out my research project from March 1st, 2020 to February 28th, 2023 under the supervision of Dr. Kjartan Kinch and Prof. Morten Bo Madsen. During the last three years, I became an active member of one of the most incredible and advanced space missions in the history of planetary exploration, the rover Perseverance. I entered the Perseverance Team, and more specifically the Mastcam-Z Team, as an inexperienced PhD expat student, and I am now ending this journey as a skilled and self-aware scientist. The first few months were quite challenging, alone in a foreign city in the middle of a world pandemic, but the cold Copenhagen welcomed me warmly, with its amazing sea, its forests, its infinite bike lanes, and its huge cultural diversity. After the landing of Perseverance on Mars (February 18th, 2021) I spent lots of hours joining shifts for the mission, during which I assisted the Payload Dowlink Leads (PDLs) of the Arizona State University (ASU) in the calibration of Mastcam-Z and the analysis of the data coming down in real time from Mars. Many months have passed, but I never got used to the fact that I was one of the first people in the world to see pictures from our neighboring planet.

In the spring of 2022 I spent almost four months in the United States, as part of the "change of research environment" required by my PhD program, during which I stayed for almost three months in Tempe (AZ) at ASU and one month in Bellingham (WA) at the Western Washington University (WWU). When I was at ASU I was supervised by Prof. Jim Bell, Principal Investigator of Mastcam-Z, I presented a poster at my first Lunar and Planetary Science Conference (LPSC) in The Woodlands (TX), started writing my first paper, and I "instructed" the PDLs to perform the reflectance calibration. Since May 2022, this task (which was done everyday by Dr. Kinch and me until then) has been carried out by the PDLs. In Bellingham I was supervised by Prof. Melissa Rice, who helped me finally acquire a basic knowledge of geology, I presented my research to the Geology Department of WWU, and I joined a field trip to amazing natural places in Eastern Washington. On two occasions I showed the results from my research to the Mastcam-Z Team: first at ASU, in December 2021, and subsequently in Hilo (HI), in September 2022. Both events were Mastcam-Z Science Team meetings.

As final remarks, during my PhD I followed three courses and I worked as labo-

ratory assistant in as many courses. I attended the course “Introduction to Spacecraft Systems and Design” offered by the Danmarks Tekniske Universitet (DTU), and the courses “Applied Statistics” and “Applied Machine Learning” offered by the University of Copenhagen, which were all extremely relevant for my research project. At the same time, I was assistant in the laboratory of the courses “Electromagnetism” and (twice) “Electrodynamics and Waves”, both held at the Niels Bohr Institute.

I want to start the acknowledgements with a huge thank you to my family. I loved the unlimited support from my wife Ayelen, my parents Roberto and Alessandra, my sister Arianna, my grandparents, uncles, aunts, cousins. To all of you: thank you from my heart. A big thank you to my friends in Italy, that I missed during my stay in Denmark, and those I met in Copenhagen. Thanks to Ilaria, who in late 2019, when I was in France, convinced me to come back to Milan to take the english IELTS exam that was required for the application to this PhD. It was worth it! Also, thank you to Max Pezzali (if you know me, you know why).

I acknowledge here the two people who believed in me for this project and always supported me in my PhD and trips: my advisors Kjartan Kinch and Morten Bo Madsen. I could not have better supervisors!

I am thankful to my US supervisors Jim Bell and Melissa Rice, Jonathan Joseph (who built the software on which we relied for calibration), Jeff Johnson, Jessica Kristensen (who realized the app for the creation of the nice plots of the linear fits in figures 6.8 and 7.10), the PDLs at ASU, the whole WWU Martian team, my colleagues in Copenhagen, Franck Montmessin and Lucio Baggio of LATMOS in France. You all have been essential for my scientific and professional growth. I am very proud to say that I had the chance to work with you.

My PhD project was funded by the European Union’s Horizon 2020 research and innovation programme under the Marie Skłodowska-Curie grant agreement No 801199. I also acknowledge the Carlsberg Foundation, that supported the realization of the calibration targets and therefore made my project possible.

March 31st, 2023

Marco Merusi

Keep studying!
And if you fail... study harder!

Matt Taylor

Chapter 1

Introduction

1.1 A trip to the Red Planet

In the middle of the summer 2020, on July 30^{th}, NASA (National Aeronautic and Space Administration) launched an ULA (United Launch Alliance) rocket from Cape Canaveral (FL) containing one of the most technologically advanced wheeled rovers in the history of space exploration. It happened approximately 130 years after the first drawings of the martian channels/canals by Giovanni Schiaparelli (1835-1910, figure 1.1), which marked the front-line of Mars research in the XIX Century. The rover was named "Perseverance" following a public essay contest won in March 2020 by the 7^{th} grader Alexander Mather. The launch, cruise phase and orbit insertion were carried out successfully, as well as the landing in the crater Jezero on February 18^{th}, 2021. The landing was very similar to that of Perseverance's predecessor, the NASA rover Curiosity, with the deployment of a parachute and a rocket-powered sky crane, which gently laid the rover down on the surface through cables.

Perseverance is a six-wheeled rover that can move on the martian surface with four main objectives: (i) study the geology of its landing site in Jezero crater, (ii) search for signs of past life, (iii) collect rock and soil samples to be brought back to Earth, and (iv) prepare for future human missions to Mars. On January 6^{th}, 2023, Perseverance achieved 670 sols on Mars, corresponding to a whole martian year. During these 670 sols the rover had traveled 14.3 km and collected 18 samples. In addition, the little helicopter Ingenuity, the surprising technology demonstrator carried by the rover, performed 38 flights and covered a distance of more than 7500 m. In addition to several engineering cameras, the rover carries a payload of seven scientific instruments for the analysis of the surface and the atmosphere, allowing a broad range of capabilities. One of the payload elements, the multispectral, stereoscopic Mastcam-Z camera, is the base for the research described in this thesis and the multispectral study of the martian rocks and minerals. Through its two sensors and its broad-band and narrow-band fil-

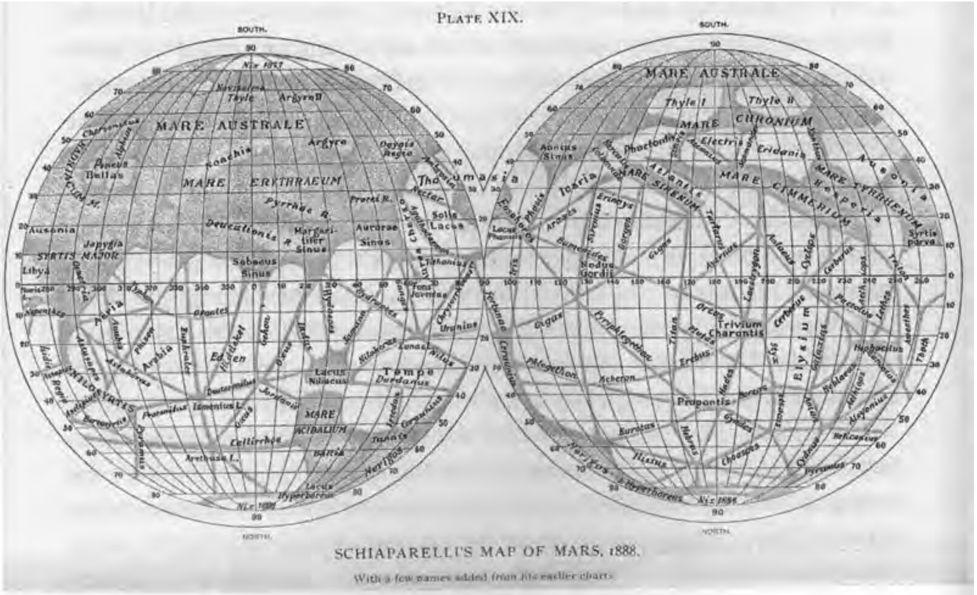

Figure 1.1: *Map of Mars realized by Giovanni Schiaparelli in 1888, with toponyms.*

ters, Mastcam-Z acquired almost 112000 images within the first 670 sols, that portray interesting rocks and boulders, amazing landscapes as mosaics, the martian sky and the Sun (even solar transits by the martian moons), and also the flights of Ingenuity and several dust devils as video frames. Nevertheless, the single object that Mastcam-Z imaged the most on Mars was its set of calibration targets.

1.2 The importance of calibration

Following the successful experience on the previous NASA rovers Spirit, Opportunity and Curiosity, and the lander Phoenix, the Niels Bohr Institute (University of Copenhagen) designed, manufactured and assembled a pair of physical passive devices composed of different color and grayscale materials and permanent magnets. These devices, named "calibration targets" (figure 1.2), were well characterized in laboratory, mounted on the deck of the rover Perseverance and imaged frequently on Mars, in order to act as efficient references to assist in the reflectance calibration of all Mastcam-Z images. This operation is meant to convert the images from the unit of radiance, that changes quickly with time, illumination and atmospheric conditions, to the unit of reflectance, that only depends on the intrinsic properties of each material, in order to realize reflectance spectra, which show how rocks and minerals reflect light at different wavelengths. Martian geologists will then study those spectra to assess the compositions of rocks and infer their origin.

The results from the calibration targets and the calibration process itself are the core of this thesis. The development of an effective calibration procedure started with an ac-

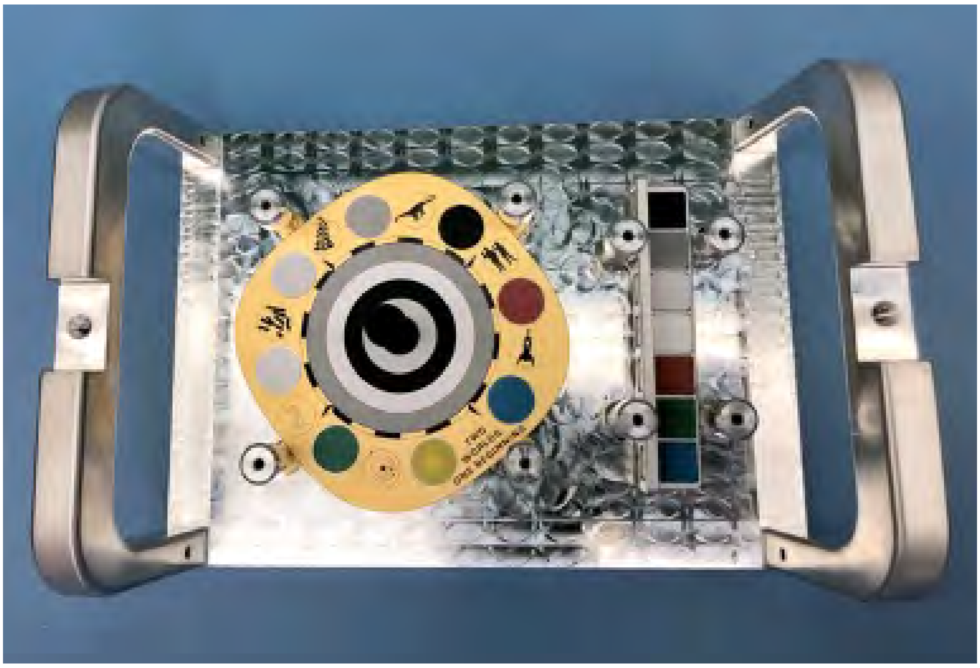

Figure 1.2: *The calibration targets (primary on the left, secondary on the right) of Mastcam-Z on their transport bracket in the laboratory, ready for delivery in 2019. Figure from Kinch et al. (2020).*

curate characterization of the ceramic materials employed as references on the calibration targets. The knowledge of their reflectance and scattering properties at different illumination conditions across the visible and near infrared spectrum was required in the comparison with their observed behavior once on Mars. The resulting reflectance model and a calibration procedure were applied systematically after landing, every time a new sequence of calibration target images in all Mastcam-Z filters was available. Although only some parts of the calibration targets were actually used for calibration, several regions of interest were recognized in the color/grayscale patterns, and the measured data from all of them were routinely documented. Therefore, we could extract a treasure trove of information regarding the health of the calibration target materials and their effectiveness at correctly performing the calibration, as well as the validity of our reflectance model. Atmospheric dust also played a very important role, as its deposition on the surfaces (figure 1.3) could be monitored through images and spectra, and its presence in suspension within the thin martian atmosphere could be assessed by keeping track of the solar irradiance over time and the variation of diffuse illumination, which reduces the contrast between illuminated and shaded regions. Within the first 670 sols, such measurements highlighted the distinction between the first half of the mission, identified by the summer season in the northern hemisphere (including Jezero) at aphelion with generally calm weather and rather clean atmosphere, and the second half, in which Perseverance experienced the winter (though mild, being only at 18°N and around the perihelion) and its long dust storm season.

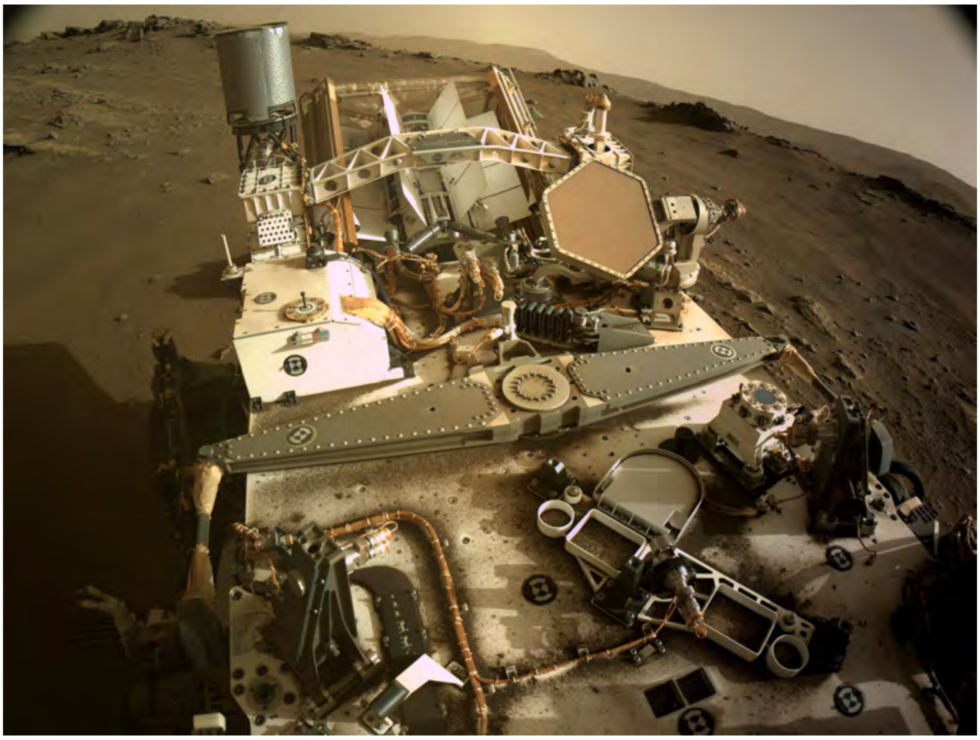

Figure 1.3: *Mosaic of images acquired by Mastcam-Z on sol 328 displaying the deck of the rover. All the surfaces experienced dust deposition. Credits: NASA/JPL-Caltech/MSSS.*

1.2.1 Motivation and structure of the thesis

This work, besides being the extensive summary of my doctoral research at the University of Copenhagen, is meant to act as a sort of "history book" of the tests before launch and the application of the calibration targets in their first 670 sols on Mars (i.e., one martian year, equivalent to 687 terrestrial days). It is intended to provide an exhaustive guide on the calibration targets and the calibration model and procedure to anyone who will take on the role of radiometric calibration specialist within the Mastcam-Z team in the future, and it is a starting point for improvements in the procedures and for collateral research projects – perhaps at Master or PhD level – that will aim at solving the open questions at the end. In addition, considering the development and deployment of future planetary missions that involve multispectral cameras equipped with calibration targets (not only rovers, but also landers and orbiters), this thesis will be a convenient support for future "calibrators" and calibration target designers.

This thesis can be divided into two parts. The first part is a general introduction to all the concepts, instruments and tests that were dealt with before the landing of Perseverance, and includes chapters 2, 3, 4 and 5. On the other hand, chapters 6, 7, 8 and 9 present methods, results and discussions from the calibration of Mastcam-Z on Mars, after landing.

Chapter 2 gives an introduction to the planet Mars, with information on its basic features, its history, its geology and atmosphere, and the crater Jezero, landing site of the Perseverance rover.

Chapter 3 illustrates the NASA Mars 2020 mission and the Perseverance rover. It first gives a quick overview on the history of Mars exploration, with more focus on the Mars Exploration Rover and the Mars Science Laboratory missions. Then it describes the main hallmarks of Perseverance, its science objectives, and the instruments in its payload. Finally, it highlights the Mastcam-Z camera that is at the center of this thesis.

Chapter 4 describes the calibration targets of Mastcam-Z. It first introduces the physical concepts of radiance, irradiance and reflectance, and then it shows the application of these concepts on the Mastcam-Z/calibration target system, with a summary of the expected implementation of the calibration process on Mars.

Chapter 5 is a complete summary of the work done on the data from the calibration targets before the launch. First it describes the characterization of the color and grayscale materials and their reflectance properties. It continues with all the calibration tests that we carried out on the images of the calibration targets before the launch of Perseverance, presenting the different models used and the relative results obtained from different image sequences. Eventually, it illustrates the reflectance model that was implemented in the calibration pipeline on Mars, and the final test at the NASA facility.

Chapter 6 summarizes the calibration procedure adopted on Mars. It describes the selection of the regions of interest of the calibration targets and how their data were documented. Then, it illustrates the imaging of the calibration targets on Mars, their statistics and the linear fits employed for calibration.

Chapter 7 is the result section from the first 670 sols of calibration on Mars. The results include the solar irradiance series and the assessment of dust on the calibration targets and in the atmosphere. Furthermore, it reports on two open topics that require more investigation regarding the linear fits and one of the materials.

Chapter 8 is a summary of the main results from the mission. In particular, it shows the impact that calibration had for the multispectral analysis of rocks and minerals.

Chapter 9 contains the discussion of the principal results, and a focus on the main points on which to concentrate the effort in order to find answers to the open questions.

Chapter 10 concludes the thesis. It summarizes the work performed in the scope of calibration and paves the way for the potential projects that could spring from this thesis.

Chapter 2

Planet Mars

The aim of this chapter is to give a brief introduction of the planet Mars, where the rover Perseverance has been "walking" and performing scientific activities since February 2021. Section 2.1 gives a list of the general characteristics of the planet, and section 2.2 tells the history of Mars, from its formation to the present day. Section 2.3 describes the main features of the martian composition and morphology, while section 2.4 deals with the atmosphere. Section 2.5 briefly describes the principal properties of the martian dust. Finally, section 2.6 focuses on the crater Jezero, where Perseverance landed in 2021 and that is the scientific target of the rover.

2.1 Basic facts and physical properties

Mars (figure 2.1), named after the roman God of war, is the fourth planet from the Sun and the farthest of the terrestrial planets. Its elliptical orbit has an eccentricity of 0.093 (it is 0.017 for the Earth), with a semi-major axis of almost 228 million km (1.52 Astronomical Units, or AU). The length of a martian day, also known as a sol, is approximately 24 hours and 40 minutes, and the sidereal year lasts 670 sols (corresponding to 687 terrestrial days). Mars is the second smallest planet in the Solar System (after Mercury), with an equatorial radius of 3396 km. Its mass and volume are 10.7% and 15% of those of the Earth, respectively, and the acceleration of gravity at the surface is 3.69 m/s^2. Due to the elongated orbit of Mars, the aphelion is at 249 million km (1.7 AU) and the perihelion is at 207 million km (1.4 AU). Mars has two natural satellites, named Phobos and Deimos, of 22 km and 12 km of diameter, respectively, and with irregular shapes. The planet hosts the tallest planetary mountain in the Solar System, the Olympus Mons (21.9 km high).

Similar to the Earth, Mars' rotation axis is tilted by 25.2°, which creates a season cycle with the summer in the northern hemisphere around the aphelion and southern summer at perihelion. In more detail, the seasons are measured through the areocentric

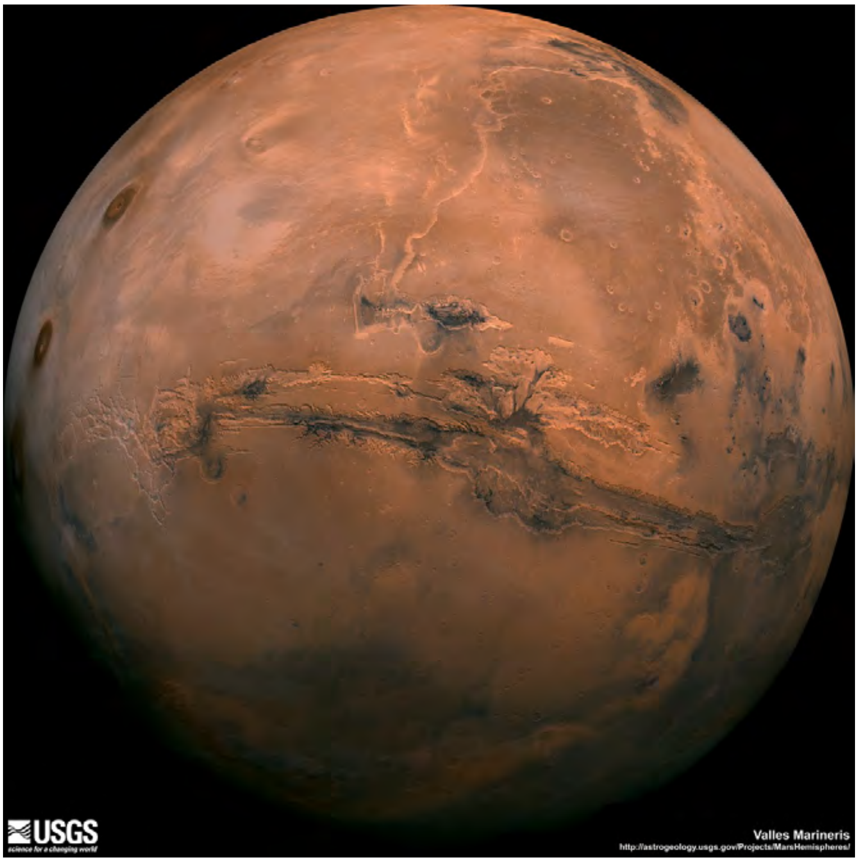

Figure 2.1: *Mars imaged by the NASA Viking Orbiter 1. Credits: NASA/JPL-Caltech/USGS.*

longitude L_s of the Sun (figure 2.2), which is 0° at the spring equinox, 90° at the summer solstice, 180° at the autumn equinox and 270° at the winter solstice for the northern hemisphere. The aphelion occurs at L_s = 71° and the perihelion at L_s = 251°. The relatively high orbital eccentricity affects the impact of the seasons, by making the southern summer (at perihelion) shorter and hotter than the northern summer, and the southern winter (at aphelion) longer and colder than the northern winter. This cycle also determines the seasonal variation in the amount of CO_2 ice forming the polar caps, that get thicker in winter and reduce during the summer in each hemisphere, whereas the water ice was observed to be more permanent (Bibring et al., 2004). The division of 12 months for the terrestrial year was also applied to the martian year, with one month corresponding to a solar longitude interval of 30°. In addition, the planet is characterized by periodical dust storms involving the whole globe, and more frequent regional-scale dust events usually taking place between the two equinoxes around perihelion (180° < L_s < 360°).

Today Mars does not have a global magnetic field, but it is characterized by several local crustal fields (Langlais et al., 2010). However, the planet had a magnetic field early in its history generated through a dynamo process in its core that probably ended around 4.1 billion years ago (Fassett & Head, 2011).

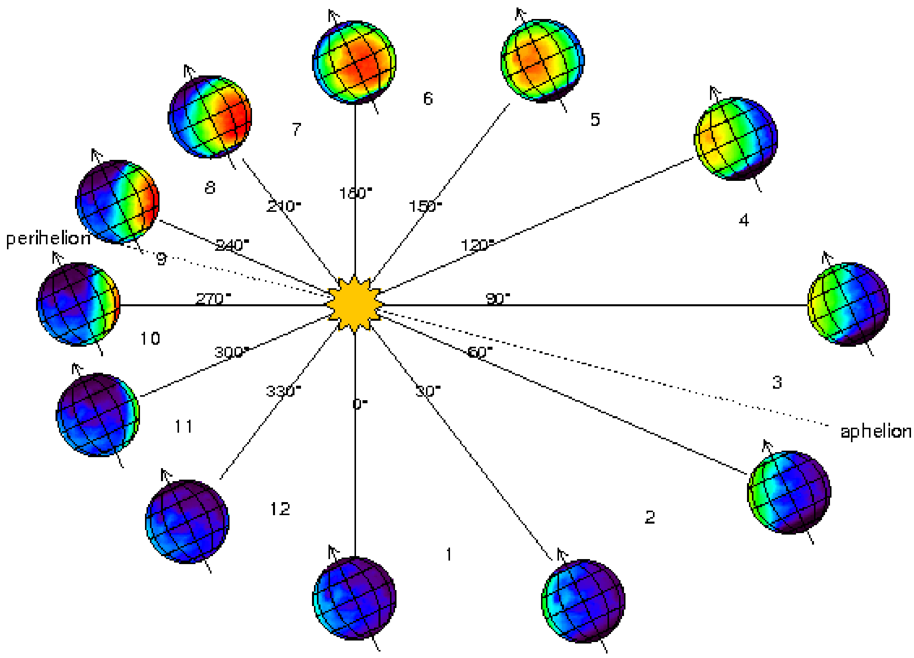

Figure 2.2: *Visual representation of the orbit of Mars. The warmer colors indicate where the planet receives the most insolation during the year. The peripheral numbers are the 12 martian months, while the numbers in the inner portion of the sketch are the solar longitudes L_s. Credits: Laboratoire de Météorologie Dynamique.*

2.2 History of Mars

Mars formed in a similar way as the other terrestrial planets, through the accretion of planetesimals within the solar protoplanetary disk around 4.6 billion years ago. The principal building blocks were rocks rich in silicon, metals and oxygen. During the late heavy bombardment, in which all the inner planets were struck by a large number of planetesimals and asteroids, Mars acquired most of the cratered aspect that it shows today (Carr & Head, 2010). During that event, a large body likely hit the northern hemisphere of the planet, forming the Borealis basin and the so-called "great dichotomy", that is the net morphological separation between the northern smooth lowlands and the southern rough and cratered highlands. In the first millions of years of the planetary formation the planet also differentiated into crust, mantle and core (Halliday et al., 2001). After the formation of the planet, the history of Mars can be divided into three age groups based on the geological features and their generation: Noachian, Hesperian and Amazonian. The Noachian age began about 4.1 Ga (billion years ago) and was preceded by a period named pre-Noachian, that started with the formation of the planet, included the global dichotomy and lasted until the time of formation of Hellas, one of the largest impact basins in the Solar System, located in the southern hemisphere of Mars (Carr & Head, 2010). Although the formation of Hellas is conventionally considered as the beginning of the Noachian age, the latter was named after Noachis Terra, a heavily cratered region just West of Hellas. The Noachian age was characterized by a high rate of cratering and erosion, as well as the formation of the giant volcanic plateau Tharsis, where most of the volcanism concentrated. The terrains that formed in the Noachian period underwent more erosion than the younger ones, and craters often present large diameters with eroded rims, and the interiors partially filled with younger, well-preserved, smaller craters (Carr & Head, 2010). It is still debated whether Mars hosted an ocean of liquid water (especially in the northern lowlands), but the Noachian was likely characterized by an episodic warm climate, favorable for the persistence of liquid water on the surface. Valley networks were quite common, as water tended to fill mainly lows and basins and move through inflow and outflow channels still visible from the orbiter images (Ehlmann et al., 2016).

The Hesperian age lasted from the end of the late heavy bombardment (3.7 Ga) to around 3 Ga and was named after Hesperia Planum, a large lava plain formed in the southern highlands. Indeed, the Hesperian was a period of intense volcanic activity forming lava plains, ridged plains, shield-like edifices, and canyons (such as the Valles Marineris). The rate of formation of valley networks decreased, whereas most of the outflow channels formed in this age, carved by liquid water. These outflow channels probably created large bodies of water at their end, especially in the northern lowlands, but it is not fully known how all this water was lost (in the planet's interiors, in the polar caps, or towards space). The average cratering and erosion rates dropped as well (Carr & Head, 2010).

The Amazonian age is the longest of the martian history, spanning from 3 Ga to the present day, and is named after Amazonis Planitia, a young volcanic plain in the northern hemisphere of Mars. Volcanism, cratering and erosion maintained a modest rate in this period (Fassett & Head, 2011). The volcanic activity was episodic and concentrated in the areas of Tharsis and Elysium (Carr & Head, 2010). In addition, significant changes in the presence of ice occurred. Indeed, during the Amazonian the obliquity of the planet varied sensibly (even up to 60°) within the last billion years due to perturbations by other planets, and during the periods of larger obliquity the polar regions experienced a higher exposure to solar radiation. Therefore, the polar water ice underwent ablation, increasing the amount of water vapor in the atmosphere which moved towards the equator and condensed into periglacial landforms at the mid-latitudes of the planet (Souness & Hubbard, 2012). Today superficial water ice is found in large perennial patches in the polar caps beneath the seasonal CO_2-ice layers, while other small periglacial deposits were observed at mid- to high-latitudes and subsuperficial deposits were detected through radar measurements (Morgan et al., 2021).

From the analysis of martian meteorites, it was suggested that the dynamo in the core, which was responsible for the sustenance of the global magnetic field, terminated around the end of the pre-Noachian and the early Noachian (Fassett & Head, 2011). This fact was proposed as one of the causes for the removal of the martian shield, which allowed a series of changes that transformed the planet to the conditions that we see today, although weak magnetism is observed at local scales all around Mars (Langlais et al., 2010). As a consequence, a significant portion of the atmosphere, which was much denser than today, was probably lost through sputtering due to the solar wind, escape and impacts (Jakosky & Phillips, 2001).

2.3 Morphology and composition

Mars is an interesting body for what concerns its structure, composition and morphology. Although it might seem geologically dead, several light "marsquakes" have been detected recently by the NASA lander InSight (Banerdt et al., 2020), and the count of craters revealed that volcanism is still an episodically ongoing process (Hartmann et al., 1999). The knowledge on the internal structure of Mars comes principally from the study of the seismic waves measured by InSight and gravity maps. The models predict a large fluid core with a radius of approximately 1800 km that might enclose a smaller solid core, a crust with a thickness of a few tens of kilometers, and a mantle in the middle (Stähler et al., 2021; Knapmeyer-Endrun et al., 2021). The core should be mainly composed of Fe, Ni, FeS and other lighter elements such as S, O and H, the mantle should be made of silicate and oxidized compounds such as SiO_2, MgO and FeO, and the crust of Si, Fe, Mg, Ca, Al, and K (Yoshizaki & McDonough, 2020; Rivoldini et al., 2011).

From a morphological point of view, the dominant feature is the martian dichotomy (figure 2.3). The large region in the northern hemisphere (called Vastitas Borealis) is characterized by low plains, rather smooth and marked by a relatively small number of impact craters. Conversely, the southern half of the planet is sensibly higher than the lowlands according to the altimeter laser measurements from orbit (in some locations, the transition between the two units is quite dramatic), and hosts a very high density of impact craters, valleys, canyons, ridges and volcanoes. The origin of this dichotomy is still debated, and exogenic and endogenic processes have been proposed as possible explanations. The most credited exogenic process is the impact with a giant body while Mars was still forming, which made the crust thinner and caused the magma to spill from underneath the crust and cover the whole lowlands, eroding the pre-existing craters and giving the region a younger appearance (Wilhelms & Squyres, 1984). Alternatively, endogenic processes involve mantle convection, which may have caused an upwelling of the southern hemisphere (Zhong & Zuber, 2001). In addition, some authors suggested a hybrid approach, in which a large-scale impact induced a magma ocean and an uplift of the southern lands, and that would be linked with the formation of the Tharsis volcanic structure (Golabek et al., 2011).

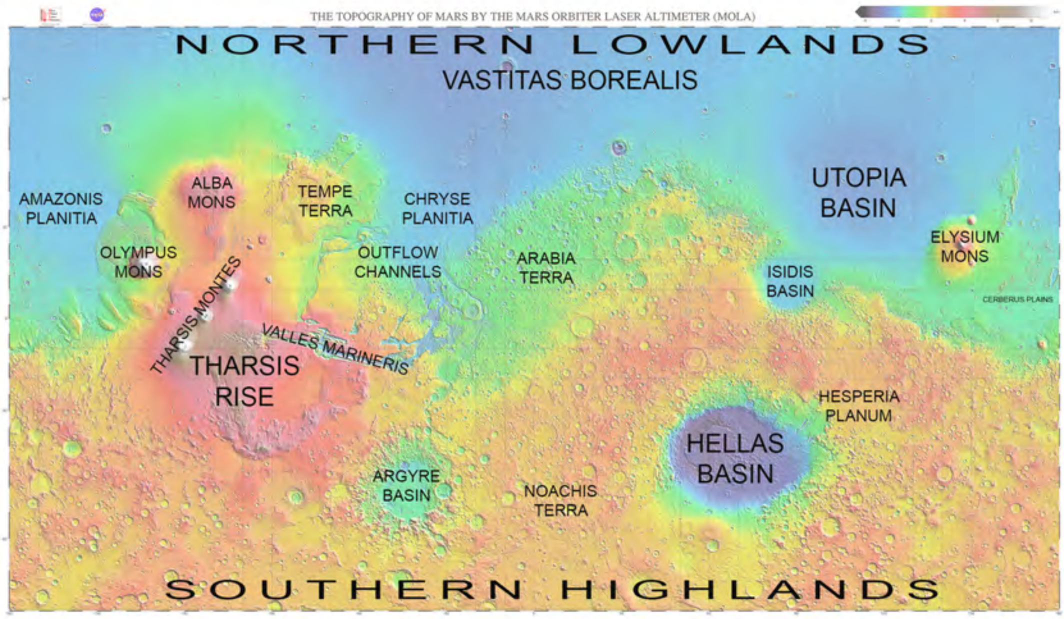

Figure 2.3: *Morphology of Mars obtained by the Mars Orbiter Laser Altimeter (MOLA) on the NASA Mars Global Surveyor. The main toponyms are reported within the map. Credits: NASA/JPL/GSFC/E. Lakdawalla.*

The Tharsis volcanic plateau in the highlands is characterized by a morphologically rich environment. This is the area where most volcanic and tectonic activity concentrated during the Noachian age, possibly as a result of the global dichotomy mentioned above, which may have generated a magmatic superplume. Tharsis hosts several volcanoes, such as the three aligned shield volcanoes known as the Tharsis Montes (Arsia, Pavonis and Ascraeus), as well as the extended Alba Mons at the northern boundary. In addition, the Olympus Mons (figure 2.4a), the tallest volcano in the Solar System (21.9 km high) is associated with Tharsis, and is located just beyond the north-west boundary of Tharsis. In the eastern part of Tharsis, the Valles Marineris canyon system (figure 2.4b) extends for 4000 km in length. This structure is characterized by a width of approximately 200 km and relief up to 11 km in the central parts (for comparison, the largest and deepest canyon on Earth is the Yarlung Tsangpo Grand Canyon in China, which has an average depth of less than 5 km). Valles Marineris is thought to have been generated through tectonism, and its walls experienced faulting, erosion, wet conditions and desiccation (Peulvast et al., 2001).

The geochemical studies of the martian mineralogy through spectroscopy from orbiters and in-situ exploration (rovers and landers) determined that the upper crust of

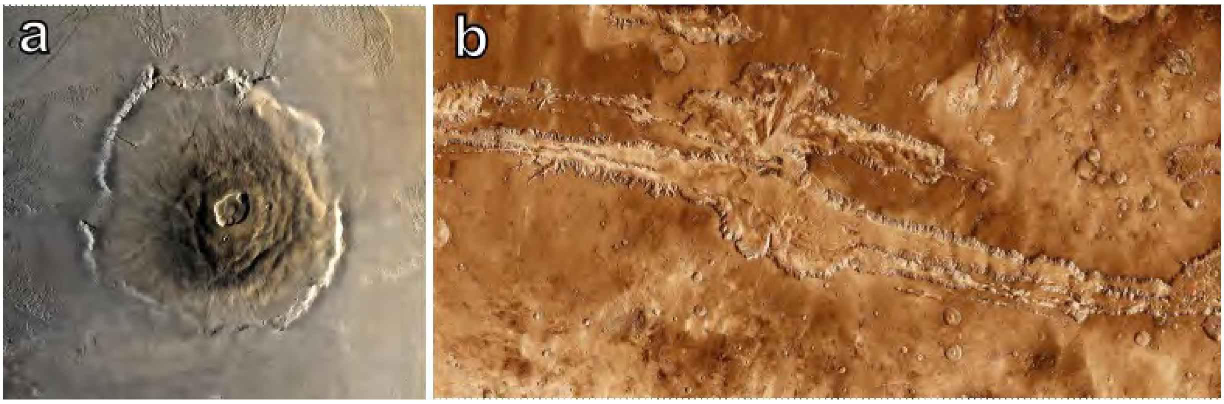

Figure 2.4: *(a) Image mosaic of the Olympus Mons acquired by the NASA Viking Orbiter 1. (b) Mosaic of the Valles Marineris obtained by the Thermal Emission Imaging System of the NASA Mars Odyssey spacecraft. Credits: NASA/JPL-Caltech/ASU.*

Mars is prominently basaltic. Most rocks contain minerals that witnessed volcanic, aqueous and hydrothermal interaction, as well as weathering. The most common minerals are pyroxenes, olivine, plagioclase, as well as clay minerals and carbonates within sedimentary rocks (Ehlmann & Edwards, 2014). For instance, the latter were analyzed by the NASA Curiosity rover (Grotzinger et al., 2012) within its landing site, the Gale crater, in a location named Yellowknife Bay. The instruments onboard the rover detected plagioclase, smectites, Fe-forsterite, orthopyroxene, phyllosilicates, oxide and sulfate minerals in mudstone (Vaniman et al., 2014). The overall mineralogic measurements within Gale revealed that those minerals experienced geochemical variations, transportation mechanisms, and depositional and diagenetic fluids (Rampe et al., 2020). Similar results had been previously obtained by the NASA Mars Exploration Rovers (Crisp et al., 2003), with the addition of hematite, goethite and ilmenite within the Gusev crater, landing site of the Spirit rover (Morris et al., 2006a), and jarosite and hematite in Meridiani Planum, which was explored by the Opportunity rover (Morris et al., 2006b).

2.4 The martian atmosphere

The surface of Mars is enclosed in a thin atmospheric shell. The average pressure is 0.6% of that of the Earth (610 Pa at the surface), and the composition is also very different. The martian atmosphere is dominated by CO_2 (95%), molecular N_2 (2.8%) and Ar (2%), with traces of water vapor, O_2, CO, H_2, and some noble gasses. In addition, it is worth mentioning the detection of volatiles such as CH_4, which is often related to life on Earth (though it can also be produced through non-organic processes), and SO_2, which might indicate active volcanic processes. Unlike the Earth's atmosphere, Mars lacks an ozone layer, and therefore its atmosphere can be divided in only three layers, following the temperature profile measured by the landing stage of several missions (figure 2.5). The first layer above the surface is a "lower level" similar to the Earth's troposphere, that extends up to 50 km. Most of the conditions that determine the weather occur in this lower level, including the presence of airborne dust and the formation of clouds at the boundary layer (40-50 km), mainly made of CO_2 ices and in minor part of water vapor. The temperature at the surface depends not only on time of sol, season and latitude, but also on the amount of dust suspended in the atmosphere. The average value at the surface is around 220 K, and it decreases roughly linearly with the altitude up to the boundary with the second layer, where an inversion occurs. The intermediate layer is the mesosphere, which extends between 50 and 100 km. The temperature in the mesosphere does not change significantly with altitude, and is characterized by the lowest value (around 100 K) due to the CO_2 that radiates heat towards space. The mesosphere is topped at 100 km by the mesopause, which separates it from the higher layer, the thermosphere, which extends from 100 to 230 km. The temperature of the thermosphere increases rapidly with the altitude due to extreme UV from the Sun (Haberle et al., 2017).

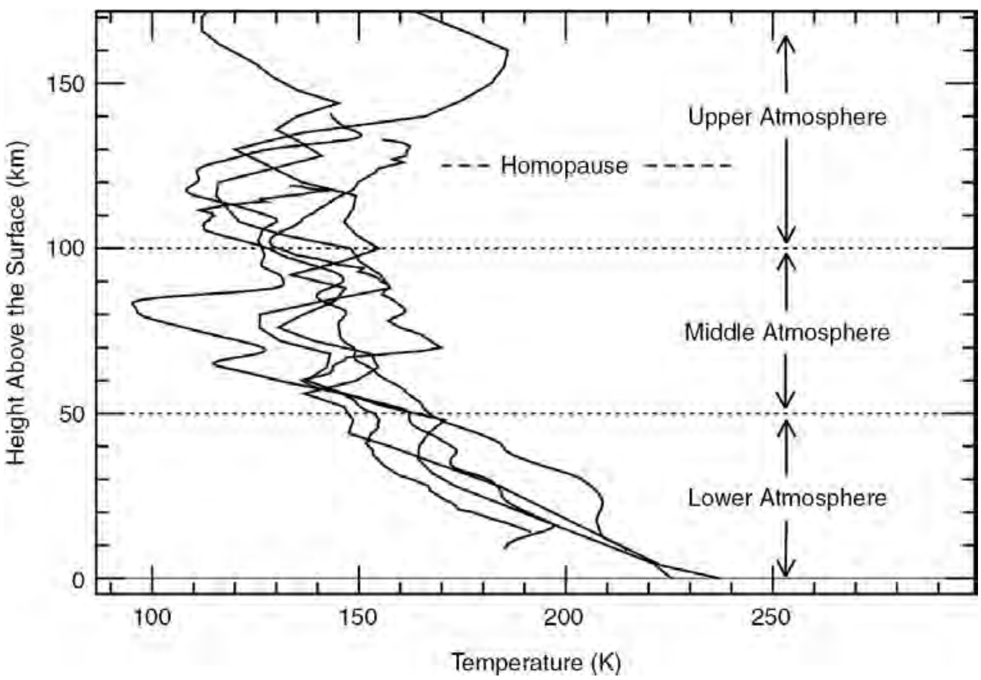

Figure 2.5: *Vertical temperature profile of the atmosphere of Mars. The three main atmospheric layers. Each profile (solid lines) was measured by the accelerometers of several NASA landers (Viking 1 and 2, Pathfinder and Phoenix) and rovers (Spirit, Opportunity, and Curiosity) that landed on the planet. Figure from Smith et al. (2017).*

Wind was detected by the "weather stations" of which previous rovers and landers were equipped on the surface. They collected several measurements concerning the direction and intensity of the wind (Martinez et al., 2017). Moreover, wind contributed significantly to modifying the morphology (i.e., the "aeolian" activity, from the Greek god of winds Aeolus) through erosion, displacement and deposition of materials. Similarly to what happens on Earth, in the desert environment of Mars wind can erode rocks, giving them smooth and even weird shapes, or carve them through the abrasion with transported sand grains. When interacting with sand, it can create ripples and dunes. Nevertheless, the stronger phenomenon observed in action is the transportation of dust, which is much finer and lighter than sand and can generate different scenarios according to the intensity.

2.5 Dust on Mars

Martian dust is a very fine material resulting from the morphologic and aeolian processes, such as mechanical breakdown of rocks and oxidized and weathered surfaces. It is very easily raised and transported by the wind in the atmosphere, where its principal effect is the extinction of the intensity of sunlight. The characteristic parameter that describes the extinction due to dust is the atmospheric optical depth τ, which is assessed along the straight line of observation and is retrieved through the following expression:

$$I = I_0 \exp\left(-\frac{\tau}{\cos i}\right), \tag{2.1}$$

where I is the measured sunlight intensity at the surface, I_0 is the intensity measured at the top of the atmosphere, and i is the angle between the zenith and the direction of illumination. From a qualitative point of view, dust is responsible for the reddening of measured spectra by typically absorbing light in the near ultraviolet and the blue bands, and scattering in the red and near infrared bands. This scattered light is a powerful source of diffuse illumination (especially when the Sun is relatively low on the horizon), which reduces the contrast between sunlit and shadowed regions.

Dust is usually displaced by atmospheric events that can go from small to global scales. The most common events are the dust devils, that form as convective vortices of air of few meters of diameter and usually move dust particles at few tens of m/s, and were observed by Spirit (figure 2.6), Opportunity and Curiosity rovers, and by the NASA Phoenix lander (Murphy et al., 2016). On a more extended scale, local dust storms are also quite common and involve the displacement of significant amounts of dust over a limited region of the planet (figure 2.7). These usually occur during the northern winter, across the perihelion ($180° < L_s < 360°$). Finally, the global dust storms manifest on planetary scale less frequently, and their effect on the martian disk can be observed even from telescopes on Earth. The last of such events happened in 2018 (Sánchez-Lavega et al., 2019) and determined the end of the mission for the rover

Opportunity. Indeed, although these storms would be rather modest for a human being due to the low density of the martian atmosphere, they lift an enormous amount of dust that can deposit on the solar panels of spacecrafts, reducing their intake of sunlight and preventing them from charging the batteries. In addition, in some cases dust storms may increase the optical depth of the atmosphere and the attenuation up to levels where the surface receives a smaller amount of energy for long time intervals, and therefore, the insolation drops significantly. Besides the rover Opportunity, the NASA lander Phoenix, and more recently InSight, were terminated for those reasons. Unfortunately, dust tends to deposit and adhere electrostatically to metallic surfaces, making it challenging to design a "cleaning" system that can remove it, though different technologies are being developed for future application (Afshar-Mohajer et al., 2015).

Figure 2.6: *Dust devil imaged by the NASA Spirit rover in 2005. Credits: NASA/JPL-Caltech.*

The composition of dust grains was inferred during the course of several missions through the use of magnets, by which a fraction of airborne dust was attracted. The analyses on the NASA Pathfinder mission, which landed in Chryse Planitia, in the northern hemisphere of Mars, revealed that airborne dust grains had an average size of 3 μm and were composed of silicates and Fe^{3+} compounds, which give the particle their typical reddish color and magnetism (Madsen et al., 1999). The multispectral analysis of dust on the Spirit and Opportunity rovers revealed the presence of basaltic minerals, such as magnetite, pyroxene and olivine, as well as the ferric oxides (Goetz et al., 2005; Madsen et al., 2009). Similar results were retrieved by the Curiosity rover in Gale crater, where rocks were covered by a dust coating which increased their reflectance in the red and near infrared bands (Rice et al., 2022). In addition, the airfall dust that deposited on the calibration targets of the multispectral cameras of Spirit and Opportunity allowed to obtain information on the reflectance of dust, which appeared brighter at the Opportunity site than at Spirit site (Kinch et al., 2007).

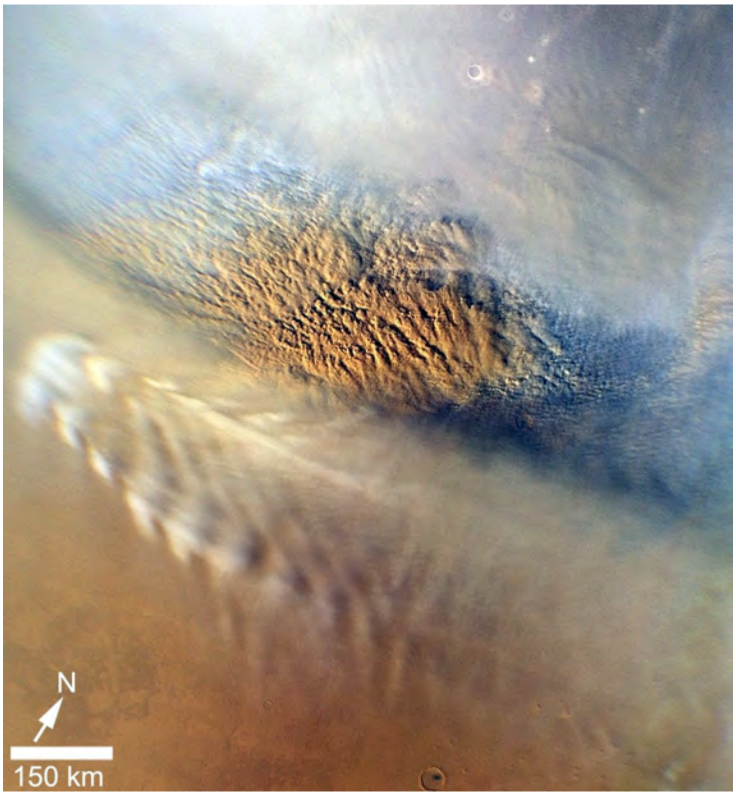

Figure 2.7: *Close-up image of a dust storm within Utopia Planitia, at the edge of the northern polar cap, captured by the Mars Color Imager (MARCI) instrument of the NASA Mars Reconnaissance Orbiter during the late northern martian winter of 2007. Credits: NASA/JPL-Caltech/MSSS.*

2.6 The crater Jezero

The landing site of the NASA Perseverance rover is Jezero (lake, in slavic language). The Jezero crater has a diameter of 45 km and is located within the Nili Fossae formation at the north-west rim of Isidis Planitia, a large impact basin in the northern hemisphere of Mars, on the boundary of the global dichotomy (figure 2.8a). The Jezero crater probably formed in the Noachian period and was selected in November 2018 for the Mars 2020 mission and its rover Perseverance, after years of workshops meant to assess and characterize several candidate destinations (Grant et al., 2018). Before February 18^{th}, 2021, when Perseverance successfully landed in the crater, all the knowledge about Jezero was limited to remote-sensing high-resolution imaging and orbital analysis. The most evident hallmark is its interesting morphology (figure 2.8b). As seen from the High Resolution Imaging Science Experiment (HiRISE; McEwen et al., 2002) camera onboard the ESA (European Space Agency) Trace Gas Orbiter, which imaged the surface of Mars at a resolution of 25 cm/pixel, Jezero appears as an old dry lake (a "paleolake". Two long and sinuous input valleys, one coming from the north and one from the west of the crater, likely transported sediments inside the paleolake forming large delta fans, while an output valley drained the basin in the eastern part of the rim, as observed by the difference in altitude measured by the altimeters (Fassett & Head, 2005).

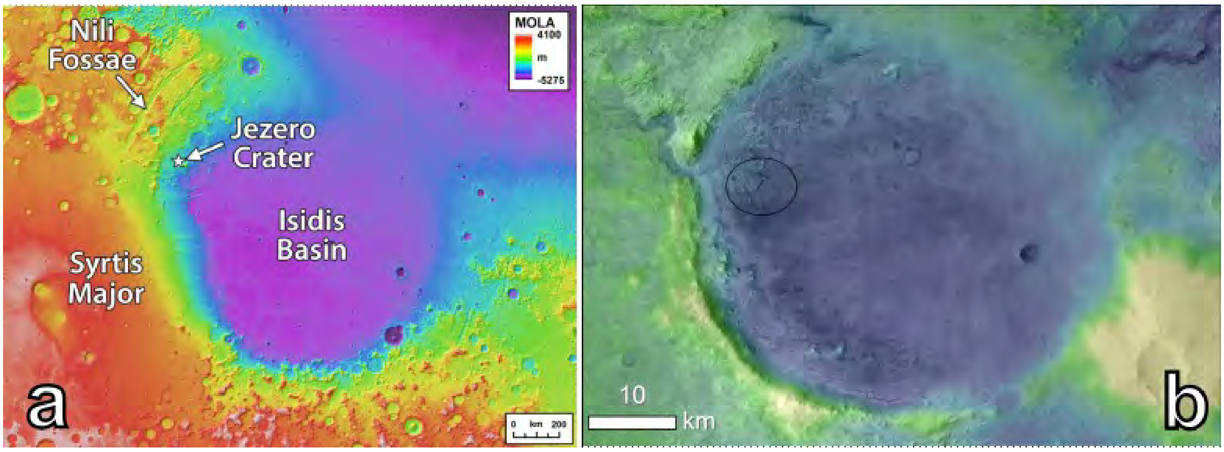

Figure 2.8: *(a) The location of the Jezero crater, landing target of the NASA Perseverance rover, at the north-western rim of the large Isidis Basin, on the edge of the martian dichotomy. Image obtained by the Mars Orbiter Laser Altimeter of the NASA Mars Global Surveyor. Credits: NASA/MIT. (b) The Jezero crater with colors indicating the elevation (dark colors are lower elevations) obtained as combination of data from the Mars Orbiter Laser Altimeter (MOLA) of the NASA Mars Global Surveyor, the Compact Reconnaissance Imaging Spectrometer for Mars (CRISM) and Context Camera (CTX) of the Mars Reconnaissance Orbiter, and the High Resolution Stereo Camera (HRSC) of the ESA Mars Express. The ellipse on the left is the predicted landing site of the Perseverance rover. Credits: NASA/JPL-Caltech/MSSS/JHU-APL/ESA.*

In the year before the launch of the Mars 2020 mission, a big effort by the Mars 2020 team led to the achievement of a complete photogeologic map of the landing ellipse of Perseverance, that is the target area within Jezero where the rover was expected to land in 2021 (Stack et al., 2020). The landing ellipse was located in the north-western portion of the crater, which included part of the crater floor and the delta fan relative to the western input channel (figure 2.9). The mapping process distinguished several surficial and bedrock units with different properties. The surficial units consisted mainly of large and small aeolian bedforms characterized by light and dark tones, respectively, with ripples oriented north-south, smooth units and boulders. The bedrock units were mapped according to the region in which they were observed. Stack et al. (2020) recognized crater floor, inner margin, delta, crater rim, and out-of-crater areas. The latter were the valley of the western input channel, named Neretva Vallis, and the outcrop located north and south of Neretva Vallis, known as Nili Planum. On the crater floor, three kinds of bedrock units with polygonal fractures were observed, two of which were quite similar, showing undulating relief, and one characterized by an overall flatness. Comparable polygonal-fractured units were found also in the inner margin of the crater, just north-west of the delta fan. On the other hand, several units were identified in the delta, which generally appeared as a layered formation with layers of different thicknesses. According to their thicknesses and compositions, they were interpreted as remnants of lacustrine deposits and alluvial deposits. Finally, the units recognized within the crater rims probably originated from the impact that generated Jezero, such as impact breccia and pre-impact uplifted bedrock, while the Neretva Vallis seemed to witness the fluvial sedimentary deposit.

The mineralogic composition of the delta region of Jezero was investigated through visible/near infrared hyperspectral images acquired by the CRISM (Compact Reconnaissance Imaging Spectrometer; Murchie et al., 2007) instrument on the NASA Mars Reconnaissance Orbiter. The most distinctive feature in the Nili Fossae region is the presence of carbonate-bearing material, which is relatively absent on the surface of Mars and is associated with olivine. This suggests that after the impact that formed the crater, the emplacement of olivine lithology and carbonatization likely occurred on the crater floor, and subsequently water transported sediments that deposited inside the lake, forming the deltas (Brown et al., 2020). When the lake dried, erosion took place and the floor was covered by a fill unit of volcanic or melt origin around the early Amazonian age (Shahrzad et al., 2019). The western delta fan deposit, which was included in the landing ellipse of Perseverance, presented a spectral signature consistent with Fe/Mg-smectite, with a lower amount of Mg-rich carbonate and olivine, and these minerals were probably aqueously altered during the transportation by water (Goudge et al., 2015). Similar mineral signatures were observed along the northern rim and interior of Jezero, suggesting that also these regions might have undergone lacustrine modification. In addition, the carbonates along the inner side of the crater, around the western delta, showed a stronger carbonate spectral signature, and might be consistent with a combination of fluvial and strandline carbonate deposits (Horgan et al., 2020).

As a result, the crater Jezero displayed a great potential for geomorphologic, mineralogic and astrobiological in-situ studies. Indeed, its environment, and especially its western delta, witnessed an interesting history of aqueous alteration, fluvio-lacustrine activity, and weathering which modeled the environment and modified the rocks. The payload instruments onboard Perseverance were aimed at gaining precious insights on the chemistry, the stratigraphy, the sedimentology, the hydrogeology and the climate that ruled in the Noachian age. Furthermore, astrobiology had a significant impact in the selection of Jezero as the landing site of Perseverance. On Earth, carbonate deposits close to the shores are deeply connected to biological activity (e.g., the stromatolites), and hence, detecting and analyzing such minerals within a setting that experienced liquid water in the past might open a new frontier of scientific research and answer the questions on the life on Mars. The main discoveries made by the Perseverance rover within Jezero and documented over its first 670 sols are summarized in chapter 8.

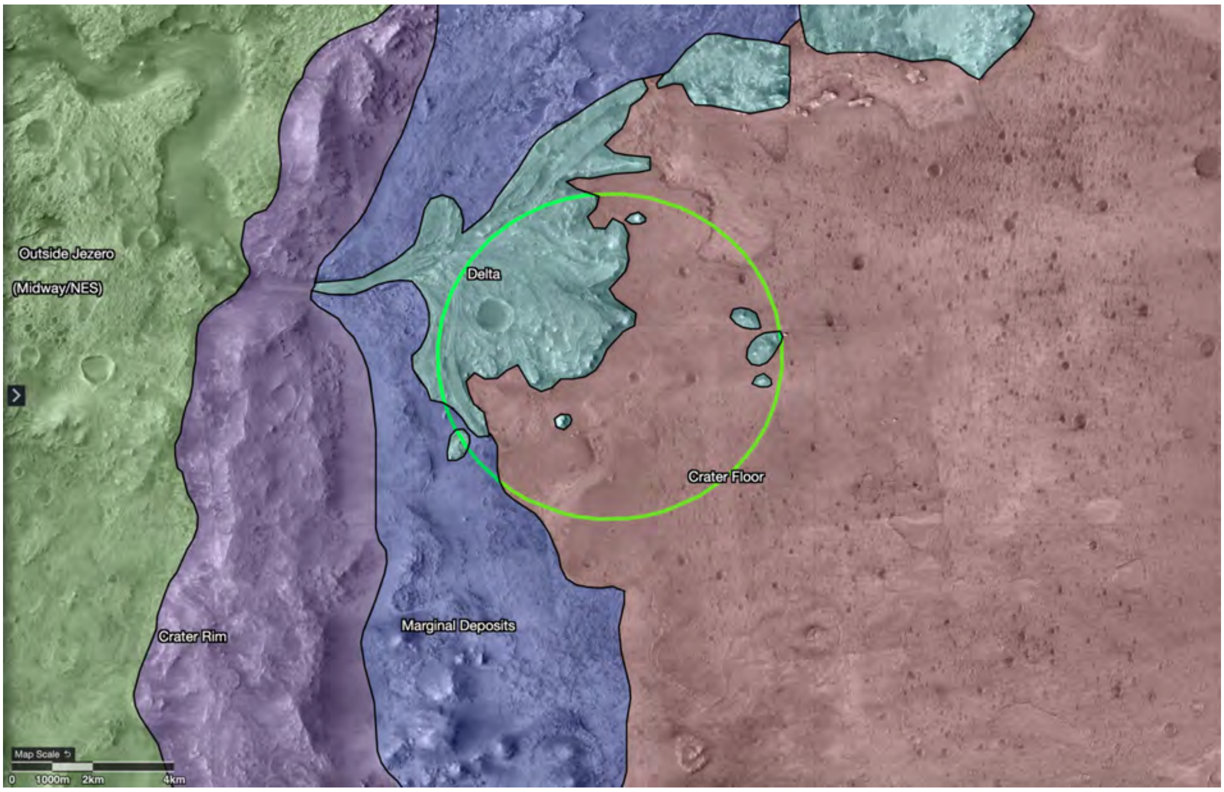

Figure 2.9: *Close-up image of the western delta fan of Jezero crater, captured by the High-Resolution Imaging Science Experiment (HiRISE) camera of the NASA Mars Reconnaissance Orbiter. The colors distinguish the five main regions of interest (crater floor, delta, marginal deposits, crater rim, and the outside of the crater). The central circle is the landing target of the Perseverance rover. Credits: NASA/JPL-Caltech/USGS/University of Arizona.*

Chapter 3

The NASA Mars 2020 mission

This chapter is intended to give an overview on the Mars mission at the center of this doctoral project: Mars 2020. To give some context, section 3.1 provides a general introduction on the history of the exploration of the Red Planet from the 1960's until today. In sections 3.1.1 and 3.1.2 more emphasis is devoted to the main rover missions of NASA, the Mars Exploration Rovers (MER) and the Mars Science Laboratory (MSL), which transferred their conceptual and technological inheritance to the Perseverance rover. Section 3.2 is an exhaustive illustration of the Perseverance rover, followed by its scientific objectives and the futuristic Mars Sample Return mission (section 3.2.1), and a description of the instruments that Perseverance is carrying (section 3.2.2). Finally, section 3.2.3 goes into details regarding one of Perseverance's instruments, the Mastcam-Z camera.
In general, all spacecraft can be divided into three categories, based on their different capabilities and objectives: i) orbiters, that just flyby or orbit a planet, ii) landers, that reach the surface and act as stationary laboratories for local measurements and analyses, and iii) rovers, robotic vehicles with wheels and instruments that can move around on the planet. Since April 2021, this list should be upgraded with a fourth category: the planetary drones (or UAVs, Unmanned Aerial Vehicles), of which the small experimental helicopter Ingenuity (as part of the Perseverance rover) is the first successful prototype.

3.1 Sixty years of Mars exploration

The first space missions for the exploration of Mars are dated back to the Sixties, a decade ruled by the "space race" between the USA and USSR and culminated with the first men walking on the Moon in July and November 1969. The Cold War resulted in the most prolific advancement in space technology and investigation of other planetary bodies, especially the Moon, Venus and Mars.

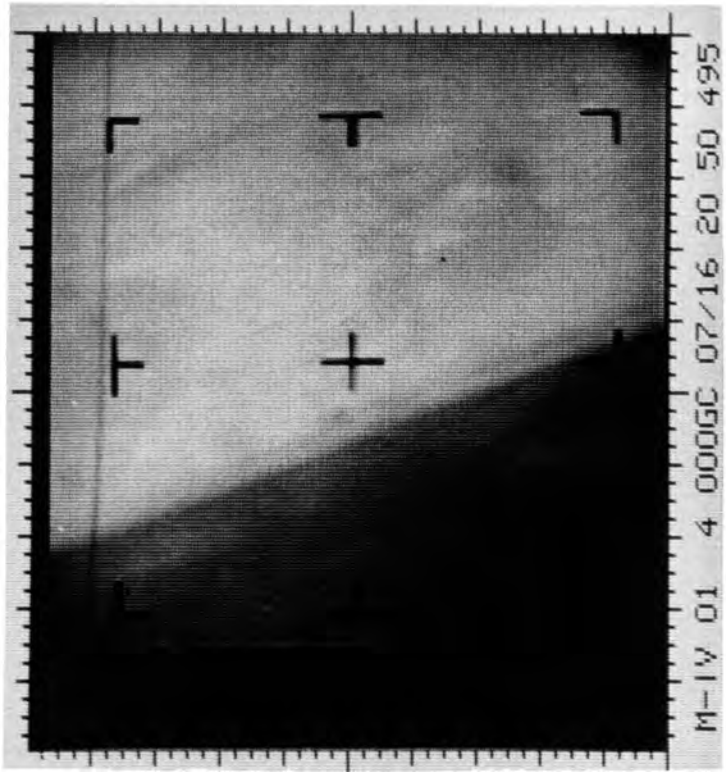

Figure 3.1: *The first close-up photograph of Mars acquired by the television camera onboard the Mariner 4 spacecraft in 1965 and recorded on tape. Credits: NASA/JPL/Dan Goods.*

Mars is one of the Earth's neighbors and it was already suspected to be the most similar planet to Earth (also biologically), and for this reason it was the destination of a large number of probes. In fact, a considerable fraction of those probes failed during launch or due to loss of communication before entering its orbit, and in 1965 NASA Mariner 4 (Leighton et al., 1965) was the first spacecraft to complete a flyby[1] of the planet. This mission returned the very first detailed images of the cratered surface, such as that in figure 3.1, suggesting that no macroscopic life forms were populating the planet and changing the sci-fi imagination of that time. In the following 10 years, the american Mariner 6 and 7 performed flybys of Mars, taking pictures of the poles and retrieving data on the atmosphere (Kliore et al., 1969), followed by the Soviet Mars 2 and 3. In 1976 NASA set an important milestone with the Viking 1 and 2 missions, both consisting of an orbiter and a lander (Soffen & Young, 1972). Viking 1 lander operated for 2245 sols within Chryse Planitia, where it took amazing pictures and carried on biological experiments meant to search for organic compounds in the soil. Only one of its experiments gave a positive result, that was however labeled as a false positive.

[1]A flyby is an orbital maneuver through which a spacecraft transits close to a planetary body. During flybys, spacecrafts can study the approached body in great detail thanks to the short distance. In addition, through a flyby a spacecraft can exploit the gravity of the massive body in order to change its own orbit (trajectory and speed) and head towards other planetary bodies.

Meanwhile, Viking 2 lander spent 1281 sols at Utopia Planitia analyzing the elemental composition of the soil and performing biological experiments as well. Even in this case some of them gave positive results, but considered not reliable and inconclusive (Levin & Straat, 1976; Klein et al., 1976). In addition, the cameras onboard took wonderful color images of the landscapes (figure 3.2). At the same time, the two orbiters contributed to the mapping of the planet and led to the hypothesis of the presence of liquid water in the past (Mazur et al., 1978), shown by the widespread nets of fluvial-like channels and valleys.

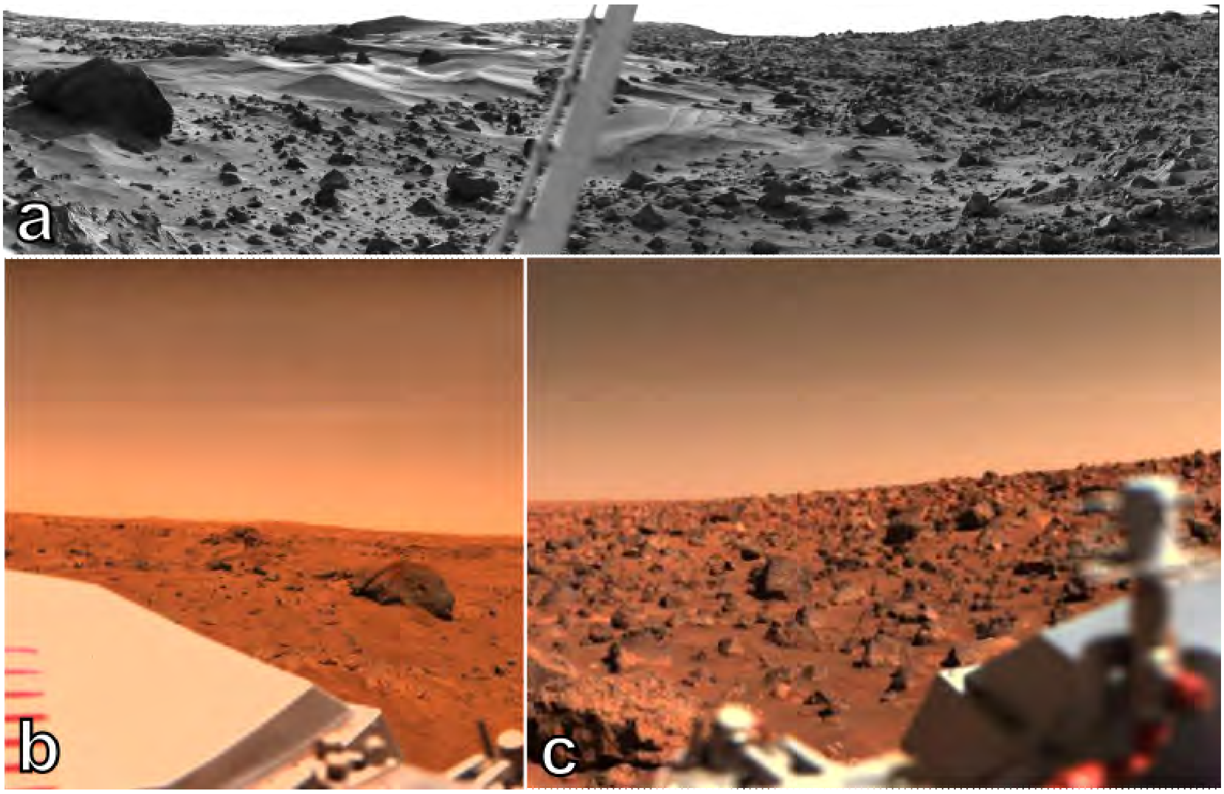

Figure 3.2: *(a) Landscape of a dune field within Chryse Planitia acquired by the Camera 1 of the Viking 1 lander in the early martian morning. (b) Color image of Chryse Planitia seen by the Camera 1 of the Viking 1 lander. The white portion of the lander in the lower left is the cover of the nuclear power supply. The dark rock on the right is 2 m long and was named "Big Joe". (c) Color image of Utopian Planitia taken by the Camera 2 of the Viking 2 lander in the afternoon. Credits for all images: NASA/JPL.*

Between 1976 and the end of the Eighties, both USA and USSR moved their attention towards a "warmer" bilateral relation and other projects, such as the space stations and the Space Shuttle, and no missions to Mars were launched until 1988, when the Soviet Phobos 2 probe reached and imaged shortly the martian moon Phobos. In the Nineties the modern era of Mars exploration began, with more and more missions targeting the planet. In 1997 the NASA Mars Global Surveyor orbiter started its activity that lasted for a decade (Albee et al., 2001). In the same year, NASA put wheels on the surface with the Mars Pathfinder mission, which consisted of the Pathfinder lander and the Sojourner rover, which both endured a few months (Golombek et al., 1997). One of the longest-lived spacecraft still in activity (since 2001) is the NASA Mars Odyssey, an orbiter carrying an imager and spectrometers (Saunders et al., 2004). The first mission launched by the European Space Agency (ESA) is Mars Express, whose homonymous orbiter is currently in function (Chicarro et al., 2004). This mission started in 2003 and also included the lander Beagle 2, which lost communication with the Earth after being released from the orbiter. A similar path was followed in 2016 by the ESA/Roscosmos mission Exomars (Vago et al., 2015), in which the Trace Gas Orbiter (TGO) was successfully inserted in orbit, while the landing demonstrator Schiaparelli, due to a command error, crashed on the martian ground. In 2006, one of the most crucial scientific asset, the NASA Mars Reconnaissance Orbiter (MRO) started its operations around the planet (Zurek & Smrekar, 2007). Two of its payload instruments, the CRISM spectrometer (Murchie et al., 2007) and the HiRISE high-resolution camera (McEwen et al., 2007), returned stunning images (figure 3.3) and allowed an extremely productive understanding of the Red Planet.

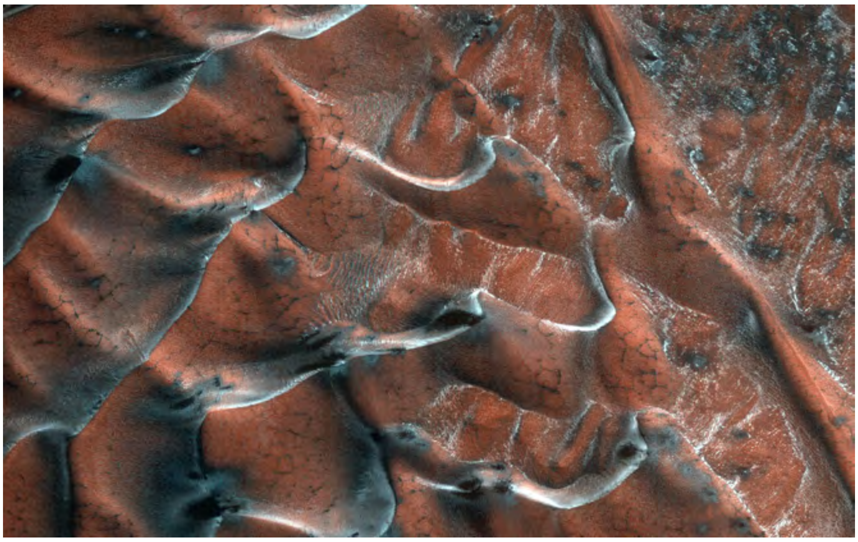

Figure 3.3: *Field of sand dunes within a crater in the high-latitudes of the northern plains of Mars, experiencing seasonal frost processes. The image was acquired by the HiRISE camera of the Mars Reconnaissance Orbiter at a resolution of 50 cm/pixel. Credits: NASA/JPL-Caltech/University of Arizona.*

MRO was followed by the MAVEN (Mars Atmosphere and Volatile Evolution) orbiter in 2014, which focused mainly on the observation of the atmosphere and the detection of auroras (Jakosky et al., 2015). More investigation on the surface, the climate and the seismicity of Mars were addressed by the two NASA landers Phoenix (Shotwell, 2005), which lasted a few months in 2008, and InSight (Banerdt et al., 2020), which arrived on Mars in 2018 and ended its mission in 2022. The first main rover missions from NASA (after Sojourner) were the Mars Exploration Rovers (MER, landed in 2004) and the Mars Science Laboratory (MSL, landed in 2012), that are described in sections 3.1.1 and 3.1.2.

Among the Mars missions from other countries, it is worth mentioning: the Mars Orbiter Mission (Sundararajan, 2013) of the Indian Space Research Organisation (ISRO), which was operative from 2014 to 2022; the Hope orbiter (Amiri et al., 2022) of the United Arab Emirates, which entered orbit in February 2021; the Tianwen-1 (Li et al., 2021) of the China National Space Agency (CNSA), consisting of an orbiter, a lander and a rover (called Zhurong), which landed in May 2021. The Hope and Tianwen-1 missions, as well as the NASA Perseverance rover (section 3.2), were launched in July 2020, within a favorable launch window. The ESA/Roscosmos Exomars rover, named after Rosalind Franklin, was expected to aim at the same window, but it was first postponed to the window of 2022 due to delays related to the Covid-19 pandemic, and then to no earlier than 2028 due to the termination of collaboration between ESA and Roscosmos in the scope of the conflict in Ukraine.

3.1.1 The Mars Exploration Rovers

The Mars Exploration Rovers (this section) and Mars Science Laboratory (section 3.1.2) are the NASA rover missions that made the strongest impact in the in-situ investigation of Mars, followed by the Perseverance rover, which inherited a large part of their technology (especially from MSL).

The Mars Exploration Rovers (Crisp et al., 2003) comprised two rovers, Spirit (also known as MER-A or MER-2) and Opportunity (also known as MER-B or MER-1), that were launched separately in 2003 and landed the following year on Mars. Spirit landed, as expected, in the Gusev crater (Golombek et al., 2003), a 160 km-diameter impact crater that, similarly to Jezero, was believed to have hosted liquid water in the past, as witnessed by an inflow channel in the southern side of the crater (Cabrol et al., 2003). Opportunity landed in the small Eagle crater within Meridiani Planum, a flat plain characterized by the orbital signature of gray hematite observed by the Mars Global Surveyor. The two rovers were expected to carry on tasks for 90 sols, but their mission was periodically extended many times due to their excellent performance. They were equipped with solar panels, which constrained them to stop frequently to charge the batteries, in particular during the martian winter. In May 2009, after driving a total of 7.7 km, Spirit got stuck in soft sand, without the luck of being freed despite the many attempts. Therefore, in 2010 it was "redefined" as a stationary research platform (similar to a lander), but on sol 2208 there was the last communication from the rover, and in 2011 the mission of Spirit was declared concluded. Opportunity carried on activities and survived until 2018, when a planetary dust storm contributed to covering its solar panels with thick dust, which reduced drastically its power levels. After many attempts to regain communication with the rover, in 2019 also Opportunity's mission was concluded, with a total distance traveled of 45 km.

Figure 3.4: *Panoramic mosaic of the "Home Plate" plateau realized with images from the Navigation Camera of the Spirit rover in 2009. Credits: NASA/JPL-Caltech.*

The principal aim of the rovers was to characterize the geology, mineralogy and geologic history of their sites, and appraise the presence of water or its effects on rocks in the past. For this reason, they were provided with some instruments, forming the Athena science payload (Squyres et al., 2003) that included the Mössbauer spectrometer MIMOS II (Klingelhöfer et al., 2003), the Alpha Particle X-Ray spectrometer APXS (Rieder et al., 2003), the miniature thermal emission spectrometer Mini-TES (Christensen et al., 2003), a rock abrasion tool (Gorevan et al., 2003), a microscopic imager to capture close-ups of soil and rocks (Herkenoff et al., 2003), a pair of stereoscopic cameras (Pancam; Bell et al., 2003), and several cameras for navigation and hazard avoidance (Navcams and Hazcams, respectively; Maki et al., 2003). Magnets were also placed in different parts of the rovers, in order to study the magnetic properties of martian dust (Madsen et al., 2003).

Several interesting results were returned by the two rovers. Although its appearance as a dry lake, Gusev crater did not show evidence for lacustrine sedimentation, but rocks were characterized by coating suggesting a limited alteration due to water (Squyres et al., 2004a), and by a basaltic nature including olivine and pyroxene minerals, but also plagioclase and magnetite (McSween et al., 2004). In particular, the latter was recognized to be the cause of magnetism in dust, which was thought to be all magnetic as result of the analysis of the magnets on the rover (Bertelsen et al., 2004). In addition, significant abundances of Nickel were found in the soil of the plain, where the rover performed abrasion on rocks, revealing similarities with komatiites and shergot-

Figure 3.5: *Mosaic of images from the Navigation Camera of the Opportunity rover showing the landscape from the top of the 135 meter-high "Cape Tribulation", on the western rim of Endeavour crater that Opportunity visited between 2014 and 2017. Credits: NASA/JPL-Caltech.*

tites found on Earth (Gellert et al., 2006). During its traverse, Spirit also investigated the Columbia Hills, a group of heights within Gusev. There, it discovered several different categories of rocks (Squyres et al., 2006), some of which showed traces of clays and carbonate, implying that the region had likely experienced liquid water (Ming et al., 2006; Morris et al., 2010). Within the Columbia Hills, Spirit explored a plateau named "Home Plate" (figure 3.4), a hot spring deposit that was also proposed as landing site for the Perseverance rover. On Opportunity's side, the Eagle crater was confirmed to have been covered in water in the past. This thesis was supported by many observations, such as the presence of spherules in the rock matrices, vugs, and sulfates, as well as sedimentary rocks (Squyres et al., 2004b). In addition, Opportunity assessed the presence of hematite, a mineral that usually forms in water, that was previously observed from orbit, and jarosite (Arvidson et al., 2006). However, this water was likely salty and acidic, and therefore not suitable for life. Similar results were retrieved also in two craters that the rover visited, named Endurance and Victoria. At the rim of the large Endeavour crater (figure 3.5), where Opportunity terminated its mission due to the high atmospheric optical depth of dust, the rover found significant fractions of clay minerals, that form in neutral-pH water. This suggested that the location of Endeavour hosted plenty of liquid water favorable to the development of life. This observation was also justified by veins of gypsum in rocks, that typically results from the evaporation of water (Squyres et al., 2012).

Both rovers also made astronomical observations. Spirit and Opportunity took the first pictures of the Earth and the Moon from another planet, and observed the martian moons Phobos and Deimos multiple times, including their transits in front of the Sun (Bell et al., 2005).

3.1.2 The Mars Science Laboratory

In 2011, a few months after the conclusion of the Spirit rover mission, NASA launched the Mars Science Laboratory mission, that landed the rover Curiosity (figure 3.6) in 2012 within Gale crater (Grotzinger et al., 2012). The rover, which is still active, is larger, heavier and more complex than any past rover, which is why it did not land using airbags and parachute as for Pathfinder and MER, but the parachute was followed by a rocket-powered descent stage (named "sky crane") that gently dropped the rover on the surface through cables. In addition, Curiosity is advantaged by its thermoelectric generator, which is not affected by dust deposition, and by a 2.1 m robotic arm. In its payload, the rover carries a number of scientific instruments for imaging, spectroscopy and analysis of minerals and textures. Twelve engineering cameras (Navcams and Hazcams, as on MER; Maki et al., 2012) are used to assist navigation and avoid obstacles. The five scientific cameras include: MastCam, a multispectral stereoscopic pair of cameras (similar to MER's Pancam; Bell et al., 2017; Malin et al., 2017); the Mars Hand Lens Imager (MAHLI; Edgett et al., 2012), mounted on the arm of the rover, that takes microscopic images of geologic targets; ChemCam (Maurice et al., 2012; Wiens et al., 2012), that employs the LIBS (Laser-Induced Breakdown Spectroscopy) technique and the high-resolution black-and-white Remote Micro-Imager (RMI); the Mars Descent Imager (MARDI; Malin et al., 2017), that acquired images during the landing of the rover. Besides the cameras, Curiosity also relies on: the Alpha Particle X-Ray Spectrometer (APXS, evolution of the homonymous on MER), that can irradiate alpha particles and extract the X-Ray spectra of rocks, to retrieve their composition, and is mounted on the robotic arm; the Chemistry and Mineralogy (CheMin; Blake et al., 2012) suite, that analyzes minerals through X-Ray diffraction and fluorescence; the Sample Analysis at Mars (SAM; Mahaffy et al., 2012), which studies gasses and organic compounds in samples; the Dynamic Albedo of Neutrons (DAN; Mitrofanov et al., 2012), that carries a neutron source and a detector to search for water under the surface; the Radiation Assessment Detector (RAD; Hassler et al., 2012), that measures radiation rates over time in the scope of future human missions; the Rover Environmental Monitoring Station (REMS; Gómez-Elvira et al., 2012), that is a meteorological station for humidity, temperature, pressure, wind and UV radiation.

The results returned so far by Curiosity are outstanding. It found evidence that Gale crater once hosted a lake and rivers that lasted for at least millions of years (Williams et al., 2013). In fact, water was detected in soil, and Gale was once a habitable environment for potential microbial life forms. In one of the sites visited by the rover, named Yellowknife Bay, Curiosity extracted a sample from mudstone, which unveiled the presence of clays and the basic bricks for life, such as sulfur, nitrogen, oxygen, carbon and phosphorus (Grotzinger et al., 2013). Heavy isotopes of carbon, together with

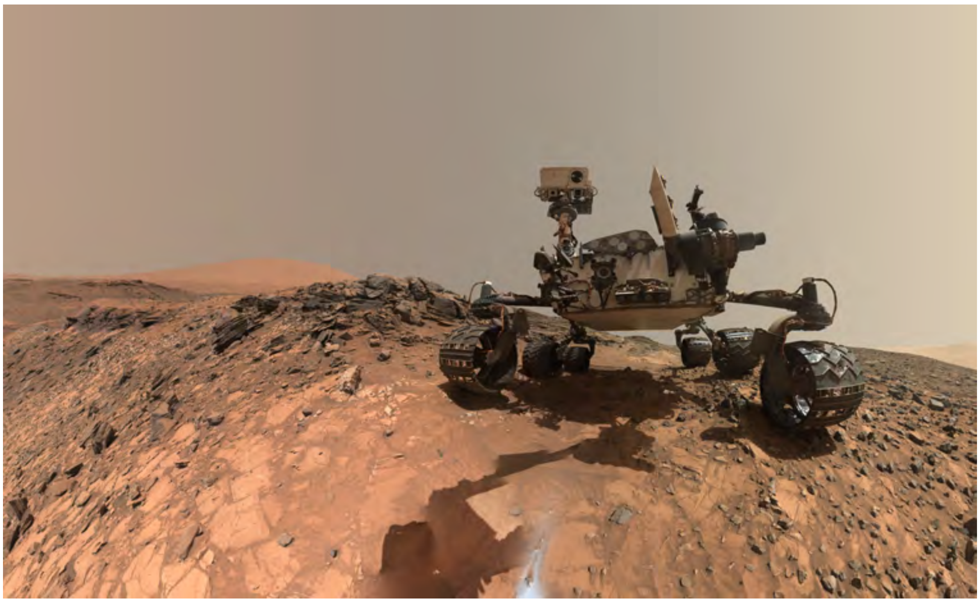

Figure 3.6: *A "selfie" mosaic of the Curiosity rover acquired in 2015 using the MAHLI instrument mounted at the end of its robotic arm. In this context, the rover was attempting to drill a rock named "Buckskin" on Mount Sharp, the central peak of Gale crater. Credits: NASA/JPL-Caltech/MSSS.*

hydrogen and argon, were found in the atmosphere by the SAM instrument, allowing to determine that a significant fraction of its atmospheric gasses and surface water was lost over Mars' history (Mahaffy et al., 2014). Curiosity observed periodic variations in the fraction of atmospheric methane (with some prominent seasonal peaks), a component that might be the result of either biological or chemical processes (Webster et al., 2014). In the scope of future human missions on Mars, the RAD instrument measured high levels of radiation (cosmic rays and solar energetic particles; Hassler et al., 2013), that will have to be considered for the design and the choice of materials for spacecraft and suits. When observing the sky, Curiosity not only took images of the Earth and the Moon and recorded the transits of Phobos and Deimos in front of the Sun (Lemmon et al., 2013), but also captured the transit of Mercury on the solar disk, an event that was not possible for Spirit and Opportunity due to the lower resolution of their Pancam cameras.

3.2 The Perseverance rover

Mars 2020 (Farley et al., 2020) is a space mission developed by NASA as part of the Mars Exploration Program. The mission is focused on the in-situ exploration of Mars from its surface through the use of a rover, named Perseverance (figure 3.7), in the wake of the previous NASA rovers Spirit and Opportunity, and Curiosity, described in the previous sections. Perseverance inherits its design from Curiosity, but with a different payload and several improvements and adjustments. The Perseverance rover has similar size as Curiosity (2.9 m of length by 2.2 m of width) and is provided with a mast (for a total height of 2.7 m) and a robotic arm of 2.1 m. It is also equipped with six wheels that allow it to move on the martian regolith and reach a maximum speed of 152 m/h on flat ground, and like Curiosity is powered by a Multi-Mission Radioisotope Thermoelectric Generator (MMRTG) based on plutonium dioxide. The wheels are slightly larger in diameter, narrower and made of a thicker aluminum than those of Curiosity and should ensure a higher endurance, while the MMRTG is expected to provide sufficient energy for more than a decade, and gives the rover the advantage of not having to rely on solar panels. At the end of the robotic arm there is a drill, which can use rotary or percussive motion and different bits to make abrasions (i.e., to scrape off the top layer of rocks) and coring (i.e., deeper penetration to collect samples). Moreover, Perseverance has more processor power than Curiosity, enabling a longer and more efficient autonomous navigation. The rover can communicate with the Earth through antennas, similarly to previous rovers. Indeed, it is equipped with an X-Band low-gain antenna for signal reception, an X-Band high-gain steerable antenna to send signal directly to Earth, and an Ultra-High Frequency (UHF) antenna to transmit signals to the Mars orbiters that will relay them towards Earth.

Figure 3.7: *The Perseverance rover performing driving tests at the end of 2019 in the clean room facility at NASA's Jet Propulsion Laboratory in Pasadena, USA. Credits: NASA/JPL-Caltech.*

After the first official announcement of this mission in the late 2012 and the final selection of the scientific instruments for its payload in 2014, the flight capsule containing the rover was launched from Cape Canaveral (FL) on July 30^{th}, 2020, on a

United Launch Alliance Atlas V rocket (figure 3.8a). The capsule reached Mars in 203 days, on February 18th, 2021. In order to brake within the atmosphere, a parachute was deployed from the descent stage (figure 3.8b), also called sky crane. During this phase, a camera located on the bottom of the rover, named Lander Vision System Camera (Cheng et al., 2021), took images of the surface that were processed by a computer onboard, which determined the ground-position of the rover by comparison with maps and directed the descent towards a safe touchdown area. Once the sky crane and the rover reached 1.9 km above the ground, they detached from the upper shield of the capsule and some small rocket propulsion jets turned on from the sky crane, which gently dropped the rover on the surface with cables at 20:55 UTC. Upon touch-down, the rockets drove the sky crane away from the landing spot of the rover. Simultaneously, the landing phase was imaged by the TGO and by the HiRISE camera of the NASA Mars Reconnaissance Orbiter. In addition, for the first time it was possible to follow the whole landing from the rover's point of view thanks to a set of cameras (Entry, Descent and Landing cameras, or EDL) installed inside the sky crane and looking upwards at the parachute and downwards at the rover. The rover landed quite close to the center of the predicted landing ellipse, on the floor of the Jezero crater at martian coordinates 18.38°N 77.58°E. The spot was later renamed after Octavia E. Butler, a famous American science fiction writer.

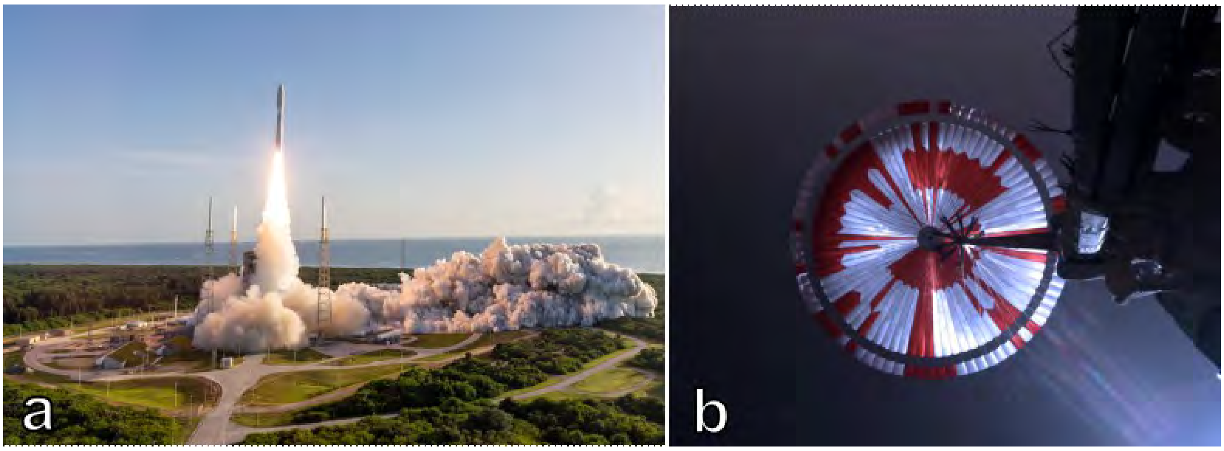

Figure 3.8: *(a) Launch of the Mars 2020 mission from Cape Canaveral (USA) on July 30th, 2020. Credits: NASA/ULA. (b) Parachute of the landing stage of the Perseverance rover imaged during the descent into the martian atmosphere by the Parachute Up-Look Camera B, on February 18th, 2021. The red and white stripes form a code meaning "dare mighty things". Credits: NASA/JPL-Caltech.*

3.2.1 Science objectives and the Mars Sample Return

Since Giovanni Schiaparelli's observations with the telescope, Mars has always been in the collective imagination as a planet crawling with life. Later exploration by orbiters and rovers showed that this is likely not the case, but the planet might have hosted life forms in the past. Astrobiology is one of the main objectives of the Mars 2020 mission. Jezero crater has the aspect of a dry lake with in- and out-flow channels, and is thought to have been filled with liquid water, which explains why it was considered as a potentially habitable environment billions of years ago (Mangold et al., 2020). There, in every location or environment that is characterized by favorable conditions for past life, the rover looks for materials with biosignatures, that is evidence of present or past microbial life, such as complex organic molecules, elements, products of biological processes or direct observation.

The most common objective for this and all previous in-situ missions is geology. Studying the geology of the martian environment is critical not only to understand the diversity of rocks and minerals of the place, but also to rebuild its geological and stratigraphic history. The presence of rocks that also appear on Earth or that show the same aqueous or volcanic alterations can be significant to give a clear idea of the large-scale processes that happened (including meteoritical impacts) and of how it must have looked like a few billion years ago. In addition, Perseverance's research is not limited to the search of favorable conditions only for ancient life, but it extends also to future human exploration. In the last few years, the world started designing and preparing for future manned missions to the Red Planet. Therefore, one of the objectives is to investigate how humans will be able to survive within a habitat that is close to that of the Earth, but still rather hostile, with the goal to establish a relatively comfortable outpost. One experiment carried by the rover is MOXIE (Hecht et al., 2021), an In-Situ Resource Utilization technology to transform martian CO_2 into O_2. Another aspect to analyze is the size of dust and its properties. Dust is measured by the MEDA suite (Rodriguez-Manfredi et al., 2021), which also contributes to the assessment of the climate within Jezero. Studies were carried out by MEDA during the entry, descent and landing phase, to test the protection to the rover by the thermal shells in the moments of highest friction, and on the ground to keep track of the local weather, in order to design the best landing system, spacesuits and essential infrastructures for the future human missions.

The Perseverance rover is just the first phase of a more complex and ambitious mission. In fact, one of the tasks of the rover (and the scientists) is to select and collect a set of rock samples for their future return to Earth, where they will be opened and studied in laboratory. This objective is part of the Mars Sample Return mission (Kminek et al., 2022), which is expected to be performed in the next years with the collaboration of the European Space Agency, for the arrival of the samples on Earth in the early 2030's (figure 3.9). Each time the rover uses the coring bit of the drill to extract a sample, the latter is imaged for reference and inserted in the tube. Then, the tube is sealed and safely stored in the caching system in the front of the rover (Moeller et al., 2021).

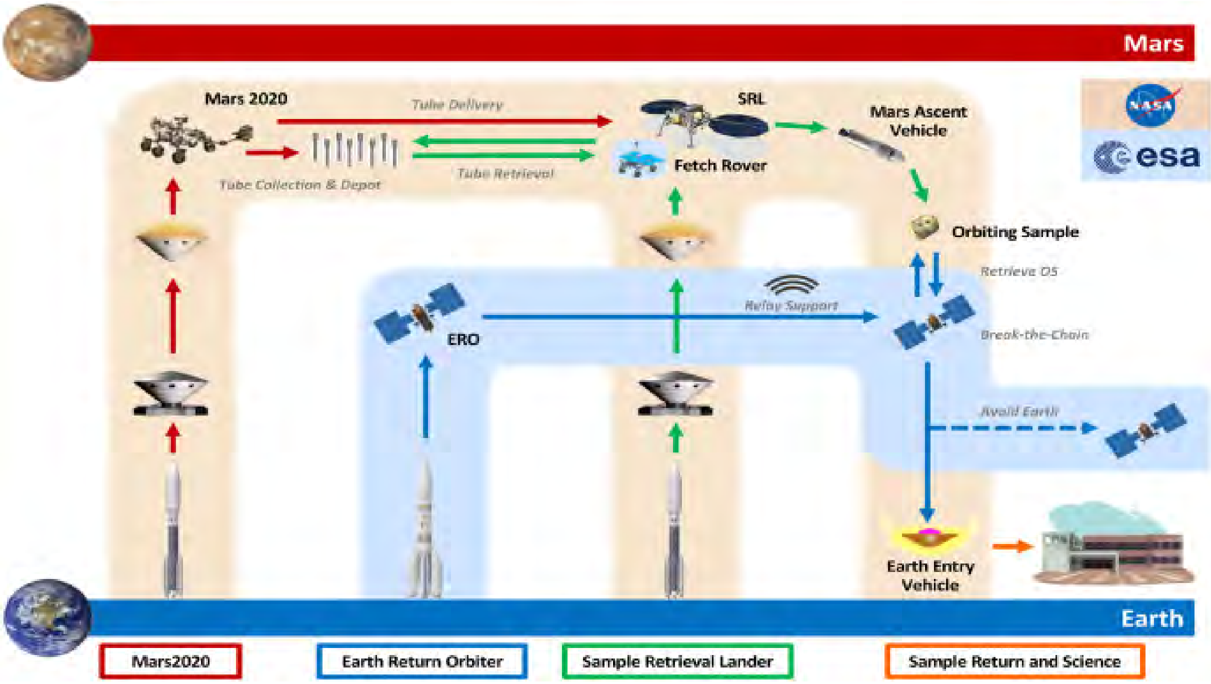

Figure 3.9: *Basic scheme illustrating the Mars Sample Return mission, which will aim at retrieving and bringing to Earth the martian samples collected by Perseverance. Figure from Muirhead et al. (2020).*

Once a sufficient number of tubes with different rock types is cached, all these tubes are released on the surface. By 2026-2027, two NASA-ESA missions are expected to be launched. One will insert an orbiter around Mars, while the other one will be a lander hosting a small probe and a small rocket. The lander will reach the surface and release the probe (a rover or a helicopter), which will collect the sample tubes and load them into the small rocket. This will then lift off and deliver the sample tubes to the orbiter, which will finally make its way back to Earth with the precious payload. The Mars Sample Return mission is extremely challenging, but for the first time it will give the chance to analyze portions of minerals chosen wisely on Mars, an unprecedented milestone of space exploration.

3.2.2 Cameras and instruments

The payload of Perseverance consists of a set of EDL and engineering cameras, seven scientific instruments and one technologic demonstrator, the mini-helicopter Ingenuity.

Seven cameras formed the EDL system (Maki et al., 2020). Of these seven: three were mounted on the backshell above the sky crane, looking up towards the parachute; one was at the bottom of the sky crane looking down at the rover; one was mounted on the deck of the rover, looking upward at the descent stage; one was on the "belly" of the rover, looking towards the surface during landing. These cameras were extremely useful at showing the world for the first time a multi-angle footage of the complete landing of a human manufacture on another planet.

In general, the engineering cameras (Maki et al., 2020) are used for safety and control. The Navigation Cameras, or Navcams, are two color cameras located on the mast of the rover acting as its "eyes" showing what is in front of the rover and helping drive it. They are critical in ensuring a safe path for the autonomous navigation of the rover, being able to resolve objects of a few cm at 25 m distance. In order to detect hazards on the surface in front and back of the rover, four Hazard Avoidance Cameras, or HazCams, are mounted on the front of the rover and two on the rear side. They assist in avoiding smaller rocks that can damage the wheels and the robotic arm in its motion. Finally, the CacheCam is one camera mounted inside the caching system of the rover. Every time a sample tube is filled with material, the CacheCam captures an image of the top of the sample in the tube before it is sealed and stored, in order to make sure that the tube was filled correctly and to allow a first assessment of its content.

The seven scientific instruments onboard Perseverance (figure 3.10) were officially announced by NASA on July 31^{st}, 2014. They are briefly described in alphabetical order as follows.

- Mastcam-Z (Bell et al., 2021) is a multispectral, stereoscopic pair of cameras capable of zoom mounted on the mast of the rover. Given that this thesis is focused on the calibration of Mastcam-Z images, it is treated more exhaustively in section 3.2.3.

- MEDA (Mars Environmental Dynamics Analyzer; Rodriguez-Manfredi et al., 2021) is a set of detectors that measure the properties of wind, temperature, humidity and dust in the atmosphere of Mars. The sensors are located on the mast of the rover, the deck, the front side and inside the rover. It can be considered as a weather station that can determine the weather conditions, the size and concentration of airborne dust, wind speed, radiation at the surface, relative humidity, atmospheric pressure and air temperature.

- MOXIE (Mars Oxygen In-situ Resource Utilization Experiment; Hecht et al., 2021) is an experimental demonstrator that electrolyzes martian carbon dioxide CO_2 to produce oxygen O_2. The concept of this instrument is designed in the optics of future human missions on Mars, where the explorers will have to use the available resources to survive. MOXIE is located inside the body of the rover.

- PIXL (Planetary Instrument for X-Ray Lithochemistry; Allwood et al., 2020) is an instrument mounted at the end of the robotic arm. It conveys an extremely thin X-Ray beam to a target rock and measures the X-Ray fluorescence emitted by fine-scale geologic features. Its X-Ray beam has a spatial resolution of 0.12 mm-diameter, which allows it to analyze the elemental composition in relation to the texture of the targets, and which is higher than the other APXS instruments on previous rovers.

- RIMFAX (Radar Imager for Mars' SubsurFAce eXperiment; Hamran et al., 2020) is a Ground Penetrating Radar located in the rear of the rover. Its objective is to study the shallow subsurface of Jezero and retrieve information on its stratigraphy, in particular how the different layers underneath are linked to the visible outcrops. It has a frequency range from 150 MHz to 1.2 GHz and can work on shallow or deep penetration, with the expectation of reaching 10 m of depth.

- SHERLOC (Scanning Habitable Environments with Raman and Luminescence for Organic and Chemicals; Bhartia et al., 2021) is a Raman and fluorescence spectrometer mounted at the end of the robotic arm. It is provided with a Deep Ultraviolet laser of 100 μm-diameter and an optical system. Its aim is to detect potential biosignatures by characterizing organic compounds and assist with mineralogical identification, as well as to appraise the aqueous history of Mars and assist in the choice of targets to sample, in particular by imaging and analyzing the abrasion patches. Besides its context camera and spectrometer, SHERLOC is supported by an integrated color camera called WATSON (Wide Angle Topographic Sensor for Operations and eNgineering) used to take detailed images of rock textures.

- SuperCam (Wiens et al., 2021; Maurice et al., 2021) is a remote-sensing instrument located at the top of the rover's mast, just above Mastcam-Z. Its objective is to determine the geochemistry of rocks and samples. SuperCam is made of a 1064 nm laser, that can study the elemental composition of targets up to 7 m distance through the Laser Induced Breakdown Spectroscopy (LIBS) technique, a spectrometer (Visible and Infrared), and a Remote Micro-Imager (RMI) that can capture high-resolution color images. It is also provided with a calibration target (Cousin et al., 2022) situated on the deck of the rover.

It is also worth mentioning the presence of a microphone on the chassis of the rover (Maki et al., 2020) and one integrated into SuperCam (Chide et al., 2020). The latter is currently used to hear not only the noise emitted upon the use of the laser, but also the motion of sand, the whistling of the wind and the driving of the rover itself.

One of the most futuristic elements of the Mars 2020 mission is the Mars Helicopter Ingenuity (figure 3.11) (Balaram et al., 2021), a technology demonstrator designed to perform at least three flights. Ingenuity has a mass of less than 2 kg and two rotors of 1.2 m each, which allow it to hover easily within the thin atmosphere, and is supplied

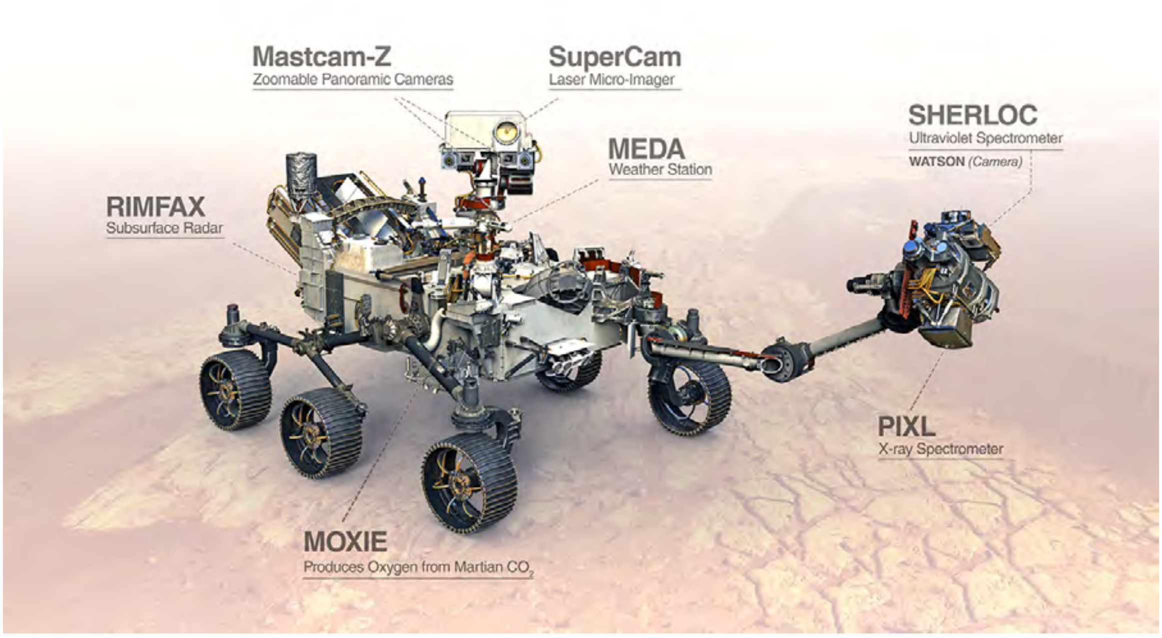

Figure 3.10: *The seven scientific instruments in the payload of the Perseverance rover. Credits: NASA/JPL-Caltech.*

with solar panels and two down-looking cameras, one in colors and one in black and white for navigation. Due to the large time-light distance between the Earth and Mars (13 light-minutes on average), the flights are not controlled remotely in real time, but they are preset and sent to the helicopter. Thanks to its result above the expectations, Ingenuity has been used for many more than three flights, to test the endurance of such technology in time, following Perseverance in its drives (the helicopter can communicate with the Earth through an antenna fixed on the rover) but keeping at safe distance, paving the way for a potential development of Unmanned Aerial Vehicles that can contribute even more to the planetary rover exploration in the future.

3.2.3 The Mastcam-Z camera

Mastcam-Z (figure 3.12a; Bell et al., 2021) is a multispectral, stereoscopic pair of cameras capable of zoom and focus, mounted on top of the Remote Sensing Mast of Perseverance, just below the SuperCam instrument (figure 3.12b). Its two CCD sensors have Bayer patterns that can acquire broad-band Red/Green/Blue color images through a broad IR-cutoff filter. In addition, each camera is equipped with six narrow-band filters that span the visible and near infrared spectrum (400-1050 nm), and one filter for the observation of the Sun, all mounted in filter wheels in front of the sensors. The cameras have resolutions that allow to distinguish objects of 1 mm from 2 m and of 3 cm from 100 m distance, with field of view ranging between 7.7° and 31.9° diagonally.

Figure 3.11: *A flight model of the Ingenuity helicopter, the technology demonstrator carried to Mars by the Perseverance rover. Credits: NASA/JPL-Caltech.*

The imaging system of Mastcam-Z was inherited from the Mastcam instrument of the Curiosity rover. The instrument relies on two passive calibration targets, fixed on the deck of the rover, that ensure a consistent calibration to units of reflectance (Kinch et al., 2020). The Mastcam-Z calibration targets and the concept of reflectance calibration are illustrated in chapter 4. Table 3.1 is a summary of all the filters of Mastcam-Z, including their names and bandwidths. The bandpasses of all the filters (except those for solar observation) are represented in figure 3.13.

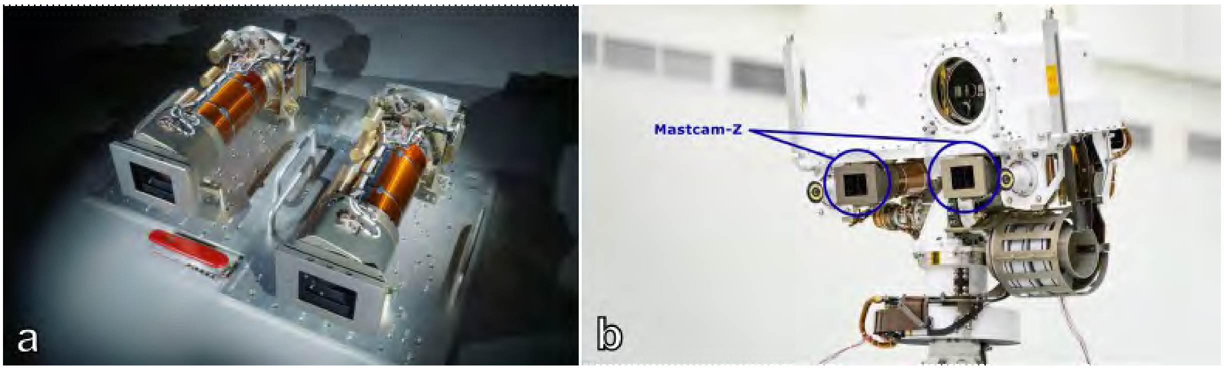

Figure 3.12: *(a) The two cameras forming Mastcam-Z. (b) The position of Mastcam-Z on the mast of the Perseverance rover. The circular lens just above is the SuperCam instrument. Credits for both images: NASA/JPL-Caltech/MSSS/ASU.*

In general, Mastcam-Z has three main goals. Firstly, it has to describe and characterize the geology and geomorphology of the rover site within Jezero. This characterization includes morphology, stratigraphy and multispectral behavior of rocks and outcrops, in order to assess their composition, history, modifications, layers and boundaries, textures, and weathering. Even the rover tracks on the regolith and other parts of the rover itself are imaged and studied. In particular, multispectral analyses are of

Filter name	Range [nm]	Filter name	Range [nm]
L0B (Blue Bayer)	480 ± 46	R0B (Blue Bayer)	480 ± 46
L0G (Green Bayer)	544 ± 41	R0G (Green Bayer)	544 ± 42
L0R (Red Bayer)	630 ± 43	R0R (Red Bayer)	631 ± 43
L1	800 ± 9	R1	800 ± 9
L2	754 ± 10	R2	866 ± 10
L3	677 ± 11	R3	910 ± 12
L4	605 ± 9	R4	939 ± 12
L5	528 ± 11	R5	978 ± 10
L6	442 ± 12	R6	1022 ± 19
L7	590 ± 88, ND6	R7	880 ± 10, ND5

Table 3.1: *Summary of all the filters of Mastcam-Z with their centroids and bandwidths expressed as Half Width at Half Maximum. The filters L0 and R0 are the Red/Green/Blue Bayer patterns integrated within the detectors. The L7 and R7 solar filters are designed to attenuate the solar flux by factors of 106 (ND6) and 105 (ND5).*

great importance in the scope of reflectance spectroscopy to gain insights on the minerals, such as their hydration and iron-bearing phases, that can be compared to analogue materials on Earth and whose spectra are known from laboratory measurements. The second goal is the assessment of atmospheric properties and processes in relation to the surface. From the direct observation of the Sun and the sky in its immediate vicinity through the thin martian atmospheric layer the optical depth can be estimated, in connection to the airborne dust content and its grain-size, as well as the motion of volatile substances and clouds. Furthermore, thanks to a highly precise computation of astronomical ephemeris, it is possible to witness interesting phenomena as the transit of natural satellites in front of the Sun (e.g., the transit of Phobos, that had already been captured by MER and MSL, was recorded at high resolution by Perseverance on sol 397) and solar sunspots. As a third – but not less important – goal, Mastcam-Z is meant to contribute to the other operations of the rover. These include navigation, sample selection and caching, and public outreach. The advantage of being a pair of cameras enables the production of stereo-DTM (Digital Terrain Model) reconstructions of rocks and outcrops, that can be obtained through the wise combination of its stereoscopic images with high-resolution remote-sensing imaging from the martian orbiters. This task is fundamental for the development of softwares for the internal team in order to "see" virtual 3D representations of the rover site in scale (with computer screens and VR visualizers) that help comprehend the distances and take decisions on the driving of the rover or the choices of targets to pursue.

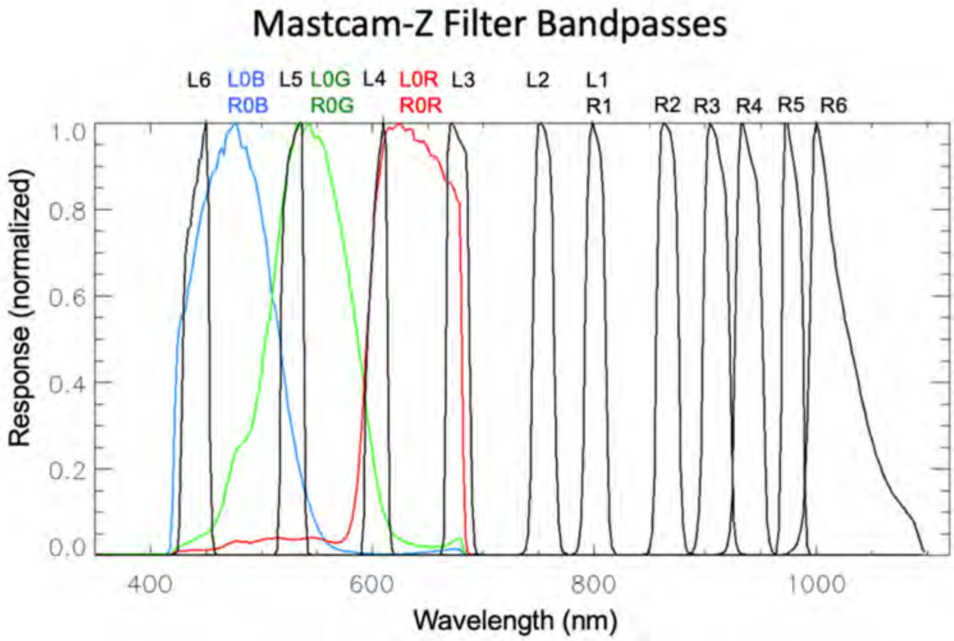

Figure 3.13: *Transmission profiles of the broad-band and narrow-band filters of Mastcam-Z normalized by their respective maxima. The solar filters L7 and R7 are not represented. Credits: NASA/JPL-Caltech/MSSS/M. Rice/A. Hayes/J. Bell.*

Chapter 4

The Mastcam-Z radiometric calibration targets

This chapter gives an overview on the calibration targets of Mastcam-Z and their principle of use a priori (as predicted before the landing of Perseverance on Mars). It opens, in section 4.1, with a basic introduction to the most important physical quantities needed for the definition of the concept of reflectance and the laws by which they are ruled, as well as the different forms of reflectance. Section 4.2 briefly reports on the calibration targets on the Mars Exploration Rovers, the Mars Science Laboratory and the Phoenix lander missions, from which Perseverance inherited the most. The calibration targets of Mastcam-Z are described in section 4.3, along with their theoretical formalism and their predicted application on Mars.
As a relevant remark, section 4.1 is based extensively on Hapke (2012) and Shepard (2017), and section 4.3 on Kinch et al. (2020).

4.1 Introduction to planetary reflectance

One of the multiple ways of investigating the nature and characteristics of rocks and minerals is to use a technique called reflectance spectroscopy. It consists in studying the dependency of reflectance, a basic property of all bodies, on the wavelength. Reflectance is the quality of a medium to reflect radiant energy, and is usually defined formally as the fraction of incident radiant flux that is reflected or scattered by the material. Three entities play a role in this phenomenon: a light source (for instance, the Sun), a reflecting medium (the surface of a rock), and an observer (the sensors of a camera or our eyes). The incident direction is the straight line that goes from the target to the light source, while the emission direction is the straight line from the target to the observer or the detector. In order to describe the illumination geometry, that is the positions of the light source and observer relative to the plane of the target, we define three angles, illustrated in figure 4.1: (i) the incidence angle i ($0° \leq i \leq 90°$) is the angle between the normal vector to the plane of the target and the incident direction, (ii) the emission angle e ($0° \leq e \leq 90°$) is the angle between the normal vector to the plane of the target and the emission direction, and (iii) the azimuth angle Az ($0° \leq Az \leq 180°$) is measured on the plane of the target and is the angle between the planes of incidence and emission. The angles i and e are measured from the normal direction: for instance, the configuration with $i = 0°$ and $e = 0°$ means that the target is illuminated and observed from straight above. The azimuth is usually measured from the plane of incidence to the plane of emission, and its higher limit is 180° (instead of 360°) due to hemispherical symmetry of the plane of incidence (e.g., $Az = 120°$ is the same as $Az = 240°$). In addition, the angle between the directions of incidence and emission (measured on the plane that contains the two directions) is called phase angle p ($0° \leq p \leq 180°$). Knowing i, e, and Az, the phase angle can be easily retrieved as follows:

$$p = \arccos[\cos i \ \cos e + \sin i \ \sin e \ \cos Az] \, . \tag{4.1}$$

When $Az = 0°$ or $Az = 180°$, the incident and emission directions lie on the same plane, that is perpendicular to the plane of the target. This is known as the principal plane.

We call "irradiance" the light flux coming from the source and hitting the surface of the medium target, with units W m^{-2} and denoted by F. After the interaction between the irradiance and the target, with possible transmission and absorption, some fraction of light will be scattered in all directions, including towards the observer. We call this observed flux "radiance", denoted by I and with units W m^{-2} sr^{-1}. The lights hitting the target and reflected by the target have different degrees of collimation depending on the model used to describe them. The collimation can be defined as directional, if the beam is highly collimated; conical, if the beam can be represented by a limited solid angle; hemispherical, if the light comes from or is scattered to the whole hemisphere above. The case, which opens to different definitions of reflectance, is determined by the overall conditions, including the light source, the target surface, and the presence of an atmosphere that might enhance diffusion. In the martian situation of Mastcam-Z, the collimation of the incident light is assumed to be directional, because it comes from the disk of the Sun. The light from the target is expected to be re-emitted in all directions (though not isotropically), but it is observed in only one direction, through the sensors of Mastcam-Z. Hence, we deal with the concept of "bidirectional" reflectance.

In order to define the bidirectional reflectance, two useful laws must be introduced. They are called "cosine laws" and are named after the illustrious scientist Johann Heinrich Lambert (1728-1777), who made meaningful progress in the field of photometry, outlined in his Photometria (1760). The cosine incident law states that the power incident on a surface is proportional to the cosine of the incident angle. This can be written

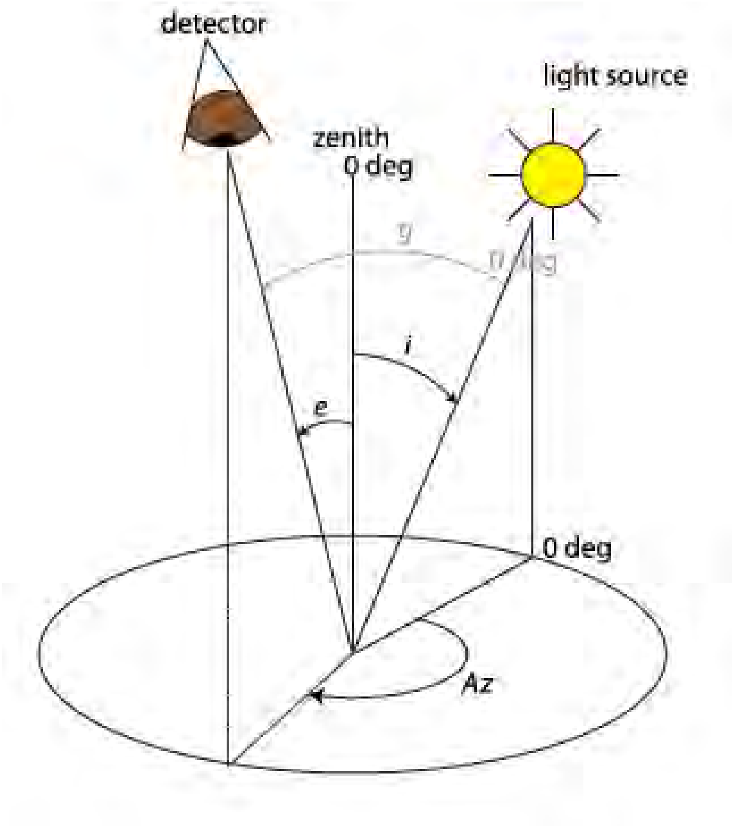

Figure 4.1: *Schematic illustration of the angles that describe the illumination geometries between the light source and the detector. Az is the azimuth, i is the incidence angle, e is the emission angle, and g is the phase angle, which is denoted by the letter p in the text. Figure from Buz et al. (2019).*

as:

$$I_{Lam}(i, e, Az) = I_{Lam}(0, 0, 0)\ \mu_0\ , \tag{4.2}$$

where $\mu_0 = \cos i$ and the subscript *Lam* represents a standard Lambertian surface, which is a surface that appears to show the same radiance regardless of the observation geometry, and can reflect a fraction k ($0 \leq k \leq 1$) of the incident light. The fact that the radiance does not change as the emission angle changes is related to the cosine emission law, which states that the intensity of light from a diffusely reflecting or emitting surface is proportional to the cosine of the emission angle. Indeed, when a surface is seen under an emission angle e, there is a balance between the increase in area observed due to projection and the decrease in the amount of energy reflected per area. When the light from a source hits a Lambertian surface, a simple radiative transfer model yields:

$$I_{Lam} = k\,\frac{F}{\pi}\ . \tag{4.3}$$

Materials approximating the Lambertian standards can be manufactured and have multiple applications, among which instrumental calibration targets (the Mastcam-

Z calibration target materials are made of alumina ceramics). In addition, a further idealization of the Lambertian surface leads to the concept of the perfect Lambertian surface, which has the same features of a Lambertian standard but reflects 100% of light back towards the upper hemisphere without absorption ($k = 1$). In practice, perfect Lambertian surfaces have never been obtained, but one of the materials that best approximate them is Spectralon®. The equations for a perfect Lambertian are obtained by simply setting $k = 1$. For example, equation (4.3) becomes:

$$I_{Perf\,Lam} = \frac{F}{\pi} \, . \tag{4.4}$$

The bidirectional reflectance r introduced above can be expressed mathematically as the ratio between the measured radiance and the collimated incident irradiance:

$$r(i, e, Az) = I(i, e, Az)\,\frac{\mu_0}{F} \, , \tag{4.5}$$

and has the unit sr^{-1}. The application to a standard Lambertian leads to:

$$r_{Lam} = k\,\frac{\mu_0}{\pi} \, , \tag{4.6}$$

and, for a perfect Lambertian surface,

$$r_{Perf\,Lam} = \frac{\mu_0}{\pi} \, . \tag{4.7}$$

Dividing the bidirectional reflectance by $\cos i$ yields the bidirectional reflectance distribution function r_{BRDF} (with unit sr^{-1}), that is simply the ratio between the observed radiance and the incident irradiance:

$$r_{BRDF}(i, e, Az) = \frac{I(i, e, Az)}{F(i)} = \frac{r}{\mu_0} \, , \tag{4.8}$$

which for a Lambertian standard becomes:

$$r_{BRDF,Lam} = \frac{k}{\pi} \, , \tag{4.9}$$

and for a perfect Lambertian $r_{BRDF,Perf\,Lam} = \pi^{-1}$. These two reflectances, r and r_{BRDF}, lead to the definition of two fundamental parameters: the radiance factor, also known as apparent albedo, I/F or IOF, and the radiance coefficient, also named reflectance factor or R*. The radiance factor is defined as the radiance of a medium under some illumination geometry relative to the radiance of a Lambertian surface illuminated and viewed normally. It can be written as:

$$r_f = IOF = \frac{I(i,e,Az)}{I_{Lam}(0,0,0)} = \pi\,\mu_0\,\frac{I(i,e,Az)}{F} = \pi\,r = \pi\,\mu_0\,r_{BRDF}\,. \tag{4.10}$$

For a Lambertian standard, equation (4.10) becomes:

$$r_{f,Lam} = k\,\mu_0\,, \tag{4.11}$$

and for a perfect Lambertian $r_{f,Perf\,Lam} = \mu_0$. On the other hand, the reflectance factor is the radiance of a medium under some illumination geometry relative to the radiance of a Lambertian surface under the same illumination geometry. It is given as:

$$R^* = \frac{I(i,e,Az)}{I_{Lam}(i,e,Az)} = \pi\,\frac{r}{\mu_0} = \pi\,r_{BRDF} = \frac{IOF}{\mu_0}\,, \tag{4.12}$$

which is $R^*_{Lam} = k$ for a Lambertian standard, and $R^*_{Perf\,Lam} = 1$ for a perfect Lambertian. Both IOF and R* are dimensionless and are extremely useful in the study of reflectances of rocks and minerals. The radiance factor "uniforms" all measurements because it compares radiances to the same standard, showing if a medium reflects more or less light towards the observer than a Lambertian surface illuminated from straight above (but the total energy over the whole hemisphere must be conserved), and therefore is easier to measure in laboratory. Differently, the reflectance factor compares two surfaces under the same geometry, but because Lambertian surfaces are not perfect it is less straightforward to measure. However, as shown by equation (4.12), they are related through the cosine of the incidence angle, which makes easier to go from IOF to R*. Eventually, it is worth mentioning a helpful application of the Law of Conservation of Energy to the concept of bidirectional reflectance, illustrated by Helmholtz and Minnaert in the last century. They introduced the so-called Principle of reciprocity, stating that, if a surface is illuminated under an incidence angle i and the reflection is observed under emission angle e, the radiance does not change if i and e are swapped:

$$I(i,e,Az) = I(e,i,Az)\,. \tag{4.13}$$

As a consequence, this principle holds for all the formulations of reflectance defined above:

$$\begin{gathered} r_{BRDF}(i,e,Az) = r_{BRDF}(e,i,Az) \\ r(i,e,Az)\cos e = r(e,i,Az)\cos i \\ IOF(i,e,Az)\cos e = IOF(e,i,Az)\cos i \\ R^*(i,e,Az) = R^*(e,i,Az)\,. \end{gathered} \tag{4.14}$$

4.2 The calibration targets on previous missions

The importance of converting planetary images from the illumination-dependent unit of radiance to the illumination-independent and consistent unit of reflectance was already noted since the first missions on Mars. The design and concept of the Mastcam-Z calibration targets, that is illustrated in the next section, was largely inherited from three previous NASA missions: the Mars Exploration Rovers, the Phoenix lander and the Mars Science Laboratory. In all three cases, the target is a physical device placed on the probe, that is imaged frequently in order to estimate the local irradiance and combine it with the observed radiance to obtain the reflectance. Every calibration target usually hosts patches and rings in various colors and materials, of which the reflectance is well known from laboratory measurements.

The two Mars Exploration Rovers Spirit and Opportunity, that concluded their operations in 2011 and 2019 respectively, were equipped with a panoramic, multispectral, stereoscopic camera named Pancam (Bell et al., 2003), which relied on a calibration target (figure 4.2a). The target was placed on the deck of both rovers, in direct and unobstructed sight of Pancam, and had a square-shaped support on which a shadow post (or gnomon), three grayscale rings and four color patches were fixed. The four color patches were located at the four corners of the base, while the grayscale rings and the gnomon were off-centered. Several magnets were placed in different spots of the rovers to study dust deposition (Madsen et al., 2003), including one called "sweep magnet", located next to the calibration target, but none was assembled within the calibration target, which was quickly covered uniformly in dust. The sweep magnet experiment on the MER rovers showed that magnets could keep some areas rather clean from dust (Madsen et al., 2009), and hence it was decided to provide the calibration targets of the next probe, the Phoenix lander (landed in 2008 and lost after few months), with six magnets. The Surface Stereo Imager (SSI; Lemmon et al., 2008) of Phoenix relied on three calibration targets (all identical) called Improved Sweep Magnet Experiments (ISWEEPs; Leer et al., 2008) placed on the deck of the lander (figure 4.2b). They were employed for both calibration of the SSI and analysis of dust properties. In fact, each ISWEEP consisted of six hollow cylinder magnets mounted on the periphery of a circular support, on which six color and grayscale circular patches were fixed. As observed on MER, the ISWEEP magnets attracted magnetic dust and kept the central portion of each patch relatively clean, also allowing for the detection of non-magnetic dust. In addition, at the center of each ISWEEP there were 10 smaller color and grayscale round patches not protected by the fields of the magnets. These regions, named dots, were useful to study the deposition of all airfall dust and compare it with the more magnetic dust.

The Curiosity rover, which landed in 2012 and is still active, has a multispectral, stereoscopic camera named Mastcam. The calibration target of Mastcam has approximately the same design as the one of the MER rovers, with the addition of the successful hollow magnets of Phoenix (Bell et al., 2017), and is located on the deck of the rover (figure 4.2c). Six strong permanent magnets are placed underneath the four color patches in the corners and two of the grayscale rings, in order to ensure the cleanliness of some small regions that can be used to perform calibration. Since this target is a flight spare of the one on Spirit and Opportunity, it has the same size (8x8 cm wide, 6 cm tall), while the ISWEEPs on Phoenix lander were a bit smaller (5.6 cm of diameter).

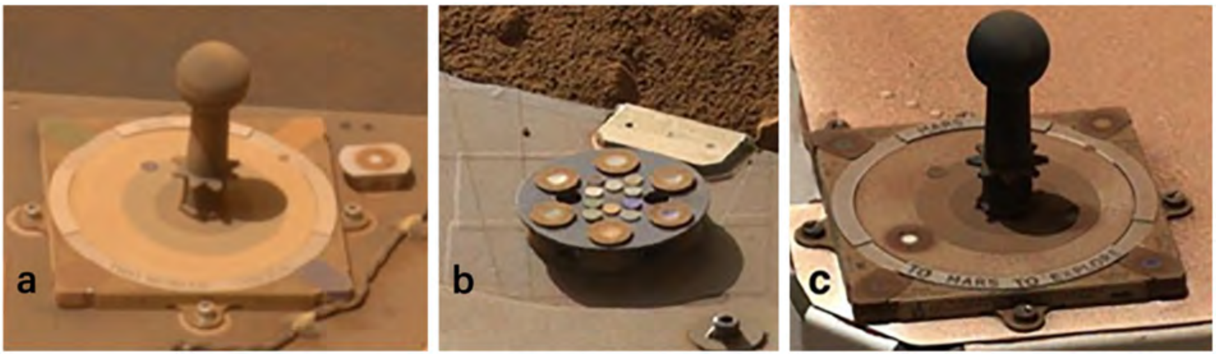

Figure 4.2: *(a) Calibration target for the Pancam instrument of the Spirit and Opportunity rovers. (b) One of the three Improved Sweep Magnet Experiments (ISWEEPs) for the Surface Stereo Imager of the Phoenix lander. (c) Calibration target of the Mastcam camera mounted on the Curiosity rover. Figure from Kinch et al. (2020).*

4.3 The Mastcam-Z calibration targets

The Mastcam-Z calibration targets (Kinch et al., 2020) are a pair of physical devices mounted on the deck of the Perseverance rover and used to assist in the conversion of Mastcam-Z images from units of radiance to reflectance (IOF). They were designed and assembled at the Niels Bohr Institute of the University of Copenhagen.

The principal device, known as "primary target" (figure 4.3a), is mounted on top of the Rover Pyro Firing Assembly (RPFA) on the deck of the rover. It consists of a gold-plated aluminum frame, on which eight round color and grayscale ceramic patches, four grayscale rings, and a shadow-post are fixed. The circular patches are located in the periphery of the primary target's frame, and are four in colors (referred to as blue, green, yellow, red) and four in grayscales (black, dark gray, light gray, white). The shadow-post, or gnomon, is painted with an IR-black paint (Aeroglaze Z307) and stands at the center of the primary target. The four grayscale rings are concentric and placed at the center of the target (around the shadow-post), and from the innermost to the outermost they are light gray, black, white, and dark gray. These four grayscales are the same as the four grayscale patches. The white patch and ring are made from AluWhite98 alumina manufactured by Avian Technologies, while all the other colors and grayscale materials are matted aluminum silicates made by Lucideon. Eight hollow-cylindrical magnets are mounted underneath the round patches. These Sm_2Co_{17} magnets are strongly magnetized (i.e., they have a high magnetic susceptibility) along their axis of symmetry, in order to attract even weakly magnetic martian dust grains on the external annular portion of the patches, while actively repelling such grains from the central circular part, leaving the latter relatively clean from dust. The round patches are glued to the base with the Henkel/Loctite EA9309NA epoxy, while for the grayscale rings the 3M-2216B/A Gray epoxy was used. The golden frame is made from aluminum with silver and gold anodization and is embellished with a motto and some graphics engraved on the top surface of the primary target, and a short inspirational message on the vertical edge. The frame of the primary target has a superellipse shape that can fit in a 98 mm-side square. The eight round patches have a diameter of 12 mm, while the hollow magnets underneath have an inner diameter of 5 mm and outer diameter of 11 mm. The central gnomon is 37.5 mm tall, while the innermost grayscale ring has an inner diameter of 10 mm and the outermost ring has an outer diameter of approximately 50 mm (all rings have the same radial width). In total, the primary target is 45.7 mm tall and weighs 103 g.

The second device is named "secondary target" (figure 4.3b) and is fixed to the vertical front side of the RPFA, just below the primary target. It is made of a horizontally oriented shelf-shaped support accommodating seven square tiles mounted horizontally (parallel to the rover deck), and seven vertically (parallel to the vertical side of the RPFA). The tiles have a side of 10 mm and have the same colors and grayscales (and are produced from the same materials) as the round patches of the primary target, except for the yellow: from left to right they are black, dark gray, light gray, white, red, green, and blue, in the same order horizontally and vertically. The secondary target has a mass of 15 g and has a total length of 80 mm.

The main objective of the primary target is the assessment of the local instantaneous solar irradiance (section 4.1), in order to generate reflectance-calibrated (IOF) images from radiance-calibrated images. Radiance-calibrated images are the result of the application of several corrections (e.g., bias frames, shutter frames, flat fields) on the raw images from Mastcam-Z (the full process is illustrated in Hayes et al., 2021). In addition, it helps estimate the fraction of direct solar illumination relative to the diffuse sky irradiance due to atmospheric scattering. For these reasons, imaging the calibration targets (figure 4.3c) frequently allows one to monitor the quality of calibration and of diffuse irradiance over time, in order to fulfill the science objectives of Mastcam-Z involving photometry and reflectance spectroscopy. The secondary target, which is an innovation and was not present in previous rover missions, is aimed mainly

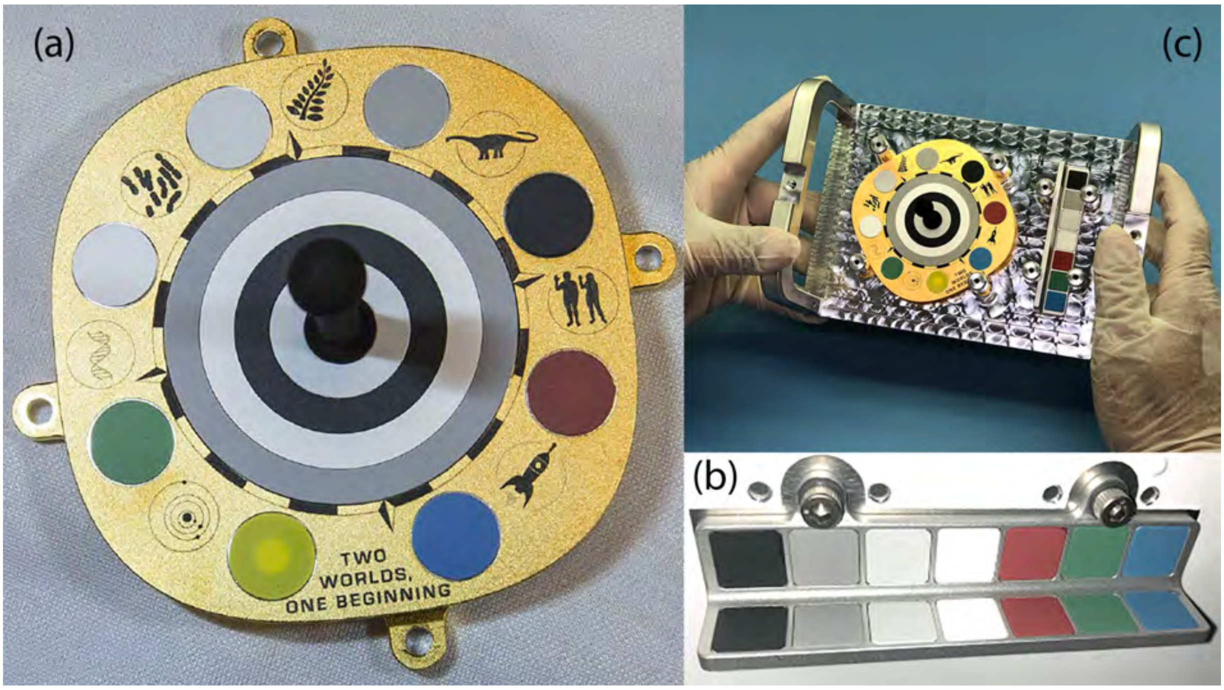

Figure 4.3: *The (a) primary and (b) secondary calibration targets of Mastcam-Z. (c) The calibration targets on a metal support ready for testing. Credits: NASA/JPL-Caltech/ASU/Niels Bohr Institute, University of Copenhagen.*

at validating the primary target. This validation consists not only in the cross-check of calibration thanks to the different orientations of its materials, but also tracking the deposition and displacement of dust on the rover's surfaces, since the secondary target is not provided with magnets.

As mentioned in section 4.2, the Mastcam-Z primary calibration target inherited part of the design from the MER and MSL rovers and the Phoenix lander, but with some changes that enhance the efficiency and the accuracy for calibration. These changes include a different choice of materials, the employment of bigger hollow magnets and more grayscales, and the removal of magnets from the grayscale rings, which are also in a different order.

In this work I adopt a simple nomenclature scheme for the different ceramic patches and rings according to their positions on the targets, which is illustrated in figure 4.4. In the primary target, the inner circular portions of the eight peripheral round patches are named "central spots" or "clean spots", while the external annular portions, which lie over the magnets, are called "magnet rings". The name "clean spots" is a consequence of the action of the magnet rings, which capture the magnetic fraction of the airborne dust. The four concentric grayscale rings at the center of the primary target are simply called "grayscale rings". For the secondary target, the seven square patches are named "secondary horizontal tiles" or "secondary vertical tiles", depending on their orientation.

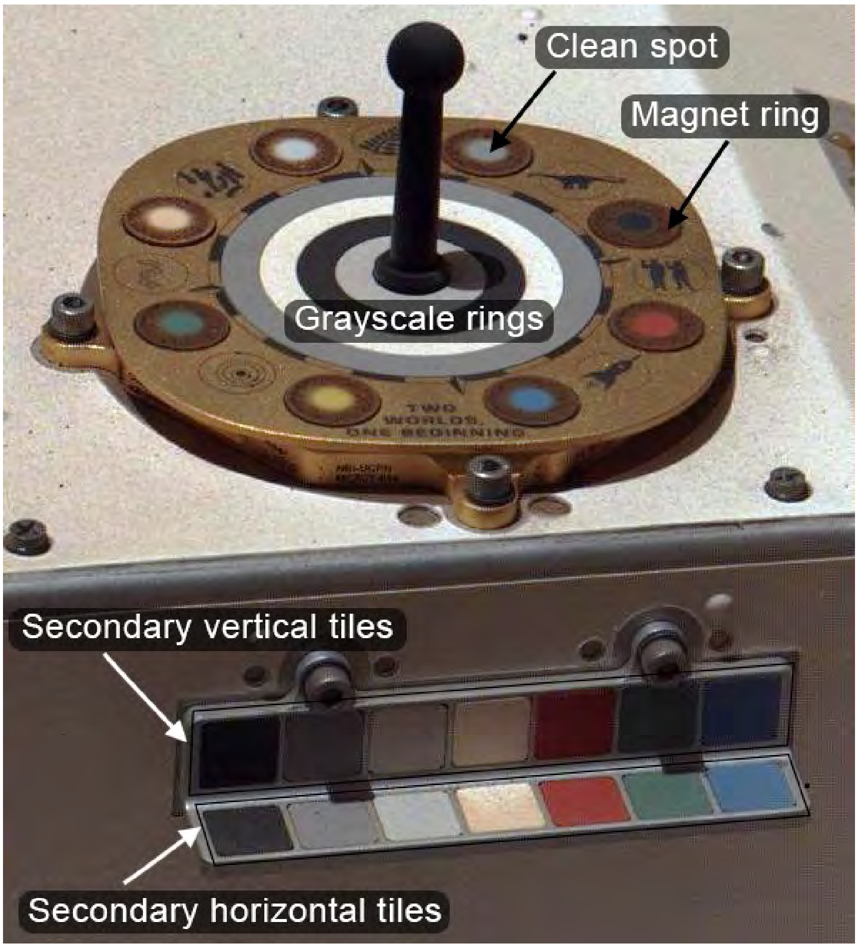

Figure 4.4: *The Mastcam-Z calibration targets imaged by the left eye (L0) of Mastcam-Z on sol 180 at 48 mm zoom (sequence ZCAM03014). The main regions of the primary and secondary targets are indicated with the names used in this work.*

4.3.1 The theory of Mastcam-Z radiometric calibration with the calibration targets

The necessity to include a set of calibration targets to convert Mastcam-Z images from units of radiance to reflectance (IOF or R*) arises from the difficulty to estimate at a reliable level the solar irradiance F at any given moment of a sol in the proximity of the rover. The irradiance changes sensibly with the time of sol and throughout the year, and is affected by atmospheric conditions, including clouds and dust content. All these effects vary on short timescales and are then challenging to model accurately. As a solution, the color and grayscale materials of the calibration targets, for which the reflectance is known from laboratory measurements at any illumination geometry and wavelength, are a critical tool that should be imaged every time is needed. The basic theoretical application of the calibration targets is illustrated in the following. By definition, as described by equation (4.5), bidirectional reflectance is the ratio between the outgoing flux from a target and the incoming flux illuminating that target. This concept can be applied to a whole image (for instance, of a rock or a mineral), where every pixel contains a value of reflectance. In the case of radiance factor IOF:

$$Image_{IOF} \approx \pi \, \mu_0 \frac{Image_{RAD}}{F}, \tag{4.15}$$

where $Image$ is the image of a scientific target in some filter, the subscript RAD refers to the radiance-calibrated value from each pixel, F is the irradiance in the image scene, μ_0 is the cosine of the incidence angle, and π is the conversion factor from bidirectional reflectance to IOF (equation (4.10)). In equation (4.15), $Image_{RAD}$ is contained in the pixels of the image, while F is unknown. Ideally, the calibration targets should be imaged close in time to $Image_{RAD}$, and equation (4.15) must hold for them as well:

$$CT_{IOF} \approx \pi \, \mu_0 \frac{CT_{RAD}}{F} \tag{4.16}$$

where CT is the image of the calibration targets in some filter. The advantage of the calibration targets is that CT_{RAD} is the radiance-calibrated value measured from every pixel, and CT_{IOF} is the reflectance value of each pixel known from laboratory measurements at any illumination geometry. Therefore, as long as $Image_{RAD}$ and CT_{RAD} are acquired by Mastcam-Z close in time, the irradiance F should be approximately the same in equations (4.15) and (4.16). The expression for F from equation (4.16) is replaced in equation (4.15), which yields:

$$Image_{IOF} \approx \pi \, \mu_0 \frac{Image_{RAD}}{F} \approx Image_{RAD} \frac{CT_{IOF}}{CT_{RAD}}. \tag{4.17}$$

Equation (4.17) is at the center of the IOF calibration. Likewise, the image expressed in terms of reflectance factor R* is obtained from $Image_{IOF}$ by just dividing its pixels by $\cos i$, as per equation (4.12), assuming that the scientific target in the $Image$ and the calibration targets have a similar illumination geometry.

In the treatment described above, some assumptions have been made. In first place, equation (4.15) is the outcome of the following approximation:

$$Image_{RAD} = \frac{1}{\pi} \int F(\lambda) \, r(\lambda) \, \rho(\lambda) \, d\lambda \approx \frac{F}{\pi} \int r(\lambda) \, \rho(\lambda) \, d\lambda = \frac{F}{\pi} Image_{IOF}, \tag{4.18}$$

where $F(\lambda)$ is the spectral flux, $r(\lambda)$ is the normalized system spectral response, and $\rho(\lambda)$ is the spectral reflectance in IOF. The first equality of equation (4.18) is easy to solve in the ideal case where the radiance of the scene, the spectral flux and the spectral response are all known over the full spectrum, and the IOF reflectance $\rho(\lambda)$ would be extracted for any λ within the considered range. In reality, only sampled spectra can be extracted from Mastcam-Z image sequences. The camera has 12 narrow-band and six broad-band Bayer RGB filters, each one with its known spectral response, or throughput curve. This implies (in the last equality of equation (4.18)) that the resulting IOF image is the spectral reflectance of the scene folded with the throughput curve of each filter and with the illumination spectrum $F(\lambda)$, but the latter is not known. Therefore, the spectral flux $F(\lambda)$ is replaced with an average of the flux over the filter band. This approximation may be affected by the larger uncertainty of the six Bayer filters (around 40 nm) rather than the narrow-band filters (around 10 nm), and is critical for the approach to calibration. Equation (4.16) can be expanded in the same way for the calibration targets, but in this case, the average F is the only unknown because the spectral reflectance of the calibration target materials folded with the throughput curve is a known quantity from laboratory measurements.

A further assumption is that the illumination is fully directional, which means that all the light comes from the Sun as a collimated beam. However, Mars has an atmosphere that scatters light (principally due to airborne dust). Hence, two components should be taken into account, one directional from the Sun and one more hemispherical coming from the sky. The reflectance of the calibration target materials is known from laboratory measurements for direct illumination from the light source, and the reflectance relative to diffuse light might be different. One way to solve this question is to measure the illuminated portions of the grayscale rings and the shaded parts due to the gnomon, in order to correct the laboratory reflectance of the calibration targets for diffuse light and retrieve new estimates for the total irradiance F. As the fraction of diffuse light increases at high incidence angles due to the thicker path to cross through the atmospheric layers, this problem is more pronounced when the Sun is lower above the horizon (in the early morning or late afternoon), while it is much reduced or even negligible when it is close to the zenith (around martian noon). An exhaustive approach to the diffuse illumination correction is reported in appendix B.

In addition, airfall dust also deposits and sticks electrostatically on surfaces. This phenomenon, that already affected the previous rovers and landers (figure 4.2 shows some examples), has the effect of changing the measured radiance from the calibration target materials that are used to retrieve the solar irradiance, causing reddening and making a convergence of dark and bright colors towards an in-between dust spectrum, depending on the thickness of the dust layers. A dust model was developed for the MER rovers (Kinch et al., 2015) and applied again for MSL, and aims at modeling two layers of dust covering each material of the calibration targets by estimating their optical depth and single-scattering albedo, in order to obtain a correction for the reference reflectance. Such a dust model was not employed for the calibration of Mastcam-Z over the first 670 sols, following the dust assessment described in sections 7.2 and 9.2.

Chapter 5

The pre-flight radiometric calibration of Mastcam-Z

The aim of this chapter is to illustrate in detail some of the main steps of the pre-flight calibration of Mastcam-Z relative to the use of the calibration targets. The techniques and tests described here were carried out in the months before landing, in order to develop a model for the reflectance calibration (from radiance to IOF reflectance) to implement once the rover would land on Mars. For the previous phase, the radiance calibration, the reader can refer to Hayes et al. (2021).

The whole procedure relies on a detailed knowledge of the reflectance properties of the color and grayscale materials of the calibration targets, whose laboratory characterization is reported in section 5.1. Section 5.2 shows the series of tests, named "standalone calibration", that I performed on different calibration target image sequences, in which I experimented with four models to convert the radiance data extracted from the images to reflectance factor and compared the results with the reference measurements. As a result of the tests, I developed the reflectance routine described in section 5.3, which allows to determine the reference reflectance factor relative to any wavelength and illumination condition. Two of the models tested and the routine that I developed were then applied to the images of the calibration targets assembled on the rover, when the latter was being prepared for launch at NASA ATLO (Assembly, Test and Launch Operations) facility (section 5.4).

5.1 The reflectance characterization of the calibration target materials

In the "theory of calibration" described in section 4.3.1, I mentioned that the values of reflectance of the color and grayscale materials of the Mastcam-Z calibration targets (named CT_{IOF} in equations (4.17) and (4.18)) were known from laboratory measurements for different wavelengths and under any illumination geometry, defined by a triplet of incidence, emission and azimuth angles (i,e,Az). Such knowledge is the pillar of the concept of the calibration targets, because it allows the description of their features in laboratory and the comparison with their behavior within the real (red) world.

The materials in the assembled calibration targets are eight, denoted by their color (green, yellow, blue, red, black, dark gray, light gray, and white), with an additional mention to the Spectralon, that is one of the closest examples of a perfect Lambertian scatterer and will be used extensively as a reference for calibration. In this chapter, when talking about the eight calibration target materials in general, I will abbreviate "color and grayscale" with just "color" materials.

The laboratory measurements were performed in Copenhagen (Denmark) in May 2019 and in Bern (Switzerland) in March 2020. In both places, an instrument typically known as "spectro-goniometer" was used. It consists of a support where the target sample is placed, and two arms that can move horizontally and vertically around the target, one with a light source at the end, and one with a detector. The former generates the irradiance that hits the target, the latter measures the radiance of the scene.

The spectrogoniometer at the Niels Bohr Institute of the University of Copenhagen had two automatically controlled arms holding optic fibers to illuminate the sample with a halogen lamp and collect the radiance and conduct it to a spectrometer (AvaSpec 2048), all enclosed in a black box to minimize stray light. The samples under examination were the eight materials in the assembled flight unit of the calibration targets, and the witness samples, i.e., larger square tiles manufactured from the same materials and colors as those in the calibration targets. The measurements in Copenhagen were reported in a dataset (hereby named "Copenhagen data" that includes the complete reflectance factor spectra of the nine witness samples and the color materials of the assembled calibration targets within the range 200-1100 nm (with steps of 1 nm) in the illumination geometry i = 58°, e = 0°, and Az = 90°. Figure 5.1 shows the complete spectra acquired in Copenhagen relative to the witness samples, the clean spots, the magnet rings, and the grayscale rings. Besides the spectra, the Copenhagen dataset also provides the 18 "folded" reflectances in that geometry. The word "folded" which will be repeated further in this chapter, means that a continuous (or discrete but denser) spectrum has been convoluted with the bandpasses – or more precisely, with the throughput curves – of a multispectral camera, yielding one value of R^* for each bandpass. In the case of Mastcam-Z, a folded spectrum is sampled in 18 bandpasses (three Bayer filters and six narrow-band filters for each eye). In the following I will refer to these 18-samples as "folded" and the more complete spectra (with steps of 1 nm) as "continuous".

The instrument used in Bern was the "gonio-radiometer" PHIRE-2 of the Planetary Ice Laboratory of the University of Bern. PHIRE-2 was designed to measure the bidirec-

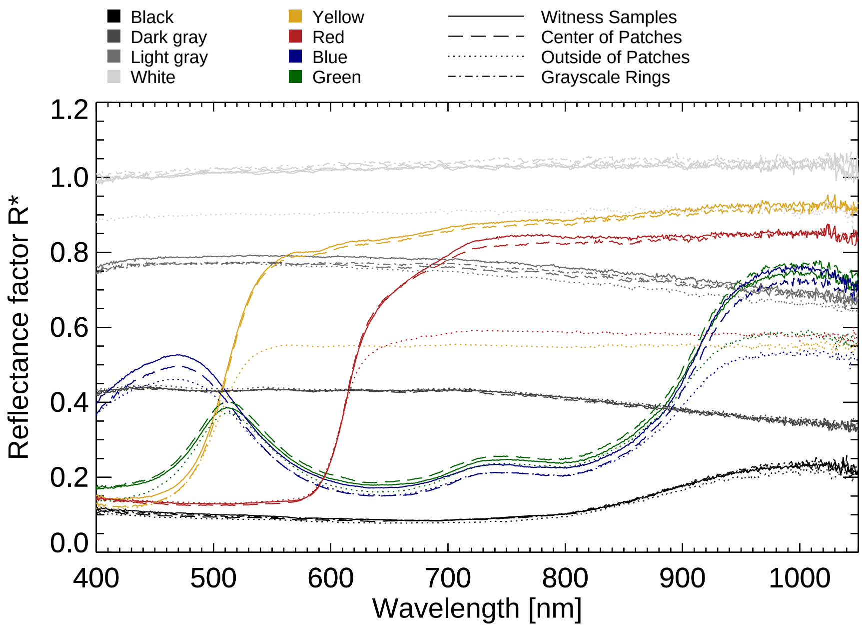

Figure 5.1: *Spectra of the eight witness samples (solid lines), the clean spots ("centers of patches" dashed lines), magnet rings ("outside of patches" dotted lines), and grayscale rings (dash-dotted lines) of the assembled flight unit of the calibration targets. The spectra were obtained with the spectrogoniometer in Copenhagen under the illumination geometry $i = 58°$, $e = 0°$, $Az = 90°$. Figure from Kinch et al. (2020).*

tional reflectance distribution function r_{BRDF} of a target in the visible to near infrared spectral range (400-1100 nm) under any illumination condition. The reflectances were extracted as r_{BRDF}, and were converted to R* by simply multiplying them by π (equation (4.12)). The instrument consisted of a sample holder where the target was placed, and two arms of fixed length, one with a source of light at its end, and one with a detector, both connected through optic fiber. The other ends of both arms were fixed on two pivots close to the sample holder: the arm with the light could rotate by 180° along a fixed vertical plane, while the detector arm could rotate by 180° in a vertical plane and 180° in a horizontal plane (azimuthally). This mechanism could provide any illumination condition on the target except for the case in which the two arms were aligned, because the arm containing the detector was shorter and would cast a shadow on the target when it was in front of the light source. A full technical description of the PHIRE-2 goniometer and its calibration is reported in Pommerol et al. (2011).

The measurements of the witness samples yielded eight datasets (hereby named "Bern data", one for each color material, plus one more dataset relative to the Spectralon. Each dataset contains a total of 7824 measurements of the reflectance factor in as many combinations of incidence, azimuth and emission angles in six bandpasses, together with the standard deviations of R*, the FWHM of the bandpasses and other features (sample temperature, air temperature, air humidity). The six bandpasses used for the measurements were: 450±70 nm, 550±70 nm, 650±70 nm, 750±70 nm, 905±25 nm, 1064 ± 25 nm. In general, the measurements were carried out under the following geometries:

- Incidence angles equal to six values: 0°, 15°, 30°, 45°, 58°, 70°.
- Emission angles from 0° to 80°, with steps of 5°.
- Azimuth angles from 0° to 180°, with steps of 15°.

Two remarks should be made. Firstly, the choice of including the value 58° in the incidence angles might be surprising, given that Mastcam-Z sees the calibration targets under an emission angle of approximately 58°. However, this is justified by the principle of reciprocity (section 4.1), according to which the reflectance values do not change (in first approximation) if the incidence and emission angles are swapped. In addition, the higher limit for the azimuth angles is 180° and not 360°, due to the symmetry of the reflectance factor with respect to the plane of incidence.

The aim of characterizing the calibration target materials was to retrieve their reflectance factor at any geometry and wavelength, thus investigating their scattering behavior. In this scope, the property of a material to scatter the light mainly towards the opposite side with respect to the position of the source is defined as forward-scattering, while it is defined as backward-scattering if the light is scattered back towards the side of the source (backward-scattering). A first way of visualizing the Bern data was in the form of two-dimensional plots, where the values of reflectance factors were investigated for each sample, filter and emission angle, while keeping the incidence angle fixed. The incidence and emission angles were contained in the same plane, named principal plane, perpendicular to the surface and corresponding to $Az = 0°$ (where the emission angle was conventionally positive) and $Az = 180°$ (negative emission angle).

Figure 5.2 shows the results relative to $i = 0°$. Each plot is a different sample material, and the six filters are represented with different symbols. Due to the aforementioned shadowing that occurred when the two arms of the goniometer were aligned, I considered the data points of $i = e = 0°$ not reliable and I discarded them. The measurements with $i = 0°$ show that none of the materials has a pronounced peak in reflectance, though they are all characterized by a more or less significant decrease at increasing phase angle. The grayscale samples do not have an appreciable separation between the data points of different filters, with a coherent increase in the reflectance factor from the dark to the bright materials, as expected. On the other hand, the color samples display more variability among the filters, but without any dramatic spikes. The maximum values of reflectance factor do not exceed 1.

Another interesting geometry was the one with $i = 58°$, reported in Figure 5.3, because Mastcam-Z sees the primary target under an emission angle of 58° (the two angles

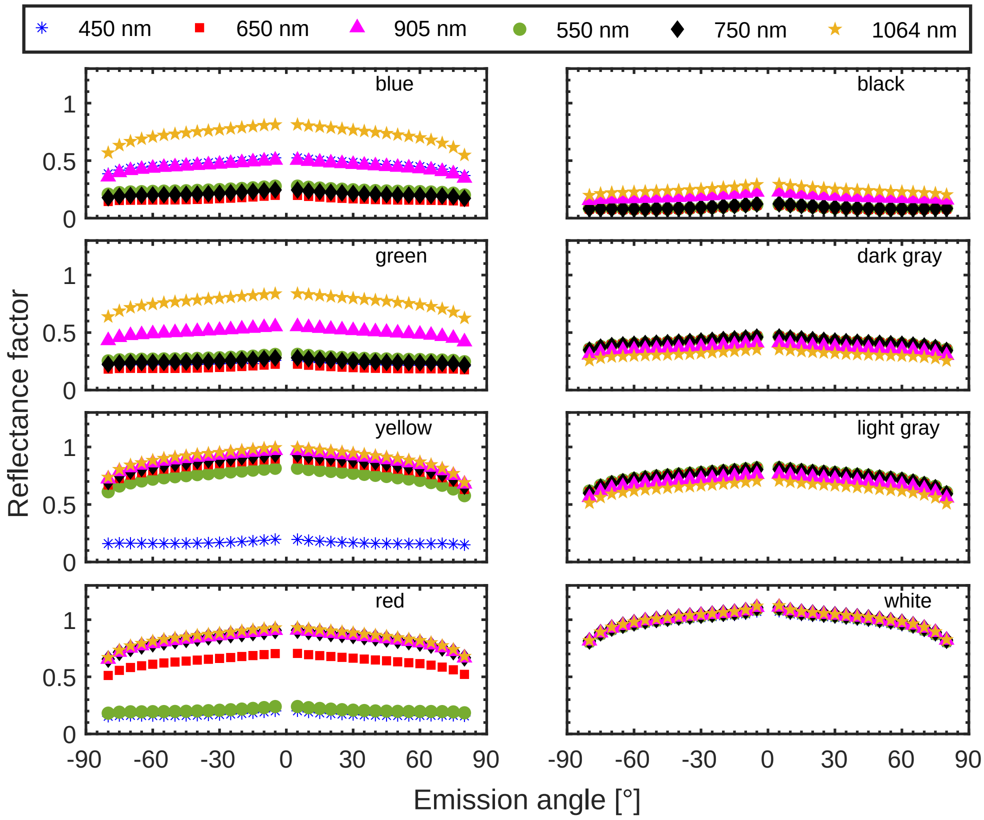

Figure 5.2: *Measurements of goniometric reflectance factor of the witness samples from the Bern data relative to $i = 0°$. Positive emission angles correspond to $Az = 0°$, negative emission to $Az = 180°$. Figure made by me, reproduced from Kinch et al. (2020).*

can be swapped for the principle of reciprocity). The settings with $e = 55°$ and $e = 60°$ were discarded due to the shadowing of the detector. The data show that the reflectance curve is quite flat for all materials in the back-scattering geometry and relatively flat in the forward-scattering geometry for incidence angles lower than 45°, while above that value all the samples except the white have a strong forward-scattering peak that exceeds $R^* = 2$ in the near infrared. The white sample, which is a different material manufactured from a different source with respect to the other samples, displays an overall flat behavior, with a very slight increase in the forward-scattering geometry.

As a following step of the analysis, I realized three-dimensional representations of the data. One example is shown in Figure 5.4 for the 650 nm filter and $i = 58°$. Each 3D plot is relative to a sample material and has the reflectance factor on the vertical axis (completed with the color bar) and the emission angle on the horizontal axis, and shows how the reflectance factor changes over the whole hemisphere (again, the positive emission angle corresponds to $Az = 0°$ and negative angle to $Az = 180°$). The conclusion is similar to that of the 2D plots, that is the white is overall flat, while all the other materials are fairly flat for $e < 45°$ and above that value the reflectance factor increases smoothly up to the peak at $Az = 180°$ and $e = 80°$, without significant

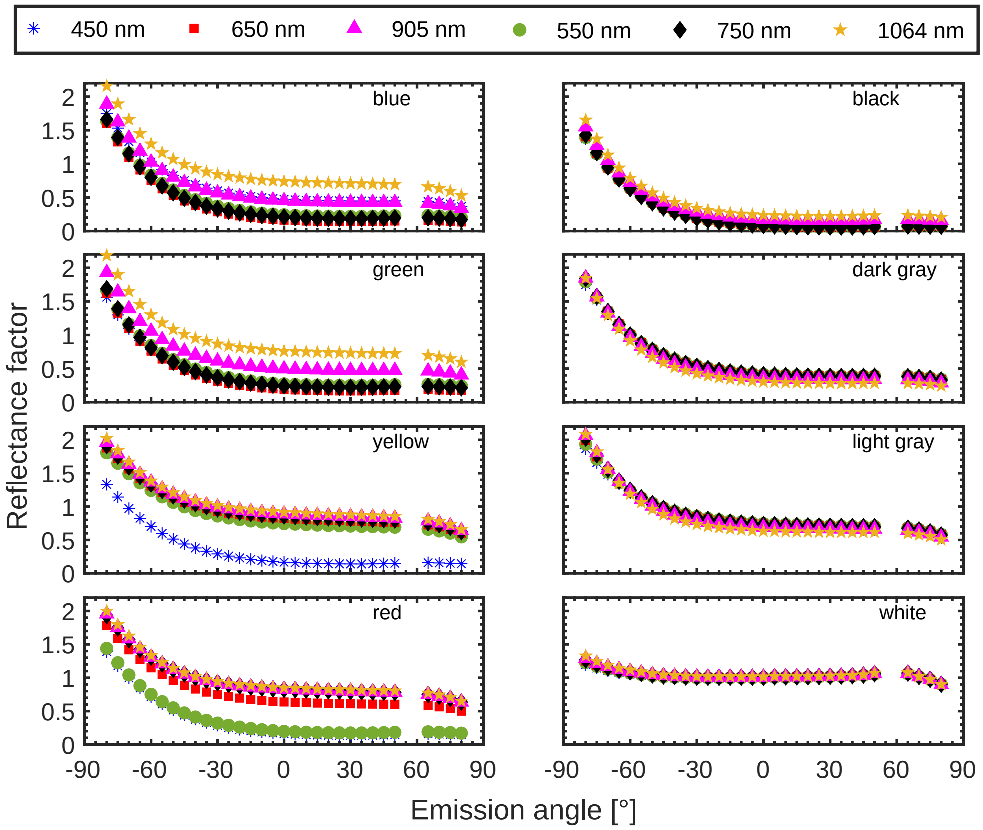

Figure 5.3: *Measurements of goniometric reflectance factor of the witness samples from the Bern data relative to* $i = 58°$. *Positive emission angles correspond to* $Az = 0°$, *negative emission to* $Az = 180°$. *Figure made by me, reproduced from Kinch et al. (2020).*

peculiarities.

The whole pre-flight sample characterization phase was extremely useful for predicting the behavior of the calibration target materials on Mars. The Perseverance rover was expected to land in Jezero crater at a latitude of $\sim 18°$N. In addition, Mars' axis is tilted by $\sim 25°$, which makes the Sun reach its higher declination (northern summer solstice) around the aphelion. Consequently, the rover (in particular, the calibration targets) was expected to be illuminated with very low incidence angles from the late morning to the early afternoon, with the minimum at noon, for several sols before and after the aphelion. On the other hand, at perihelion Mars experiences the winter solstice in the northern hemisphere, and hence, the incidence angle was expected to be relatively large already around noon. Therefore, in the optics of the Bern data, the strongest forward-scattering effects could be expected to occur in the early morning and late afternoon of the sols around aphelion, and already in the mid-morning and mid-afternoon of the sols around the perihelion, with the Sun behind the rover (i.e., exactly in front of Mastcam-Z when observing the calibration targets).

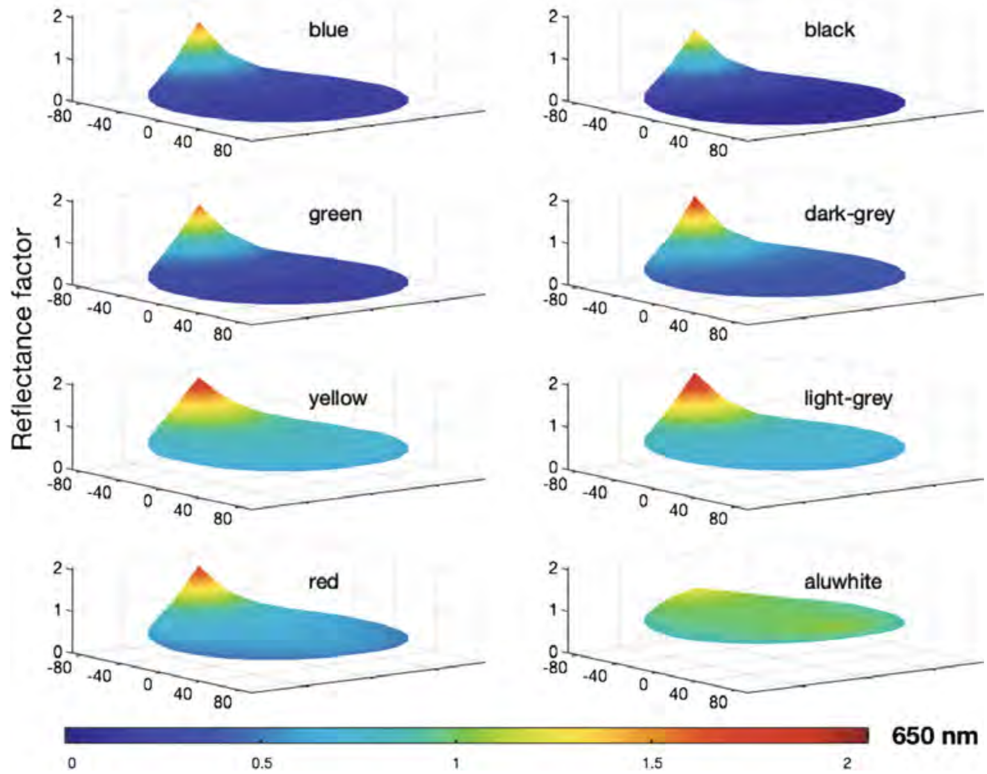

Figure 5.4: *Measurements of goniometric reflectance factor of the witness samples from the Bern data relative to $i = 58°$ for all the upper hemisphere (all values of e and Az) at 650 nm. Positive emission angles correspond to $Az = 0°$, negative emission to $Az = 180°$. Figure made by me, reproduced from Kinch et al. (2020).*

5.2 The standalone calibration

Before the launch of Perseverance, and as part of the standalone calibration of Mastcam-Z before integration on the rover, I carried out a series of tests in which I experimented with different methods on radiance-calibrated images of the calibration targets in order to calibrate them to reflectance. The term "standalone" came from the fact that the camera was standing alone on a support in laboratory, and was not mounted on the mast of the rover. The tests were justified by the requirement for a reliable and accurate procedure on how to perform the reflectance calibration and to manage and correctly combine the reflectance data from Bern and Copenhagen. Indeed, those datasets were considered not only relevant, but also complementary in illumination angles and wavelengths: the Copenhagen data were relatively continuous spectra of the samples but only in one geometry, whereas the Bern data covered a large number of geometries but were only sampled in six bandpasses.

I developed and tested four calibration models (the "only-white" the "black-white" the "one-term fit" and the "two-term fit" on different image sequences of the calibration targets, where each sequence was made of 18 frames, one for each filter (three Bayer broad-band RGB and six narrow-band filters for each eye). These images were acquired and calibrated to radiance by our teammates at Cornell University (Ithaca, NY). They used Mastcam-Z as the camera, and a spare unit of the calibration targets mounted on a flat surface with several other targets, including rock samples and the witness samples of the calibration targets. For each image sequence and model employed, the product by which I could verify the efficiency of the model was a calibration spectra plot, that is a plot showing the resulting reflectance-calibrated spectra of the calibration targets (sampled in the 18 filters of Mastcam-Z) and the corresponding reference laboratory spectra in the same illumination geometry, obtained by combining the Copenhagen and Bern data.

The preliminary operation before applying any model was to extract the values of radiance from the images. I were interested in the spectral behavior of the eight clean spots and the four grayscale rings. Therefore, I used a software (already employed in the MER and MSL missions) to draw rectangular selections of the regions of interest (ROIs) on the images in the two eyes. Our ROIs were the clean spots and small non-shadowed parts of the grayscale rings. The software returned a comma-separated value (CSV) file containing, for each ROI in each filter, the radiance value averaged over the pixels of the ROI and its associated standard deviation.

Before moving on to the description of the models, it is worth making an important remark. As shown below, all the calibrated and reference spectra are multiplied by the spectrum of Spectralon, which is displayed in figure 5.5. I obtained this spectrum by selecting the six sample values of R* of the Spectralon in the geometry with i = 58°, e = 0°, and Az = 90° from the Bern data, and interpolating those values over the range 400-1065 nm. The result is an almost flat spectrum around $R* = 1$. This operation of Spectralon scaling was made to convert the data (which had been measured relative to Spectralon) to absolute values.

5.2.1 The four calibration models

The four calibration procedures that I tested are presented in the following. I define here the parameter K, which appears in all models. In general, it is used to convert the reflectance spectra of the Copenhagen data from their original illumination geometry (i = 58°, e = 0°, Az = 90°) to the geometry of the images, in order to ensure consistency. To obtain it for some color material (which is added as a subscript), the six values of reflectance are extracted from the Bern data in the image geometry and in the Copenhagen geometry for that color. The ratio between the six pairs of values is performed by corresponding wavelength, and the six results are interpolated with a spline over the range 400-1050 nm. Finally, if required by the model, the ratio-spectrum can be folded and denoted as K_{fold}.

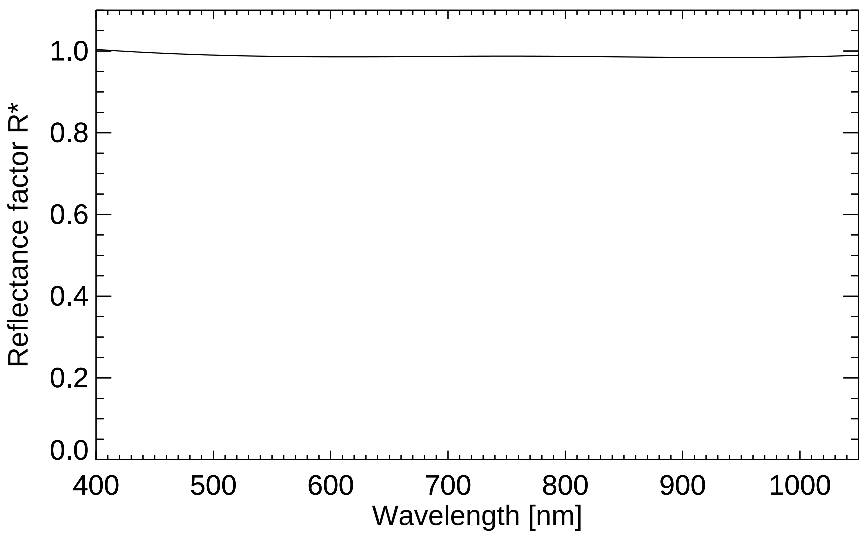

Figure 5.5: *Reflectance factor spectrum of Spectralon. The spectrum was obtained by extracting the data for Spectralon from the Bern data in their six filters and interpolating over the range 400-1050 nm. The illumination geometry is* $i = 58°$, $e = 0°$, $Az = 90°$.

- The "only-white" model
  This simple model consists in applying a series of corrections based only on the white (AluWhite98), that is the brightest material of the calibration targets. If RAD_{img} is the radiance of each ROI within the images, its resulting reflectance factor $R*_{img}$ is:

$$R^*_{img} = RAD_{img} \frac{R^*_{fold,white}}{RAD_{whitering}} K_{fold,white} \cdot R^*_{fold,spectralon}, \tag{5.1}$$

  where:

  - $R^*_{fold,white}$ is the folded spectrum of the white sample from the Copenhagen data.
  - $RAD_{whitering}$ is the radiance of the ROI in the white ring within the images.
  - $R^*_{fold,spectralon}$ is the folded spectrum of Spectralon.
  - $K_{fold,white}$ is the folded ratio defined above, relative to the white sample.

- The "black-white" model
  This model differs from the only-white for the fact that this is also based on the black material, which is the darkest one on the calibration targets. Indeed, the black and white samples are represented by rather flat spectra below and above all the other materials, respectively, and therefore the radiance of each ROI is calibrated using the two extremes of the reflectance spectrum. One further difference is that this method relies on two terms, one multiplicative and one additive,

in the form:

$$R^*_{img} = RAD_{img} \cdot A + B. \tag{5.2}$$

The multiplicative term A is defined as:

$$A = \frac{R^*_{fold,white} \cdot K_{fold,white} - R^*_{fold,black} \cdot K_{fold,black}}{RAD_{whitering} - RAD_{blackring}} R^*_{fold,spectralon}, \tag{5.3}$$

and the additive term B is:

$$B = R^*_{fold,black} \cdot K_{fold,black} \cdot R^*_{fold,spectralon} - A \cdot RAD_{blackring}, \tag{5.4}$$

where:

- $R^*_{fold,white}$ and $R^*_{fold,black}$ are the folded spectra of the white and black, respectively, from the Copenhagen data.
- $K_{fold,white}$ is the same folded ratio as in the only-white model. In this case, the same operation is made with the black sample, which yields $K_{fold,black}$.
- $RAD_{whitering}$ and $RAD_{blackring}$ are the measured radiances from the ROIs in the white and black rings, respectively..
- $R^*_{fold,spectralon}$ is the folded spectrum of Spectralon.

• The "one-term fit" model
This method consists in performing one least-squares linear fit with one multiplicative term (in the form $y = a \cdot x$) between the measured radiances and laboratory reflectances of the ROIs in the eight clean spots of the primary target. The measured radiance of each ROI is the average of the radiance over all the pixels of the ROI. Before making the fits, the radiances are only multiplied by the folded spectrum of Spectralon. The laboratory spectra, suitably folded from the Copenhagen data, are multiplied by the folded spectrum of Spectralon and then by the ratio K_{fold} relative to each corresponding color material. The fits are weighted on the uncertainties of the data points, which are obtained as the standard deviations associated to the average radiance of the ROIs. The slope of each linear fit (one for each image in each filter) is an estimate of the solar irradiance F, and is applied to the radiances of every material according to equation (4.10). Considering that all the image sequences were taken in laboratory under "calm" conditions (no dust, clouds, solar weathering or turbulence typical of the martian atmosphere), I expected the fits to describe the data points with high accuracy, as well as to have a very small uncertainty on the slope. This is the method that was actually employed for the reflectance calibration on Mars.

- The “two-term fit” model
  This model follows the same concept of the one-term fit model, but with the inclusion of an additive component, in the form $y = a \cdot x + b$. The measured radiances and laboratory reflectances are processed in the same way as in the one-term fit, but this time the least-squares fit is computed with two free parameters. Again, besides the high accuracy and small uncertainty on the slopes, I expected the additive term b to be extremely small as well.

5.2.2 The image sequences and the test results

In total, I applied the four models on five image sequences acquired at Arizona State University (AZ) using three different focal lengths and calibrated to radiance. As a result of each test, I plotted the calibration spectra mentioned in section 5.2, showing the calibrated reflectance spectra and the reference laboratory spectra. Whereas the calibrated spectra are sampled in the 18 filters of Mastcam-Z, the reference laboratory spectra were the Copenhagen continuous spectra suitably multiplied by the spectrum of Spectralon and by the spectral ratio K defined above, which made use of the Bern data to translate the reference spectra from the Copenhagen geometry to the image geometry in each color. When applying the one- and two-term models, for a more quantitative approach I computed the root-mean-square error (RMSE) relative to the two fit models. It is defined as:

$$RMSE = \sqrt{\frac{1}{N} \sum_{i=1}^{N} \left(R^*_{i,lab} - R^*_{i,img} \right)^2}, \tag{5.5}$$

where $R^*_{i,img}$ are the calibrated reflectance factors of the eight clean spots in the 18 filters of Mastcam-Z and $R^*_{i,lab}$ are the corresponding reference laboratory values. Therefore, the total number N of values is typically $8 \cdot 18 = 144$. All the values of RMSE obtained for the sequences on which I applied those models (#2, #3, #4 and #5) are recapped in table 5.1 at the end of this section.

Sequence #1

The first sequence consisted of images of the primary target in all the 18 filters at 100 mm zoom. The illumination geometry was $i = 58°$, $e = 30°$ and $Az = 90°$. Figure 5.6 shows an example of the primary target in the filter R2 (866 nm) at 100 mm of zoom, with the rectangular ROI selections in different colors within the clean spots and the grayscale rings. As a first experiment, I only applied the only-white method, which returned the calibration spectra plot in Figure 5.7. As expected from this model, there is an almost perfect coincidence of the white data points with the reference spectrum, while a larger discrepancy is evident in the darker materials (dark gray and black) especially starting from the red/near infrared bands.

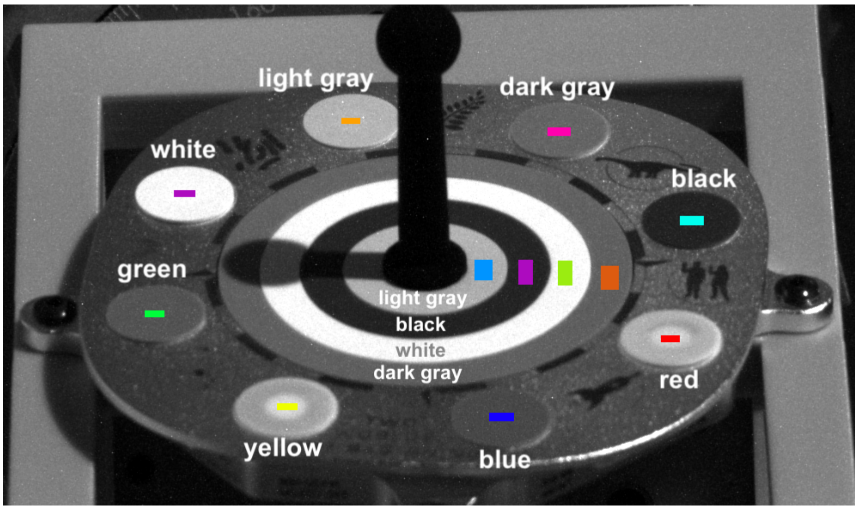

Figure 5.6: *Example of the ROI selections in different colors within an image of the primary target from sequence #1, acquired in filter R2 (866 nm) at 100 mm of focal length. The illumination geometry is $i = 58°$, $e = 30°$ and $Az = 90°$.*

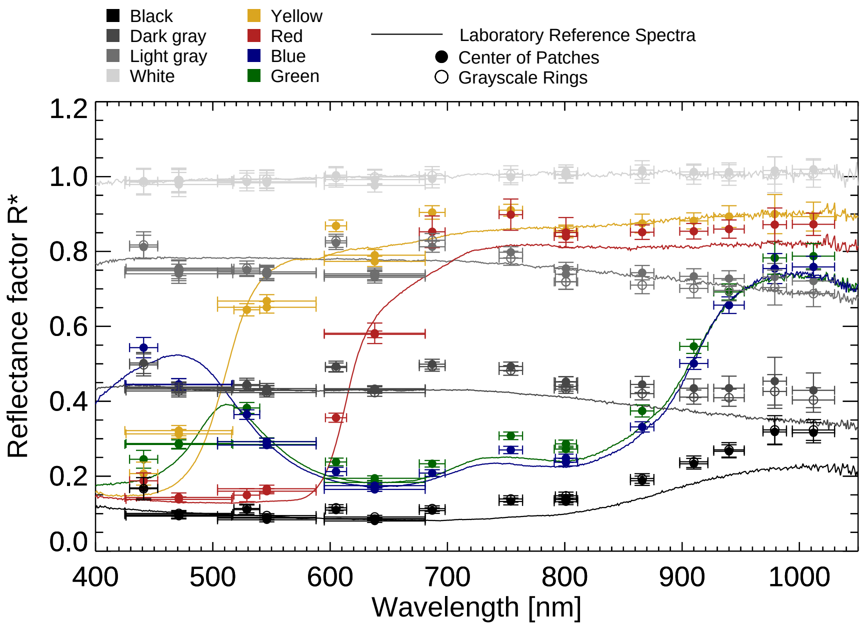

Figure 5.7: *Calibration spectra plot of dataset #1 using the "only-white" model. The data points represent the calibrated centers of the patches (filled dots) and grayscale rings (open dots), while the solid lines are the reference spectra. The error bars along the x axis are the widths of the bandpasses, those along the y axis are the standard deviations of the data points within the ROIs.*

Sequence #2

The second sequence was obtained by including a correction for the dark current in the radiance calibration of Sequence #1. The black-white model, applied to this sequence, returned the plot in Figure 5.8. The inclusion of the black data in the model affects the vertical distribution of the data points in each filter, and makes the black and white sampled reflectances to lie precisely on their reference spectra.

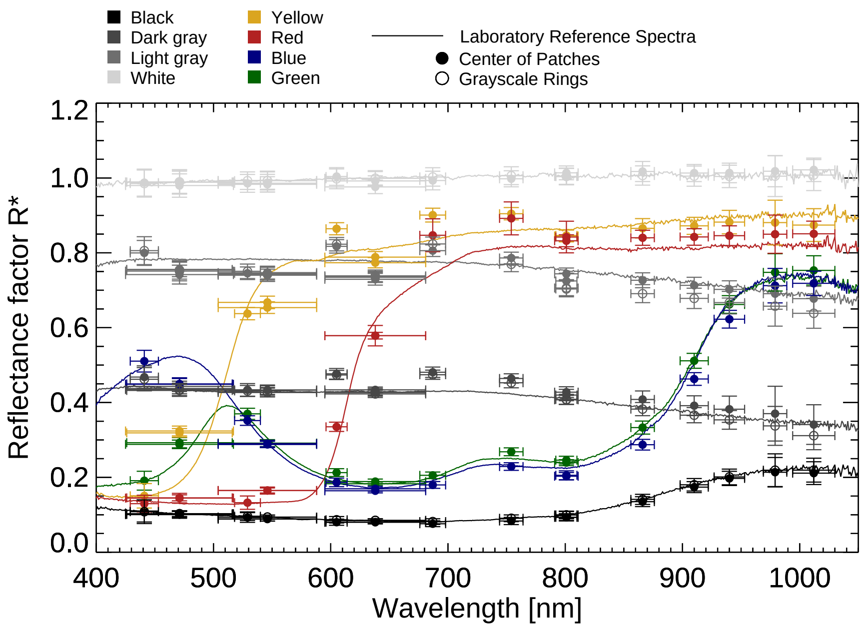

Figure 5.8: *Calibration spectra plot of dataset #2 using the "black-white" model. The data points represent the calibrated centers of the patches (filled dots) and grayscale rings (open dots), while the solid lines are the reference spectra. The error bars along the x axis are the widths of the bandpasses, those along the y axis are the standard deviations of the data points within the ROIs.*

In addition, I tested for the first time the one- and two-term fit models. Only the ROIs in the eight clean spots were used to compute the fits. Figure 5.9a shows an example of one-term fit for filter L2 (754 nm). The fit describes the data points rather well, with relatively small standard deviation on the slope. Figure 5.9b is the spectrum of the one-term fit slopes, which represents the irradiance spectrum of the light source employed. Slightly larger errors can be seen in filter L3 and in the near infrared (R3-R6). The parameters from the two fit models were applied to the radiances of the ROIs (clean spots and grayscale rings), which yielded the spectra in Figure 5.10a (one-term model) and 5.10b (two-term model). Despite some small deviations of the data points (especially in the white and black), the result from this dataset provided a first proof in favor of the one-term model. On the other hand, the offset in the two-term fit model helped reduce some of the discrepancies of the one-term model, particularly in the dark materials in the near infrared filters. Equation (5.5) yielded a RMSE of 0.024 for the one-term model and 0.021 for the two-term model. In addition, distinguishing between the broad-band and the narrow-band filters returned 0.023 and 0.025 respectively for the one-term model, and 0.022 and 0.021 respectively for the two-term model. The errors between expected and measured values are satisfyingly small for both models, though the two-term model is slightly more accurate (not surprisingly, thanks to the one more free parameter).

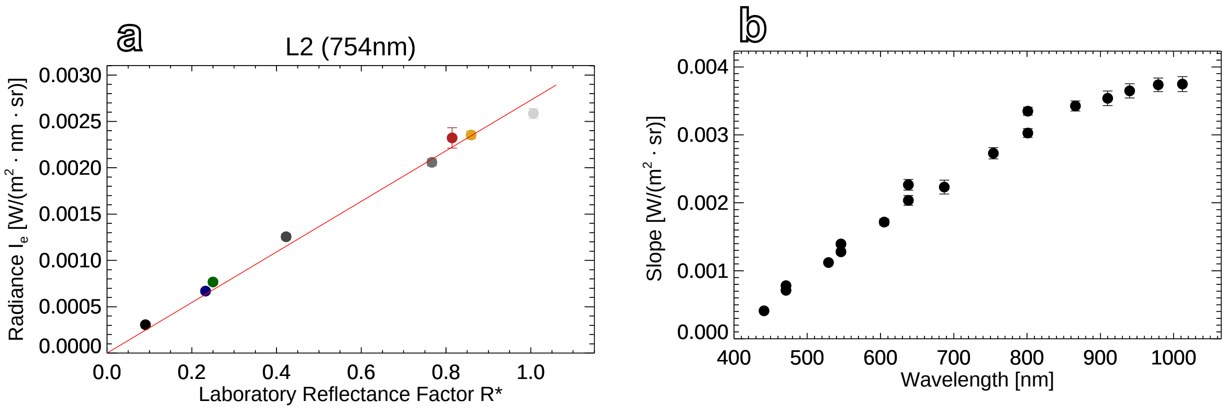

Figure 5.9: *(a) Example of one-term linear fit model applied to the data points of dataset #2 in filter L2 (754 nm). The red line is the fit. (b) Irradiance spectrum of dataset #2. Each data point is the slope of a one-term fit in the corresponding filter.*

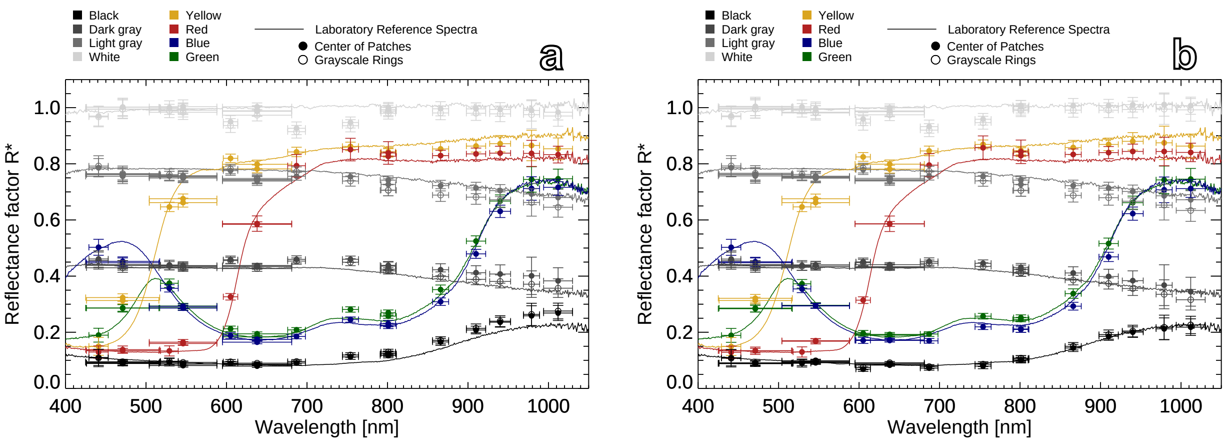

Figure 5.10: *Calibration spectra plots relative to sequence #2 obtained using (a) the one-term fit and (b) two-term fit models. The data points represent the calibrated centers of the patches (filled dots) and grayscale rings (open dots), while the solid lines are the reference spectra. The error bars along the x axis are the widths of the bandpasses, those along the y axis are the standard deviations of the data points within the ROIs.*

Sequence #3

The third sequence was made of 18 images of the calibration targets at 34 mm zoom, which allowed a complete view of the primary and secondary targets and all the other rock samples and materials. The geometry on the primary target was similar to the first two sequences, but I noticed the presence of two shadows cast by the gnomon, which implied two light sources of similar intensity, and with one of the shadows covering the dark gray primary patch (Figure 5.11a). First I applied the black-white model to the images, which yielded the plot in Figure 5.11b. The model worked acceptably for the black and the white patches, while other materials such as the dark gray, light gray, red and yellow are systematically lower than the expected values. One reason for this behavior is likely due to the two light sources, which did not allow a precise estimation of the azimuth angle and justifies the sensibly lower values of the dark gray data points. In addition, the focal length of 34 mm corresponds to a rather low resolution, which made the ROI selection challenging because the regions to select were made of very few pixels.

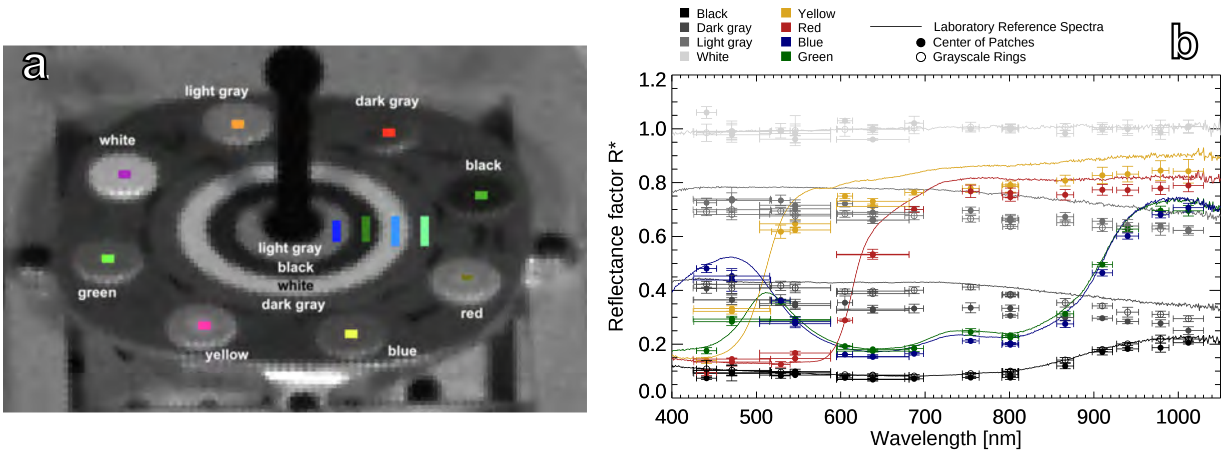

Figure 5.11: *(a) Image of the primary target from sequence #3 in filter R3 at 34 mm zoom, with the ROI selections in different colors. The image was cropped and magnified four times. (b) Calibration spectra plot of sequence #3 using the "black-white" model. The data points represent the calibrated centers of the patches (filled dots) and grayscale rings (open dots), while the solid lines are the reference spectra. The error bars along the x axis are the widths of the bandpasses, those along the y axis are the standard deviations of the data points within the ROIs.*

Subsequently, I tested again the one- and two-term fit models, which yielded the calibration spectra plots in figure 5.12a and 5.12b, respectively. The dark gray appears lower than its reference spectrum but far less than with the black-white model, thanks to the other six patches that counterbalance this effect in the fits. The result with the two-term model does not seem highly better than the one-term model, but overall the data points do not reach the accuracy of sequence #2 (figure 5.10) due to the low resolution of the images. The RMSE for the one-term model returned 0.027 overall, with 0.028 for the broad-band filters and 0.026 for the narrow-band filters, whereas the two-term model gave 0.024, with 0.027 and 0.023 for broad- and narrow-band filters, respectively. Although the low resolution and the double illumination increased the deviation between data and reference with respect to sequence #2, the numbers maintained rather small even without the need for an offset, proving the quality of the fit models.

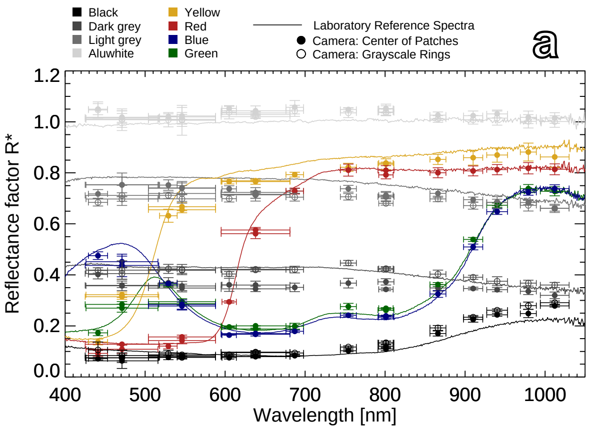

Figure 5.12: *Calibration spectra plots relative to sequence #3 obtained using (a) the one-term fit and (b) two-term fit models. The data points represent the calibrated centers of the patches (filled dots) and grayscale rings (open dots), while the solid lines are the reference spectra. The error bars along the x axis are the widths of the bandpasses, those along the y axis are the standard deviations of the data points within the ROIs.*

Sequence #4

The fourth sequence was similar to #3, as the same exact scene was acquired under the same illumination conditions (including the unfortunate double light source) but at a focal length of 63 mm (figure 5.13a). Figure 5.13b shows the result from the application of the black-white method on sequence #4. Again, the dark gray clean spot is systematically lower than expected, but the discrepancies between data points and reference spectra are slightly improved with respect to the case with 34 mm of focal length.

As expected from the focal length and illumination conditions, the results from the fit models applied to sequence #4 (figure 5.14) could be placed between those of sequence #2 (higher resolution and single light source) and sequence #3 (lower resolution and same double illumination). Once again, the addition of an offset reduces slightly the deviation of some data points, especially in the darker colors in the near infrared filters. The one-term model yielded a RMSE of 0.024, equal to the case with high resolution, while the two-term model had a value of 0.022, in-between sequences #2 and #3. For sequence #4, the narrow-band filters returned significantly lower values than the broad-band filters in both models (0.028 and 0.022 for the broad- and narrow-band filters, respectively, for the one-term model, and 0.026 and 0.020 for the two-term model).

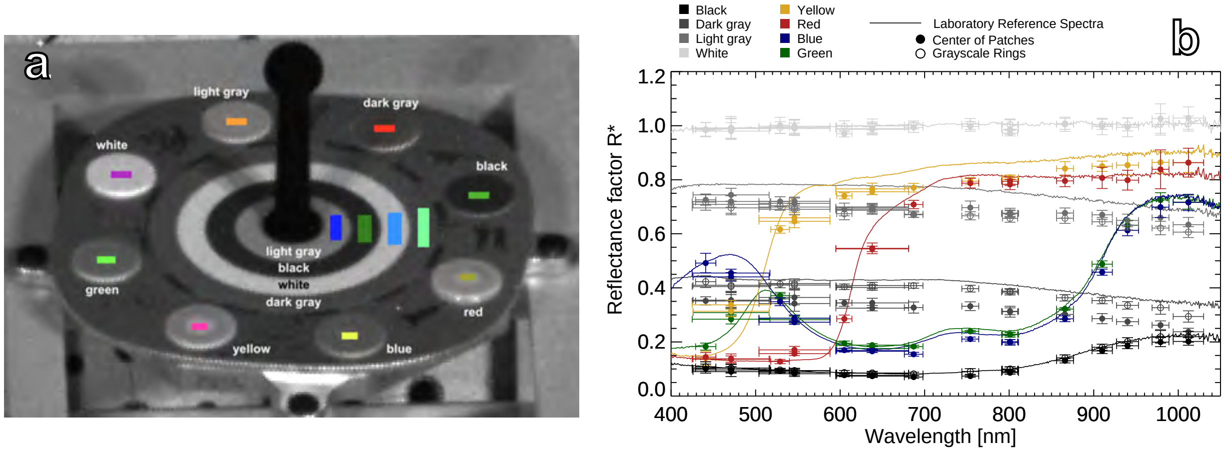

Figure 5.13: *(a) Image of the primary target from sequence #4 in filter R3 at 63 mm zoom, with the ROI selections in different colors. The image was cropped and magnified three times. (b) Calibration spectra plot of sequence #4 using the "black-white" model. The data points represent the calibrated centers of the patches (filled dots) and grayscale rings (open dots), while the solid lines are the reference spectra. The error bars along the x axis are the widths of the bandpasses, those along the y axis are the standard deviations of the data points within the ROIs.*

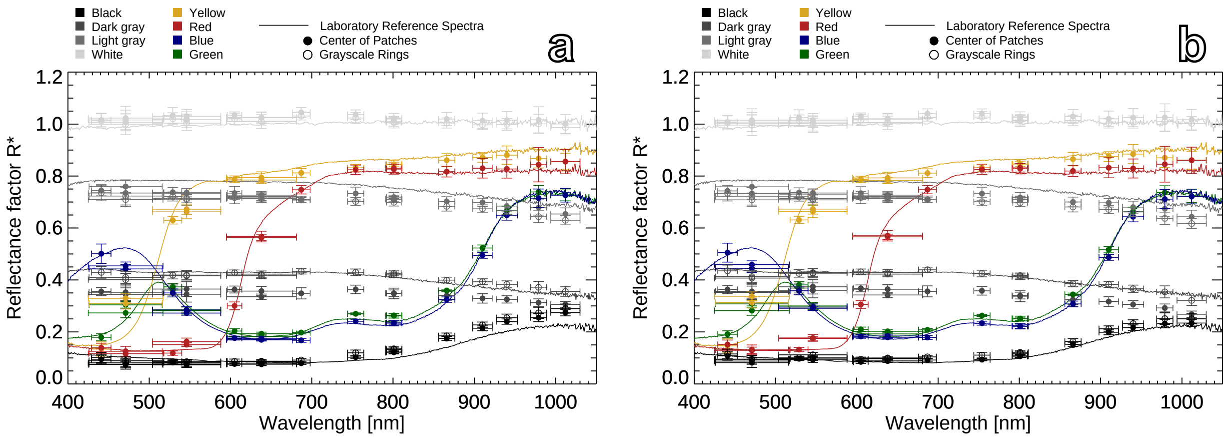

Figure 5.14: *Calibration spectra plots relative to sequence #4 obtained using (a) the one-term fit and (b) two-term fit models. The data points represent the calibrated centers of the patches (filled dots) and grayscale rings (open dots), while the solid lines are the reference spectra. The error bars along the x axis are the widths of the bandpasses, those along the y axis are the standard deviations of the data points within the ROIs.*

Sequence #5

For the last test I used the same images of sequence #3 at 34 mm zoom, but focusing on the witness samples (shown in colors in figure 5.15a). Instead of selecting the ROIs on the clean spots of the primary target, I drew them on the witness samples (figure 5.15b), which were located in one corner of the images, and hence the illumination geometry was $i = 0°$, $e = 20°$ and $Az = 90°$. Figures 5.16a and 5.16b illustrate the calibration spectra of the witness samples adopting the one- and the two-term fit models, respectively.

Even with a low resolution, the data points are characterized by very small errors in reflectance thanks to the large ROI selections on the witness samples, that are bigger tiles than the primary patches. In addition, for the same reason, the points follow the reference spectra quite well, with almost unperceivable improvements of the two-term fit with respect to the one-term model. As shown in the previous tests, the only deviations between data points and laboratory spectra could be due to the double illumination which made it difficult to state the preferential azimuth angle. The goodness of the fit models on the witness samples was reflected into the measured RMSE. The one- and two-term models yielded 0.021 and 0.019, lower than all the previous tests, as well as their respective narrow-band filters (0.018 and 0.016). The broad-band filters, on the contrary, contributed to adding some uncertainty, with the values of 0.026 for the one-term model and 0.023 for the two-term model.

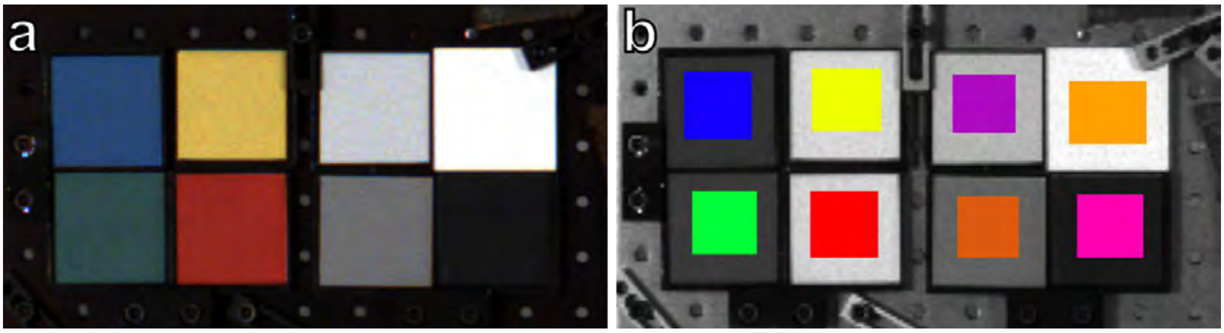

Figure 5.15: *(a) Color image of the witness samples from sequence #5 in filter L0 at 34 mm zoom. (b) Witness samples imaged in sequence #5 at 34 mm zoom in filter L1 (800 nm) with the ROI selections in different colors. The images were cropped and magnified two times.*

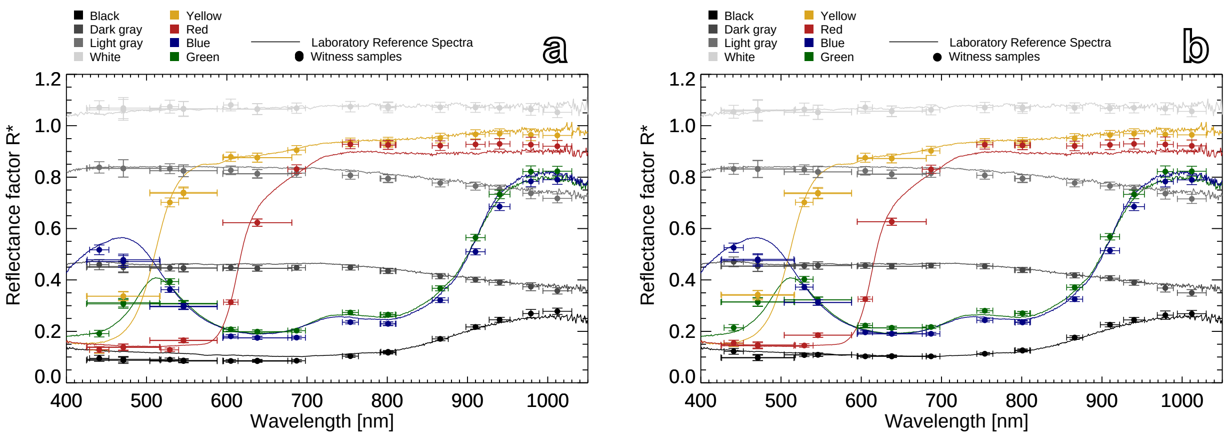

Figure 5.16: *Calibration spectra plots relative to sequence #5 obtained using (a) the one-term fit and (b) two-term fit models. The data points represent the calibrated witness samples, while the solid lines are the reference spectra. The error bars along the x axis are the widths of the bandpasses, those along the y axis are the standard deviations of the data points within the ROIs.*

	One-term			Two-term		
	Overall	Broad-band	Narrow-Band	Overall	Broad-band	Narrow-Band
#2	0.024	0.023	0.025	0.021	0.022	0.021
#3	0.027	0.028	0.026	0.024	0.027	0.023
#4	0.024	0.028	0.022	0.022	0.026	0.020
#5	0.021	0.026	0.018	0.019	0.023	0.016

Table 5.1: *Summary of the Root Mean Square Errors (RMSE) computed for sequences #2, #3, #4 and #5 when the one- and two-term models were applied. For both methods, the columns show the results relative to all filters ("overall", only the broad-band filters ("broad-band", and only the narrow-band filters ("narrow-band". The RMSEs were retrieved through equation* (5.5).

5.2.3 The "dark gray" test

As a complementary test, I investigated the uniformity of one of the grayscale rings in order to find significant variations in the reflectance within the same ring, which I chose to be the dark gray ring. The image sequence used was the #2 from the tests in section 5.2.2, because its high resolution (100 mm) would ensure a large number of pixels in each selection. I selected eight ROIs within the dark gray ring (figure 5.17a), from which the radiances were extracted in the 18 filters of Mastcam-Z. In order to convert them to reflectance factor, all the ROIs were multiplied by the folded spectrum from the Copenhagen data relative to the dark gray, and then divided by the radiance of one of the ROIs (I arbitrarily chose the yellow ROI in figure 5.17a). Figure 5.17b shows the reflectance spectra of the eight ROIs (relative to the yellow selection) together with the reference laboratory reflectance of the dark gray for comparison. The latter was extracted from the Copenhagen data without any correction, while the data points, through the process described above, were converted from the illumination geometry of the images to that of the Copenhagen data. In order to evaluate the uniformity of the ring, I computed the weighted average and uncertainty of the calibrated reflectance of the eight ROIs for each filter. Overall, the minimum and maximum relative uncertainties are 0.50% in the broad-band R0B (638 nm) and 2.40% in R5 (979 nm), respectively, with R5, R6, L6 and R4 being the only filters above 1%. As a result, this test proved a high uniformity of calibrated reflectance among all the ROIs, and more in general within the dark gray ring, allowing us to assume a similar degree of uniformity within all the other regions of the calibration targets.

5.3 The development of the reflectance routine

In section 5.2 I illustrated how I used the Bern and Copenhagen datasets to obtain the reference laboratory (folded) spectra for each color and grayscale material that had to be used in the one- and two-term linear fits for the calibration tests. The folded spectra from the Copenhagen data were multiplied by the spectrum of Spectralon, and by

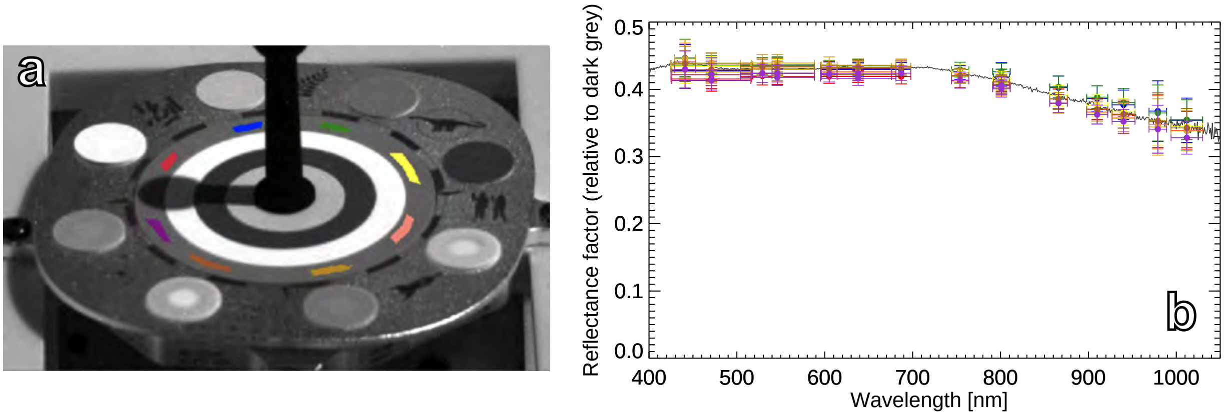

Figure 5.17: *(a) Image of the primary target from sequence #2 in filter R3 at 100 mm zoom, with the eight ROI selections in different colors within the dark gray ring for the "dark gray" test. (b) Reflectance factor spectrum of the dark gray ring. The data points represent the eight ROIs of figure (a) of the same color, while the solid line is the reference laboratory spectrum for the dark gray. All the measured radiances were normalized to the yellow ROI in figure (a). The error bars along the x axis are the widths of the bandpasses, those along the y axis are the standard deviations of the data points within the ROIs.*

the ratio K_{fold} described in the one-term fit model of section 5.2.1, that was extracted from the Bern data to convert the reflectance factors from the geometry of the Copenhagen data to that of the images to calibrate. This task was carried out easily in all the standalone tests before the launch because the illumination geometry triplets (i, e, Az) of the images were always available in the Bern data. Indeed, the emission angle was almost always 58°, while the Azimuth was typically 0°, 90° or 180°, and the incidence angle was a multiple of 5° listed within the emission angles of the Bern data (by principle of reciprocity, emission and incidence can be swapped with no significant variation in the reflectance factor). However, I could reasonably expect that, once on Mars, the incidence angle of the Sun would have been any real number between 0° and 90°, as well as the azimuth between 0° and 180°. In addition, in all our tests the emission angle was 58°, as expected from the positions of Mastcam-Z and the primary target on the rover, but when observing the secondary target the angle was 54°, which was not one of the values sampled in the Bern data. For all these reasons, I developed a model that, for each material of the calibration targets, filter of Mastcam-Z, and illumination triplet (i, e, Az), returned the corresponding value of reflectance factor. The model was organized in the three code functions on three levels described in the following.

Lower level: the "angle detective"

The first routine receives one color material of the calibration targets and the three angles (i, e, Az). The output is an array containing the six values of reflectance factor (in the six wavelengths) from the Bern data in the color and geometry given in input.

The concept is elaborate but extremely intuitive. The routine opens the dataset of the input color and searches for correspondences between the triplet given in input and all the combinations of triplets in the dataset. There are four possible outcomes:

- If it founds the complete triplet, it extracts R* in the six wavelengths and returns them in output.
- If it finds triplets where only two angles coincide, it interpolates the reflectance factor corresponding to those incomplete triplets over the range of the third (missing) angle. Then, the value of R* can be retrieved from the interpolation and returned in the six wavelengths.
- If only one angle of the triplet is present in the dataset, the routine will interpolate the reflectance factor twice (once for each missing angle). The six values of R* are obtained from the double interpolation and returned as output.
- Last and "worst" case: if none of the angles in the input triplet are present in the dataset, the routine identifies the two closest values relative to the input incidence angle that appear in the dataset, and performs the double interpolation (as described in the previous case) over emission and azimuth for both values. Finally, it interpolates the result over the two initial values of the incidence to find the R* in each wavelength.

The routine works on four assumptions. Firstly, the angles given in input are rounded to the closest integer. This approximation does not affect sensibly the resulting value of reflectance factor and helps save computational time in the interpolations. In second place, thanks to the hemispherical symmetry of the reflectance factor with respect to the plane of incidence, if the input $Az > 180°$, the routine forces it to be included between 0° and 180° by calculating $360° - Az$. Another assumption is given by the fact that, because the typical emission angle of 58° is listed in the Bern data within the incidence angles, the values of the angles i and e given in input are swapped, as a consequence of the principle of reciprocity. Although the principle is valid in theory, a measurement of R* using (i, e, Az) and one with (e, i, Az), where i and e have been swapped, might differ slightly. In all the Bern datasets this discrepancy was calculated to be less than 3%, which is a fairly low deviation. Finally, another potential source of uncertainty might be due to the fact that most values of R* are obtained through interpolation. I adopted the quadratic interpolation in order to achieve simplicity and high efficiency in the computation. Significant deviations between the interpolated and the real values of R* are not expected to occur, because both incidence and azimuth angles are densely sampled (i has steps of 5° up to 80° and Az of 15°). In addition, the routine makes use of the interpolation also when the phase angle is smaller than 5°, as it corresponds to the configuration in which the light source and the detector of the PHIRE-2 instrument were aligned, and the resulting measurement is not reliable due to the shadowing of the sample.

Intermediate level: the "ratio maker"

The second routine of the reflectance model is aimed at performing ratios between the reflectance factors in the Copenhagen geometry and the image geometry (given in input). It receives the name of a color material, the three angles and one of Mastcam-Z filters in input, and it returns the folded value of the ratio of the reflectance factors in the two geometries in the chosen filter. Firstly, this function calls the lower level routine in order to compute the six values of R* (in the six wavelengths of the Bern data) in the Copenhagen geometry and in the image geometry. Thus, the ratio between the two arrays of six elements is computed, and the six ratios are interpolated with a spline over the range 400-1065 nm. Finally, the folded ratio is calculated as an average of the ratio spectrum within the bandpass of the selected filter.

In this routine also one potential uncertainty may be due to the interpolation of the ratios over the spectrum. However, this method proved to be highly efficient. In addition, another approximation to consider is the fact that the folded value of the ratio in the chosen filter is computed through an average over the bandpass, whereas the ratio spectrum should have been convoluted with the throughput curve of that Mastcam-Z filter.

High level: the R* calculator

The high-end routine of the model receives one color material, the three angles and one of Mastcam-Z filters in input, and returns the fold value of the reference laboratory reflectance factor. It simply extracts the folded value of R* from the Copenhagen data in the chosen color and filter, and divides it by the ratio obtained by calling the "ratio maker" routine. The result is the reflectance factor relative to those material, filter and illumination conditions.

5.4 The calibration at NASA ATLO

The ultimate calibration test before the launch of Perseverance was accomplished in May 2020 when the rover was at NASA ATLO (Assembly, Test, and Launch Operations) facility of the Jet Propulsion Laboratory (Pasadena, CA). Mastcam-Z took an image sequence of the calibration targets (assembled on the deck of the rover) at 27 mm of focal length, with the rover illuminated by an artificial light from the zenith ($i = 0°$, $e = 58°$, $Az = 90°$). Figure 5.18 shows a color image (in filter L0 RGB) of the scene imaged by

Mastcam-Z. The images were processed and radiance-calibrated by a pipeline developed by the teammates at Cornell University. I calibrated the ATLO sequence using the one- and two-term models, in which I applied the reflectance routine described in section 5.3. Exactly as in the tests of section 5.2, the ROIs used to make the fits were the eight clean spots and their values of radiance were only multiplied by the folded Spectralon, while the corresponding reference laboratory spectra were retrieved using the reflectance routine.

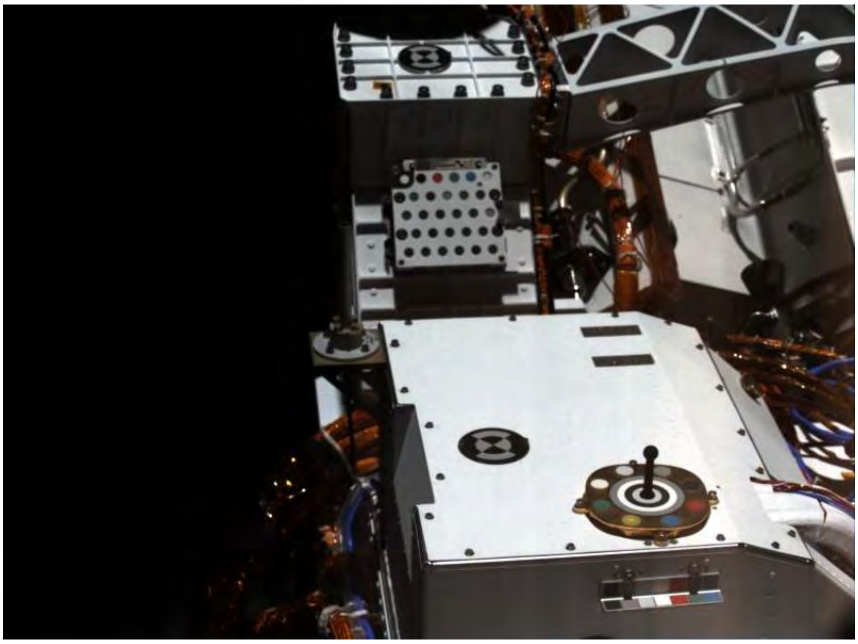

Figure 5.18: *The calibration targets (in the lower right) fully assembled on the deck of the rover before launch at NASA ATLO facility, imaged through the RGB Bayer filter of the left eye of Mastcam-Z.*

The plots in Figure 5.19 show the linear fits computed with the one-term model in the filters of the left eye of Mastcam-Z. The RMSE for the one-term model was 0.042, approximately double of the one computed for the witness samples. The main reason for this higher value was likely the contribution by the broad-band filters, which yielded a RMSE of 0.060, double of the narrow-band filters (0.029). The addition of an offset in the fits returned better results, with the RMSE of the two-term model being 0.019 overall, similar to the broad- and narrow-band filters (0.020 and 0.019, respectively). Figure 5.19 illustrates the calibration spectra plots of the clean spots and grayscale rings from the ATLO sequence. The difference in RMSE between the two models is quite evident also in the spectra. The data points treated with the two-term model (figure 5.20b) seem to follow the reference spectra better, whereas the results from the one-term model (figure 5.20a) present a noticeable deviation in the darker materials especially in the red and infrared bands, as in the previous tests. However, as witnessed by the RMSE of the broad-band filters in the one-term model, some of the broad-band data points show a significant distance from the reference spectra, in particular in the Blue Bayer band. In general, the broad-band filters appear slightly "squeezed" towards intermediate values of reflectance factor.

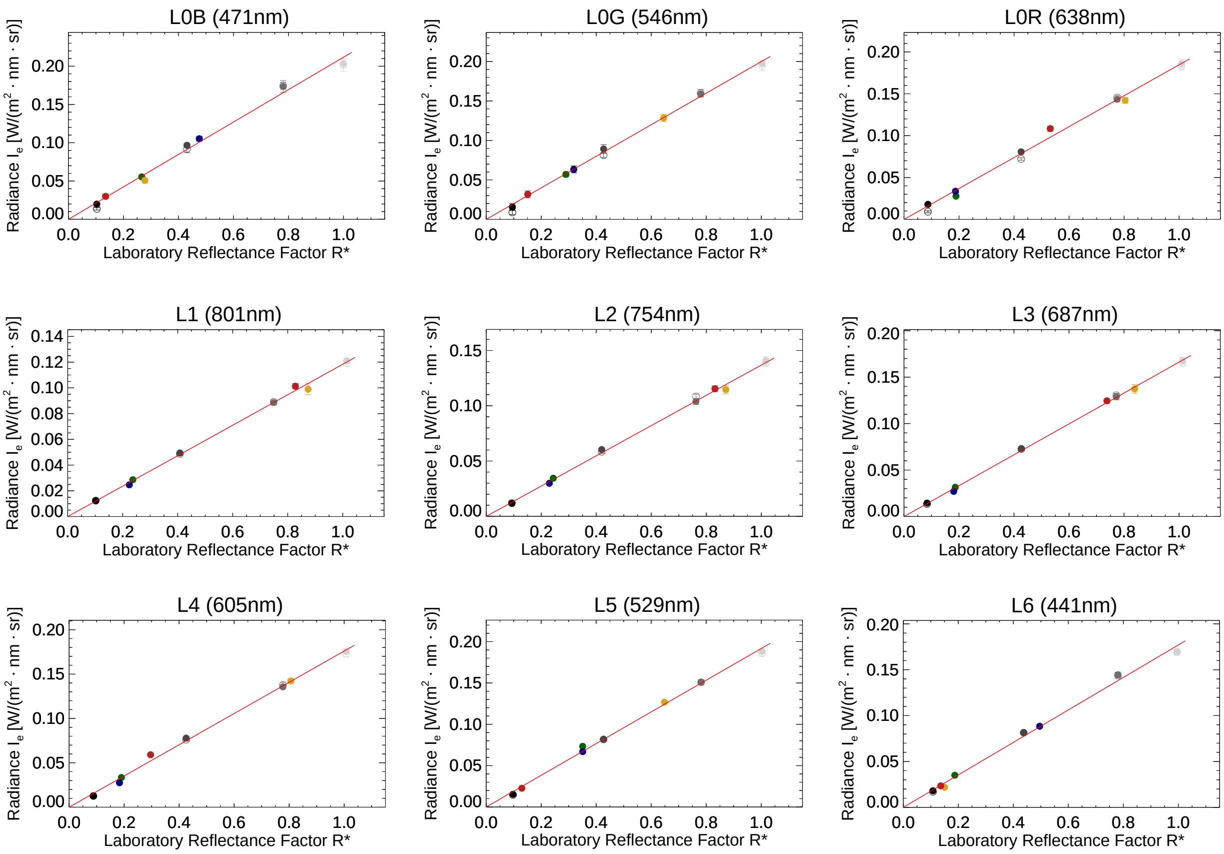

Figure 5.19: *One-term linear fits applied to the left eye images from Mastcam-Z at ATLO. In each plot, the dots are the data points of radiance-versus-reflectance of the eight clean spots, while the red line is the fit. Figure generated by me, reproduced from Kinch et al. (2020).*

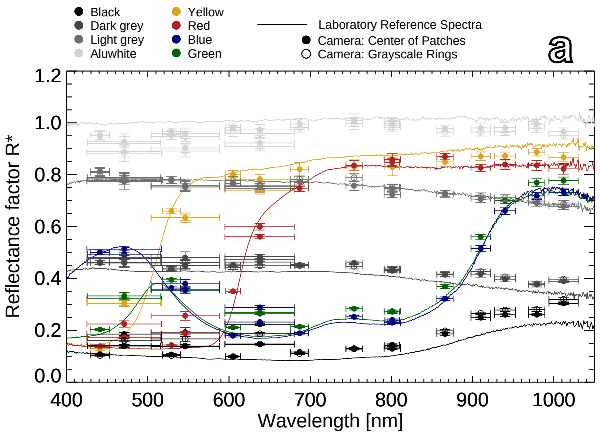

Figure 5.20: *Calibration spectra plots relative to the image sequence acquired at NASA ATLO, obtained using (a) the one-term fit and (b) two-term fit models. The data points represent the calibrated centers of the patches (filled dots) and grayscale rings (open dots), while the solid lines are the reference spectra. The error bars along the x axis are the widths of the bandpasses, those along the y axis are the standard deviations of the data points within the ROIs.*

Chapter 6

The data processing on Mars

In this chapter I present the methods adopted to collect data from the calibration target images and perform the reflectance calibration after the landing of Perseverance on Mars. A brief summary of the calibration procedure is given in section 6.1. Section 6.2 reports on the process of ROI selection implemented on Mars, while section 6.3 describes the documentation of the data from the ROIs in text files. In section 6.4 I give an overview on the imaging of the calibration targets, with a focus on the statistics that concerns illumination geometries, focal lengths and pixels, and a mention of the other cameras of Perseverance that acquired images of the Mastcam-Z calibration targets. Finally, in section 6.5 I show the first results from the application of the “one-term” model for the linear fits employed for calibration. The whole content of this chapter, with the exception of sections 6.1 and 6.4.2, is an extension and rearrangement of sections 2, 3.1, 3.2, 3.3 and 4.1 from my peer-reviewed article (Merusi et al., 2022), that was limited to the sol range from 0 to 350.

6.1 The reflectance calibration procedure

In the practical implementation of the reflectance calibration on Mars, we followed the procedure already employed for the pre-flight calibration at ATLO (section 5.4). The procedure required the selection of the ROIs within the eight primary clean spots of the radiance-calibrated images, the linear fits, and the application of the slopes to all the images that must be calibrated. By the time of the landing in Jezero, the functionalities of the software used for the ROI selections were increased and optimized, in order to make the calibration process faster and more accurate. Basically, the steps of ROI selection, linear fits and extraction of the slopes were automated. In this way, our tasks consisted in opening the full calibration target sequence in the software, performing some quality control and sometimes editing of the regions of interest. In addition, the automatic selection of the regions of interest was not limited to the eight clean spots, but included several other ROIs, as illustrated in section 6.2.

Subsequently, the software printed all the data relative to the ROIs of each calibration target image in a text file (one file for each image) called Radiometric Coefficient file, or RC file (section 6.3). The most important number within the RC files was the rad-to-iof coefficient, namely the inverse of the solar irradiance F, that had to be multiplied by all the pixels of the images to calibrate. Once generated, the RC files were treated by the calibration pipeline, that extracted the rad-to-iof coefficient and generated the IOF products. The section of the pipeline described in the last sentence was implemented around three months after landing. Before then, the IOF generation was relatively more manual: first we had to run a routine to retrieve the rad-to-iof coefficients, and then through another routine the IOF-calibrated images were created.

The development of an automated program for the ROI selection and creation of RC files, as well as the calibration pipeline, were fundamental not only for the correct and continuous calibration of Mastcam-Z images, but also for the scientific analysis of the results on which this thesis is based, that led to a consistent assessment of the performance of the calibration targets.

6.2 Selection of the regions of interest on the calibration targets

The selection of ROIs on the calibration targets was not limited to the eight clean spots, and the whole process was automated. An algorithm in our software recognized the pattern of the calibration targets in both eyes, and overlaid two model templates (one for each eye) on the images. Each template consisted in a graphic mask over a transparent background containing all the ROI selections in different colors. Although being quite accurate, this operation required regular human intervention, because the algorithm could not always recognize the boundaries between regions in sunlight and in shadow. Indeed, the only shaded regions that we wanted to select (when visible) were those on the grayscale rings under the shadow of the gnomon, while we wanted to discard any others.

The maximum number of ROIs was 41, though not all of them were always selectable because the shadow of the gnomon was often behind the gnomon itself, depending on incidence and azimuth angles. Therefore, these regions in the gnomon's shadow ranged from 0 to 4, while one or both rows of the secondary target were commonly in shadow due to their location on the side of the RPFA. The list of ROI selection groups is reported in table 6.1.

In addition, after applying and carefully editing the selections where necessary, we could indicate which ROIs (if any) should be neglected because they were completely

Figure 6.1: *Example of regions of interest (ROI) selections over an image of the cal-targets taken by the left eye of Mastcam-Z in the L1 filter (800 nm) on sol 69 at 48 mm focal length (sequence ZCAM03014). All 41 ROI are visible in colors, including those under the gnomon's shadow on the grayscale rings. The two ROIs partially selected in the secondary target were edited to exclude the shadows due to the bolts of the support.*

in shadow. These regions were "marked bad" and their data were stored but not used in later processing. In particular, if one of the clean spots was marked bad, it was excluded from the computation of the linear fits for calibration.

6.3 The Radiometric Coefficient files

After the selection of the ROIs on the calibration target images, our software retrieved their data and stored them into plain text files named Radiometric Coefficient files, or RC files. Each image in any filter produced one unique RC file. An RC file was divided in two parts. The first part listed basic metadata of the image, such as the image filename and the local martian time at which the image was taken. The second part of the file was a series of arrays, each one made of 41 elements corresponding to

Target	Regions	Number of selections
Primary	Clean spots	8
Primary	Magnet rings	8
Primary	Sunlit grayscale rings	4
Primary	Grayscale rings in the gnomon shadow	Up to 4, depending on observation geometry
Secondary	Horizontal tiles	7
Secondary	Vertical tiles	7
All scene	Primary target and rover deck	3 (portion of deck, portion of the golden base and top of the gnomon)

Table 6.1: *Summary of the main groups of regions of interest of the calibration targets. For each group, the target, the position on the target and the number of selections are listed.*

the 41 ROI selections in a precise order. Among the different arrays, one listed the average radiance values of the ROIs and the related uncertainty, the number of pixels selected in each ROI, the three illumination angles (incidence, emission, azimuth) of each ROI, and the reference laboratory reflectance factor of each ROI (computed using the routines described in section 5.3). The uncertainty of each ROI was simply the standard deviation associated to the average radiance over all the pixels of the ROI. Furthermore, three arrays gave useful information on the ROIs: one stated if the ROIs had been selected (usually all ROI's except a few of the shadowed grayscale ring regions that would not be present at high sun), one stated if they had been marked bad (usually because of shadowing common on the secondary target), and one stated if they should be used to compute the linear fits (in most cases the only regions selected where seven of the eight clean spots, excluding the white). These three arrays contained the Boolean values 0 and 1, where 0 = no, 1 = yes. If an ROI was not selected in the images, its corresponding field in the data arrays was replaced by a NaN (Not a Number).

At the end of each RC file the "rad-to-iof" coefficient was reported, together with its associated uncertainty. This coefficient was simply a positive number equal to the inverse of the slope of the linear fit between observed radiances and reference reflectances of the clean spots, that our software computed while printing the RC file. This number was the conversion factor from radiance to IOF reflectance, and was multiplied by all the pixels of all the radiance-calibrated images (reasonably close in time) in the same filter to convert them to reflectance. An example of a typical RC file is shown in appendix A.

One final remark on the RC files regards the splitting of the broad-band L0/R0 color images. Although Mastcam-Z can acquire each RGB color image in a single exposure (indicated by L0 for the left eye, R0 for the right eye), our software automatically splits it into the three frames corresponding to the three primary color channels of the Bayer pattern installed in each sensor of Mastcam-Z. Each frame, in its channel, is recognized by its name (L0B, L0G, L0R for the left eye, R0B, R0G, R0R for the right eye) and bandpass, and produces one RC file. As a result, each color image produces three RC files, and a full calibration target sequence will yield 18 RC files (three stereo broad-band channels, one stereo narrow-band channel - L1/R1 at 805 nm, and 10 mono narrow-band channels).

6.4 Imaging of the calibration targets on Mars

From landing to sol 670, Mastcam-Z acquired 111889 images on Mars, of which 4524 were of the calibration targets either in broad-band colors (L0, R0) or in the narrow-band filters (L1-L6, R1-R6). In particular, the color images allowed a regular quick qualitative check of the conditions of the targets over time, including the accumulation and the displacement of airfall dust on the surfaces, and monitoring the health of the materials. Figure 6.2 is a visual comparison of four color images taken by the left eye of Mastcam-Z (L0) at four different sols of the mission. Two phenomena can be assessed from the comparison. The first one is the progressive increase in the amount of dust with time. The airfall dust deposited everywhere on both targets, on the surrounding deck surface, and even stuck electrostatically to the vertical surfaces. The regions that were covered first and accumulated most dust very quickly were the magnet rings, as expected, due to their strong magnetic fields. This made dust concentrate also on the outer grayscale rings (close to the magnets) and to the thin vertical side of the golden base, where the intensity of the magnetic fields is still quite strong. The same outcome was observed in the Magnetic Properties Experiment on the Mars Exploration Rovers (Madsen et al., 2009) and the Mastcam calibration target on the Curiosity rover (Bell et al., 2017). The underlying colors, that were already attenuated but still visible after the first sols (Figure 6.2a), were no more discernible at the end of the period under analysis in this work (Figure 6.2d).

On other parts of the calibration targets or the deck, the deposition seemed to be ruled by either original deposition of small grains during the landing event, wind activity capable of transporting larger grains on top of the deck, and/or airfall dust. Airfall dust and larger grains were displaced frequently, allowing the cal-targets to remain rather clean. In addition, the deposition of dust on the secondary target was affected by its position on a vertical surface, which would limit the fraction of dust falling on the horizontal tiles. During the first 670 sols of the mission Perseverance experienced several significant episodes of high wind and local dust lifting. The first strong event occurred between sols 314 and 316 (Lemmon et al., 2022), with consequences visible for several sols (Figure 6.2b). Appreciable layers of brownish airfall dust and sand were conspicuous on the grayscale rings, on the deck next to the primary target (including the vertical side of the golden base), and on the secondary horizontal target following this event. Subsequently, when Mars entered in the northern winter, also known as the

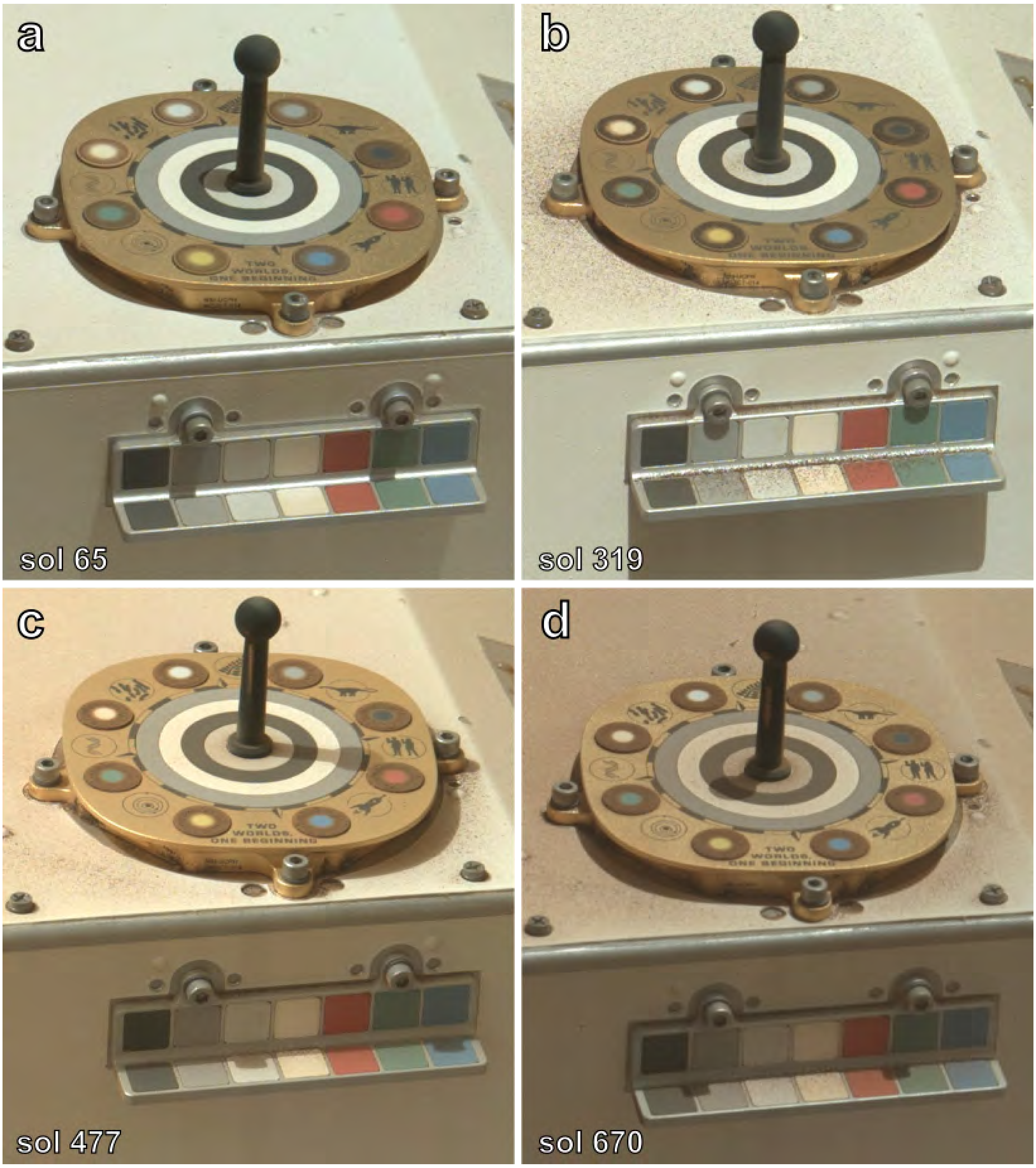

Figure 6.2: *Appearance of the calibration targets in four Mastcam-Z color images taken by the left eye (L0) on (a) sol 65, (b) sol 319, (c) sol 477, and (d) sol 670. All images have 48 mm of focal length and the sequence ID ZCAM03014.*

dust storm season, the raising of dust in the atmosphere became more frequent and sustained over longer time intervals, and the optical thickness of dust reached comparable or even higher peaks than the episodic events of the summer.

The second phenomenon that we noticed soon after landing and that became more and more evident sol after sol was the apparent change in hue of the white clean spot, from its original white to a sort of dirty yellow. For this reason, this effect was referred to as the "yellowing" of the white patch, and I analyzed in more detail its impact on the measured radiance in the different filters, as well as whether it also affected other ROIs made of the same white material. An exhaustive description of the issue will be given in section 7.4, but the effect on the measured radiance and the linear fits is already anticipated in section 6.5.

6.4.1 Image statistics

Over the first 670 sols, Mastcam-Z acquired a total of 346 sequences of the calibration targets for different purposes. Of those 346, 315 were made using all filters and were employed for the calibration of full multispectral sequences of scientific targets. At the same time, a large number of sequences of scientific targets were only imaged in L0/R0, and hence, these were not accompanied by calibration target observations. On average, one full sequence of the calibration targets for reflectance calibration was acquired every 2.1 sols.

During the first martian year, the Mastcam-Z Team also focused on photometric analysis (Johnson et al., 2022), which consisted in acquiring images of the same geologic target in two or more times of sol in only six filters (L1-L5-L6 and R1-R2-R6) in order to infer the spectral scattering properties of minerals under different illumination geometries. Mastcam-Z performed 13 photometric observations, each one followed by a calibration target sequence in those six filters. In addition, the calibration targets were imaged 18 times in only L0/R0, especially over the first 26 sols of the mission, for testing and verification of the camera and the calibration targets in different focal lengths, and public outreach.

The total number of images in each filter (with a reminder of the relative spectral range) is listed in table 6.2. In the table, the three Bayer filters of each eye are shown split, but they all have the same number because they were acquired together in the same shot. Of the 4524 images, 386 were transmitted losslessly, without any lossy compression that would slightly affect their quality. The remaining 4138 were transmitted using an 85% quality level compression.

Each sequence was identified by its illumination geometry (i, e, Az), where the emission angle was always approximately 58° for the primary target, and 54° for the horizontal surface and 36° for the vertical surface of the secondary target. All the 346 sequences are shown in figure 6.3, which presents their combinations of azimuth and incidence angles on the x and y axis, respectively. In addition, summing the points within intervals of incidence and azimuth angles yielded the histogram on the right in figure 6.3. Given the changing orientations of Perseverance in its exploration of Jezero, the azimuth angles are fairly evenly distributed, though with a larger frequency in the

Filter name	Range [nm]	Total images	Filter name	Range [nm]	Total images
L0B	480 ± 46	333	R0B	480 ± 46	333
L0G	544 ± 41	333	R0G	544 ± 42	333
L0R	630 ± 43	333	R0R	631 ± 43	333
L1	800 ± 9	328	R1	800 ± 9	328
L2	754 ± 10	315	R2	866 ± 10	328
L3	677 ± 11	315	R3	910 ± 12	315
L4	605 ± 9	315	R4	939 ± 12	315
L5	528 ± 11	328	R5	978 ± 10	315
L6	442 ± 12	328	R6	1022 ± 19	328

Table 6.2: *Summary of the total number of images of the calibration targets taken by Mastcam-Z in each filter within the first 670 sols on Mars. For each filter, the corresponding spectral range is reported.*

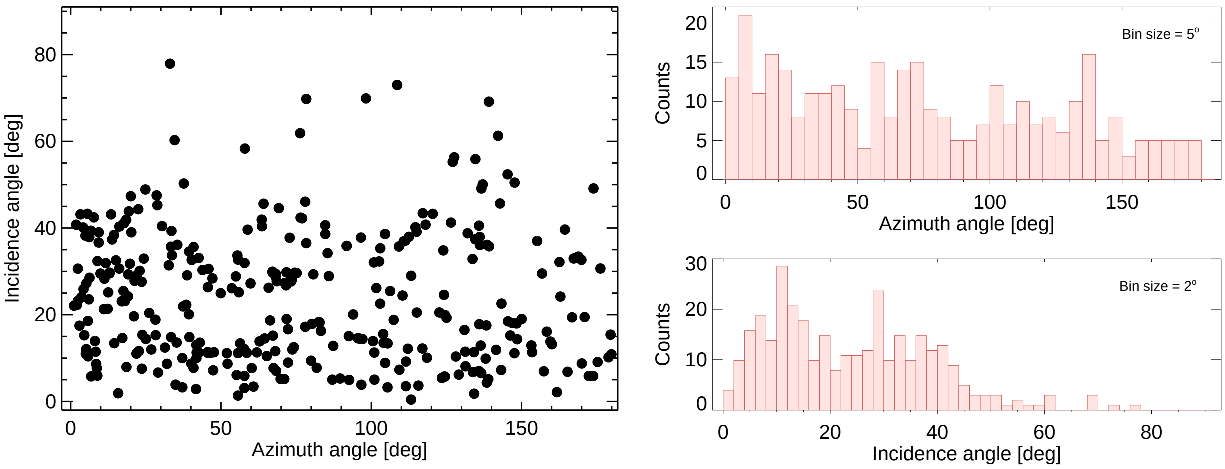

Figure 6.3: *Distributions of incidence and azimuth angles of all the 346 calibration target image sequences. The plot on the left shows the incidence-azimuth combinations of the sequences, while the histograms on the right illustrate how those sequences are distributed in terms of azimuth and incidence. Each data point in the plot on the left, corresponding to an entry in the two histograms on the right, is a single calibration target sequence, which includes at least one image for each eye of Mastcam-Z in the same observation (in most cases it is either in all filters or only in L0/R0).*

5°−10° interval, which corresponds to the Sun being approximately behind Mastcam-Z during the observation (Sun in front of the rover), and a much lower frequency of observations at opposite azimuth. In addition, from figure 6.3 we can recognize two main peaks of incidence angles around which most observations were made. One is around 10° and extends between 0° and 20°, and is typical of the first 350 sols, during which the northern summer occurred and the Sun was always very close to the zenith in the hours around noon. The second peak is around 30° and is concentrated between 20° and 45°, typical of the period of northern winter between sols 350-670, when the Sun was farther from the zenith at noon.

The relatively small number of observations on Mars with the Sun opposite to the camera (high azimuth) reduced the impact of the forward scattering, which in a few cases ($i \geq 50°$) was quite significant. In addition, at higher incidence angles (especially during the winter) the diffuse light acquired importance within the dusty atmosphere, reducing the contrast between the sunlit and shadowed regions. Early martian morning or late afternoon observations proved challenging for estimating the solar irradiance as part of the reflectance calibration. However, such configurations were a small number, and I developed a simple model that could be employed – and further improved – in the future to correct for the diffuse illumination (see section 9.3 and appendix B). The most accurate estimates of the solar irradiance were obtained when the Sun was high in the sky, with a smaller atmospheric path length, negligible forward or backward scattering, and less dusty atmosphere. However, since the diffuse illumination had a major impact when the Sun was low, this geometry was particularly useful to monitor the dust suspended in the atmosphere. This was done by comparing the radiance from the regions in the gnomon's shadow on the grayscale rings to those in direct sunlight (see section 7.2.3).

As a final statistical remark, it is interesting to focus on the zoom settings of the images and the numbers of pixels of the clean spot ROIs selected at different focal lengths. All zoom settings (26 mm, 34 mm, 48 mm, 63 mm, 79 mm, 100 mm, and 110 mm) were used by Mastcam-Z to take images of the calibration targets at the beginning of the mission, within the first 30 sols. The main aim of this experimentation was to find a compromise between the quality and resolution of images in connection to our ability to select the ROIs, and the weight of these images on the internal memory budget of the rover and the downlink of data from the rover to the Earth. Images at low resolution (26 mm and 34 mm) would have been light and easy to store and downlink, but the ROI selections would have been rather small to ensure an optimal quality for calibration (less pixels in a selection enhance the uncertainties). On the other hand, images at 100 mm or 110 mm would have been excellent for calibration thanks to their high resolution and pixel counts, but they would have been too heavy to be stored in the rover's memory and downlinked on average once every two sols. Therefore, after the first 30 sols the focal length of 48 mm was chosen as the standard, while the 34 mm was only used for one sequence and the 100 mm for three sequences. It is also worth mentioning that the 48 mm zoom had the advantage of being the highest focal length that allowed the imaging of the calibration targets with both eyes simultaneously without having to move the mast (unlike the other higher focal lengths), which implied a substantial saving in time. Moreover, when imaging the calibration targets at 48 mm, the images were systematically cropped to show only the two targets and save memory and time. Figure 6.4 displays the distribution of the image zooms over time, from landing to sol 670. The table on the right in figure 6.4 lists the numbers of images acquired by Mastcam-Z at the different focal lengths. The 48 mm dominates the scene, being employed in 95% of images.

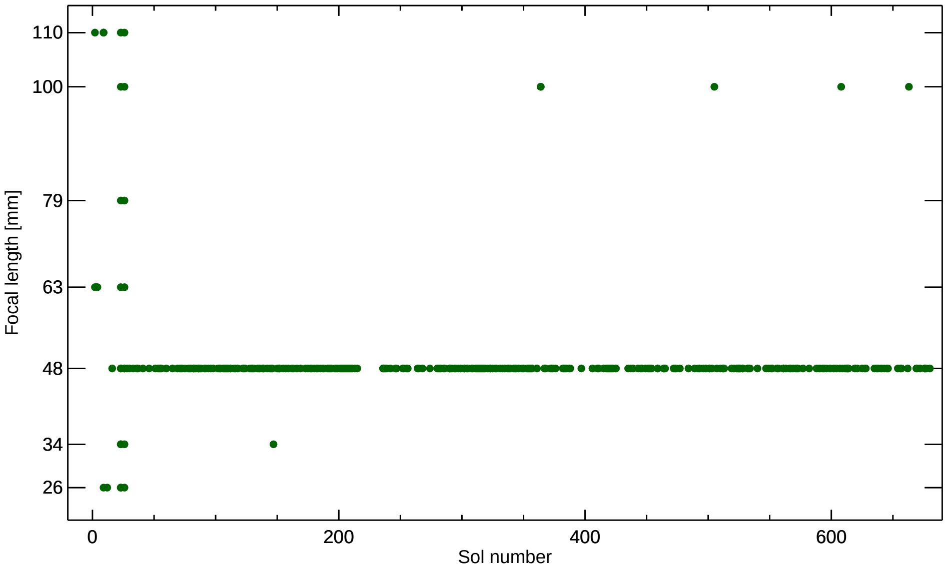

Focal length	Images
26 mm	34
34 mm	32
48 mm	4312
63 mm	22
79 mm	16
100 mm	86
110 mm	22

Figure 6.4: *Distribution of all the 4524 calibration target images over the first 670 sols according to the focal lengths (on the y axis) with which they were acquired. Each circle represents one of the 346 sequences to which the images belong. The table on the right is a list of the number of images in each focal length.*

For what concerns the numbers of pixels, I focus on the 26 mm, the 110 mm, and the most used, 48 mm. The average number of pixels over the eight clean spots and the 34 images at 26 mm was approximately 14.7. For the 110 mm zoom, the average on the 22 images obtained on Mars was 396.3 pixels. Before landing, Kinch et al. (2020) computed a prediction of the number of pixels in these two focal lengths. They considered the shapes of the clean spots as ellipses when seen from Mastcam-Z, retrieving their major and minor axes respectively of 10 by 5 pixels for the 26 mm zoom and 40 by 20 pixels for the 110 mm zoom. These numbers give areas of 40 and 630 pixels, respectively. The values that we measured on Mars resulted to be lower than these estimates, because the prediction was computed over the entire surface of the clean spots. The algorithm of our software, that selected those regions, always picked a smaller central portion of the clean spots, leaving a reasonable margin from the boundary of the magnet rings in order not to select dusty pixels that could systematically affect our measurements. Finally, in the standard zoom setting (48 mm) the average number of pixels was 67.0.

6.4.2 Cross-instrument imaging of the calibration targets

Thanks to their exposed location on the deck of the rover, the Mastcam-Z calibration targets were also imaged by other cameras of the rover's payload. The cameras that acquired the most interesting shots were the EDL, WATSON, and SuperCam.

One of the first images of the rover (and the calibration targets in particular) within the martian environment is shown in figure 6.5 and was taken on February 18^{th}, 2021, at 20:55 UTC by the Down-Look EDL Camera mounted on the descent stage (also known as the "sky crane"). It shows the Perseverance rover being taken down to a few meters from the martian surface by the rocket powered skycrane, which subsequently placed gently the six wheels of the rover on the surface, then disconnected by cutting the three cables and flew away.

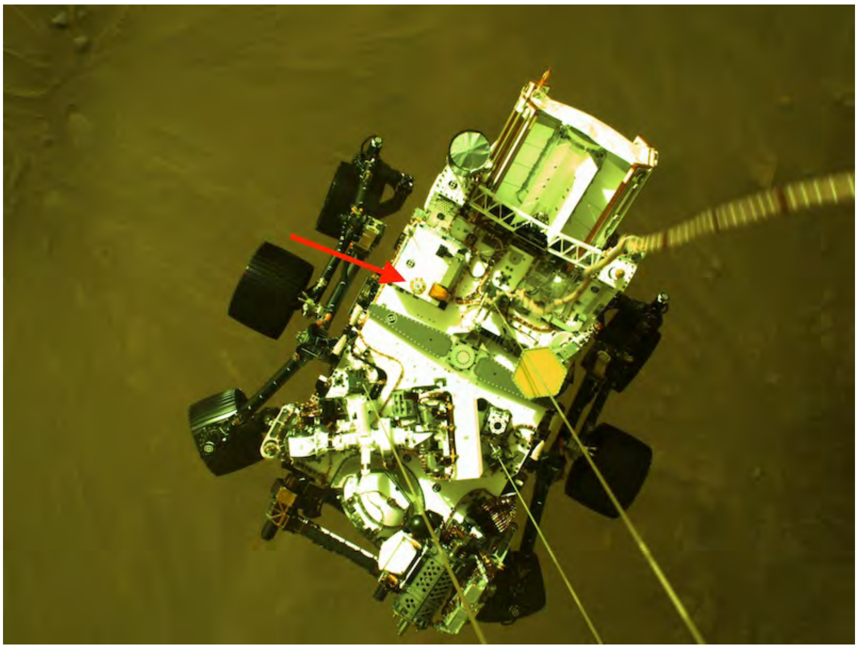

Figure 6.5: *One of the video-frames from the down-look camera mounted on the sky crane showing the Perseverance rover being lowered on the martian surface through cables on February 18^{th}, 2021. The rover was covered in sand and dust raised by the rockets of the sky crane. The red arrow indicates the location of the Mastcam-Z calibration targets.*

The WATSON camera of the SHERLOC instrument mounted at the end of the robotic arm of the rover captured images of the Mastcam-Z calibration targets. The first observation was performed on sol 26 (figure 6.6a) for color calibration, since images of the calibration targets at the beginning of the mission, when the calibration targets were still relatively pristine, could be compared with future WATSON sequences. Figures 6.6b and 6.6c show images taken on sol 368 and 545, respectively. The two images from sol 26 and 368 in figure 6.6 were acquired at 50 cm standoff, with the WATSON camera as close as physically possible to the calibration targets, whereas the one from sol 545 was at 130 cm standoff, where the robotic arm was placed as close to the rover's mast as possible to mimic the Mastcam-Z view of the calibration targets.

Some of the patches of the primary and secondary target were imaged by the Remote Micro-Imager (RMI) of the SuperCam instrument as part of ongoing calibration and monitoring activities. Figure 6.7 shows some examples of images of the red and black patches from sol 80, and the white patch from sol 541. In particular, the latter in figure

6.7c was captured in the martian morning, with the Sun low on the horizon enhancing the thick dust layer on the magnet ring.

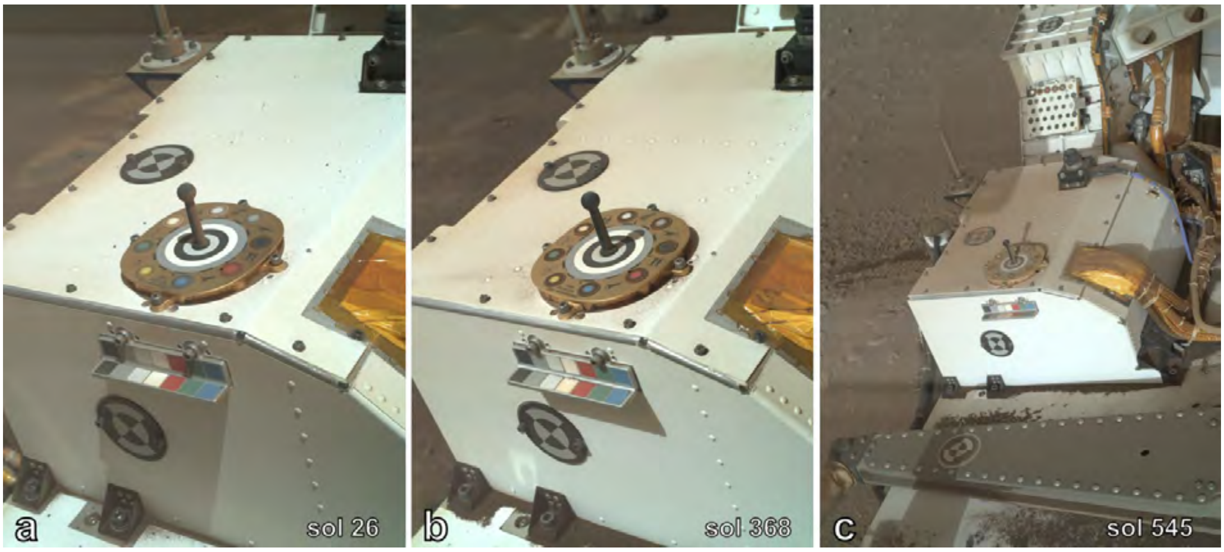

Figure 6.6: *The Mastcam-Z cal-target imaged by the WATSON camera on (a) sol 26 at 50 cm standoff, (b) sol 368 at 50 cm standoff, and (c) sol 545 at 130 cm standoff.*

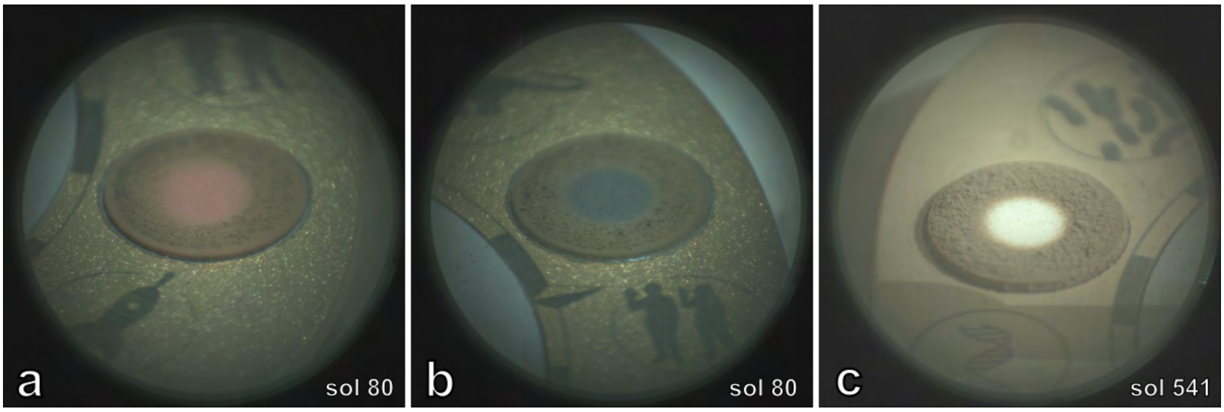

Figure 6.7: *Close-up images of the patches of the primary target acquired by the Remote Micro-Imager of SuperCam. (a) Red patch on sol 80, (b) black patch on sol 80, and (c) white patch on sol 541.*

6.5 The one-term linear fits

As displayed in this chapter, for each single radiance-calibrated image of the calibration targets that was processed, a unique RC file documented the measured radiances and reference reflectances of the eight clean spots, and the IOF-conversion factor that resulted from the linear fit. The linear fits, that adopted the one-term model of section 5.2.1, were indicators of the state of the clean spots in time and under different atmospheric conditions and illumination geometries. Figure 6.8 shows some examples of linear fits between radiance and reflectance relative to three different filters (L6, L3 and R5) and four sols of the mission (71, 314, 503 and 621).

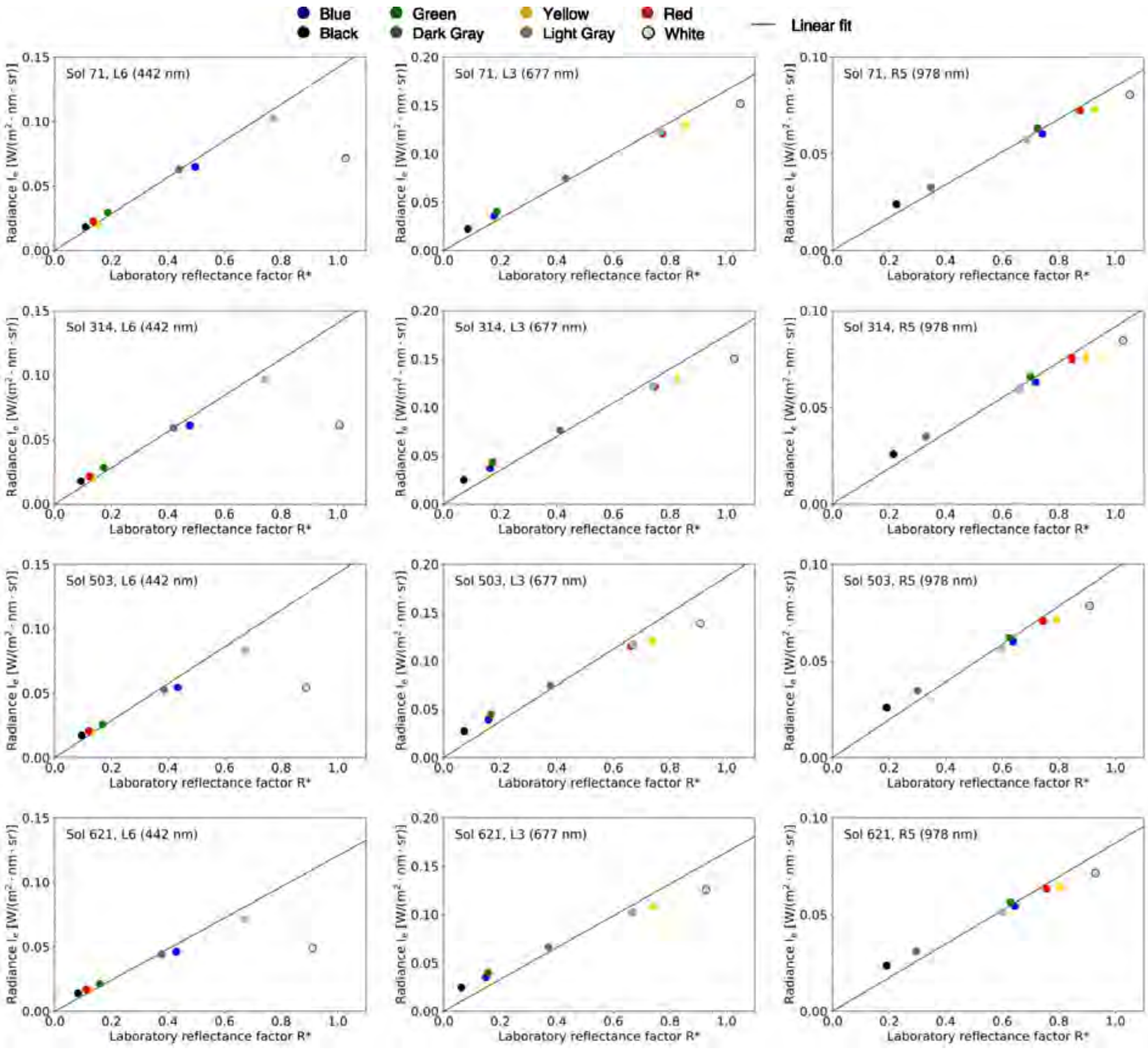

Figure 6.8: *Examples of one-term linear fits (in the form $y = a \cdot x$) over the data points of measured radiance and model reflectance factor for four sols (71, 314, 503, 621) in three filters (L6, L3 and R5). The straight lines are the fits. All the eight clean spots are plotted, but the white was not used to compute the fits.*

While seven clean spots did not present any problem, the white data point fell systematically below the fit, especially at shorter wavelengths (L6, L5 and L4). Indeed, the average radiance extracted from the white clean spot ROI in those filters was sensibly lower than expected, but this observation followed the discovery of the yellowing of the white patch. We concluded that the low radiance at short wavelength of the white patch was the spectral translation of the visual yellowing, and likely caused by some sort of degradation in the ceramic used to manufacture the patch (see section 7.4 for the full treatment). Since using the white clean spot would have significantly affected the results of the fits, and hence the reflectance calibration, we decided to exclude completely the ROI of the white clean spot from the computation of the fits. Therefore, starting from sol 0 all the linear fits for calibration were performed using the other seven clean spots, except for a few cases in which one of those seven was marked bad because of unwanted shadows. All the fits in the plots of figure 6.8 have been computed in this way.

In general, the relative uncertainty on the slopes of the fits was included between 2.58% in R5 and 5.02% in L4, with a mean value of 3.81% over all narrow-band filters. In addition, the one-term fits used for calibration had a reduced chi-squared χ^2_{red} of 28.6, with values ranging from 13.6 in R5 to 43.5 in L4. The relative uncertainties and χ^2_{red}, averaged over their narrow-band filters, are listed in table 6.3. It is useful to remind the reader that the uncertainties on the radiances of the clean spots in the plots of figure 6.8 (vertical error bars) are the standard deviations of the average radiances computed over all the pixels of each clean spot ROI, while the slopes of the fits (and their uncertainties) are retrieved by weighing the fits on the error bars of the clean spot radiances.

Filter [nm]	**Relative error**	$\chi^2_{\mathbf{red}}$
L6 (442 ± 12)	3.13%	17.59
L5 (528 ± 11)	4.09%	25.70
L4 (605 ± 9)	5.02%	43.54
L3 (677 ± 11)	4.11%	43.43
L2 (754 ± 10)	4.08%	43.15
L1 (800 ± 9)	4.03%	42.06
R1 (800 ± 9)	4.12%	42.72
R2 (866 ± 10)	3.52%	19.25
R3 (910 ± 12)	2.78%	15.05
R4 (939 ± 12)	2.65%	14.22
R5 (978 ± 10)	2.58%	13.56
R6 (1022 ± 19)	3.24%	22.43

Table 6.3: *Summary of the relative uncertainties on the slopes of the linear fits (central column) and associated reduced χ^2_{red} (right column) averaged over each narrow-band filter.*

Although the uncertainties on the fits were quite small, suggesting a fairly good quality of the model employed for calibration, I noticed that the fitted line, which was constrained to pass through the origin, was not the very best line fit for the data. I observed that a line with a small positive constant additive term (an offset) would produce a better fit (a "two-term" model in the form $y = a \cdot x + b$, described in section 5.2.1). This slight discrepancy between data points and fit lines was not present in the tests at ATLO of section 5.4 (or if it was, it was negligible). For the radiometric calibration of Mastcam-Z on Mars, we never employed an offset in our linear fit model (we only always used the one-term model), but we investigated the time evolution and spectral properties of such an offset, in order to understand its origin. A complete treatment of this side-investigation is reported in section 7.3.

Figure 6.9 shows four examples of calibration spectra plots of the clean spots relative to sols 71, 314, 503, and 621 (the same sols as figure 6.8), with the calibrated data points and the reference laboratory spectra. The uncertainties along the x axis are the measured bandpasses of Mastcam-Z filters, while those along the y axis are the standard deviations of the ROIs in the clean spots suitably converted to reflectance.

The radiometric decline of the white patch, more impactful at shorter wavelengths, is evident, while the other clean spots were apparently not affected by the same effect. The data display a good agreement with their laboratory spectra, whereas small deviations might be due to the presence of the offset mentioned above (likely caused by non-magnetic dust and/or slight residuals in the radiance calibration).

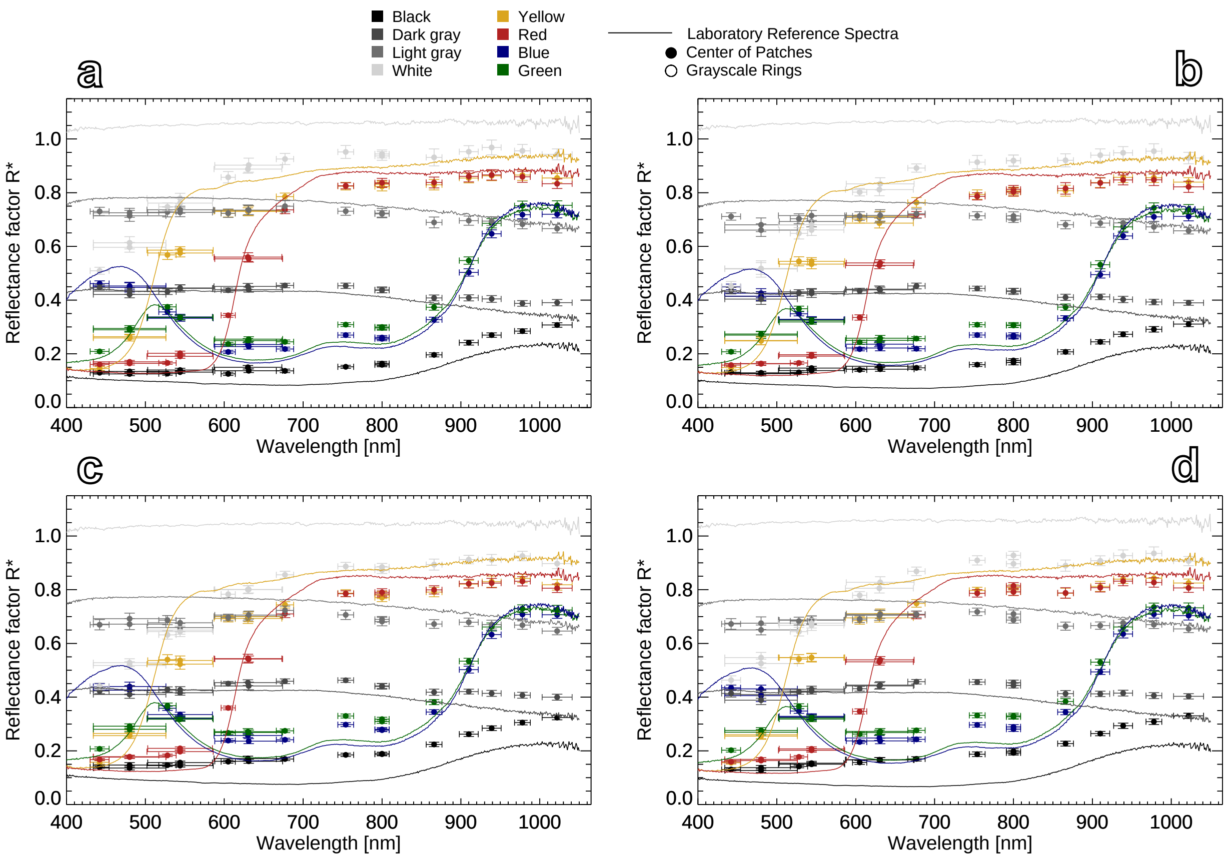

Figure 6.9: *Calibration target spectra from (a) sol 71, (b) sol 314, (c) sol 503, and (d) sol 621. The circles are the calibrated R^* reflectances of the clean spots, while the solid lines represent the corresponding laboratory spectra.*

Chapter 7

Results from the calibration targets

In this chapter I illustrate all the main results retrieved from the calibration targets during the first 670 sols on Mars. Sections 7.1 presents the solar irradiance time series, and its dependence on dust and the martian seasons. Section 7.2 is devoted to dust: it assesses the deposition and displacement of dust and other material on the calibration targets and the deck of the rover (section 7.2.1) and, in particular, on the magnets (section 7.2.2), and the effects of airborne dust on the diffuse illumination (section 7.2.3). In 7.3 I report on the investigation on the two-term linear fits, which were never employed for calibration. Finally, in 7.4 I summarize the results regarding the unexpected behavior of the white (AluWhite98) material on the calibration targets and I report on the tests that were performed in order to make light on the issue. All the results presented in this chapter are an extension (up to sol 670) of those published in my peer-reviewed article Merusi et al. (2022), which were obtained up to sol 350.

7.1 The solar irradiance time-derived series

The slopes of the linear fits between the measured radiances and reference reflectances performed for calibration are accurate estimates of the local instantaneous solar irradiance in each filter of Mastcam-Z. Given that the irradiance can be affected by multiple factors, such as the distance of Mars from the Sun, specific illumination geometry, atmospheric conditions, diffuse illumination and dust, monitoring the values of the slopes is an indirect way to assess the martian environment over time.

Figure 7.1 shows the time evolution of the solar irradiance in the 12 narrow-band filters over the first 670 sols on Mars. It is possible to recognize the contrast between the two halves of the martian orbit, separated by a boundary at approximately sol 315. During the first 315 sols, Perseverance experienced the whole northern summer (the vertical dashed line on the left is the martian aphelion), that was clearly characterized by a calm weather, as witnessed by the rather smooth and stable trend of all filters. The

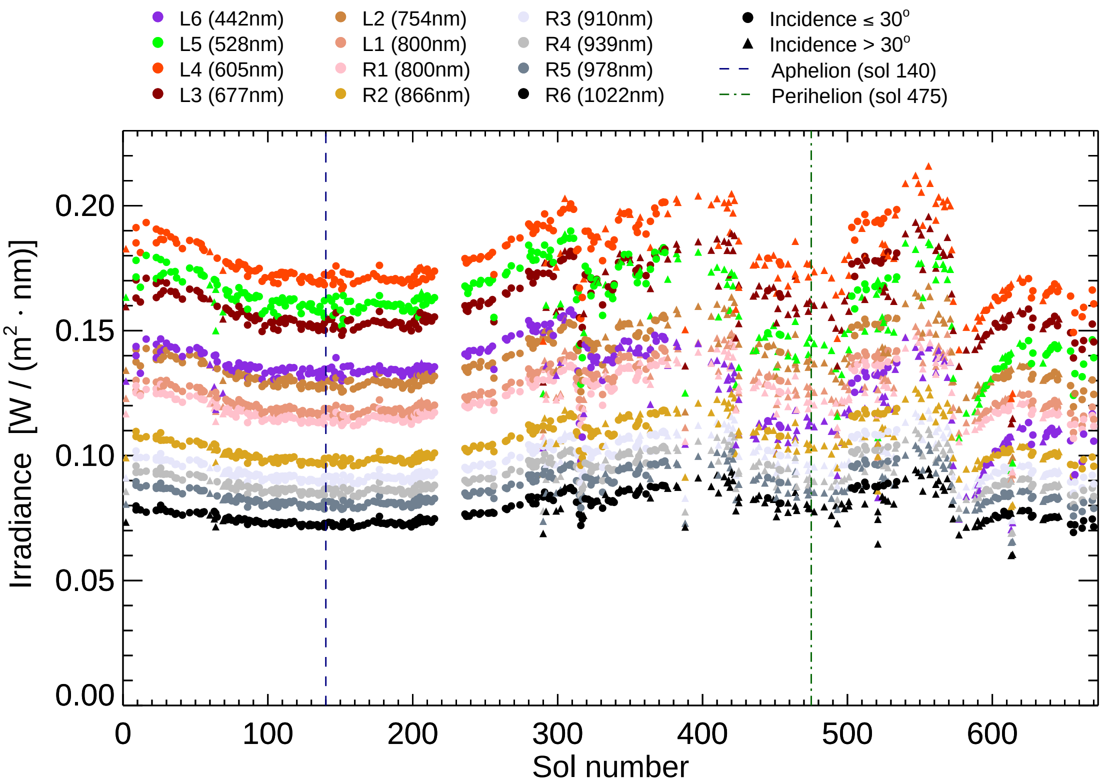

Figure 7.1: *Time evolution of the solar irradiance from landing to sol 670, in terms of slopes of the one-term linear fits between radiance and reflectance of the calibration targets. The colors represent the different narrow-band filters of Mastcam-Z. The blue dashed line is the Martian aphelion, the green dot-dashed line is the martian perihelion. The two vertical solid lines on sols 100 and 180 are the boundaries of the time range considered for the making of the spectrum in figure 7.3.*

irradiance in the filter L1 (800 nm) went from 0.13 W/($m^2 \cdot$ nm) after landing to 0.12 W/($m^2 \cdot$ nm) at aphelion (sol 140), and then it went back up to 0.14 W/($m^2 \cdot$ nm) on sol 315. The depression of the irradiance around the aphelion was due to the larger distance from the Sun. As expected before landing, the Sun was always very close to the zenith around noon, and even in the few observations carried out in different times of sol (higher incidence angle, denoted by the triangles in the plot) the irradiance did not deviate much from the general trend. Sol 315 marked the first important dust event striking the landing site of the rover and caused a sudden trough in the local irradiance, which went from 0.140 W/($m^2 \cdot$ nm) to 0.115 W/($m^2 \cdot$ nm) and back up to 0.134 W/($m^2 \cdot$ nm) in a span of three sols. Starting just after that event, the trend of irradiance can be divided into a few intervals. Firstly, the irradiance increased slowly from 0.135 W/($m^2 \cdot$ nm) in L1 on sol 320 to 0.143 W/($m^2 \cdot$ nm) on sol 375, and the higher incidence angles of the observations decreased it to 0.135 W/($m^2 \cdot$ nm) on sol 425. Between sols 435 and 500 the irradiance maintained approximately flat around 0.126 W/($m^2 \cdot$ nm) in L1, after which it “jumped” up to 0.138 W/($m^2 \cdot$ nm) and increased slowly to 0.143 W/($m^2 \cdot$ nm) on sol 570. After sol 570, the irradiance dropped again to 0.109 W/($m^2 \cdot$

nm) in L1 (800 nm), and from sol 575 it went through three short periods in which it experienced a growth followed by a little decrease. First the irradiance in L1 reached the value 0.125 W/($m^2 \cdot$ nm) on sol 625, then it went from 0.119 W/($m^2 \cdot$ nm) to 0.121 W/($m^2 \cdot$ nm) between sols 635 and 645, and finally from 0.110 W/($m^2 \cdot$ nm) to 0.115 W/($m^2 \cdot$ nm) between sols 652 and 670. The changes in the trend, such as increases, decreases and drops, were due to changing dust loads in the atmosphere associated with significant wind activity. I will deal with dust assessment in section 7.2, but it is useful to anticipate here that any growth of the atmospheric optical depth due to a higher amount of airborne dust can cause a decrease or even a drop in the derived solar irradiance. Conversely, when the wind placates and the optical depth decreases after a dust event, the irradiance rises thanks to the lower attenuation. A helpful reference is the time series of the direct measurements of atmospheric optical depth, that is an effective indicator of the amount of airborne dust suspended in the atmosphere around the rover's location, and that will be introduced in section 7.2.3.

The irradiance time series for the other regions of the calibration targets were very similar to that of the clean spots. Figure 7.2a shows the results for the grayscale rings, figure 7.2b for the secondary horizontal and figure 7.2c for the secondary vertical tiles. They are all characterized by a fairly stable and coherent trend, which was quite calm up to the dust event of sol 315, and several changes in the irradiance in correspondence of the variations in the atmospheric optical depth related to dust.

In order to assess the quality of calibration with the targets, I extracted the averaged spectral irradiance for comparison with the solar spectrum. I focused on the period of time in which the trend of the irradiance in all filters in figure 7.1 appeared as flat as possible, which I recognized to be an interval of 81 sols around the aphelion (i.e., sol 140 ± 40, from sol 100 to 180). I computed the average of the irradiance for each filter, and I plotted these values as a function of their wavelengths. The result is represented as the black dots in figure 7.3, where the blue solid curve is a black body model for the Sun for comparison. The solar black body model was obtained through the following expression:

$$E(\lambda, T) = \frac{2\pi h c^2}{\lambda^5} \cdot \left[\exp\left(\frac{h c}{\lambda k T}\right) - 1\right]^{-1} \cdot \cos i \cdot D_{Sun}\,, \tag{7.1}$$

where h is the Planck constant, c is the speed of light, λ is the wavelength, k is the Boltzmann constant, T is the temperature of the solar photosphere that I approximated as 5775 K, i is the average incidence angle from sol 100 to 180 (which turned out to be 10.5°), and D_{Sun} is the solid angle of the solar disc as seen from Mars. In this case, the latter was computed as:

$$D_{Sun} = \pi\left(\frac{R_\odot}{d_♂}\right), \tag{7.2}$$

where $R_\odot$ is the radius of the Sun, which is about 696340 km, and $d_♂$ is the average

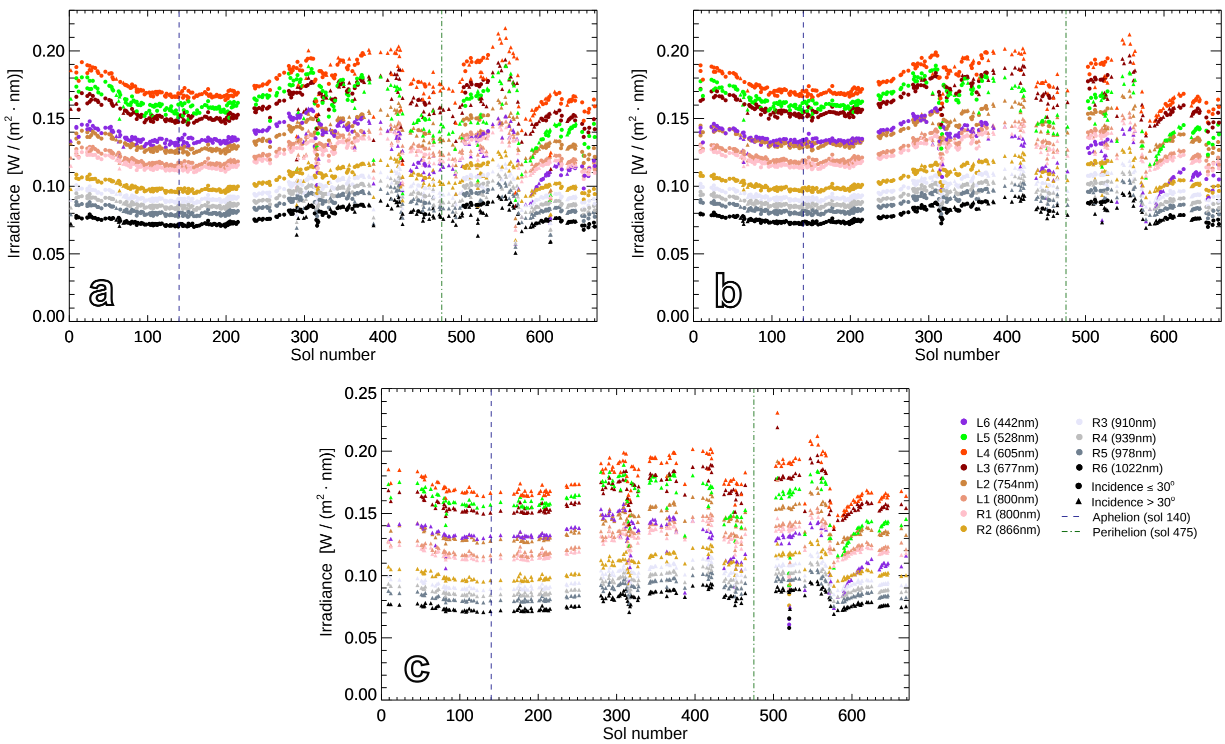

Figure 7.2: *Time-derived series of the solar irradiance obtained for (a) the grayscale rings, (b) the secondary horizontal tiles, and (c) the secondary vertical tiles. All the irradiances were computed through linear fits between the measured radiances and the reference reflectances. In each plot, the circles and the triangles represent observations with incidence angles smaller or greater than 30°, respectively, with respect to the normal line of the surfaces. The blue vertical dashed line is the solar aphelion, the green vertical dot-dashed line is the solar perihelion.*

distance between Mars and the Sun in the sol range 100-180, that I retrieved to be $2.372 \cdot 10^8$ km. Hence, the solid angle resulted to be $D_{Sun} = 2.46 \cdot 10^{-5}$ sr. The data points are obtained at the surface, whereas the model spectrum is computed at the top of the atmosphere of Mars and does not consider the effects of turbulence, dust and diffusion. However, data points and model show a good agreement at longer wavelengths, while the data points fall below at shorter wavelengths as expected, due to the absorption by dust suspended in the atmosphere.

7.2 Dust assessment and properties

During the first 670 sols of Perseverance on Mars, dust interacted directly and indirectly with the calibration targets. The direct interaction involved the deposition of airfall dust and other material on the calibration targets and its magnets, while I could observe the indirect effects of the dust suspended in the atmosphere through its attenuation of the sunlight, which increased the scattering and reduced the contrast between sunlit and shadowed regions. Such observations gave information on the magnetic

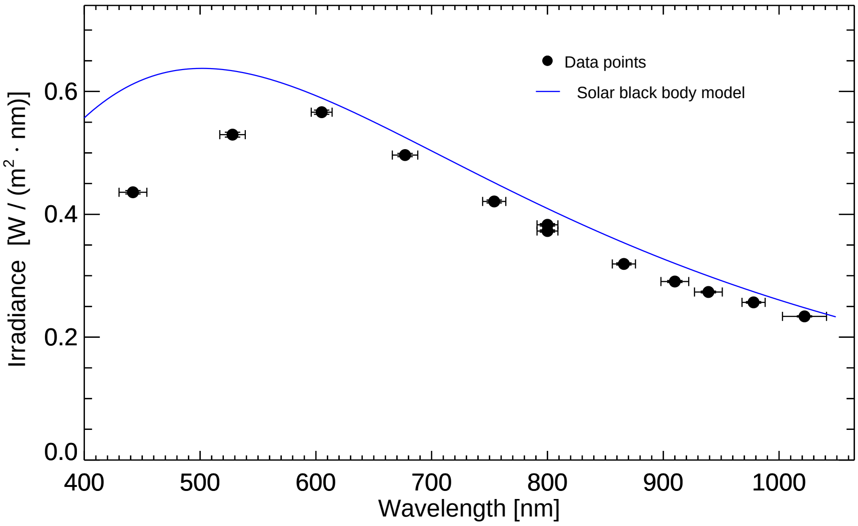

Figure 7.3: *Solar irradiance spectrum around the Martian aphelion. The black points are the sample spectrum of solar irradiance obtained as the average of the slopes in each filter between sols 100 and 180 (indicated by the two vertical solid lines in figure 7.1). The blue solid line is a model black body curve for the Sun (T = 5775 K) as seen from Mars.*

properties of dust and the evolving atmospheric dust content.

7.2.1 Deposition of material on the calibration targets

Due to its typical grain size and mass, the martian dust is usually subject to the weather conditions, especially to the wind, which can raise it in the atmosphere and transport it. As a result of the displacement, dust grains fall towards the ground and can adhere electrostatically to surfaces. In its first 670 sols, the rover Perseverance experienced a variability in the dust patterns on all its surfaces. On those flat areas, dust was deposited and cleaned out frequently by wind events, and possibly by the vibrations due to the motion of the rover. In order to assess the dust settlement and displacement, I checked all the radiance-calibrated RGB images of the calibration targets acquired by the left eye of Mastcam-Z from landing to sol 670 in sequence (some examples are shown in figure 7.4). The deposition of dust and sand was very modest up to sol 86 (figure 7.4a for sol 84), when several small grains were transported on the deck. Between sols 124 and 138 there was a more intense wind activity (figure 7.4b for sol 130), which continuously displaced larger sand grains and swept away the finer dust. Around sols 166 and 169 fine grains deposited on the deck, the grayscale rings and the secondary horizontal target. From sol 280 to 299 more fine grains deposited on the grayscale rings (figure 7.4c for sol 280), while the larger sand grains were translated several times by a few millimeters. On sol 314 a major dust event struck, bringing a large amount of dust and fine sand grains on all the surfaces of the deck and the cal-targets, that was more perceivable from sol 316 (figure 7.4d for sol 318). A considerable

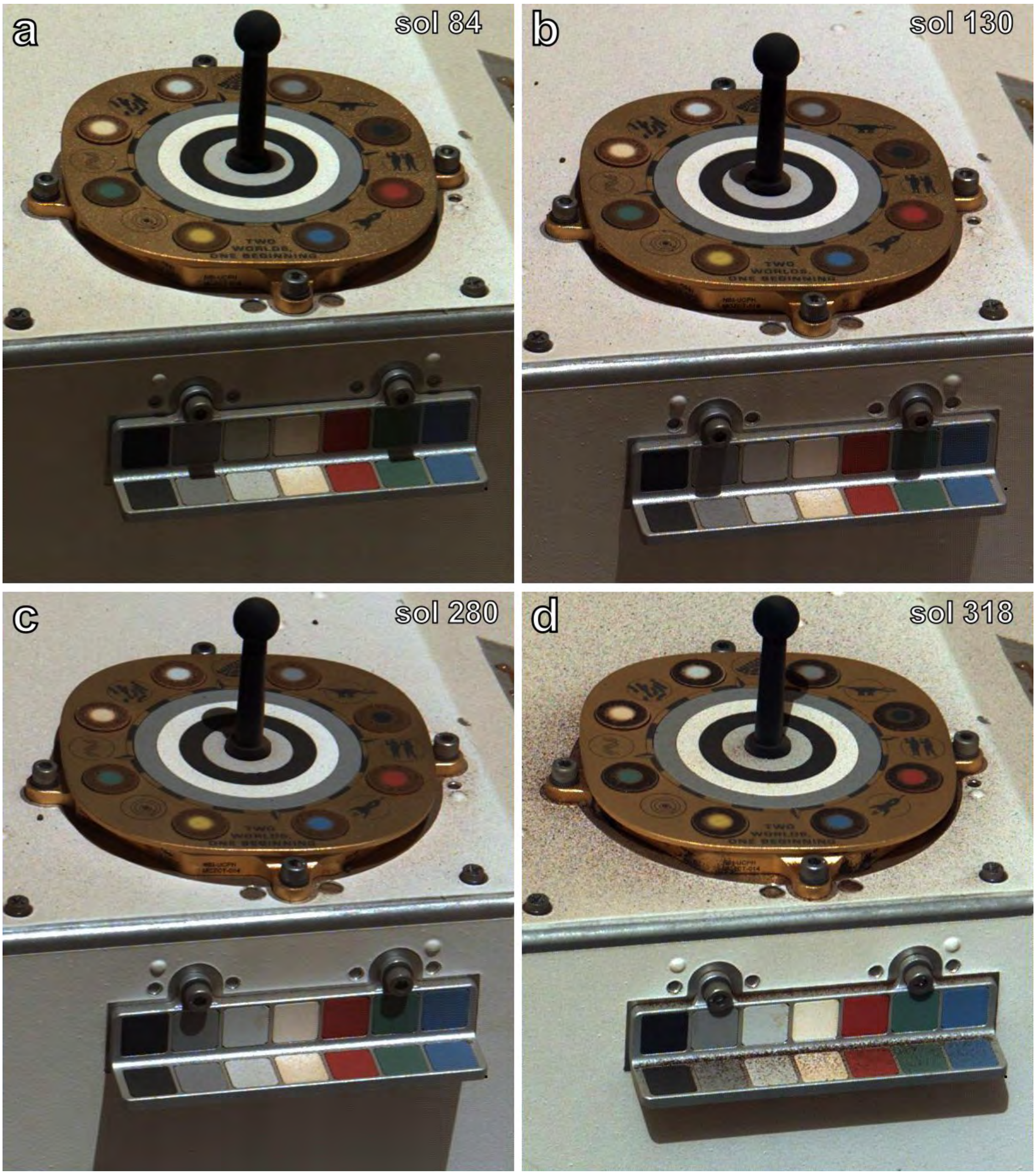

Figure 7.4: *The calibration targets imaged in colors by the left eye of Mastcam-Z (L0) at a focal length of 48 mm on (a) sol 84, (b) sol 130, (c) sol 280 and (d) sol 318. All the images have the sequence ID ZCAM03014.* *It continues on page 103.*

fraction of this dust was swept off of all these surfaces first between sols 327 and 333, and then on sols 349 and 350, when the deck and the grayscale rings appeared quite clean and on the secondary target the dust is concentrated along the side between the horizontal and the vertical rows. After sol 350, the dust movement on the calibration

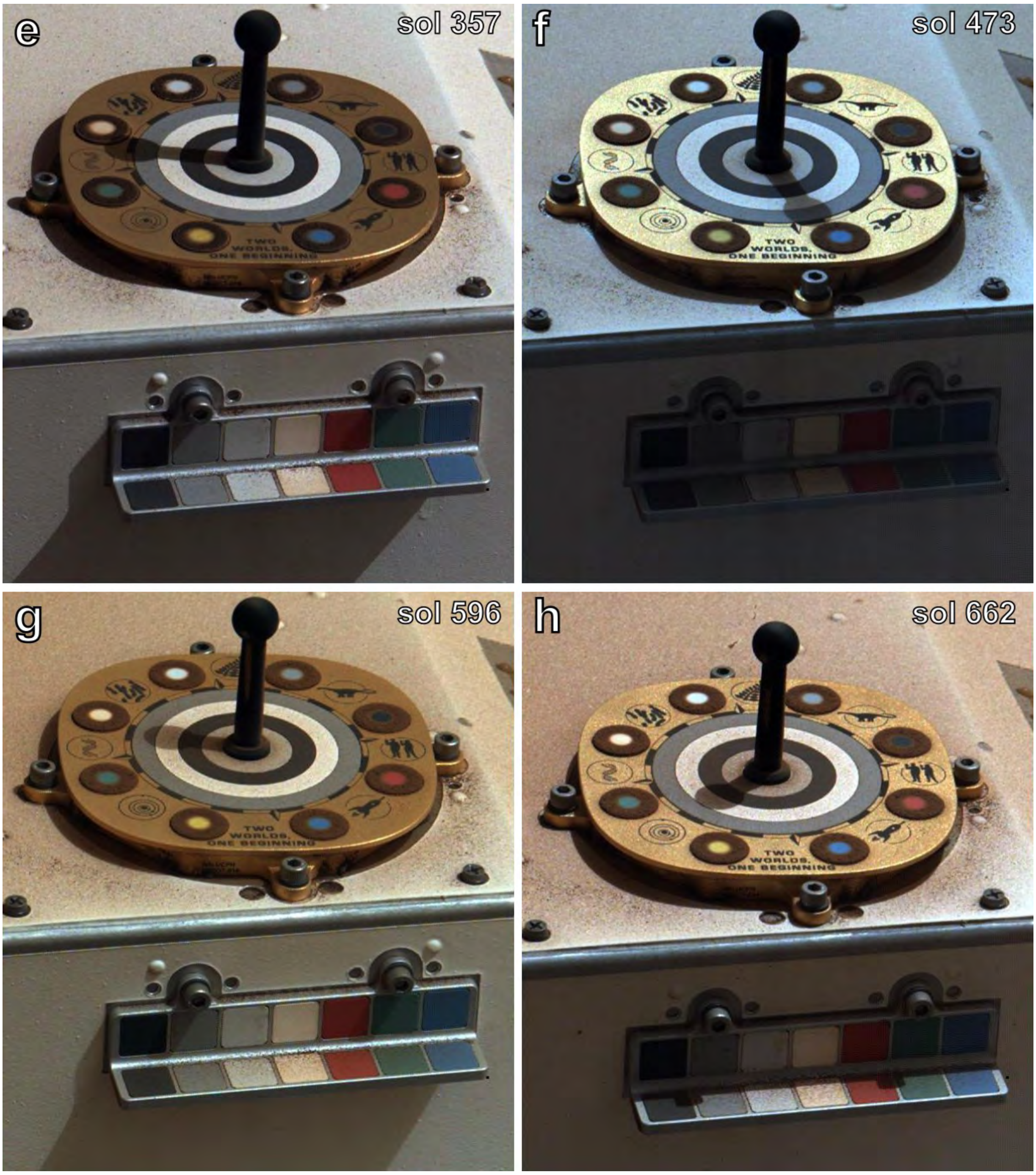

Figure 7.4 (continued from page 102. *The calibration targets imaged in colors by the left eye of Mastcam-Z (L0) at a focal length of 48 mm on (e) sol 357, (f) sol 473, (g) sol 596, and (h) sol 662. All the images have sequence ID ZCAM03014.*

targets was rather low (figure 7.4e for sol 357). The dust layers that remained after the major dust event did not show any significant variation for several sols, except for a slight cleaning between sols 465 and 473 (figure 7.4f for sol 473). Around sol 570, which corresponded to a peak in the atmospheric optical depth (figure 7.9b), the surfaces of the targets and the deck were characterized by a reddish hue, likely due to a higher amount of airfall dust which persisted until the end of the time range that I am considering (figures 7.4g and 7.4h for sols 596 and 662). As a curious remark, around sol 397 I noticed that some dust stuck to the central gnomon, from half of its height up to the lower portion of the top sphere. The visibility of this dust stripe was enhanced under specific illumination geometry, such as when the Sun was behind Mastcam-Z. Between sols 596 (figure 7.4g) and 602 the stripe seemed to become slightly broader, and the upper part of it disappeared around sol 656 and 662 (figure 7.4h), likely due to the wind activity and vibrations. A close-up of the primary target is shown in figure 7.5 at high resolution (focal length of 100 mm) for sol 608, when the dust stripe was at its maximum display.

Figure 7.5: *Close-up on the primary target imaged by the left eye of Mastcam-Z on sol 608 in filter L0 at 100 mm of focal length (sequence ID ZCAM03022). All the surfaces are covered in a thin layer of reddish dust. The vertical dust stripe on the gnomon is indicated by the arrow.*

One useful way to visualize the distribution of dust on the calibration targets is a technique called Decorrelation Stretch, or DCS. The DCS is an image processing method that can be applied to images belonging to the same multispectral sequence, in order to enhance the color differences (Gillespie et al., 1986). Once three frames from the sequence are assigned to the red, green and blue channels, the DCS applies linear transformations that remove the correlation between the frames, and then stretches the contrast, in order to obtain an image in exaggerated false colors, where the pixels are distributed among all possible colors but maintaining the saturation and intensity of the original frames. The DCS allows distinguishing units and peculiar features, which depend on the filters used. Figure 7.6a shows a color image of the calibration targets from sol 318, and figure 7.6b represents the same image after the DCS with filters L2, L5 and L6 for the Red, Green and Blue channels, respectively. The airfall dust, which in the color image appears a dark brownish tone, in the DCS is represented by a purple coating that is spread on all the flat surfaces parallel to the ground, including the deck, the grayscale rings, the secondary horizontal tiles, and even on the thin support between the two bolts of the secondary target. In addition, it is possible to recognize small mounds of dust stuck to the vertical sides of the golden base in proximity to the magnets. These aggregates display a darker color similar to the dust on top of the magnet rings, suggesting that the size and composition of this magnetic dust might be different from the purple coating. This is consistent with the observations in Kinch et al. (2006) that dust attracted to permanent magnets can be distinguished as darker and less reddish due to a higher magnetite content and/or larger average grain size. Such a distinction was challenging to observe in the RGB image, thus confirming the power of the DCS technique.

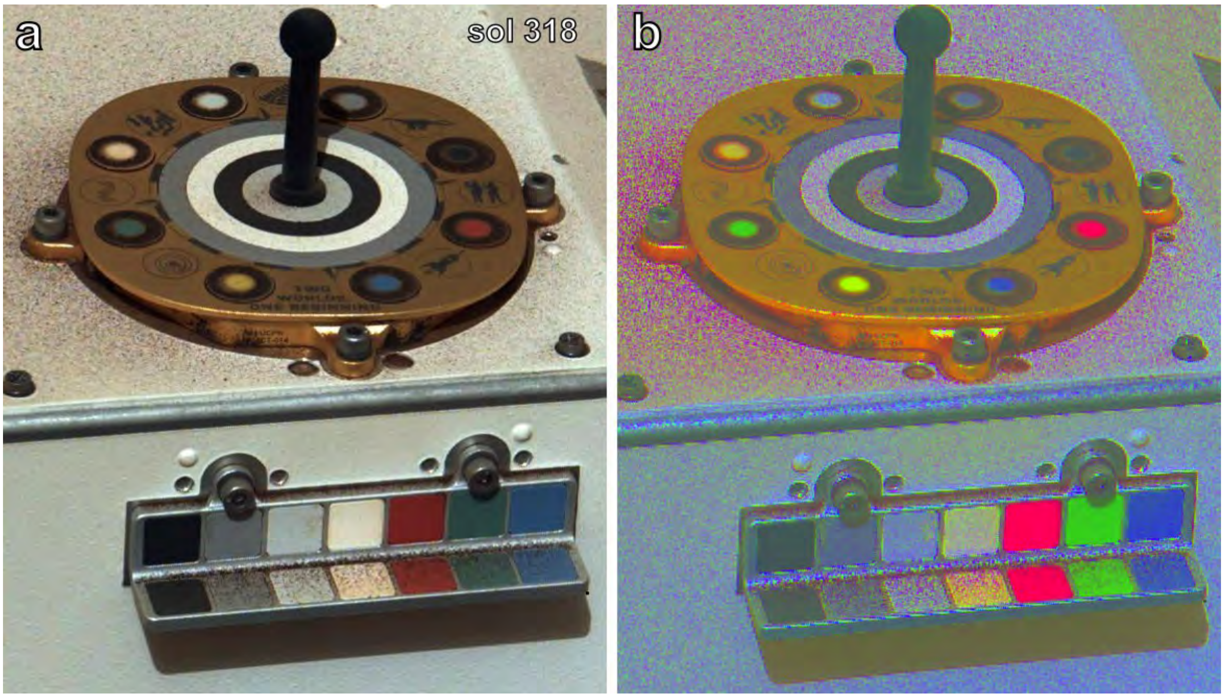

Figure 7.6: *Highlight of the airfall dust on the cal-targets and the rover deck on sol 318, as result of the dust event that started on sol 314. Image (a) is a RGB shot by the left eye of Mastcam-Z (L0) on sol 318 at 48 mm zoom (sequence ID ZCAM03003), while image (b) is the outcome of a decorrelation stretch (DCS) performed on the left image. The DCS was obtained using the L2 (754 nm), L5 (528 nm) and L6 (442 nm) filters for the Red, Green and Blue channels, respectively. Figure from Merusi et al. (2022).*

Dust was not the only sort of material that I spotted within the calibration target images. Large sand grains with a characteristic dark color appeared frequently, but their occurrence was limited only to the first 350 sols, despite the atmosphere being dustier later. These grains were raised from the ground by the wind and deposited on the deck around the primary target, and were able to persist for several sols without being swept off, because a strong aeolian drag force or intense vibrations were required to move such massive and large grains. They usually moved a few mm or cm from one sol to the next one.

Figure 7.7a shows two examples of large sand grains, indicated by arrows, on the deck around the primary target imaged on sol 23 at 100 mm of focal length. Using the same software employed for calibration, I selected one region in each grain in the IOF-calibrated sequence of sol 23, thus obtaining the reflectance spectra in figure 7.7b. Despite the high resolution of the images in the sequence, selecting the regions was challenging due to the small sizes of the grains (one dozen of pixels, on average) and a very slight shift in the pointing of the images from one filter to the next, which forced me to select fewer pixels. Therefore, the green spectrum does not seem to be consistent with any shape expected of martian sand or soil. The red spectrum displays a slightly better shape that reminds of the typical spectrum of the martian regolith, though with artifacts such as the high slope from R5 to R6.

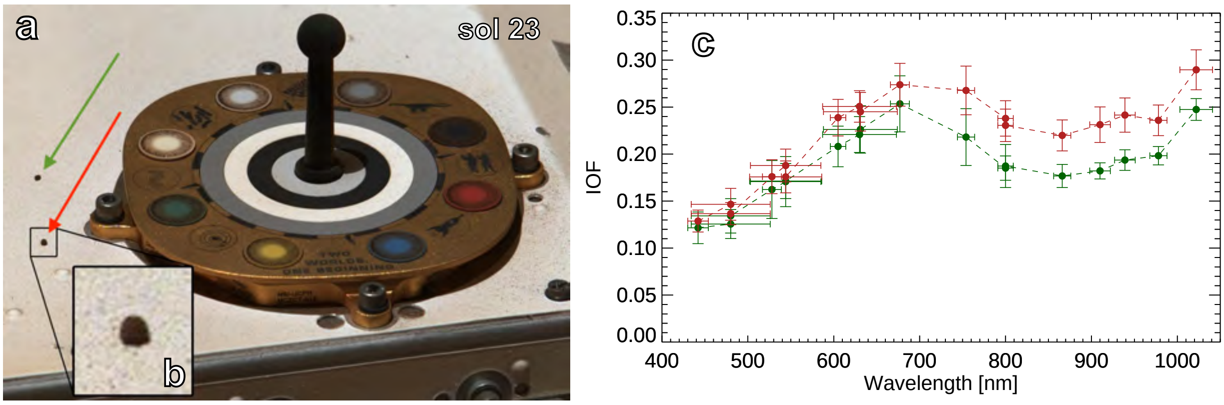

Figure 7.7: *(a) The primary calibration target imaged in colors by the left eye of Mastcam-Z (L0) on sol 23 at 100 mm of focal length (sequence ID ZCAM03003). Two large sand grains are pointed at by arrows. (b) Zoom-in on one of the two sand grains. (c) Reflectance spectra of the two large sand grains on the left. The colors of the spectra correspond to those of the arrows pointing at them.*

7.2.2 Dust on the magnets

The regions that experienced the greatest accumulation of airfall dust on the calibration targets were the magnet rings. This outcome, which was also their purpose, was expected from their design. The magnet rings started to accumulate dust during and after landing. On sol 23 (figure 7.7a) the magnet rings were already covered in a thin layer characterized by a slightly thicker accumulation of dust on the left outermost side of each round patch (as seen from Mastcam-Z), which appeared darker, and by sol 65 (figure 6.2a) the layers were thick enough to make it challenging to see the colors of the patches underneath. As time passed, airfall dust continued to pile up on those regions, and the boundaries of such layers slowly expanded towards the inner and outer edges of the magnetic regions (outwards, up to the external edges of the round patches, and inwards, almost reaching the boundaries with the clean spots). In order to analyze the

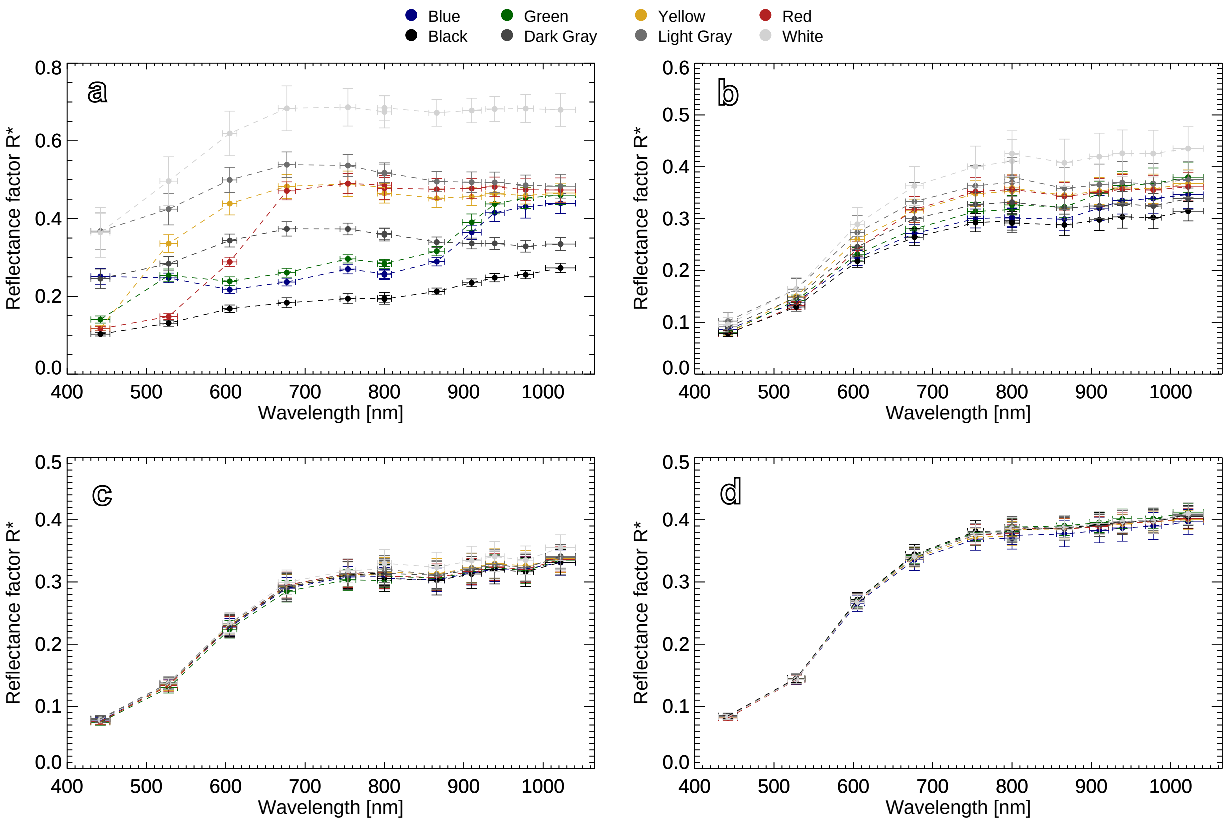

Figure 7.8: *Reflectance spectra of the magnet rings on sols (a) 12, (b) 157, (c) 435, and (d) 669.*

effect of this dust on the reflectance of the primary patches, I computed the IOF reflectance of the ROIs in the magnet rings for four different sols. The reflectance spectra of the magnet rings are represented in figure 7.8 for sols 12, 157, 435, and 669. The comparison between the spectra in figures 6.9a (clean spots) and 7.8a (magnet rings) gives a good idea of the distortion caused by the dust accumulation on the ceramic materials of the primary target after a short time. The dust layers had two outcomes: firstly, they decreased progressively the reflectance of the brighter patches and raised that of the darker patches, bringing their spectra to a convergence with a reduction of the contrast, and secondly, they absorbed more efficiently the solar radiation in the short-waves (blue) than in the long-waves (red), a typical phenomenon known as reddening. Around the end of the time range under consideration (figure 7.8d), the magnet rings were almost coincident at shorter wavelengths, while they showed a very slight separation in the near infrared, suggesting that in that range the dust was less optically thick to the color patches underneath.

7.2.3 Direct and diffuse sunlight on the grayscale rings

The way the sunlight is diffused in the atmosphere is strictly connected with dust, especially the amount of airborne dust suspended in the thin air. When a ray of light crosses the martian atmosphere, it is partially diffused to all directions by dust or in some cases grains of ice. When diffusion is stronger, the areas in shadow on the surface will receive more diffuse light at the expense of the sunlit areas, which will appear slightly dimmer. Following the basic physics of the atmosphere, we should expect this diffuse illumination effect to be enhanced in two (possibly overlapping) cases: (i) the incidence angle is high, and (ii) the amount of suspended dust is high. The former is typical of planets with an atmospheric shell, and comes from the fact that when the Sun is low on the horizon its light has to cross a thicker section of atmosphere than when it is at the zenith, and hence, the light is attenuated along its direction (and slightly diffracted) and is scattered by gasses and dust grains. Secondly, a high density of airborne dust can significantly reduce the intensity of the light that reaches the surface (landers and rovers with solar panels know it well) and increase the scattering.

In order to investigate the impact of airborne dust on diffuse illumination and verify their correlation, I compared the time-series of the fraction of sunlight that hits directly on the grayscale rings of the primary target, and the atmospheric optical depth. The direct fraction of sunlight was obtained from the measured radiance of the grayscale rings. As listed in section 6.2, up to eight ROIs can be selected on the grayscale rings: the four illuminated portions and the zero-to-four portions in the gnomon's shadow. Basically, the surfaces directly illuminated by the Sun should receive the sum of direct sunlight and diffuse light, while the shaded regions should receive only light from the diffuse component. I followed the approach from Kinch et al. (2007), which defined the direct fraction of sunlight F_d as:

$$F_d = \frac{RAD_{illum} - RAD_{shad}}{RAD_{illum}}\,, \tag{7.3}$$

where RAD_{illum} and RAD_{shad} are the measured radiances of the illuminated regions and shadowed regions of the grayscale rings, respectively. Since F_d depends on the radiance of the shaded regions, the value of F_d could be computed only for the images in which the illumination geometry allowed at least one shadowed region to be selected, meaning that the "worst cases" were those with very small incidence angle (Sun right above the gnomon and no shadow at all) and those where the shadow was hidden behind the gnomon. In all the other configurations, within every image I calculated the value of F_d of each ring in which the shadow was selected, and extracted the average value over the rings.

The atmospheric optical depth describes the attenuation of solar radiation penetrating the atmosphere, and is a good indicator of the density of dust along the line of sight. It was measured frequently by the Atmospheric working group of the Perseverance team by acquiring images of the Sun with Mastcam-Z using the solar filter R7 (880 nm), and is denoted by τ_I (Lemmon et al., 2015). Figure 7.9a shows the trends of the direct fraction F_d in four narrow-band filters, and figure 7.9b displays the atmospheric optical depth τ_I over the first 670 sols. In figure 7.9a, the circles denote incidence angles $\leq 30°$ and the triangles have incidence $> 30°$. An increase in F_d indicates a decrease of diffuse illumination, and vice-versa. Similarly, an increase in τ_I implies an increase in the amount of dust suspended.

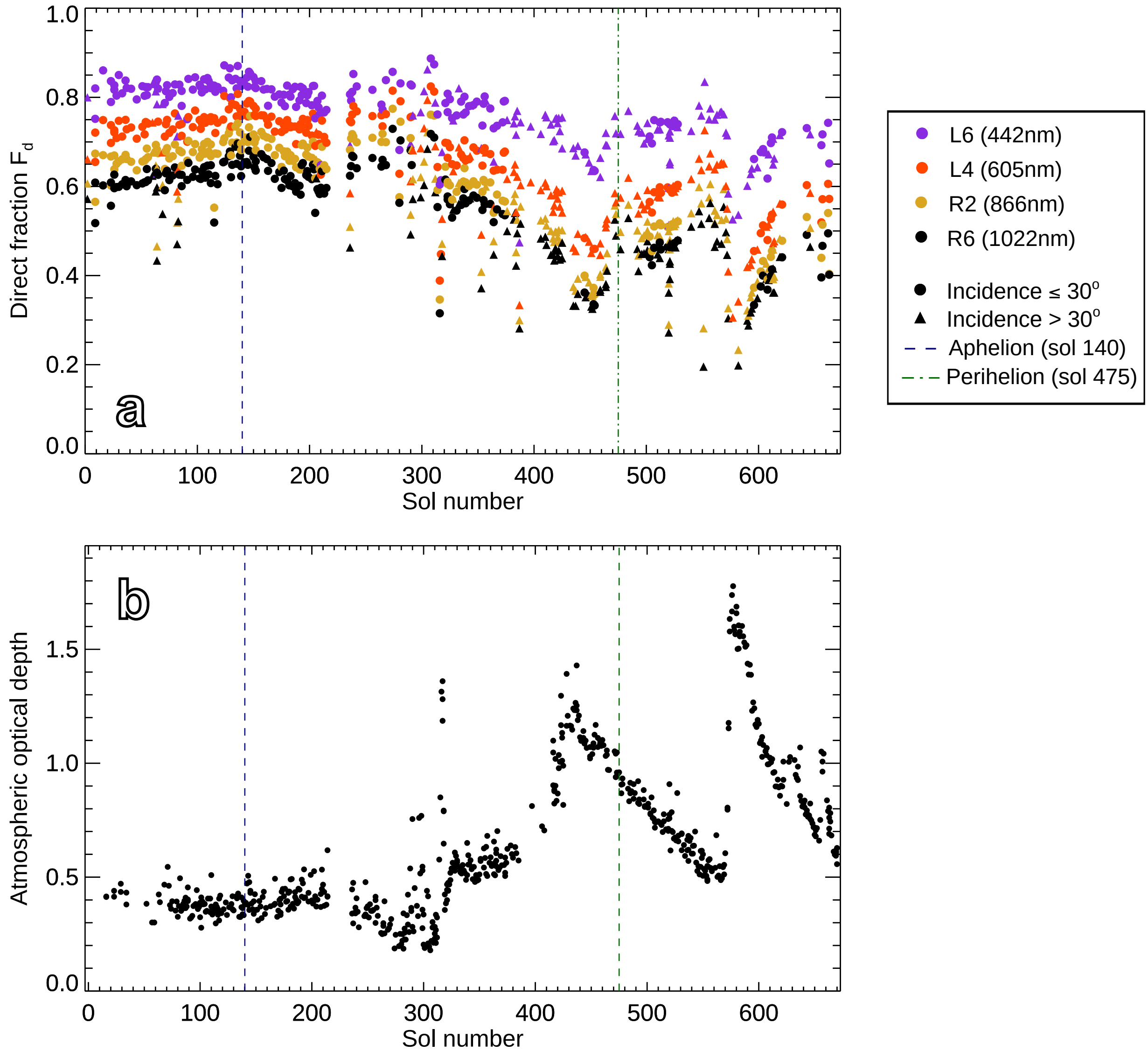

Figure 7.9: *(a) Time evolution of the direct fraction F_d of sunlight on the grayscale rings, as computed using equation (7.3), for the filters L6 (purple circles), L4 (red circles), R2 (yellow circles), and R6 (black circles). (b) Time evolution of the atmospheric optical depth τ_I measured at 880 nm through Mastcam-Z observations of the Sun. In both plots the blue vertical dashed line is the solar aphelion, the green vertical dot-dashed line is the solar perihelion.*

The first 217 sols, from landing to the solar conjunction, were characterized by a fairly stable trend, where F_d reached a local peak of 0.81 in L4 and τ_I showed a depression around the aphelion. After conjunction (sol 236) a first decrease in τ_I was followed by a couple of spikes between sols 285 and 305. Subsequently, a major dust event struck on sols 314-316, witnessed by a peak in τ_I at 1.4 and a narrow drop in F_d to 0.41 in L4. In the aftermath of the dust event, τ_I went up to 0.55 on sol 330 and started a roughly parabolic growth that culminated with a value of almost 1.5 on sol 435. F_d had a similar inverse trend, which reached a minimum of 0.45 in L4 on sol 455. The peak in τ_I was followed by a quite linear decrease between sols 440 and 570, and by another sudden peak on sol 575, where τ_I reached 1.8, the highest value so far. From sol 455 to 580 F_d rose slowly until it showed a drop on sol 583, in which it touched the value of 0.3, the lowest since landing. After the sol 575 peak, τ_I declined again, while F_d rose again. From the comparison between the two plots, I can conclude that the direct fraction of sunlight on the grayscale rings and the atmospheric optical depth show a roughly inverse correlation. Every change in the optical depth is always accompanied by an opposite turn in F_d, which is a powerful demonstration that an increase of the airborne dust density enhances the sunlight attenuation and the diffusion, which reduces the relative contrast between lights and shadows. Whereas the dust event of sols 314-316 was episodic and increased the optical depth for a very short time, the two storms between sols 400-570 and between sols 570-630 were characterized by a quick growth of the dust density in the atmosphere and a slower but linear “cleaning” and settling as dust falls out of suspension to the ground or is transported away by the wind.

7.3 The two-term linear fits

Since the landing of Perseverance, the linear fits employed for the calibration of Mastcam-Z images were always performed involving one multiplicative term, in the form $y = a \cdot x$. As illustrated in chapter 5, this is a consequence of the fact that the radiances and reflectances of the clean spots are expected to be directly proportional and lie on a line passing through the origin, which was shown in the test at ATLO (section 5.4), and the slope is the solar irradiance. I mentioned in section 6.5 that our data suggested a second term, an additive offset, might provide a better consistency between the measured data and the fits. Such a “two-term” model, in the form $y = a \cdot x + b$ with $b \neq 0$, was already tested before the launch (section 5.2.2), but we decided to adopt the one-term model for calibration on Mars because it had given consistent results and small uncertainties, and it was the direct application of the theoretical approach.

Although the two-term model was never implemented on Mars, I investigated the behavior of its multiplicative and additive terms in time, in an attempt to understand its origin using the data from the RC files. Before diving into this "parallel" investigation, one of the possible explanations suggested was airfall dust on the clean spots, which was dealt with also in the MER and MSL missions. Figure 7.10 shows some examples of radiance-versus-reflectance plots of the clean spots from four sols in three different filters, in which the one-term fit is represented by a solid line and the two-term fit by a dashed line. Even in this analysis, the white clean spot was excluded from the computation of all the fits, due to its yellowing effect introduced in section 6.5. The fits with the offset appeared to be systematically less steep than their one-term counterparts and followed better the data points. Indeed, the average reduced chi-square values χ^2_{red} for the two-term fits range from 1.27 in R5 to 4.51 in L4, with an overall average of 2.28 in all narrow-band filters (the latter is 1/12.5 of the average for the one-term fits). The mean χ^2_{red} of the narrow-band filters are listed in table 7.1.

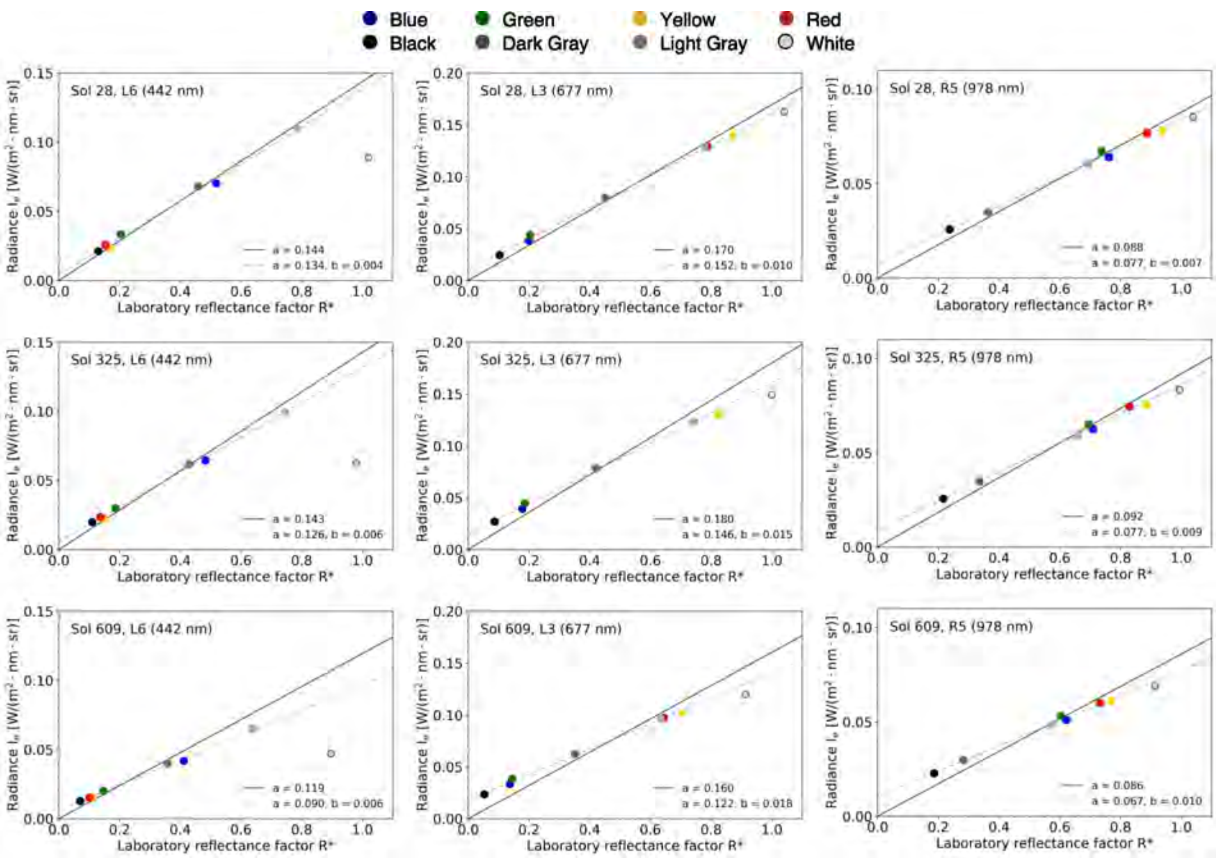

Figure 7.10: *Linear fits of the clean spots obtained through the one-term model (solid line) and the two-term model (dashed line) for sols 28, 325 and 609 in the filters L6, L3 and R5. In all the plots the white patch was excluded from the computation of the fits due to its yellowing effect. The numbers in the lower right corner of each plot are the slopes and offsets of the one-term fits (where a is the slope) and two-term fits (where a is the slope and b is the offset).*

The slightly greater flatness of the two-term fits also resulted from the relative dif-

Filter [nm]	χ^2_{red}
L6 (442 ± 12)	3.09
L5 (528 ± 11)	3.63
L4 (605 ± 9)	4.51
L3 (677 ± 11)	2.45
L2 (754 ± 10)	2.05
L1 (800 ± 9)	2.02
R1 (800 ± 9)	2.35
R2 (866 ± 10)	1.35
R3 (910 ± 12)	1.51
R4 (939 ± 12)	1.34
R5 (978 ± 10)	1.27
R6 (1022 ± 19)	1.82

Table 7.1: *Summary of the average reduced χ^2_{red} over each narrow-band filter associated to the two-term model.*

ference D_s between the slopes in the two models. I quantified this parameter as:

$$D_s = \frac{slope_{2t} - slope_{1t}}{slope_{1t}}\,, \tag{7.4}$$

where $slope_{1t}$ and $slope_{2t}$ are the slopes of the one-term and two-term fits, respectively.

Figure 7.11a shows the time-series of D_s for four filters (L6, L3, R2 and R6), where observations with $i \leq 30°$ are denoted by circles and those with $i > 30°$ by triangles. The trend of the first 315 sols is fairly stable, with a very slow decrease. The difference in filter L6 (442 nm, purple circles) had a net decrease from -0.09 to -0.12 (-35%), while R6 (1022 nm, black circles) went from -0.17 to -0.20 (-13%). All the other filters followed a similar trend, with rates between -15% and -28%. From the first dust event of sols 314-316, a significant amount of airborne dust began to fill the martian scene and create perturbations in the measured radiances of the clean spots, especially when the calibration targets were imaged under larger incidence angles, which happened frequently during the martian winter (sols 360-670). Amidst the higher data point dispersion, the average trend declined faster than in the first half of the time range, reaching an overall minimum around sol 580 (-0.28 in L6) and then upturning. In addition, D_s did not follow any linear dependence on wavelength. The plot of figure 7.11b displays the averages of D_s for each narrow-band filter over the sol range 100-180, across the martian aphelion (the two vertical solid lines in figure 7.11a). The filters show a roughly flat behavior within the errors, with deviations in L6 and R6 that might be due to lower signal and sensitivity of the CCD at the edges of the spectral range. All the points in figure 7.11b are included between -0.2 and -0.07 (considering the error bars), with L6 being the highest at -0.09 and R6 the lowest at -0.19. The other filters are concentrated between -0.17 and -0.12, but their error bars seem consistent with a mean D_s of -0.14.

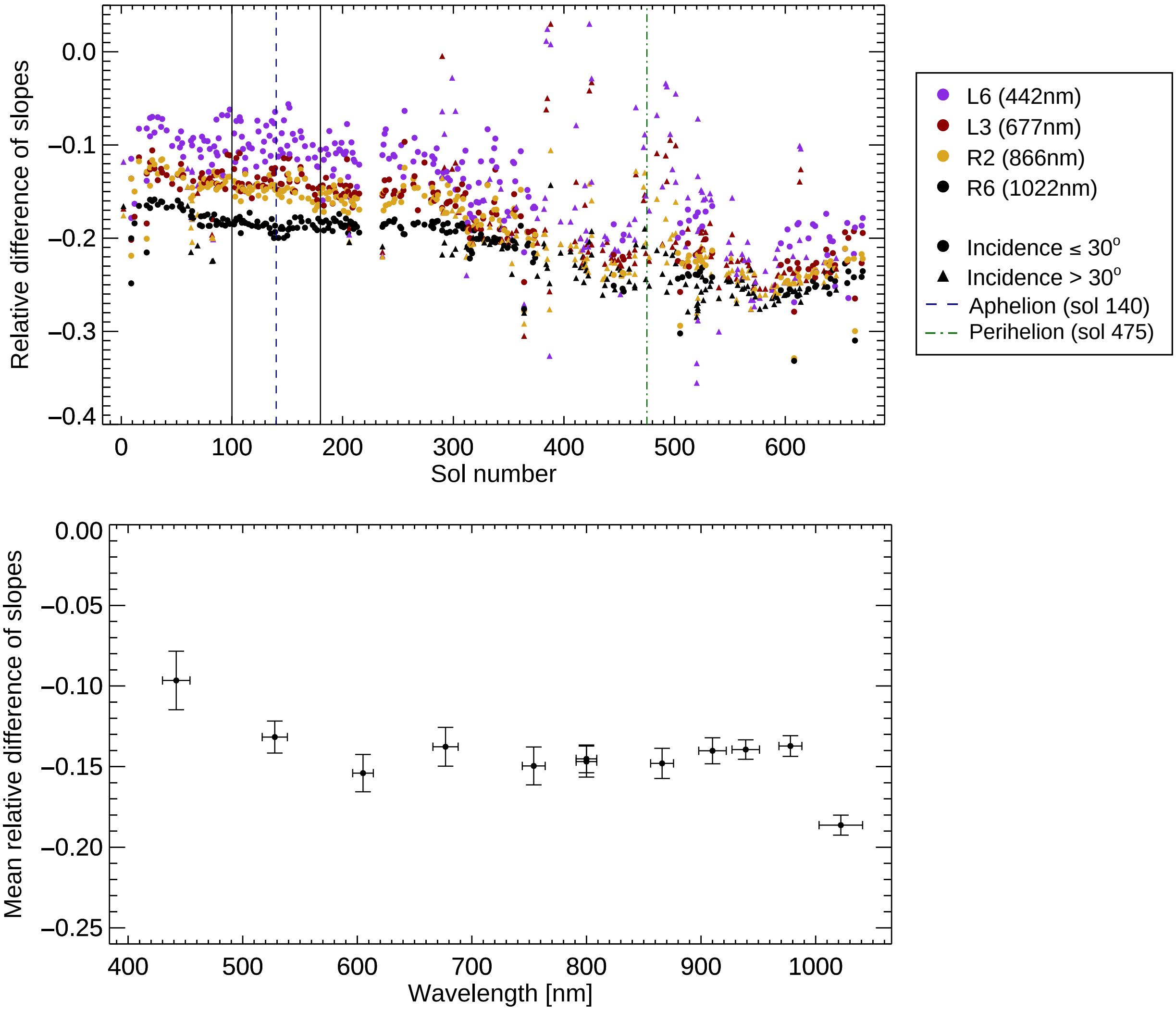

Figure 7.11: *(a) Time evolution of the relative difference between the slopes of the two- and one-term fits for four narrow-band filters. Each color corresponds to a different filter. The relative difference D_s is computed using equation (7.4). The circles are observations with $i \leq 30°$, the triangles are $i > 30°$. The vertical blue dashed line is the Martian aphelion, the vertical green dot-dashed line is the martian perihelion. (b) Average of the relative difference of slopes for all 12 narrow-band filters, over the range from sol 100 to 180 (corresponding to the two vertical solid lines in panel (a)).*

Eventually, after investigating the slopes in the two models, I focused on the offsets of the two-term fits. I computed the linear fits with the offset on the clean spots, on the grayscale rings and on the secondary horizontal tiles, between their measured radiances and the reference reflectances obtained from the RC files. Each of the three groups of patches/rings was managed separately, and the white patch was excluded from the computation for the clean spots and for the secondary tile, because the same yellowing effect was observed there. The effect was not present on the white ring, which was not excluded. All the offsets were converted to units of IOF, for easier comparison of filter-to-filter and sol-to-sol. As a result, figures 7.12a, 7.12b, 7.12c and 7.12d show the time evolution of the offset for the clean spots, the grayscale rings, the secondary horizontal tiles and the secondary vertical tiles, respectively. The offset values for the clean spots are roughly wavelength dependent, growing with increasing wavelength. At aphelion (vertical blue dashed line), most filters fall fairly close in a tight band between 0.07 and 0.10 while the shortest and longest wavelengths fall outside this range. The clean spots and secondary horizontal tiles are quite similar in trend and wavelength dependence of the offsets, while the grayscale rings, that only rely on four data points in the linear fits, are characterized by a more dramatic divergence in the near infrared filters (R4-R6, from 900 nm to 1000 nm), though also in this case the L6 is consistently well below the other filters. On average, the increase of the offsets for the clean spots is 51.2%, while it is 20.5% for the grayscale rings, and 54% for the secondary horizontal target. In addition, figure 7.13 shows the offsets of the clean spots as function

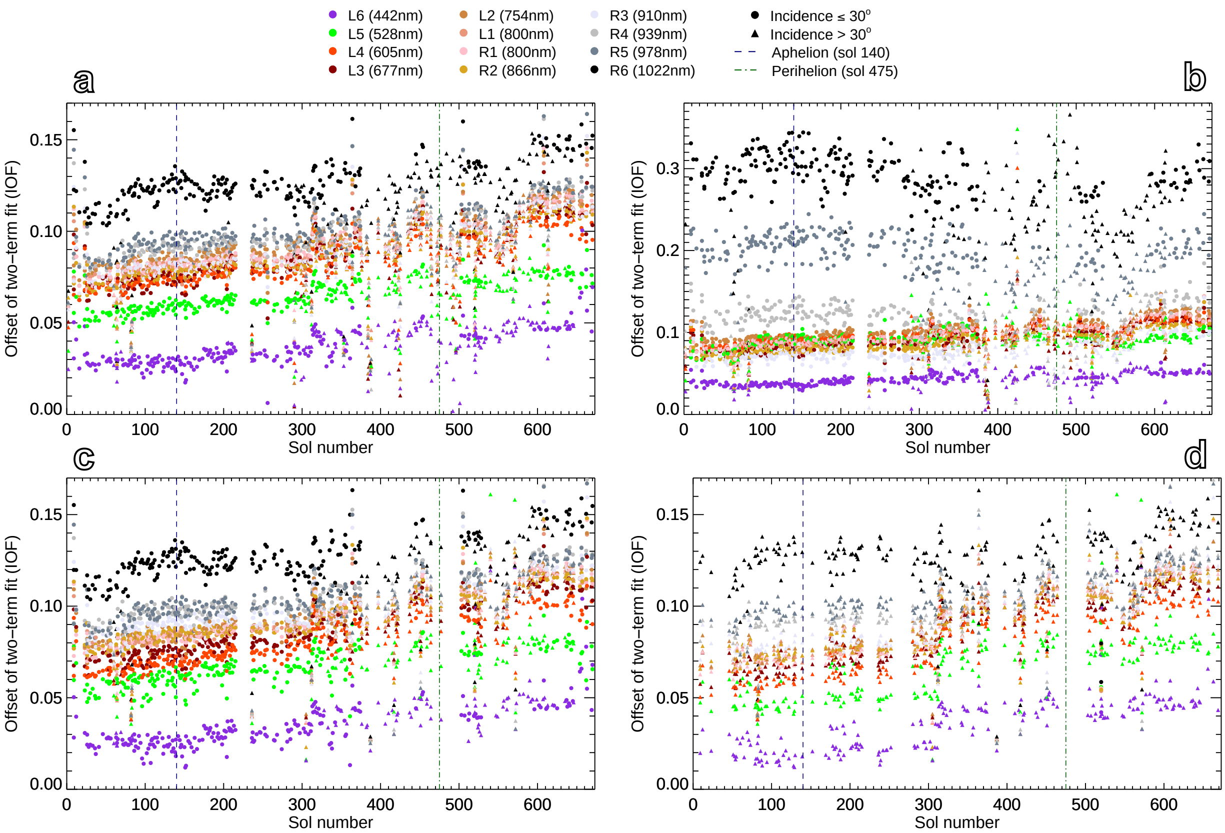

Figure 7.12: *Time evolution of the two-term linear fit offsets within the first 350 sols on Mars for (a) primary clean spots, (b) grayscale rings, (c) secondary horizontal tiles and (d) secondary vertical tiles. Each color corresponds to a different narrow-band filter. The blue vertical dashed line is the Martian aphelion, the green dot-dashed vertical line is the martian perihelion. The vertical solid lines in (a) are the boundaries of the two sol ranges (0-100 and 570-670) considered to compute the offset spectra presented in figure 7.13.*

of the wavelengths of the 12 narrow-band filters, where the offsets in each filter have been averaged over the first 100 sols (blue circles) and the last 100 sols (red circles) considered in our analysis (sols 0 to 670). The spectral shape of the offsets showed a smooth trend with first increase between L6 and L2, followed by a slight decrease and a final increment from R2 (866 nm) to R6 (1022 nm). In addition, the mean offsets in the 570-670 sol interval were 49.0% higher than those in the first 100 sols of the mission, with a minimum increase in the near infrared (29.2% in R6) and larger increase at shorter wavelengths (85.3% in L6).

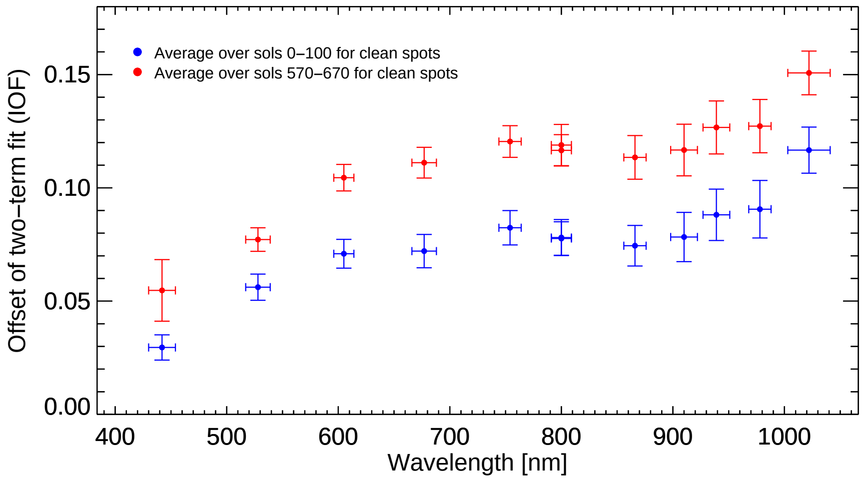

Figure 7.13: *Spectral representation of the offsets of the linear fits for the clean spots computed as the averages (in each narrow-band filter) over the first 100 sols of mission (blue circles) and over the last 100 sols considered in this thesis (570-670). The two sols ranges are highlighted by the vertical solid lines in figure 7.12a.*

7.4 The yellowing of the AluWhite98

One of the prominent discoveries that arose from the observation and processing of the calibration target images was the unexpected behavior of the white clean spot, which appeared to be changing the hue towards a "dirty" yellow in the color images over time. Its measured radiance was systematically lower than the linear fits at shorter wavelengths (filters L6, L5 and L4). The issue was introduced in section 6.4, where I focused on the visual appearance of the calibration targets on Mars (figure 6.2), and was mentioned again in section 6.5, where I presented some examples of linear fits (figure 6.8) and calibration spectra plots (figure 6.9). Due to this misbehavior, the white clean spot was never included in the computation of the linear fits for calibration on Mars. Since the beginning of the mission on Mars, this issue has been referred to as "yellowing" because of the observed change of color of the patch from a pristine white to a faded yellow.

Unlike all the other materials that were produced by Lucideon, the white clean spot, the white ring, and both secondary white tiles of the calibration targets were manufactured by Avian Technologies from a ceramic material named AluWhite98. In order to have a better overview on whether this problem was limited to the white clean spot or it was spread, I investigated the behavior of all the white regions of the two targets. None of the other colors and grayscale materials showed any appreciable misbehavior in their measured radiances or in the images, and therefore, I concluded that they were not affected.

As a first step, I examined the visual appearance in the color images. The images in figure 7.14 show close-ups on three regions (white clean spot, white ring, and light gray clean spot) for four sols of the mission (16, 157, 435 and 669). The visual yellowing of the white clean spot is rather evident and can be compared with the brighter white color of the ring, which did not seem to be affected.

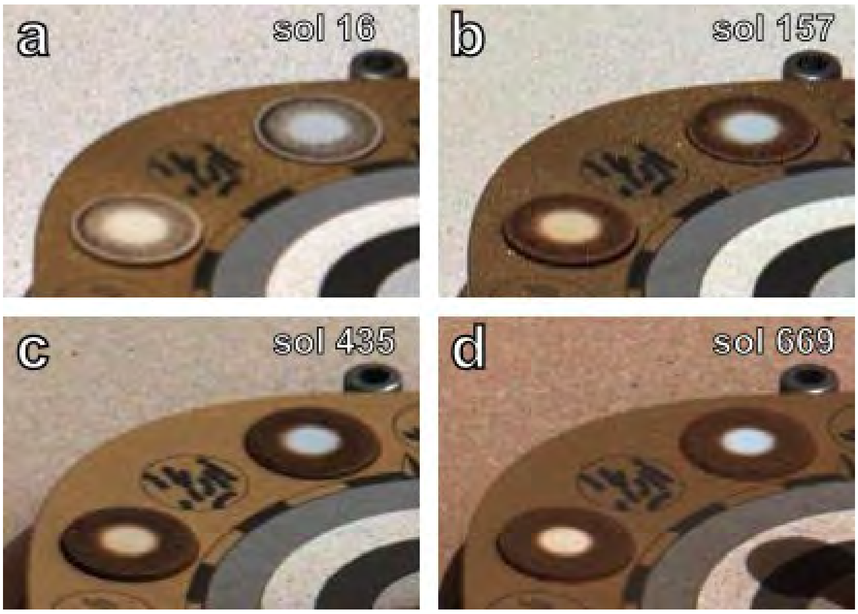

Figure 7.14: *Visual juxtaposition of four close-ups of the primary white and light gray patches and the white ring of the primary calibration target imaged by the left eye of Mastcam-Z (L0) on sols 16, 157, 435, and 669 at 48 mm of focal length to highlight the progressive visual yellowing of the AluWhite98. The white patch is in the lower left, the light gray patch is in the upper right, and the white ring is in the lower right of each image. Image (a) has sequence ID ZCAM03002, the others have ZCAM03014.*

Secondly, I analyzed the spectral performance of the same four regions in time. For each one, I computed the ratio between the calibrated IOF reflectance and the model IOF reflectance for all the narrow-band filters in time. The calibrated reflectance was obtained differently for the clean spot, ring and secondary horizontal tile, and the secondary vertical tile. For the first three regions, I simply extracted the measured radiance from the RC files and I multiplied it by the rad-to-iof coefficient, which converted it to units of IOF. I treated the secondary vertical tile separately due to its distinct inclination from the other regions. In all the observations in which it was sunlit, I performed a one-term linear fit between the radiances of the other six vertical tiles and their reference laboratory reflectances, and I divided the radiance of the white vertical tile by the slope of the fit. Finally, I multiplied it by the cosine of the incidence angle (relative to the normal of the vertical tile) to transform it to IOF.

For all the four regions, the model IOF was obtained by multiplying the reference reflectances from the RC files (in units of R*) by the cosine of the incidence angle (as per equation (4.12)). Figure 7.15 shows the time-series of these measured-over-model IOF ratios for the white clean spot (7.15a), the white ring (7.15b), and the white secondary horizontal (7.15c) and vertical (7.15d) tiles. The narrow-band filters are represented in different colors, and the observations with $i \leq 30°$ (circles) are distinguished by those with $i > 30°$ (triangles). In addition, figure 7.15e is the same sort of plot but relative to the light gray clean spot, for reference.

As expected from the observations and the fits, the white clean spot (figure 7.15a) is characterized by a sensibly lower ratio in L6, L5 and L4, while the other filters seem to follow a more consistent trend that was stably just below 1 before the dust storm season, and then showed perturbations after sol 360 due to the intense dust activity. The filters at shorter wavelengths were already quite low in the first sols, decreased linearly and quickly until sol 100, and then maintained a more stable fashion until the dust season. A not-too-dissimilar behavior was followed by the secondary horizontal tile (figure 7.15c), where, however, the scattering of data points is enhanced also before sol 360 due to its exposure to dust without magnets. Also in this case, L6 reported the lowest values, followed by L5, but with L4 closer to all the other filters. The time evolution for the white ring (figure 7.15b) only showed a very small separation of the short-wavelength filters until sol 360, when the dust-related perturbations kicked off. The situation of the secondary vertical tile (figure 7.15d) was much flatter and more stable, likely due to the vertical orientation of the tile that prevents most airfall dust from depositing. This plot is less "rich" than the other regions because the secondary vertical tiles were very often in complete shadow, but I can conclude that also in this case the filter L6 (and L5, to a lesser extent) is lower than all the other filters. Finally, the light gray clean spot (figure 7.15e) is the clear example of a reference patch that was not touched by the yellowing effect. It displays the same peaks and troughs as the other white horizontal features, especially during the dust storm season, but all the filters are coherent and there are no major or systematic discrepancies.

7.4.1 The tests on the AluWhite98 patch

In the months of June and July 2021, a few months after the landing of Perseverance on Mars, I worked on the preparation of some samples of AluWhite98 material with my supervisor, Prof. Morten Bo Madsen in Copenhagen. The aim of the experiment

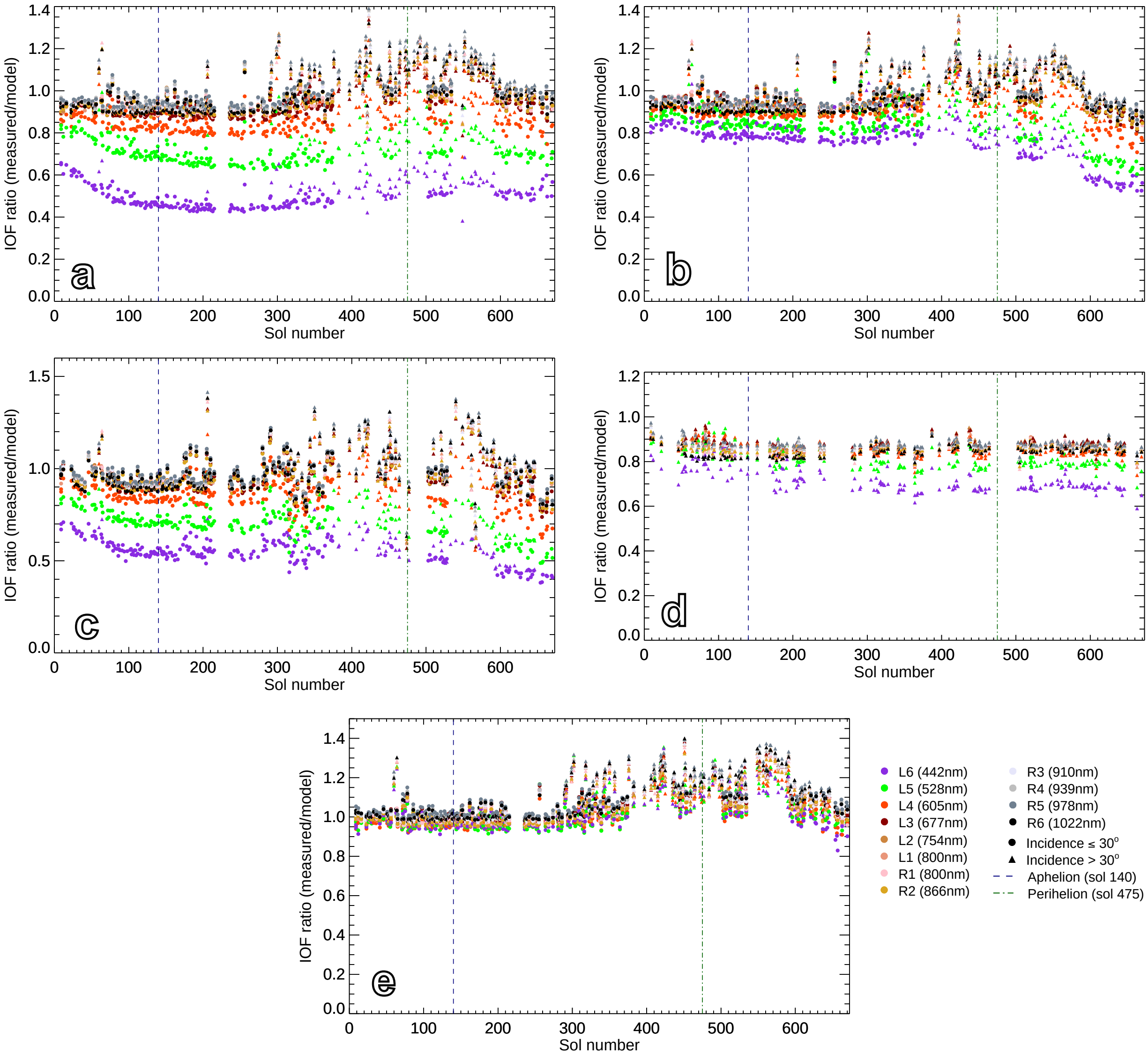

Figure 7.15: *Ratio between the measured IOF and the model IOF values of (a) the primary white clean spot, (b) the white grayscale ring, (c) the secondary horizontal white tile, (d) the secondary vertical white tile, and (e) the primary white light gray clean spot. The colors of the points are the same for the five plots and represent the 12 narrow-band filters. The vertical blue dashed line is the Martian aphelion, the vertical green dot-dashed line is the martian perihelion.*

was to test different pieces of the white material with UV irradiation in the attempt to reproduce the visual and spectral yellowing that we were observing in Mastcam-Z images from Mars. The object of the analysis was an aluminum test unit carrying four small samples of AluWhite98 delivered by the manufacturer Avian Technologies. We prepared four test units in total that underwent the same treatment, and of which one was exposed to the irradiation and the others were stored as spare units.

Each test unit, acting as a support, was an aluminum disc hosting four square gaps, with a tiny hole at the bottom center of each gap. The four gaps were denoted by the

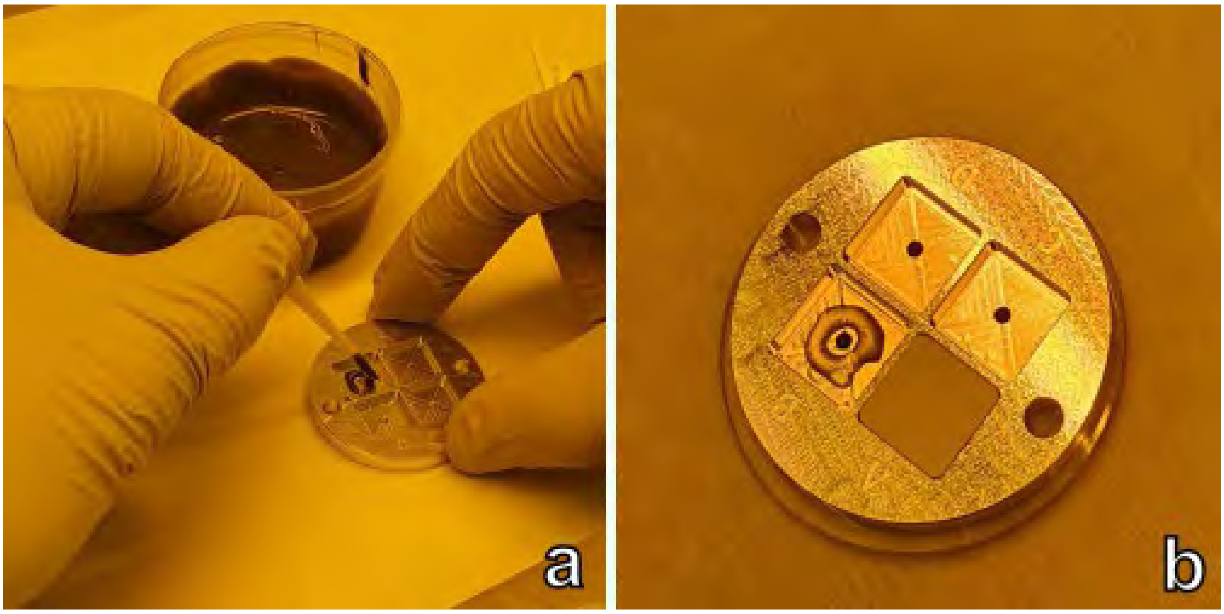

Figure 7.16: *(a) The 3M-2216B/A Gray epoxy is applied into gap A. (b) The AluWhite98 chip has been inserted in place in gap A, and the Henkel/Loctite EA-9309NA epoxy has been applied within gap B of the test unit. Credits: Morten Bo Madsen.*

letters A, B, C, D. Using a set of thin plastic sticks, I applied a little amount of epoxy on the floor of A, B, and C (figure 7.16a). The epoxy in A was the 3M-2216B/A Gray (which had also been used for the grayscale rings of the primary target), while that in B and C was the Henkel/Loctite EA-9309NA (the same of the primary patches and secondary tiles of the calibration targets). No glue was put into gap D. The four square AluWhite98 samples (or "chips" had a side of 60 mm and rounded corners. The chips were inserted in the four gaps with high precision (figure 7.16b). When pushing them into the gaps, the excess epoxy leaked through the tiny holes at the bottom (as expected) instead of from the sides. Three chips (A, C and D) were manufactured similarly to the white material of the calibration targets, while the chip in B had a glaze on its bottom surface to potentially prevent penetration of epoxy into the material. The chip in D was loose. This assembly phase was carried out at the HCØ building of the University of Copenhagen in June 2021.

As a second step, all the test units were secured inside the TVAC (Thermal Vacuum Chamber) in the laboratory of the University of Copenhagen at Vibenshuset, where they were heated at 115°C for approximately 50 hours (figure 7.17). This operation was concluded over a few days of July 2021.

At the end of the preparation, one test unit was shipped to our colleagues Dr. Dan Applin and Prof. Ed Cloutis at the University of Winnipeg (Canada). The unit was UV-irradiated in order to simulate the equivalent of 2 weeks, 1, 2, 4, 8, 16, 32, 64, and 4140 months in the environment of Mars, and the reflectance spectra were measured

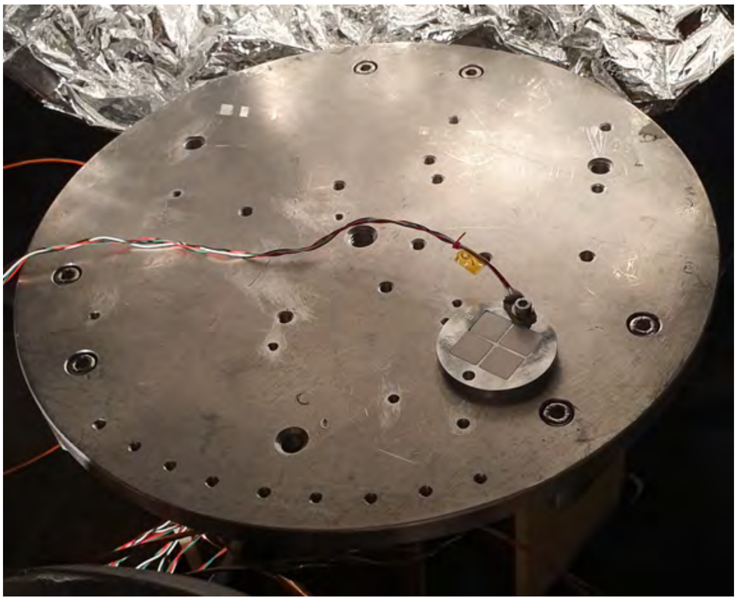

Figure 7.17: *One of the fully assembled test units bolted to the support inside the thermal vacuum chamber at the University of Copenhagen in July 2021. Credits: Morten Bo Madsen.*

for each of the four white chips. Figure 7.18 shows four plots relative to interesting results from the experiment. As expected, the chips do not show any decline at short wavelengths before the irradiation, unlike the white clean spot of the calibration targets (figure 7.18a). A similar outcome is shown in figure 7.18b, where the decline of the patch on sol 80 on Mars is even more conspicuous but an irradiation equivalent to two months does not perturb the chips. In these two cases, the white spectrum on Mars and the spectra of the chips are in agreement for wavelengths greater than 650 nm. After the longest exposure (4140 months equivalent) a small yellowish spot appeared within chip B (figure 7.19). Although the spectra of the four chips after the 4140 month equivalent started to show a deeper decrease in the blue band, the yellow spot resulted to be lower than the general trend, being closer to the spectrum of the white patch from sol 12 (figure 7.18c). However, the spectrum from sol 124 got even lower than the yellowish spot at the shorter wavelengths (figure 7.18d).

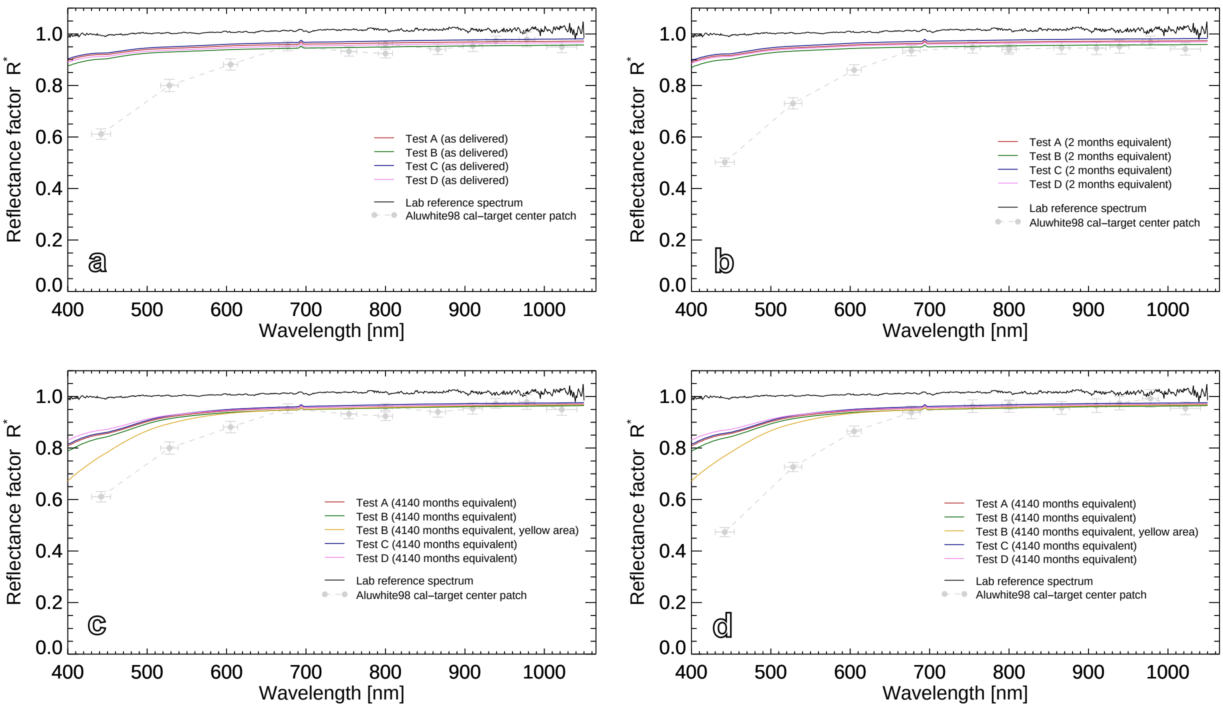

Figure 7.18: *Results of the tests on the AluWhite98 patches. In all plots the black solid line is the reference spectrum of AluWhite98 from the Copenhagen data at i = 0°, Az = 90°, e = 58°, the gray dashed line and the dots represent the spectrum of the white clean spot in different sols, and the other colored solid lines are the spectra of the white chips measured after the UV irradiation. (a) Spectra of the white chips as delivered (before the irradiation) compared to the white patch on sol 12. (b) Spectra of the white chips equivalent to two months on Mars compared to the white patch on sol 80. (c) Spectra of the white chips equivalent to 4140 months on Mars compared to the white patch of sol 12. (d) Spectra of the white chips equivalent to 4140 months on Mars compared to the white patch of sol 124. In (c) and (d) the yellow line (which does not appear in (a) and (b)) is measured on a limited spot of chip B (figure 7.19).*

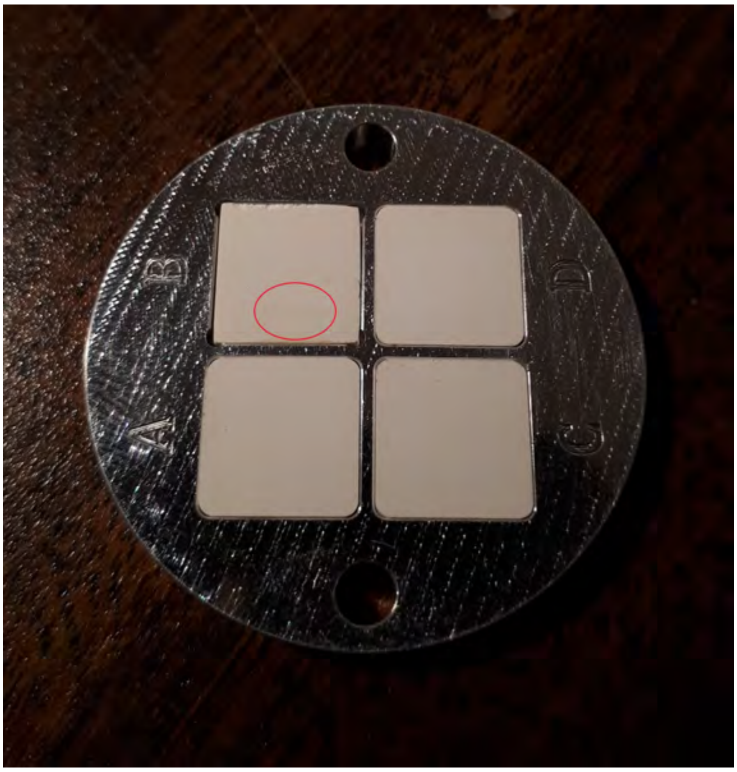

Figure 7.19: *The test unit at the end of the 4140 months equivalent UV irradiation exposure, displaying a small yellowish spot on the chip in position B (in the red circle). Credits: Dan Applin.*

Chapter 8

The first 670 sols of Perseverance on Mars

This chapter is a general summary of the main results from the Perseverance rover during the first 670 sols on Mars. Section 8.1 gives a basic chronology of the mission from landing to sol 670. Section 8.2 summarizes some of the most prominent scientific articles regarding the big-picture discoveries of the mission. Section 8.3 illustrates the performance of Mastcam-Z, with a focus on the results from the multispectral analysis of the reflectance-calibrated images in section 8.4. The outstanding performance of the helicopter Ingenuity is described in section 8.4, while section 8.5 gives an overview of the sample collection so far and the current plans for the Mars Sample Return Mission.

8.1 The chronicle of one martian year

On January 7^{th}, 2023, Perseverance spent its 670th sol on the Red Planet, which marked the milestone of its first martian year. The rover performed an intensive campaign of research and analysis which involved the use of all the instruments of its payload and the successful deployment of the helicopter Ingenuity. As of sol 670, Perseverance traveled a total of 14340 m (the white line in figure 8.1), part of which in autonomous navigation. The navigation cameras mounted on the mast and the hazcams placed under the belly had been programmed to recognize obstacles along the path, and the rover was able to drive without the need for human intervention frequently and for relatively long distances. On February 18th, 2021, Perseverance landed on the crater floor of Jezero, well inside the predicted landing ellipse, on a geologic unit named Máaz but close to the boundary with another unit that was called Séítah. The first phase was the Surface Operation Transition (SOX), which lasted 100 sols and consisted in "turning on" the power generator and all the instruments, check their aliveness and test them (Lange et al., 2022). On sol 13 the rover performed its first drive, and on

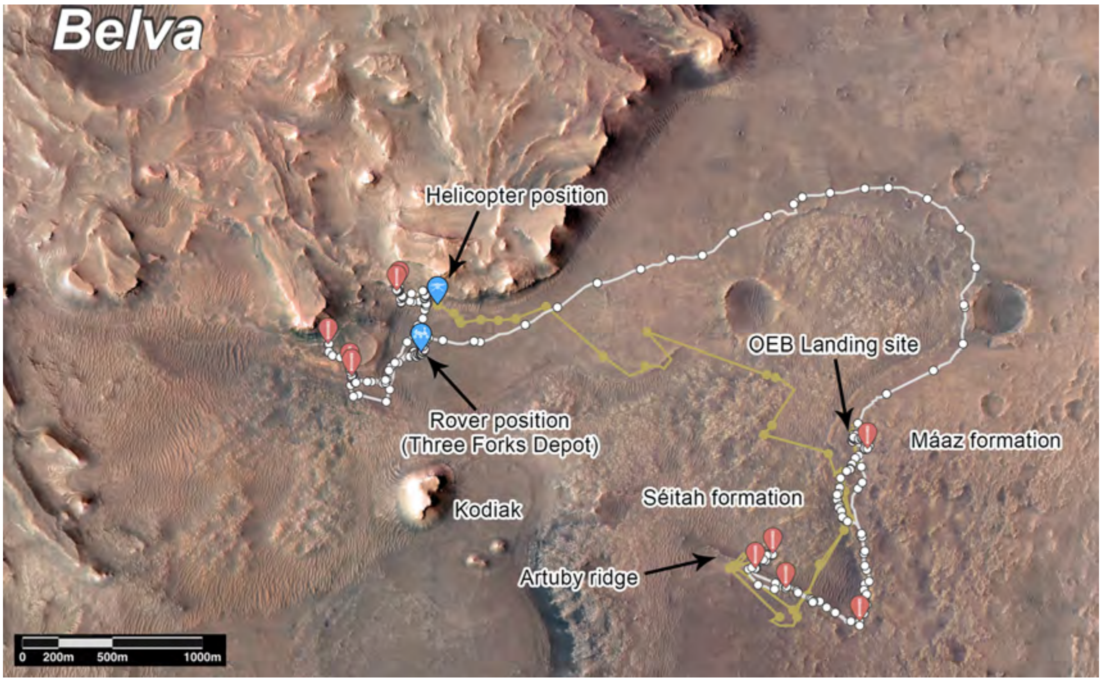

Figure 8.1: *Map of the exploration of the rover showing the drive of Perseverance (the white line) with its waypoints (white circles) and the flights of Ingenuity (yellow lines and circles). The Máaz and Séitah formations and the Artuby Ridge are indicated on the map. As of sol 670, the rover is in a location named Three Forks Depot (center left). The blue labels are the positions of the rover and the helicopter, while the red labels are the core sampling locations. Credits: NASA/JPL.*

sol 22 it jettisoned the belly pan which protected the sample tubes. On sol 41, the helicopter Ingenuity was also deployed and positioned on the surface, and it performed the first flight on sol 58. Between sols 59 and 60, the MOXIE instrument successfully extracted oxygen from the martian atmosphere. After the SOX phase, during which Perseverance stayed near the Octavia E. Butler (OEB) landing site, performed several test observations and analyses, and Ingenuity showed its potential, the rover entered the first science phase, called Green Zone Campaign. Perseverance left the landing site and started moving south through Máaz, following the boundary with Séitah. On sol 160 the rover performed the first abrasion with the proper bit mounted on the robotic arm on the flat rock Guillaumes. On sol 164 the rover attempted the core sampling on another flat rock named Roubion, but the sample tube turned out to be empty, likely due to the high friability of the rock. Between sols 168 and 169, Perseverance turned north-west and followed the exploration of the south of Séitah along what it was called Artuby Ridge. The journey on Artuby continued until sol 201, when the rover left the ridge and ventured among the ripples inside Séitah. Perseverance spent approximately 135 sols exploring Séitah, during which it collected four rock samples and was parked upon the solar conjunction from sol 216 to 236. After coming out of the Séitah region, the rover retraced its step and drove back towards the OEB, which reached around sol

360. It continued driving north and then west, circumnavigating the northern portion of Séítah, thereby concluding the Green Zone Campaign and starting a long traverse that took it to the western Delta fan, in an area named Three Forks, for the next science campaign. The rover went to the southern portion of the delta first, up to a waypoint called Enchanted Lake, and then on sol 422 it went back north, to an area that was named Hogwallow Flats. Between sols 500 and 600 it went back south of the delta, at Enchanted Lake, where it collected the last two samples of the first 670 sols (#17 and #18). As of sol 670, Perseverance is in Three Forks traveling back north (figure 8.1), with the plan of passing through the delta fan towards a small crater named Belva, heading towards the rim of the crater Jezero. During the last crossing of Three Forks, the rover began the deposition of the sample tubes on the surface, which will serve as a backup for the Mars Sample Return mission (section 8.4).

8.2 General results from the mission

The principal focus of the Perseverance team was the geology of Jezero, the search for water and, ultimately, evidence of life forms. A first geologic report on the structures related to water, especially the delta, was realized by Mangold et al. (2021), which is summarized here. The delta was imaged frequently by Mastcam-Z and the other cameras, and presented a structure characterized by hills. The most prominent one was an isolated flat-topped hill (a butte) located south of the main fan deposit and was called Kodiak (figure 8.2a). It was interpreted as the remnant of a larger fan deposit that underwent sedimentary processes in the past. This interpretation was consistent with the stratigraphy of the Kodiak, showing the presence of mudstone or sandstone and suggesting a lower limit of 10 m of water depth in this area of Jezero, but with fluctuating lake levels and varying types of flow at later stages. As a result, Mangold et al. (2021) suggested that the water level during the expansion (or progradation) that formed Kodiak of the delta was too low to allow for the water to flow out through the outlet channel (figure 8.2b), and hence Jezero was a closed-system lake, at the time Kodiak formed. The observation of the delta during the first three months of the mission also led to the identification of smaller fluvial channels (with depths of a few meters) that used to feed the lake and transport sediments. The multispectral analyses of the delta boulders and conglomerates revealed the presence of low-calcium pyroxenes, phyllosilicates and olivine. All these observations seemed to point towards a warm and humid martian climate around the end of the Noachian and the early Hesperian, which could sustain an episodic hydrologic cycle on the surface. Such a cycle might have involved rainfall, snowmelt episodes, impacts, volcanism, or even the formation of glacial lakes, and the characteristics of the boulders might be consistent with strong sudden flooding events. As mentioned in section 8.1, before heading towards the delta

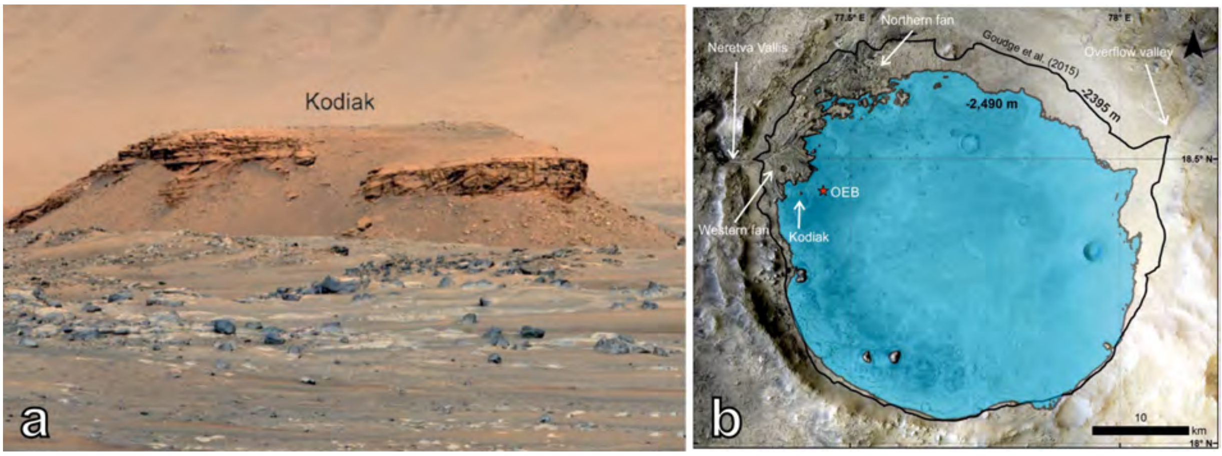

Figure 8.2: *(a) The Kodiak butte within the western delta of Jezero imaged by Mastcam-Z on sol 63 at 110 mm of focal length. (b) Paleolake level inside Jezero crater during the formation of Kodiak. The area in blue is the level inferred by Mangold et al. (2021), which is 100 m lower than the previous estimate by Goudge et al. (2015). Both images are reproduced from Mangold et al. (2021).*

Perseverance spent almost 400 sols exploring two different units, Máaz and Séítah, on which the principal findings were described by Farley et al. (2022) and outlined in the following. The bedrock of Máaz (figure 8.3a) is massive and layered, eroded by aeolian abrasion, though structures of sedimentary transport were not observed. Deeper studies were made through the Mastcam-Z, SuperCam, and PIXL instruments. Some of the rocks analyzed (and abraded) within Máaz displayed textural features consistent with igneous rocks that experienced alteration due to the interaction with water. The composition of Máaz rocks showed basaltic members with common igneous minerals, such as augite, plagioclase and iron oxides, as well as hematite and goethite, which agree with the aqueous alteration. Conversely, the Séítah formation consisted of ridges, sand ripples, loose rocks and boulders (figure 8.3b). Despite their undulating appearance, the outcrops were likely not formed through transport by wind or water. Interestingly, due to the particular layering of Séítah observed from along the Artuby ridge, it resulted that Séítah is the lowest exposed stratigraphic unit on the crater floor of Jezero, which is overlain by Máaz. The separation between the two formations is covered in regolith, and therefore it is not visible. Some rocks within Séítah show the presence of olivine (much more than Máaz), augite, and plagioclase, not too dissimilar to those in Máaz, whereas rocks of different members are characterized by feldspar and augite, but not olivine. In general, the rocks in Séítah consist of igneous minerals and secondary aqueous alteration phases. According to Farley et al. (2022), the floor of Jezero crater was probably filled with magma from volcanic activity in several distinct episodes, and subsequently water modified the mineralogy and composition of the igneous rocks, for example by carbonation and serpentinization. In addition, Farley et al. did not find any geochemical or mineralogical indication of open-system aqueous alteration, in agreement with Mangold et al. (2021). In fact, no evidence for lacustrine sedimentation in the crater floor was found, implying that the sediments were likely buried by igneous or impact processes or eroded away (Bell et al., 2022).

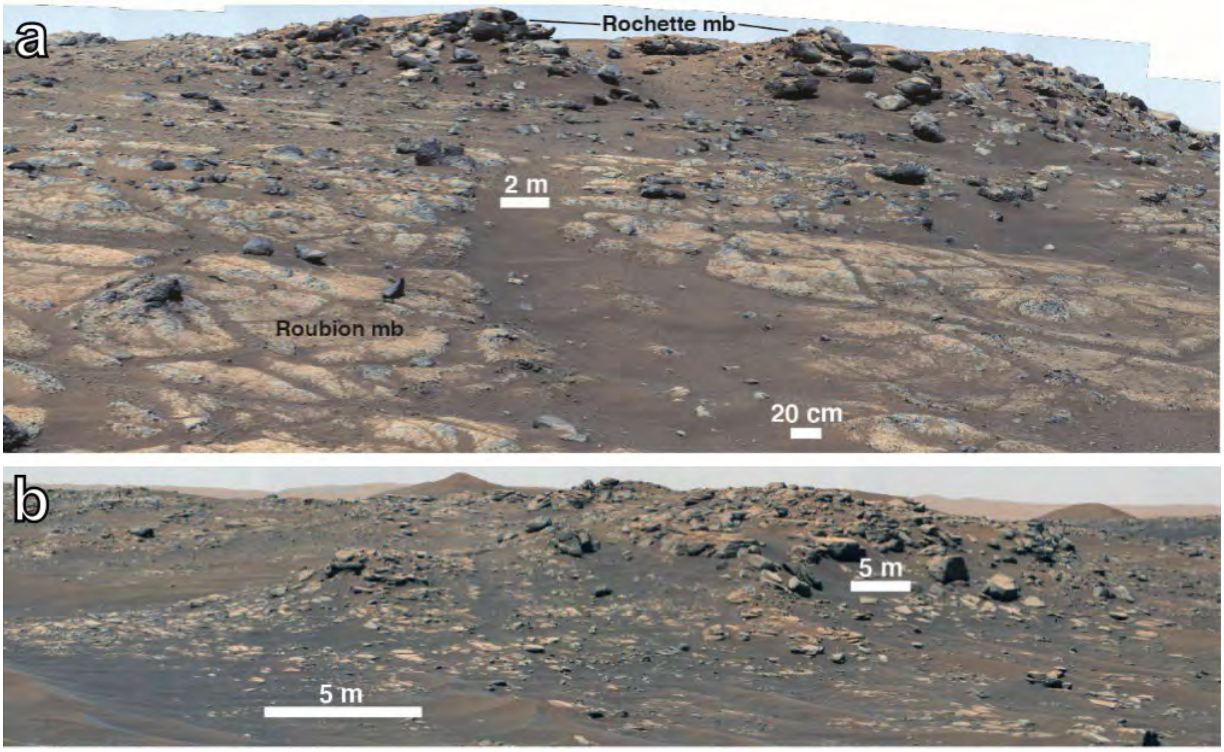

Figure 8.3: *(a) Panoramic view of an outcrop within the Máaz formation imaged on sol 138 by Mastcam-Z. Two members of the outcrop, named Rochette and Roubion, are indicated. (b) Mosaic showing bedrock exposures of the Séítah formation acquired on sol 201 by Mastcam-Z. Both images are reproduced from Farley et al. (2022).*

8.3 The first martian year of Mastcam-Z

Mastcam-Z acquired 111889 images in all the color and narrow-band filters (including the solar filters L7 and R7) over the first 670 sols on Mars. Of those, 57284 were taken from the left eye and 54605 from the right eye. Mastcam-Z images contributed significantly to the exploration and the scientific campaigns within the Jezero crater in many forms (Bell et al., 2022). Besides the radiometric calibration, which was treated exhaustively in the previous chapters, images were acquired with the aims of documenting the main activities of the mission, realizing amazing mosaics portraying near fields and panoramas, inspecting the rover deck, performing multispectral analysis, building virtual 3D models, studying the astronomy from the martian surface, and observing the Sun to retrieve the atmospheric optical depth (see section 7.2.3). Some details of the multispectral analysis will be illustrated in section 8.4. All images in their raw version, suitably elaborated in order to enhance their colors, are continuously added to the official Mars 2020 mission media webpage[1] and the calibrated products are uploaded on the Mastcam-Z website[2] by the Team, thereby emphasizing the importance of the public outreach.

Several color images were captured upon all the milestones of the first 670 sols. For instance, the helicopter Ingenuity completely deployed and ready to fly was imaged on sol 45 (figure 8.4a). Similar close-ups were realized every time the abrasion or the coring bits of the robotic arm were used, in order to verify their condition and the appearance of the abrasion patches or the boreholes made by the drill (figure 8.4b). Among the documented events, it is also worth mentioning that on some occasions Mastcam-Z acquired videos. It recorded some of the first flights of Ingenuity, and in some circumstances it even captured dust devils. In particular, in the images and videos of Ingenuity's flights the camera captured the dust lifted by the rotors of the helicopter upon every flight, allowing for an accurate assessment of the optical depth of such dust clouds.

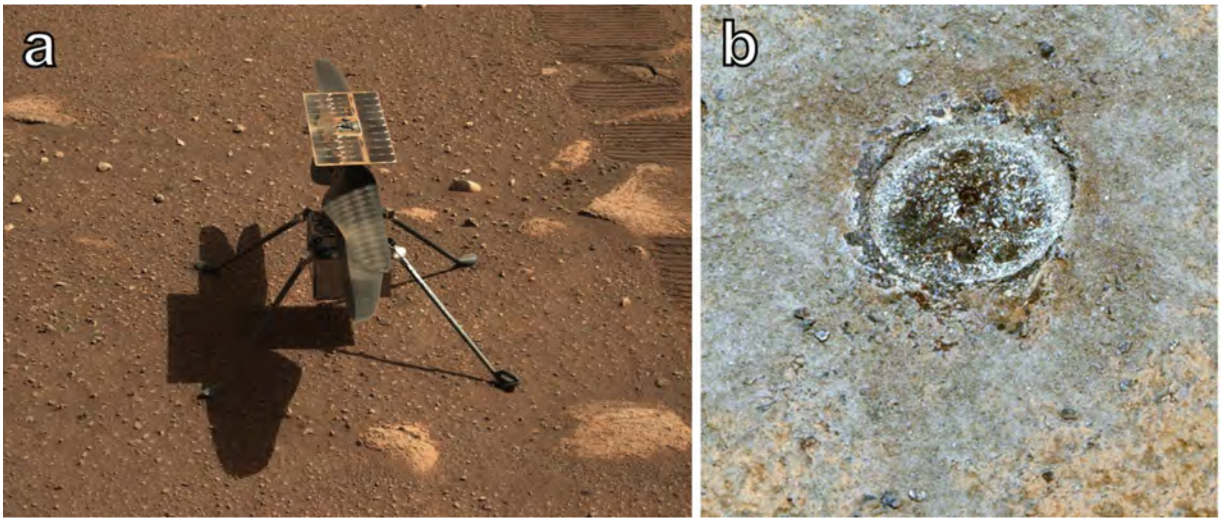

Figure 8.4: *(a) Close-up (110 mm zoom) on the helicopter Ingenuity on sol 45, fully deployed and ready to fly. (b) The "Guillaumes" abrasion patch imaged on sol 160 at 110 mm of focal length, exposing the internal texture of the rock. Credits: NASA/JPL-Caltech/ASU/MSSS.*

In several occasions, Mastcam-Z scanned portions of the landscape by tilting the mast of the rover by few degrees, leading the Team to make mosaics. These were composed by images in a matrix with slightly overlapping margins, which were then merged by correcting for spherical distortions. Some of these mosaics focused on the deck of the rover, in order to assess its status (especially with respect to dust), while others were meant to display the rocks and boulders in the immediate surroundings of the

[1]https://mars.nasa.gov/mars2020/multimedia/raw-images/
[2]https://mastcamz.asu.edu/mars-images/images-videos/

rover (figure 8.5a). However, the most extensive mosaic products of Mastcam-Z were the far-field panoramas, which appear as long horizontal stripes achieved by simply making the camera turn partially around its axis and "scan" the horizon at high focal lengths (figure 8.5b). A few of such panoramas were 360° and gave a superb overview of the floor of Jezero and the structures forming the delta fan (Bell et al., 2022).

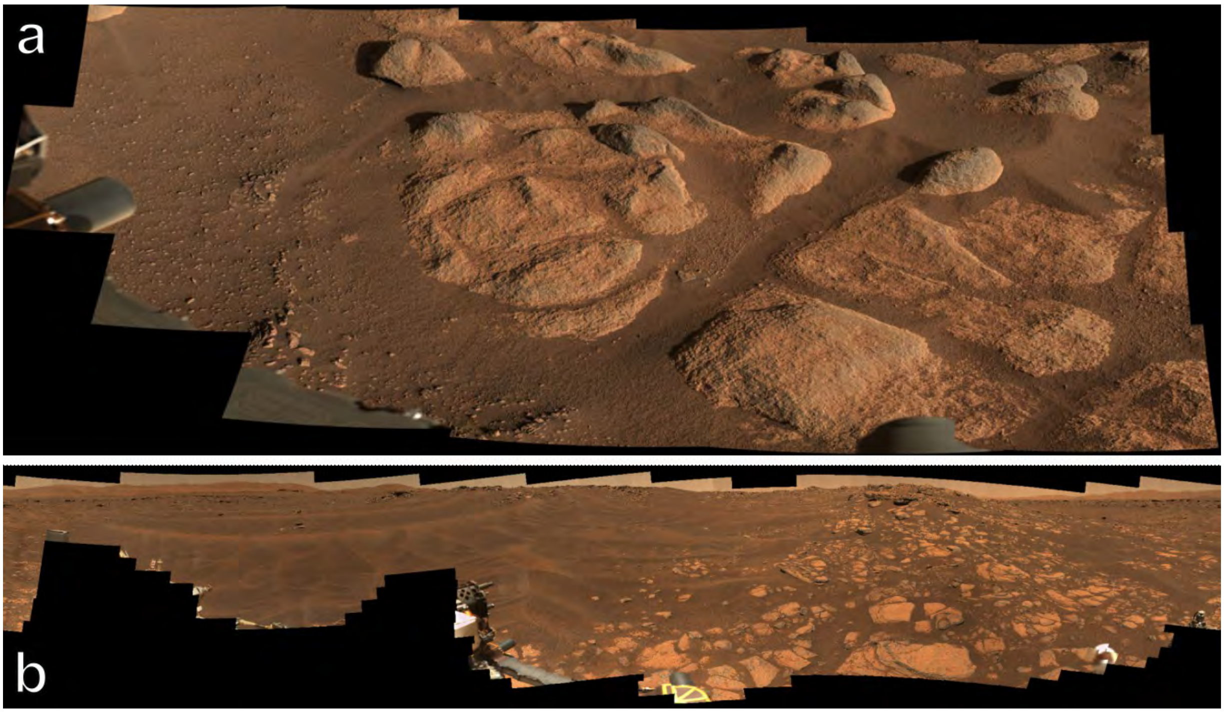

Figure 8.5: *(a) Mosaic of 21 images showing some rocks near the rover acquired on sol 66 at a focal length of 110 mm. (b) 360° panorama of "Village" outcrop realized by Mastcam-Z on sols 214 and 215 at 110 mm of zoom within the Séítah formation. Credits: NASA/JPL-Caltech/ASU/MSSS.*

The production of three-dimensional models was supported by the stereoscopic design of Mastcam-Z. Most products were created by the Stereo-DTM (where DTM stands for Digital Terrain Model) working group, which processed stereoscopic color images of the same targets and remote sensing images from orbiters together and obtained accurate reproductions of those targets that could be visualized through virtual reality goggles[3]. Among the other products that were included in the 3D field, the easiest ones to make were the anaglyphs, that are obtained by assigning properly the filters of the two eyes to the RGB channels of the resulting image. The typical outcome is a stereoscopic image with the targets in red and blue, that can be appreciated through red-blue glasses (figure 8.6).

As a last important remark, Mastcam-Z performed atmospheric and astronomical studies. The camera carried out direct solar imaging and near-Sun observations which allowed the computation of the atmospheric optical depth and the characterization

[3]https://mastcamz.asu.edu/mars-in-3d-update-1/

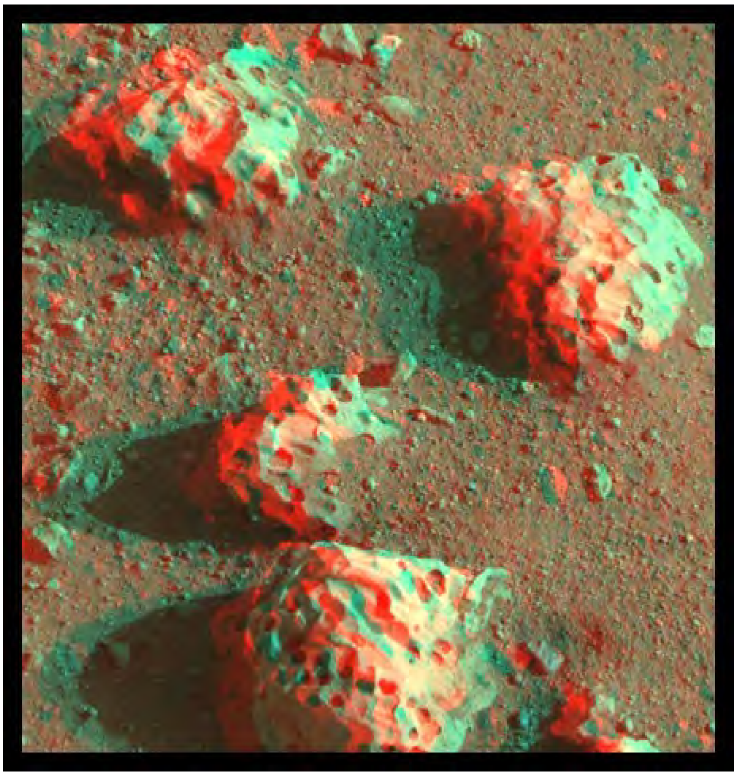

Figure 8.6: *Color anaglyph of some rocks realized with Mastcam-Z images acquired on sol 3 at a focal length of 34 mm. The 3D effect can be seen by using a pair of red-blue glasses. Credits: NASA/JPL-Caltech/ASU/MSSS/C. Manzoni/B. May.*

of the column-integrated aerosol abundance very frequently. These observations, that were often made during the martian dawn and dusk, revealed morning water-ice hazes during the first 300 sols of the mission (Bell et al., 2022). In addition, the frequent imaging of the Sun through the solar filters L7 and R7 (and the precise ephemeris knowledge) led to witnessing the transit of Phobos, one of the martian moons, in front of the Sun. The event occurred on sol 397, lasted approximately 40 seconds and was recorded as a video at a focal length of 110 mm (figure 8.7).

8.4 The multispectral analysis of Mastcam-Z reflectance-calibrated images

The multispectral analysis is a useful method that allows to infer the mineralogical properties of rocks and other geologic features. In the case of Mastcam-Z, a full image sequence of some scientific target in all filters is acquired by the camera and calibrated to IOF reflectance through the calibration targets. Therefore, the IOF images can be processed in the same software that I used for the selection of the ROIs in the calibration targets. Firstly, some regions of interest are selected within the calibrated images

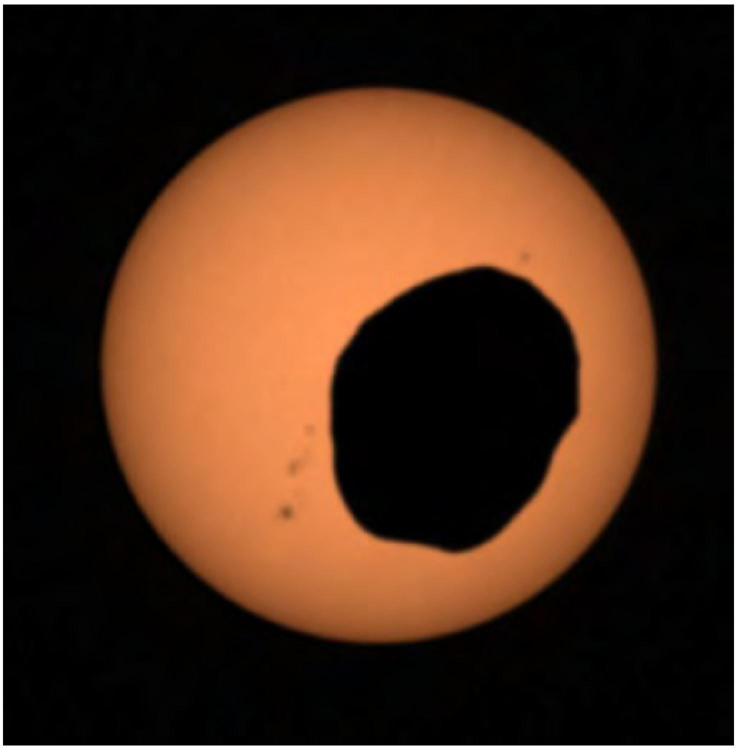

Figure 8.7: *The transit of the martian moon Phobos in front of the Sun, that occurred on sol 397. The image is one of the frames of a video showing the full transit, which can be watched on NASA JPL Youtube account at https://www.youtube.com/watch?v=aKK7vS2CHC8. Credits: NASA/JPL-Caltech/ASU/MSSS/SSI.*

of the multispectral sequence in the two eyes. The software computes the average IOF (or R*) reflectance over all the pixels of the selected ROI and the related standard deviation for each image (i.e., each wavelength), and those reflectance values can be plotted against the wavelength to retrieve the reflectance spectra of the different regions selected. The selection of the ROIs is generally based on operator's choice, but the aim is to identify and extract data from geomorphological features that would be interesting to study (e.g., flat or floating rocks, boulders, regolith, dust coating, etc.).

Such a choice is often aided by some spectral products in the form of "informative images" displaying a specific spectral behavior in all its pixels. They include: (i) the decorrelation stretch (introduced in section 7.2.1), which enhance the different components by oversaturation; (ii) the band depth, which expresses the depth of a data point at a wavelength with respect to two other enclosing data points (the "shoulders" and quantifies the depth of the absorption band; (iii) the band ratio, which simply shows the ratio between the data points at two different wavelengths; and (iv) the slope, which gives the computed spectral slope between two data points at different wavelengths. When these products are available, their comparison usually leads to spotting peculiarities that are worth investigating by selecting them in the IOF sequence. It is worth mentioning here that over the summer of 2021, a few months after landing, the Multispectral Working Group, which focuses on this sort of analysis, developed and tested two applications that automate the process described above. The first one, named "asdf", takes a multispectral sequence and a selection file (namely, a file containing the image coordinates of the regions of interest selected) in input and returns a plot of the reflectance spectra of the ROIs and a rich set of the four spectral products listed above in different wavelength combinations. All the numerical data of the reflectance spectra from all the sequences that have been processed through asdf can be consulted in the second application, which was called "Multidex". The latter is provided with an interface where the user can make three-dimensional plots of spectral data (the axes can represent reflectances, band depths, slopes, band ratios, etc.) and even apply the Principal Component Analysis (PCA), a statistical method that expresses how the data points can be separated in groups according to prominent differences in their three axes. Both asdf and Multidex were developed by Million Concepts[4]. Some examples of spectral products made by asdf are shown in figure 8.8 for a rock called Hedgehog imaged by Mastcam-Z on sol 37. The products are an enhanced color image (figure 8.8a), a decorrelation stretch (8.8b), an example of band depth (8.8c) and a slope (8.8d).

Mastcam-Z acquired about 500 multispectral sequences over the first 670 sols, many of which consisting of two- or three-pointing mosaics. The spectral signatures of the geologic targets of the crater floor show a combination of rock surfaces, dust, regolith and coatings, and they are characterized by pyroxene compositions, such as orthopyroxene and Fe-rich clinopyroxene (Horgan et al., 2022). The coating was observed as a purple-hued material in less dusty areas on the Séítah and Máaz rock surfaces. This spectra of this material showed features of pyroxene or ferric minerals, hematite, and ferric oxides (Garczynski et al., 2022). While olivine was not detected within Máaz (Bell et al., 2022), the thinly and massive layered cap rocks within Séítah showed absorption bands consistent with olivine, in particular in the abrasion patches and tailings of two outcrops named Bastide and Brac (Nuñéz et al., 2022). The ROIs in the grains inside other abrasion patches (on rocks named Rochette and Roubion) yielded spectra consistent with the presence of Mg-rich orthopyroxene and Fe-rich clinopyroxene (Horgan et al., 2022). Figure 8.9 shows some examples of reflectance spectra relative to seven members from Máaz and Séítah. The nature of rock surfaces is consistent with pyroxene and iron oxides for the Máaz members, and with olivine for the Séítah members (Bell et al., 2022).

In a very limited number of sequences (around 5% of the multispectral database) the reflectance spectra displayed unexpected anomalies such as bumps or drops at different wavelengths, or very large error bars. In most cases, the issues could be determined as due to small flaws in the radiance calibration or a non optimal selection of the ROIs,

[4] https://www.millionconcepts.com/

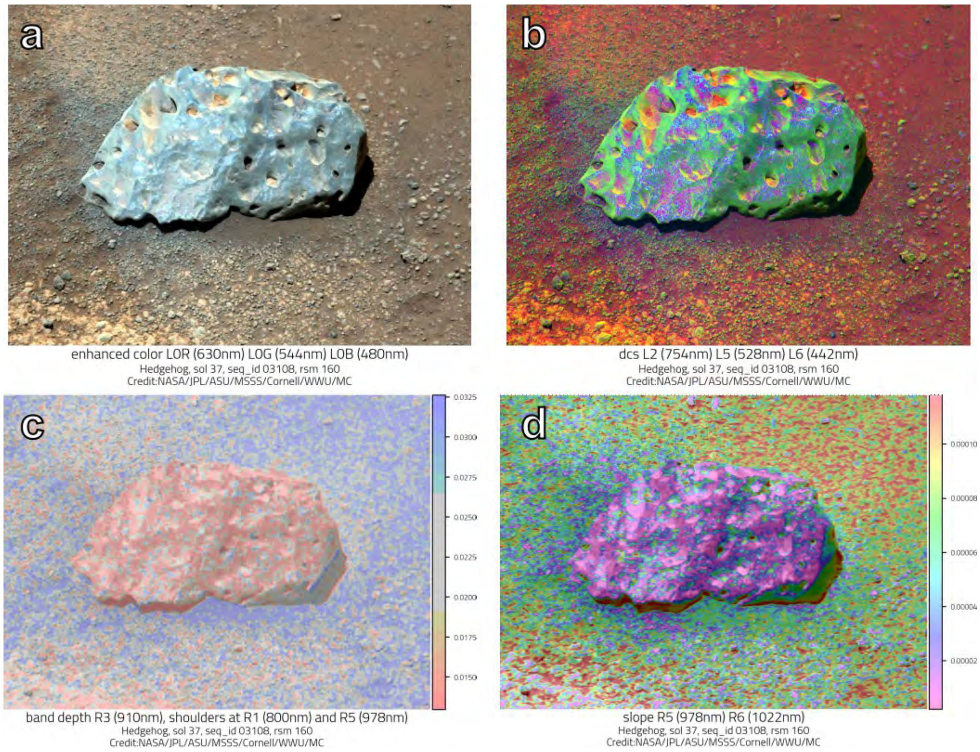

Figure 8.8: *Four spectral products relative to a target rock named Hedgehog imaged on sol 37 by Mastcam-Z at 110 mm of focal length. (a) Enhanced color imaged in L0R, L0G and L0B. (b) Decorrelation stretch in the filters L2, L5 and L6. (c) Band depth of R3 between the shoulders in R1 and R5. (d) Slope value between R5 and R6. The filters for (a) and (b) are assigned to the red, green and blue channels, respectively. Credits: NASA/JPL-Caltech/ASU/MSSS/Cornell/WWU/MC.*

especially on targets with a high pixel variance (for instance, rocks with lights and shadows on small scale), or a mix of both. The former were solved through slight corrections in the codes of the calibration pipeline, while the error bars were usually reduced by selecting smaller ROIs with a higher illumination uniformity and ensuring that the ROIs in both eyes were selecting the exact same areas. In a few other cases, after excluding all the other possibilities, the spectral oddities were caused by discrepancies in the reflectance calibration. I analyzed those calibration matters and I identified two (sometimes overlapping) explanations.

Firstly, as I mentioned in section 6.4.1, the calibration target observations at high incidence angle (larger than 50°) might often deviate from our reflectance model, especially on sols with a high amount of suspended dust in the atmosphere. Fortunately the number of calibration target sequences illuminated by the Sun close to the horizon was relatively low, but the corresponding azimuth value was able to enhance the problem. Figure 8.10 shows three examples of low-Sun observations of the calibration targets. For each example, an image of the calibration targets is displayed on the left and the corresponding derived irradiance spectrum (black circles) is reported on the right together with the solar black body model (blue line), for reference. The black

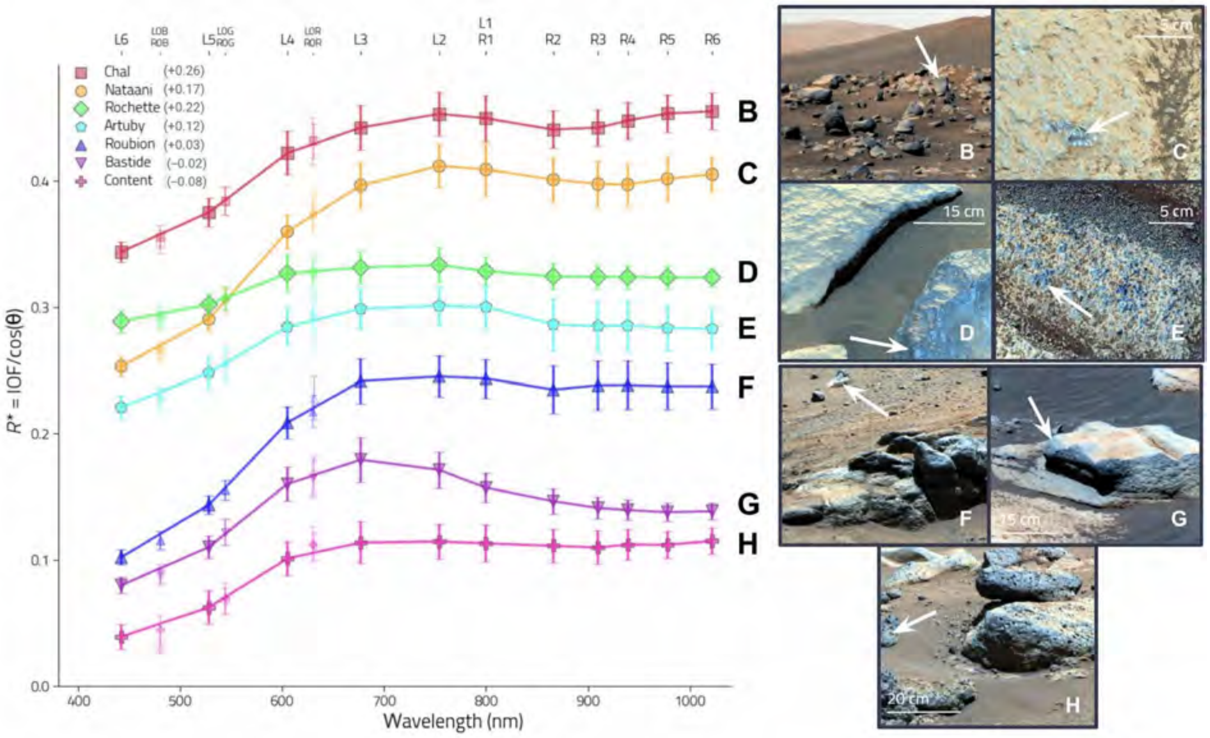

Figure 8.9: *Reflectance spectra (in terms of reflectance factor R*) of some stratigraphic members from the Máaz and Séítah formations. Each spectrum is provided with a context image from Mastcam-Z (on the right) and the given name (in the upper left). The Chal, Nataani, Rochette, Artuby and Roubion members belong to the Máaz formation, while Bastide and Content members are located within Séítah. Figure from Bell et al. (2022).*

body model was computed using equation (7.1), assuming the Sun-Mars distance at that sol, and scaled by the cosine of the incidence angle, to make it more consistent with the observed data. Given that the solar model was referred to the light reaching the top of the martian atmosphere, it did not account for the scattering properties of the atmospheric gasses and dust at low-Sun, and hence it appears lower than the derived irradiance spectra as expected.

It is useful to start from the last case. In the observation of sol 387 the Sun was very low almost behind Mastcam-Z (low azimuth). The measured radiance from the clean spots was relatively high due to the presence of diffuse illumination that our reflectance model did not predict. In fact, as witnessed by the goniometric data of figure 5.3, the reference reflectance of the clean spot materials for very high incidence angles (such as that of sol 387) was almost equal to that for the Sun at the zenith, when the scattering is almost negligible. As a consequence, the derived irradiance spectrum resulted even higher than the other sols of figure 8.10. A similar outcome was observed on sol 353, when the Sun illuminated the calibration targets from one side. The lower incidence and the higher azimuth than sol 387 reduced slightly the radiance and increased the reference reflectance, thus decreasing the irradiance. The sequence from sol 385 was a completely different situation. The Sun was almost in front of Mastcam-Z, thereby causing a mirror effect on the surfaces of the primary target. In this case from figure 8.10, the predictions of our reflectance model yielded high values of reference reflectances in the fits, which returned a relatively low irradiance spectrum due to the low diffuse illumination.

The results presented in the previous paragraph and in figure 8.10 only concerned the specific illumination geometry of the calibration targets, and were independent from the multispectral sequence that they were employed to calibrate. In fact, only a fraction of those was affected by irregularities in their reflectance spectra. The second explanation that I found for the spectral anomalies was due to the great difference between the illumination geometry of the calibration targets and the scientific target, which were usually acquired a few minutes apart, because the codes for the reflectance calibration assume that the incidence angle is the same. When the target of interest was a roughly horizontal surface, such as a flat rock or regolith, the best time to image it was around martian noon, when it was illuminated from above. This geometry never created any sort of issues in the spectra. Conversely, when the target was a boulder or a float rock with a vertical side, the plan was to take pictures when it was illuminated normally, that is with a low-Sun configuration. However, the clean spots of the primary calibration target were always relatively horizontal, and hence the high incidence angle on the calibration targets caused not only the discrepancies presented in figure 8.10, but also in the spectra of the multispectral sequence due to the completely different angle. Figure 8.11 shows a didactic "worst case scenario" that illustrates the problem excellently. On sol 236, Mastcam-Z took full sequences of a layered rock named Gaubert around 17:00 LMST and the calibration targets immediately after. The calibration targets (figure 8.11a) were illuminated with $i = 70°$ from one side, giving the derived irradiance spectrum in figure 8.11b a higher trend than the expected solar model, similar to sol 353 in figure 8.10. At the same time, Gaubert (figure 8.11c) was well illuminated frontally, with an incidence angle close to 0° on its lit surface. Using the values of irradiance of figure 8.11b on the Gaubert sequence yielded the funky spectra in figure 8.11d.

The calibration issues described in this section are discussed in section 9.3, where I suggest a model for the correction for the diffuse illumination. The model is reported exhaustively in appendix B.

8.5 The helicopter Ingenuity

In the first 670 sols, the technology demonstrator Ingenuity performed a total of 38 flights. At the beginning of April 2021, after the rover dropped the lid that contained the helicopter under its belly, Ingenuity was deployed on the martian ground, in a site

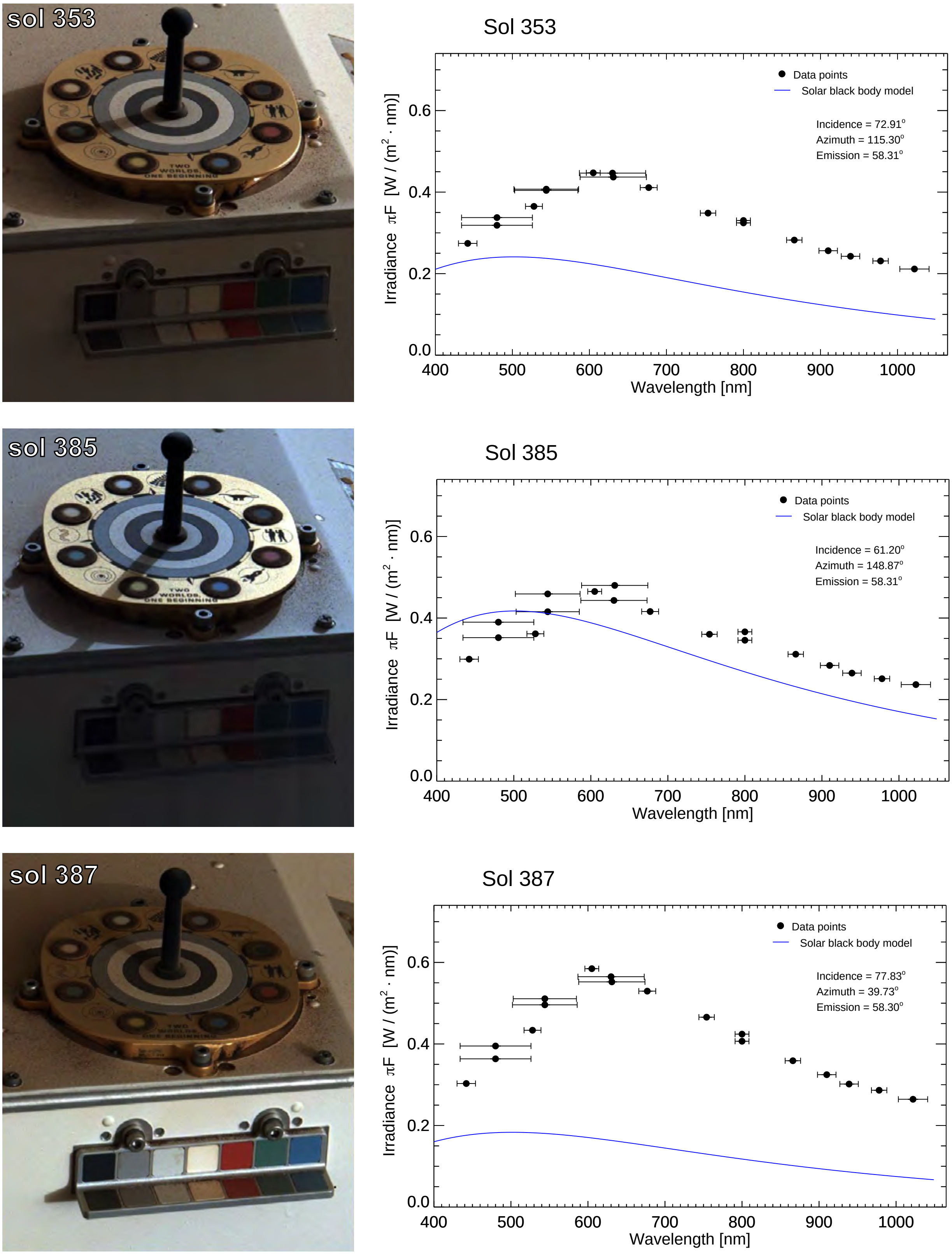

Figure 8.10: *The calibration targets (on the left) and the derived irradiance spectrum (on the right) relative to three sols (353, 385 and 387) of the mission. The images on the left were taken by the left eye of Mastcam-Z (L0) at 48 mm of focal length and have all the sequence ID ZCAM03014. In the plots on the right, the black circles are the derived irradiance spectrum, the solid blue line is a solar black body model computed using equation* (7.1).

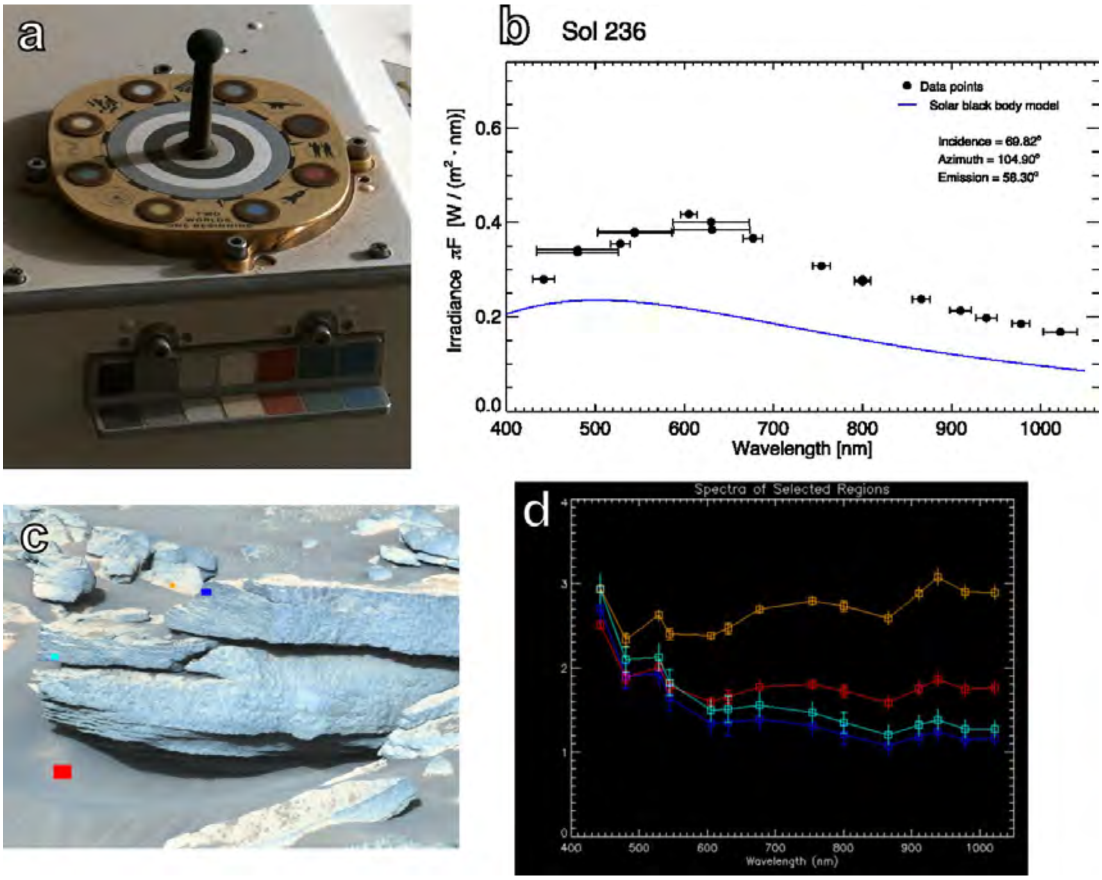

Figure 8.11: *Worst case scenario regarding the high difference of illumination geometries between (a) the calibration targets and (c) a layered rock named Gaubert, both imaged in the late martian afternoon of sol 236. The calibration targets in figure (a) yielded the derived irradiance spectrum (black circles) in figure (b), where the blue solid line is a solar black body model under the same illumination geometry as (a). The colored rectangles in (c) are the selected ROIs for the multispectral analysis, which produced the spectra in figure (d). The image in (a) was acquired by the left eye of Mastcam-Z (L0) at 48 mm of focal length (sequence ID ZCAM03014).*

that was named "Wright Brothers Field". Then, the rover moved in order to leave a safe flying zone, and on April 19^{th}, 2021, on sol 58, the helicopter hovered vertically in the thin air for 39.1 seconds, reaching an altitude of 3 meters. During the second flight, on sol 61 (figure 8.12a), Ingenuity reached 5 m of altitude and moved horizontally by 4 m. Over the whole month of April 2021, Ingenuity performed four flights, in which it maintained a maximum altitude of 5 m but increased the horizontal distance up to 266 m. As a consequence of the excellent conduct of the helicopter, after the 5^{th} flight (figure 8.12b) the team changed its role from technology demonstration to operation demonstration, and Ingenuity was employed to support the rover by following it in its traverses (while always keeping at safe distance) and exploring the terrain through its two cameras. Among the several color images taken by Ingenuity, it is worth mentioning that during its 26^{th} flight, on sol 414 (April 19^{th}, 2022) the helicopter captured

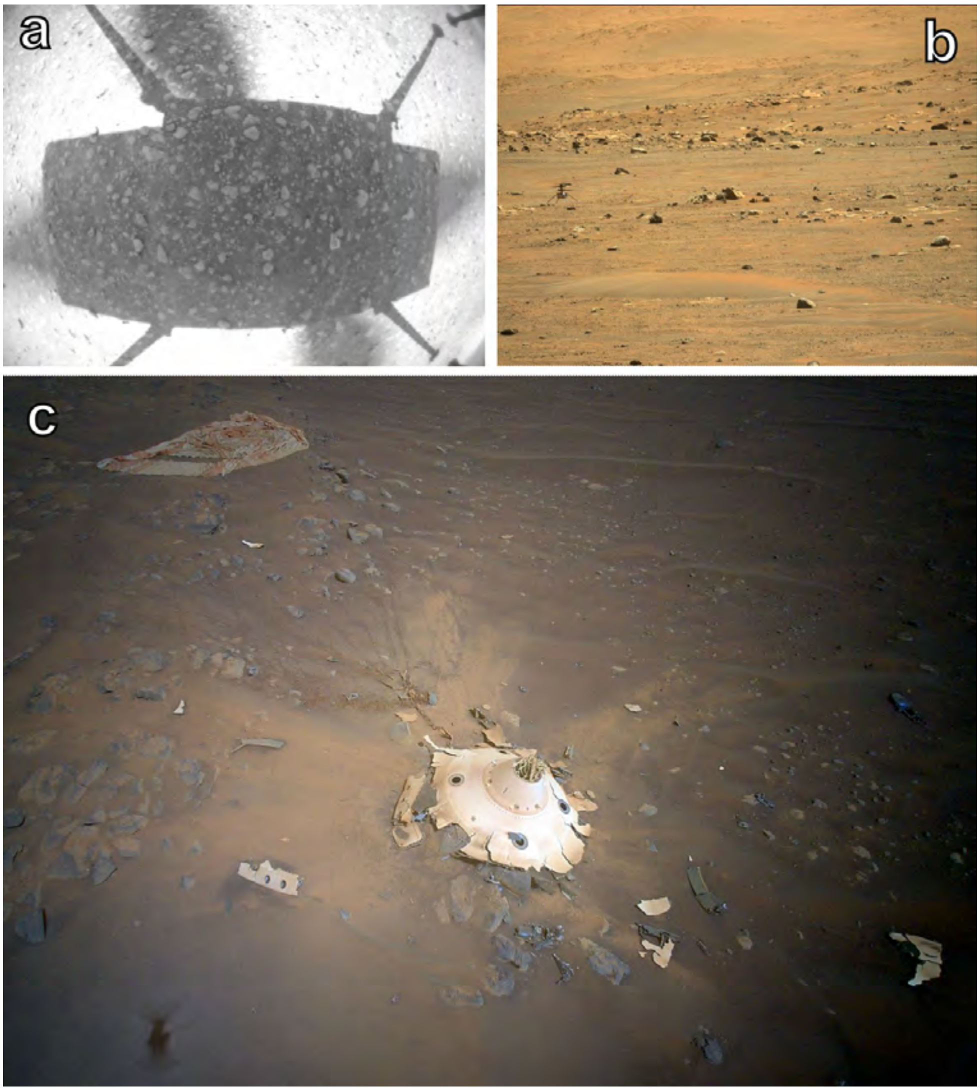

Figure 8.12: *(a) Image taken by the black and white down-looking camera of Ingenuity on sol 61 during its second flight. (b) The helicopter Ingenuity (on the left of the frame) as seen from Mastcam-Z just after its fifth flight on sol 76. (c) The remains of the back-shell and the parachute that landed the rover Perseverance safely on Mars, captured by the color camera of Ingenuity on sol 414 during its 26th flight. Credits: NASA/JPL-Caltech/ASU/MSSS.*

the backshell and the parachute of Perseverance's descent stage (figure 8.12c), which were expelled moments before the landing in February 2021. Those two elements were found approximately 1 km north-west of the landing site. Over the first martian year, in its 38 flights Ingenuity flew for 3700 s (1 hour) and covered almost 7580 m, reaching a maximum altitude of 14 m, a maximum flight duration of 170 s, and a maximum horizontal distance of 704 m in individual flights.

8.6 The sample caching and deposition

In the scope of the Mars Sample Return mission (section 3.2.1), Perseverance used the coring drill mounted at the end of the robotic arm to extract samples of rocks and other materials and paved the way for the future return of those samples to Earth. The first attempt was made on sol 164 in an area called Polygon Valley, in the proximity of Artuby Ridge, on a rock named Roubion. After the drilling, the Cachecam images showed that the extraction did not succeed. However, the sample tube was sealed and cached, and it was the only failed attempt. In the first 670 sols, Perseverance collected 18 samples. Following Roubion, which was labeled as an atmospheric sample, the rover extracted two rock cores from one rock on Artuby Ridge (sols 194 and 196) and four from two rocks in South Séítah (sols 262, 271, 298, and 337). The rock core from sol 271, named Coulettes, is shown in figure 8.13a. Subsequently, two samples were collected within the OEB landing site on sols 371 and 377. After the first part of the mission in which the rover focused on the igneous rocks of the crater floor, the rover reached the delta (Delta Front), rich in sedimentary rocks. There, between sols 490 and 631 it extracted a total of seven rock samples from four different geologic features, and two regolith samples (on sols 634 and 639), which were expected to contain a mix of sedimentary and igneous grains. The amount of material inserted in the tubes depended on the type of target, its density and friability, and the sample heights were included between 3.1 cm and 7.4 cm. In addition, three witness tubes were sealed, out of the five available. One of such witness tubes was opened before launch, in order to mark the level of terrestrial contaminants that the rover carried to Mars, and the others were opened one at a time on Mars to detect the local environment, for future analysis and calibration. Figure 8.14 shows a summary of all the 21 sample tubes filled until sol 670, with the locations in which they were filled and sealed and a context image of their corresponding abrasion patches.

In the second half of December 2022, the rover was programmed to release ten sample tubes on the surface in a limited area. This operation was considered as a backup, in the contingency that the rover cannot deliver the tubes in the future. The designated area, located at the delta, was named Three Forks Depot, and between sols 653 and 670 five tubes were dropped (one with atmospheric gasses, two with igneous rocks, one with sedimentary rock, and one with regolith). The deposition of the tubes was documented with several images of Mastcam-Z and WATSON (figure 8.13b shows the tube containing the Coulettes sample), and the exact geographic locations were retrieved in order for the next return mission to find the tubes in the highly unlikely event that they are buried by sand or dust storms.

As of sol 670, the concept of the retrieval of the samples evolved significantly with respect to the first plan described in section 3.2.1. According to the new idea developed

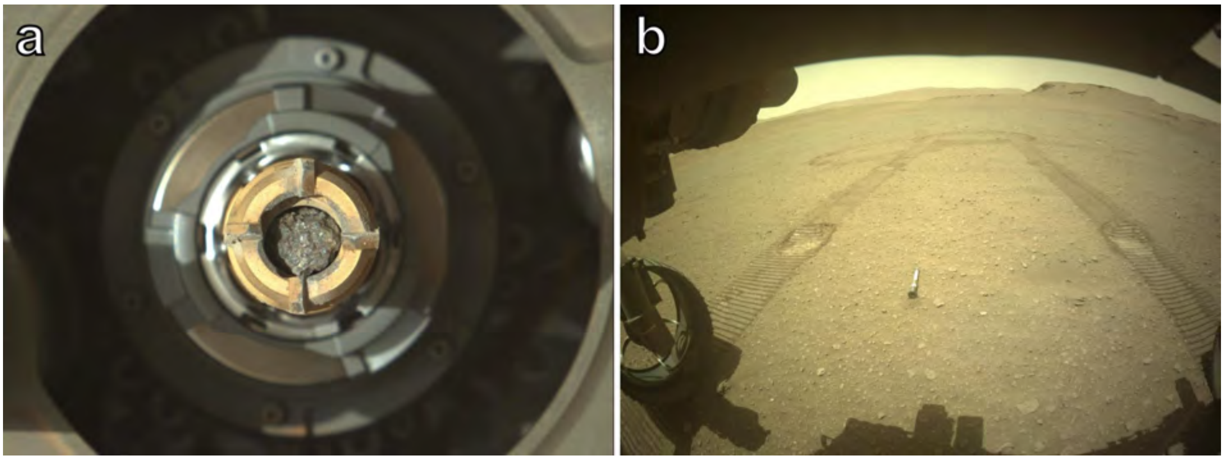

Figure 8.13: *(a) Close-up image of a rock sample named Coulettes extracted from a feature called "Brac" on sol 271. The image was taken by Mastcam-Z at 110 mm of focal length. (b) The sample tube containing the Coulettes rock core deposited on the surface within the Three Forks Depot on sol 670 and imaged by the front left Hazcam. Credits: NASA/JPL-Caltech/ASU/MSSS.*

by scientists and engineers of the Mars Sample Return team of NASA and ESA[5], a Sample Retrieval Lander will land in 2028 in the vicinity of Perseverance. The payload of the lander will consist of a couple of helicopters and a small rocket. The former, the Sample Recovery Helicopters, were considered a better (and less expensive) choice than a small rover, thanks to the outstanding experience with Ingenuity. They will receive the tubes from Perseverance, and will bring them to the lander, where a robotic arm will load the tubes in the rocket, named Mars Ascent Vehicle (MAV). Once fully loaded, it will be sent to orbit, where another spacecraft will secure the precious load and bring it back to Earth.

[5]https://mars.nasa.gov/msr/

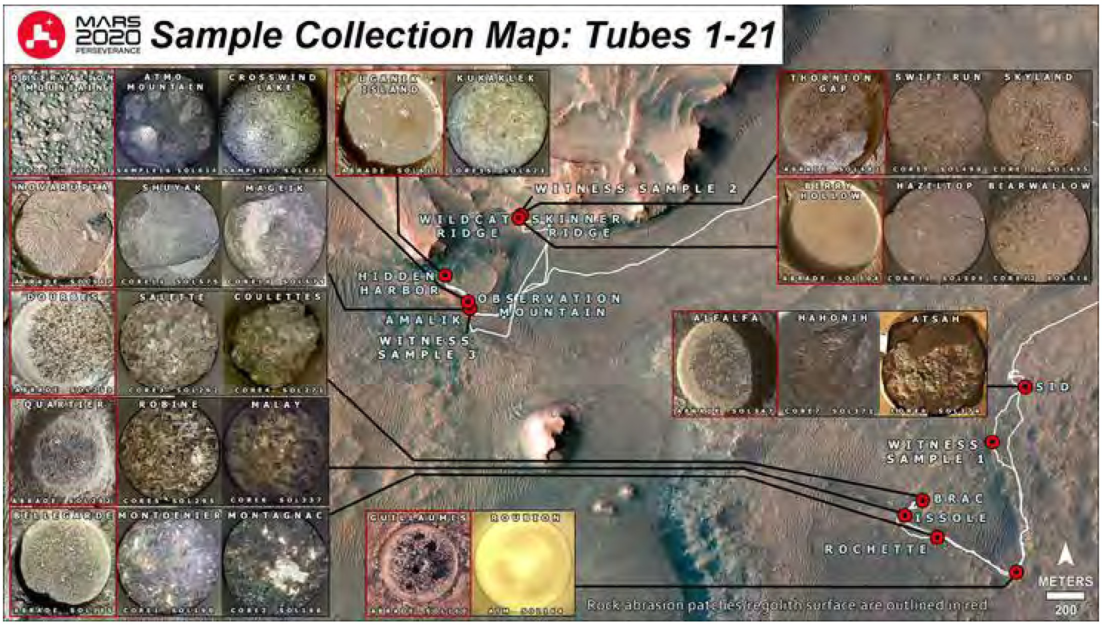

Figure 8.14: *Summary of the 21 sample tubes that were collected during the first 670 sols by the rover. The thumbnails of the samples show the abrasion patches that were excavated before the extraction of the cores. The given name and the sol of the coring are written for each sample, and their original locations are shown on the map. Credits: NASA/JPL-Caltech.*

Chapter 9

Discussion

This chapter is devoted to the discussion of the main results that I obtained during the first 670 sols of the mission. In section 9.1 I assess the performance of the calibration targets and the models and procedures that we employed for the reflectance calibration. In section 9.2 I interpret the results concerning the martian dust that deposited on the surfaces and that interacted with the sunlight. Section 9.3 is focused on the discussion of slight calibration anomalies in some multispectral sequences. Finally, in section 9.4 I comment on the yellowing effect of the AluWhite98 material, which was observed since the earlier sols of the mission.

9.1 The calibration target performance and the linear fit model for IOF calibration

The performance of the calibration targets and our model on Mars can be assessed from the observations and the results shown in chapters 6 and 7. In the first place, the plots in figure 6.8 display a very limited dispersion of the data points with respect to the fit lines (with the exclusion of the white patch) where such a dispersion was quantified as a relative uncertainty on the slopes of 3.8% on average over all filters, and no filters showed a mean value greater than roughly 5%. This deviation is satisfyingly small, especially if we keep in mind that the overall average was 3.5% in the first 350 sols (Merusi et al., 2022). The slight increase from 3.5% to only 3.8% occurred in the time range between sols 350 and 670, when the rover's site underwent a series of peaks (in particular around sols 430 and 580) in the amount of airborne dust in the atmosphere (figure 7.9b). This dust, if settled on the calibration targets, could be expected to perturb significantly the measured radiance of the clean spots, and hence the fits, given that our reflectance model (described in section 5.3) did not include any correction to the reference reflectances for dust. However, figure 7.1 shows that even during the dust storm season (after sol 350) the trends of data points of most narrow-band filters follow approximately the same spectral dependence with the irradiance that was observed in the first 350 sols, when the northern summer ensured a fairly nice stability. The time-derived irradiance series shows changes in correspondence of the variations in the atmospheric optical depth, suggesting that the calibration targets were not affected significantly by dust, but our model was able to describe the effects of dust on the irradiance. In addition, the solar irradiance spectrum around the aphelion (figure 7.3) was quite consistent with a solar black body model allowing for some atmospheric absorption, in particular at short wavelengths. All these considerations bring to the conclusion that the calibration targets and our calibration model were successful in achieving their main goal. The principal reason probably comes from the design of the targets, especially the primary and the position of the regions employed for calibration, the clean spots. The permanent strong magnets, with a shape that encircles completely the clean spots, attracted most airfall dust and maintained the clean spots protected and fairly free from dust over time, as witnessed by the irradiance derived time series mentioned above. Moreover, the higher number of round patches in the primary target, with respect to the previous missions, was extremely advantageous when we implemented the exclusion of the white patch from the calibration procedure, because the latter could still rely on other seven clean spots that did not show any unexpected behavior.

One of the steps of the reflectance calibration procedure is the careful visual check of the linear fits in all filters of the calibration target sequence that is being processed. This check is critical to verify the quality of the fits and spot any significant outliers in the data points, in order to identify unexpected behaviors. It is through this systematic control that we noticed the presence of the small offset in the data points (figure 7.10), suggesting that some unexplained mechanism was acting on the measured radiance of the clean spot by slightly reducing the "real" slope of the data points and adding a small offset, thus implying that the two-term model might follow the observed data better. As explained in section 7.3, although the two-term model was never used or implemented in the reflectance calibration on Mars, I investigated it by applying it to the actual data of the RC files from Mars, with the aim of understanding the origin and evolution of such an offset. From a statistical point of view, adding an offset to the linear fit model improved substantially χ^2_{red} by a factor of more than 10, passing from the 43.54 of the one-term model to 4.51 in L4 (605 ± 9 nm) and from 13.56 to 1.27 in R5 (978 ± 10 nm), with the overall narrow-band average dropping from 28.60 to 2.28. Nevertheless, not replacing such a statistically better model to the solid one-term fit model was justified by the fact that, in the first martian year of Perseverance, we did not comprehend the nature of the offset in a fully convincing way. Some hypotheses were suggested within the Mastcam-Z team and are still the most credited. For example, the offset might come from computational sources, which means that it is a residual of the radiance-calibration process when the corrections (e.g., bias frames, flat fields, shutter frame subtraction) are applied to the raw images. If this explanation is true, all Mastcam-Z images should contain the residual, which could be computed through the two-term approach and removed. Another reason may be some discrepancy in the reflectance model that I developed (section 5.3), which computes the reference reflectance of each color and grayscale material under any illumination geometry. Indeed, the routines that are devoted for this task are based on the rounding of the angle triplets and on spline interpolations (and in some cases extrapolation) of reflectance factor values over missing angular ranges up to 15°. In case this is an impactful source of the offset, the best solution would be to perform a new complete characterization of the eight witness samples of the calibration targets (plus the Spectralon) using a similar spectrogoniometer to those of Bern or Copenhagen, with spectral steps of 1 nm and angular sampling of no more than 1° in incidence, emission and azimuth angles.

One of the external sources of the offset, especially for its increasing trend in time, is dust. Airfall dust deposits (and actually deposited) on all the surfaces of the rover's deck, and in particular on the calibration targets. The images in figure 6.2 and the spectra in figure 7.8 showed that a considerable amount of dark, large-grained, magnetic dust accumulated on the magnet rings of the primary target, but I expected that some minor fraction of weakly or even non-magnetic, fine-grained dust would fall and adhere electrostatically on the clean spots such that it could not be swept by wind interaction, altering slightly their measured radiance. For instance, the effect of dust on the regions of interests for calibration was already observed in the previous rover missions (see figure 2 from Kinch et al., 2015, for the Spirit rover), where the data points in the radiance-reflectance plots displayed a clear offset due to dust. The fact that the offset was not observed during the tests at ATLO (figure 5.19) but it was present in the first calibration target sequences shortly after landing pushes in this direction. During landing, while the rover was being dropped on the surface by the sky crane, the latter raised a lot of dust over the rover with its retro-rockets, as witnessed by figure 6.5. This event might have been the first "shock" for the rover on Mars, on which dust kept depositing in the first 670 sols, giving the offset time series the gradually and linearly increasing trend that it shows in figure 7.12.

All the arguments of uncertainty treated above are plausible theories that could potentially be, together, at the source of the offset in the fits. The most exhaustive evidence points towards a significant contribution by dust, and therefore a deeper investigation is required not only to understand the other causes, but also to study the properties of the different populations of this dust. As Mastcam-Z Calibration Working Group, we decided not to change the way we perform the reflectance calibration for two reasons. Firstly, not knowing for sure the cause of the issue could affect systematically all the other Mastcam-Z images (especially the multispectral sequences) that we calibrate, for causes that are only due to the calibration targets and not to the way images are calibrated to radiance, with the risk of introducing unwanted artifacts in the pixels, and hence in the reflectance spectra. Secondly but not less importantly, our calibration procedure, the one-term model and the reflectance model proved to be well performing in the first 670 sols. Whereas it is true that the addition of an offset improved the statistics, the one-term model (that follows the theoretical approach) achieved small deviations between the measured data points and the fits, as confirmed also by the high quality of the hundreds of reflectance spectra of rocks and minerals obtained during the mission.

9.2 Dust assessment

The martian dust interacted both directly and indirectly with our measurements of the calibration targets during the first 670 sols. Sooner or later, all surfaces of the rover were covered in a more or less thick blanket of dust, which gave the rover the typical reddish color. The airfall dust that deposited within the ROIs of the calibration targets contributed to change the measured radiance according to the optical thickness of the dust layer. As I stated in the previous section, dust did not affect our ability to perform calibration, though some light, fine-grained dust might have fallen in the clean spots. I could recognize light patterns of fine dust on the grayscale rings, that were partially protected by the magnet rings, and on the deck around the primary target thanks to the light/dark-toned contrast. On the deck and on the secondary horizontal target the accumulation and variation in the dust patterns were probably ruled by the wind and possibly by the vibrations caused by the motion of the rover. Moreover, I find the "dust skid mark" on the gnomon (figure 7.5) very interesting. The gnomon was already covered by a an almost unperceivable dust layer in the first 400 sols, but the appearance of such a net stripe just before sol 400 (when the first dust storm of the northern winter began) and its partial erasure around sol 650 (in the aftermath of the second dust storm of the northern winter) likely points towards the occurrence of some phenomenon that led the dust of the storms to adhere in that peculiar position.

Over the course of the first 670 sols, the magnets attracted a considerable amount of dust (figure 6.2), which formed a thick brownish-red build-up that made it impossible to discern the color of the patch underneath (figure 6.7c). The spectra of the dust in the magnet rings after one martian year (figure 7.5d) are consistent with previous observations of martian dust attracted to permanent magnets (Madsen et al., 2009). They have a very low reflectance factor in the ultraviolet and blue bands, a characteristic rise from green to red consistent with the presence of ferric iron, and a higher reflectance factor in the red and infrared bands, as expected. At the same time, the spectra appear darker than a typical spectrum of martian bright dust. In fact, this magnetically attracted material is expected to be richer in magnetite and with larger average grain size (Kinch et al., 2006). In general, the magnetic dust increased the reflectance of the darker materials and decreased that of the brighter materials, squeezing all the other colors until convergence. In the near infrared band the spectra are more separated than at the short wavelengths, implying that at the longer wavelengths the magnetic dust is less optically thick. In order to have a deeper understanding, it would be interesting to investigate this magnetic dust differently. For instance, for each primary round patch, instead of selecting the whole magnet ring one could draw a number of concentric ROI selections within the area of the magnet ring at different radii from the center of the patch. This would probably give insights on the optical thickness and density of the dust layer along the radius of the magnet. I would expect a priori to find the dust pile to have approximately a wide gaussian shape along the radial section, but a significant skewness may indicate a preferential wind direction that could be compared with data from the MEDA instrument. In addition, this experiment can be integrated with images from the Remote Micro Imager of SuperCam, which provides a very high resolution (the images in figure 6.7 allow to perceive dark grains and small dust aggregates).

For what concerns the indirect effects of dust, the most important one is the variation of the direct fraction F_d of sunlight on the calibration targets, that is illustrated in section 7.2.3. I already noticed that the derived irradiance time series (figure 7.1) showed some degree of susceptibility to the change in the amount of airborne dust in the atmosphere, because more suspended dust leads to a reduced irradiance. Even before making the plot of the atmospheric optical depth of figure 7.9b, I was able to identify dust events in the changes and sudden peaks or drops of the measured solar irradiance. When processing together the radiances of illuminated and shadowed regions of the grayscale rings and retrieving the direct fraction F_d of sunlight, the rough inverse correlation with the atmospheric optical depth τ_I became even more evident (figure 7.9). Every rise in the density of dust in the atmosphere was followed by an enhancement of the diffuse illumination, reducing the contrast between lit and shaded regions and therefore the solar irradiance and the direct fraction of sunlight. In this scope, the parameter F_d introduced by Kinch et al. (2007) revealed to be a powerful tool when applied to the data from the RC files of Mastcam-Z, being able to predict the situation of the atmosphere before the availability of the optical depth data. Such a tool could be used for several potential analyses covering the nature of airborne dust (helped by the imaging and spectra of the deposited dust that I mentioned above) and its interaction with wind and light, including the development of a dust radiative transfer model or the dynamics of dust transported by the wind within Jezero.

In the reflectance calibration of Pancam images from the Spirit and Opportunity rovers, the large quantity of dust that piled up on the regions of interest of their calibration targets, that were not sufficiently shielded by the magnets, added considerable perturbations in the linear fits and forced the MER team to adopt a dust model (described in Kinch et al., 2015). The model received some parameters related to dust, such as the optical depth of the deposited dust layer and the single-scattering albedo (computed over several sols) of those dust particles, and performed a correction to the reference reflectance factor of the color materials of the calibration targets. After 670 sols and 346 sequences of the Mastcam-Z calibration targets (and at least three acute dust events), I can assert that the design of the primary target prevented the clean spots from being covered in a concerning dust blanket, unlike the MER rovers, as confirmed by the goodness of the fits, the consistency of the irradiance time series and the visual inspection. As a result, I do not contemplate the need for a similar dust model for the calibration of Mastcam-Z. Of course, this does not mean that the camera will never require a dust correction, but the data at our disposal from the first martian year of Perseverance clearly display once again that the calibration targets were not vigorously impacted by the dust activity, or at least not to the point of considering to change the way we perform the reflectance calibration.

9.3 The calibration anomalies in the low-Sun observations

In section 8.4 I pointed out that in some observations characterized by a high incidence angle on the calibration targets, the corresponding calibrated multispectral sequences were affected by anomalies in the spectra of the selected regions of interest. The number of sequences that required an accurate inspection was very modest and therefore the issue did not raise particular concerns. Many of those cases regarded the calibration targets illuminated under a high incidence angle and high amount of airborne dust. As mentioned in the previous section, dust can diffuse light well when the Sun is low, and this does not cause only a drop in the direct fraction of sunlight, but also an increase in the measured radiance, which will account for direct+diffuse light and will yield the irradiance spectra of figure 8.10. The reflectance model that we employed is directional, which means that it does not take into account the diffuse illumination coming from the sky. Some other cases of spectral anomalies are related to the complete difference between the illumination geometries of the two targets, especially when the illuminated face of the rock is perpendicular to the ground. In these cases, when the Sun was low on the horizon the scientific target was lit frontally, and sometimes the spectra presented oddities. However, when the Sun was close to the zenith and the ROIs were drawn on the vertical face of a rock, the spectra were rarely affected. All this information led me to a few possible solutions according to the specific case. One could be to perform the calibration using a different calibration target sequence. This method was tested in a few cases when the Sun was low on the horizon and some ROIs within the multispectral sequence were placed on rocks almost perpendicular to the surface. The re-calibrated IOF were not included in the official NASA PDS (Planetary Data System) releases, but their spectra showed improvements and some anomalies disappeared. The outcome was expected, because a primary calibration target illuminated from directly above would be more consistent with the vertical surface of a rock lit frontally. This method, which should be considered as a provisional patch, should only be used when a suitable calibration target sequence is available from a very close sol to that of the multispectral sequence, in order to maintain some degree of consistency in the atmospheric conditions. In addition, the effects of diffuse illumination between the two sequences (calibration targets with high Sun, multispectral target with low Sun) would be slightly different, and hence the resulting spectra will not account for this difference.

The second method, which would probably be valuable when the Sun is low and the multispectral target is not illuminated frontally, is a model that I developed and that could be expanded and implemented in the future. The model is based on the fact that in the linear fits used for calibration the radiance of the clean spots is the sum of direct sunlight and diffuse illumination from the sky, while the gnomon's shadow only contains information on the diffuse illumination. The reference reflectances computed by our reflectance model are only referred to direct light, and therefore the aim of my model is to provide a correction for those reference reflectances in order for them to also account for the diffuse illumination. The model is fairly accurate but has some limits, such as the fact that it is only applicable when the ROIs in the gnomon's shadow are selected. A thorough step-by-step description of the model is given in appendix B.

As a further option, the calibration could be aided by accurate stereo terrain models. By employing those models, each pixel of the images would contain information on the surface of the geologic target which is represented by that pixel, such as the normal vector to the surface. It would allow for a separate $\cos i$ correction for each pixel, giving the chance to solve this kind of challenges.

9.4 The yellowing of the AluWhite98

The decline of the AluWhite98 patches at the shorter wavelengths is an intriguing puzzle that is worth a much deeper investigation. I analyzed the issue, kept monitoring the visual and the spectral trend of this material, but I was not yet able to identify a root cause for the yellowing. The fact that the white is the only material affected and is manufactured by a different company than the others (Avian Technologies and Lucideon, respectively) leads to the conclusion that the material itself or its production process must enclose the source of the effect. Likewise, the different kinds of epoxy used for the patches (that show the yellowing) and the rings (not affected, or to a very limited extent) would address us towards the way the white patches were glued to their supports. The experiments carried out on the AluWhite98 chips at the Winnipeg University (section 7.4.1), which involved ultraviolet irradiation, did not reproduce the visible, radiometric, and spectral outcomes of the in-flight materials. The UV irradiation simulating 4140 equivalent months on Mars caused some decrease in the spectra of the white chips, which was not sufficient to emulate the decline of sol 12. However, if I consider the yellow spot that came out on one of the chips after this phase (figure 7.15), which was likely caused by an unexpected leak of epoxy inside the chip or by a little contamination of epoxy with a glove during the preparation of the test unit, I see that its spectrum gets much closer to that measured on Mars. Therefore, the "best" result that emerged from the experiment was reached after an intense irradiation of the samples (4140 month equivalent, which is 345 years), while the yellowing on Mars was already more marked after only 12 sols. The issue remains currently unsolved, though the experiment showed that the direction was probably correct, but more factors other than UV light might be critical to reproduce the observations. A plausible explanation could include UV light, epoxy, porosity and impurities of the material (at molecular level), as well as intense space weathering (i.e., cosmic rays and solar wind) and dust. Further investigation could find an answer to this open question, and this would be an essential support for other teams (the white patch of the SuperCam calibration target showed a similar behavior) and provide a useful reference for the manufacturing companies and for scientists in the design of new calibration targets for the cameras of planetary missions.

Chapter 10

Conclusion and future work

On February 18^{th}, 2021 the NASA rover Perseverance successfully landed on Mars, and since then it has been performing activities of exploration and scientific analysis of its geologic location, the crater Jezero. Perseverance's investigation can rely, among the instruments of its payload, on Mastcam-Z, a multispectral stereoscopic camera capable of zooming, which helped the rover carry out important scientific assessments. The radiometric calibration of Mastcam-Z is made through a set of calibration targets. In this thesis I described the work that I carried out before the landing of Perseverance, which involved the design of a suitable reflectance procedure to convert the radiance-calibrated images of Mastcam-Z to units of IOF or R*, and the scientific analysis on the quantitative and qualitative data that were extracted from the images of the calibration targets over the first 670 sols on Mars.

The tests on the different methods of calibration (the standalone calibration) led me to determine that the linear fits with only one multiplicative term (the one-term model) constituted the simplest method, which was closest to the theoretical approach, for the making of reflectance-calibrated products. The reflectance model that I developed, which is based on three routines that handle the measurements from the laboratories of Bern and Copenhagen, was implemented in the calibration pipeline of Mastcam-Z before the landing of Perseverance and worked correctly by ensuring a high quality of calibration over the whole time range covered by this work. Such a quality was also promoted by the design of the primary target, more specifically the shape and position of the round color and grayscale patches and the underlying permanent strong magnets, which prevented the large-grained magnetic dust from accumulating within the central portions of the patches (the clean spots), as confirmed by the limited dispersion of the data points around the fit line and the relatively small uncertainties on the slopes of the fits.

The time series of the derived solar irradiance showed a smooth stability in the first 315 sols, after which the martian winter in the northern hemisphere gave rise to the dust storm season, where the varying amount of dust suspended in the atmosphere caused changes and sudden drops in the irradiance. However, such dust events did not affect our ability to perform the calibration, mainly thanks to the magnets. Similar trends were observed also on the grayscale rings and on the vertical and horizontal tiles of the secondary target. Although the calibration approach was not perturbed, I noticed frequent variations in the dust patterns on the calibration target surfaces and the deck of the rover, where the wind activity deposited thin layers (which even stuck to vertical sides) and larger sand grains and swept them away over timescales of a few sols. Most of this airfall dust piled up on the external portions of the primary patches, where it was attracted by the strong underlying magnets. Already after just 200 sols, the color of the patches under the dust was almost indiscernible. My analysis of the reflectance spectra for these dusty regions revealed that this magnetic dust was darker than the typical bright martian dust and likely made of larger grains. The spectra of magnet rings converged towards a reddened dust spectrum with low reflectance in the blue band and high reflectance in the red and infrared bands, involving the brightening of the darker patches and darkening of the brighter patches. In addition, I studied the time series of the direct fraction of sunlight on the grayscale rings and I found a rough inverse correlation with the measured atmospheric optical depth. Because the latter was principally ruled by airborne dust, I could conclude that the radiance measurements on those specific regions of the primary target provided precious information on the conditions of the martian atmosphere and that the computation of the direct fraction of sunlight was a powerful tool in this scope.

The tests on the two-term fit model on the measured radiances of the clean spots in the first 670 sols presented better statistical outcomes, with smaller slopes than the one-term model and small offsets. Even though the origin of the offset has not been exhaustively explained yet, the parallel study that I carried out clearly pushes towards a dusty nature. While most dust is attracted by the magnets, a small fraction made of finer and non-magnetic dust has been falling on and sticking to the clean spots. My conclusion is that this slow but fairly linear accumulation generated the offset of the data points detected in the plots of the linear fits (probably upon or immediately after landing) and has been growing linearly.

Finally, I did not find any plausible interpretation or evidence for the yellowing of the AluWhite98. The different manufacturer from the other materials suggested that it could be related to the particular way of production, and then the different kind of glue used for the white grayscale ring, where the effect was not observed, led me to consider the epoxy as a probable cause. However, the tests performed in Winnipeg on the samples which I prepared in the laboratory did not satisfyingly reproduce the observed behavior of the white material on Mars.

In the first 670 sols on Mars, the rover Perseverance performed cutting edge scientific research. It explored the floor of the crater Jezero close to its landing site, it traveled more than 14 km, and it is starting its climb to the delta of the crater, in order to reach the crater rim and the terrains outside. In addition, it completed the delivery of the first contingency rock samples, and the helicopter Ingenuity flew 38 times. The performance of Mastcam-Z calibration targets is positive, and will assist Mastcam-Z in the production of high quality reflectance calibrated data for the assessment of the terrains it will encounter in the future.

10.1 Future projects

The topics presented in this research work contain several open questions that can be developed in the form of projects, for example for a master thesis or a PhD. As I stated in the introduction, this thesis will act as a "guide" on the reflectance calibration of Mastcam-Z for the future calibrators, and therefore the main long-term task will be to provide the Perseverance and Mastcam-Z Teams with a human reference for any question or concern from Team members of other Working Groups whose data and analysis are based on reflectance-calibrated Mastcam-Z images. In addition, the future person(s) of contact for calibration will have the possibility to keep monitoring the time series shown here, such as the irradiance, the direct fraction of sunlight, the two-term offset, and the AluWhite98, from the data documented in the RC files.

The potential projects are listed as follows.

- **The two-term fits**. I proposed some possible causes (dust is the most likely), but knowing the precise influence of each one on the measurements would be extremely useful, because the two-term model might be implemented in the future, according to the outcome of such an analysis.

- **Deposited and airborne dust**. As I mentioned in section 9.2, the dust on the magnets could be inspected in more detail by selecting more than one concentric region inside the magnet ring, in order to show how magnet dust accumulates on those areas. This observation could be integrated by the images from SuperCam, in which different dust aggregates can be separated. The ultimate aim for this project would be to determine whether a dust model should be implemented as in Kinch et al. (2015). In second place, it would be interesting to investigate the suspended dust by making a model of radiative transfer of dust starting from the data of the direct fraction of sunlight on the grayscale rings.

- **The low-Sun observations**. Although the number of low-Sun observations that produced flaws in the calibrated sequences was low, it is worth studying the issue further. In this scope, the correction model that I developed in appendix B can be put into code, tested, improved, and possibly implemented.

- **The AluWhite98**. The yellowing effect is an open question that requires a deeper investigation. The tests in Winnipeg were only limited to UV irradiation, but there may be other physical phenomena that were not considered and might be tested in the laboratory or modeled, such as sputtering due to the solar wind.

Index of acronyms

APXS	Alpha Particle X-Ray Spectrometer
ASU	Arizona State University
ATLO	Assembly, Test and Launch Operations
AU	Astronomical Unit (1 AU = 149597871 km)
CCD	Charged Coupled Device
CheMin	Chemistry and Mineralogy Suite
CNSA	China National Space Agency
CRISM	Compact Reconnaissance Imaging Spectrometer for Mars
CSV	Comma-Separated Value
CTX	Context Camera
DAN	Dynamic Albedo of Neutrons
DCS	Decorrelation Stretch
DTU	Danmarks Tekniske Universitet
EDL	Entry, Descent and Landing
ESA	European Space Agency
FWHM	Full Width at Half Maximum
Ga	Giga-year ago (10^9 years ago)
GSFC	Goddard Space Flight Center
Hazcam	Hazard avoidance Camera
HiRISE	High Resolution Imaging Science Experiment
HRSC	High Resolution Stereo Camera
IOF	I/F, radiance over irradiance
IR	Infrared
ISRO	Indian Space Research Organization
ISWEEP	Improved Sweep Magnet Experiments
JHU-APL	Johns Hopkins University Applied Physics Laboratory
JPL	Jet Propulsion Laboratory
LATMOS	Laboratoire Atmosphères, Observations Spatiales
LIBS	Laser-Induced Breakdown Spectroscopy

LMST	Local Mean Solar Time
LPSC	Lunar and Planetary Science Conference
MAHLI	Mars Hand Lens Imager
MARCI	Mars Color Imager
MARDI	Mars Descent Imager
MAV	Mars Ascent Vehicle
MAVEN	Mars Atmosphere and Volatile Evolution
MC	Million Concepts
MSSS	Malin Space Science Systems
MEDA	Mars Environmental Dynamics Analyzer
MER	Mars Exploration Rovers
MIMOS II	Miniaturized Mössbauer Spectrometer
Mini-TES	Miniature Thermal Emission Spectrometer
MIT	Massachusetts Institute of Technology
MMRTG	Multi-Mission Radioisotope Thermoelectric Generator
MOLA	Mars Orbiter Laser Altimeter
MOXIE	Mars Oxygen In-situ Resource Utilization Experiment
MRO	Mars Reconnaissance Orbiter
MSL	Mars Science Laboratory
NaN	Not a Number
NASA	National Aeronautics and Space Administration
Navcam	Navigation Camera
MAHLI	Mars Hand Lens Imager
OEB	Octavia E. Butler
PCA	Principal Component Analysis
PDL	Payload Downlink Lead
PDS	Planetary Data System
RAD	Radiation Assessment Detector
RC file	Radiometric Coefficient file
REMS	Rover Environmental Monitoring Station
RGB	Red/Green/Blue
RIMFAX	Radar Imager for Mars' SubsurFAce eXperiment
RMI	Remote Micro-Imager
RMSE	Root-Mean-Square Error
ROI	Region of Interest
RPFA	Rover Pyro Firing Assembly
SAM	Sample Analysis at Mars

Sci-fi	Science-fiction
SHERLOC	Scanning Habitable Environments with Raman and Luminescence for Organic and Chemicals
SOX	Surface Operation Transition
SSI	Space Science Institute
SSI	Surface Stereo Imager
Stereo-DTM	Stereoscopic Digital Terrain Model
TGO	Trace Gas Orbiter
TVAC	Thermal Vacuum Chamber
UAV	Unmanned Aerial Vehicle
UHF	Ultra-High Frequency
ULA	United Launch Alliance
USA	United States of America
USGS	United States Geological Survey
USSR	Union of Soviet Socialist Republics
UTC	Coordinated Universal Time
UV	Ultra-violet
VR	Virtual Reality
WATSON	Wide Angle Topographic Sensor for Operations and eNgineering
WWU	Western Washington University

List of Mastcam-Z calibration target figures on Mars

In the next couple of pages I list all the images of the Mastcam-Z calibration targets acquired on Mars and shown in the figures of this thesis. For each image, the following information is given:

- Image ID: the name of the image file, without the extension, which can be used to retrieve the image in the online NASA database (Planetary Data Survey). The image ID contains a series of letters and digits expressing useful basic information[1].
- Sol: the martian day (sol) on which the image was acquired.
- Instrument: the instrument from the Perseverance rover that took the image. Most images were acquired by Mastcam-Z, but the calibration targets were also imaged by the WATSON camera of SHERLOC and the Remote Micro Imager of SuperCam.
- Eye: if the image was captured by Mastcam-Z, it specifies which eye (left or right) was used.
- Filter: if the image was captured by Mastcam-Z, it is the name of the spectral filter through which the image was taken.
- Sequence ID: the code identifying the original sequence of which the image is part.
- Zoom: if the image was captured by Mastcam-Z, the focal length used to acquire the image (in mm).
- Figure in text: the number of the figure in this thesis that shows the image.
- Color balance: if the image was captured by Mastcam-Z, it specifies the lower and higher thresholds employed for the red (R), green (G) and blue (B) channels (or the grayscales) to display the image in this thesis.

[1] The Mastcam-Z online blog provided a simple guide on how to decipher the filenames of Mastcam-Z images at https://mastcamz.asu.edu/decoding-the-raw-publicly-released-mastcam-z-image-filenames/

Image ID	Sol	Instrument	Eye	Filter	Sequence ID	Zoom [mm]	Figure in text	Color balance
ZL0_0180_0682919878_394RAD_N0062666ZCAM03014_048085A01	180	Mastcam-Z	Left	L0 (Bayer RGB)	ZCAM03014	48	4.4	R=[0.00458944, 0.169932], G=[0.00531645, 0.161903], B=[0.000918062, 0.146524]
ZL1_0069_0673052731_973IOF_N0032208ZCAM03014_048085A03	69	Mastcam-Z	Left	L1 (800 nm)	ZCAM03014	48	6.1	Grayscale=[0.030484, 0.814523]
ZL0_0065_0672707348_318IOF_N0032046ZCAM03014_048085A03	65	Mastcam-Z	Left	L0 (Bayer RGB)	ZCAM03014	48	6.2a	R=[0.0340445, 1.04816], G=[0.0278293, 0.944407], B=[0.00840683, 0.905195]
ZL0_0319_0695259284_613IOF_N0090000ZCAM03014_048085A01	319	Mastcam-Z	Left	L0 (Bayer RGB)	ZCAM03014	48	6.2b	R=[0.0258940, 0.907286], G=[0.0317297, 0.803857], B=[0.0101724, 0.778669]
ZL0_0477_0709276822_069IOF_N0260850ZCAM03014_048085A01	477	Mastcam-Z	Left	L0 (Bayer RGB)	ZCAM03014	48	6.2c	R=[0.0359108, 0.974316], G=[0.0306170, 0.907738], B=[0.00715136, 0.935054]
ZL0_0670_0726416844_769IOF_N0320580ZCAM03014_048085A02	670	Mastcam-Z	Left	L0 (Bayer RGB)	ZCAM03014	48	6.2d	R=[0.0329261, 0.905954], G=[0.0219674, 0.756075], B=[0.0112178, 0.693263]
SIF_0026_0669252912_124FDR_N0030792SRLC07009_0000LUJ02	26	SHERLOC			SRLC07009		6.6a	
SIF_0368_0699610141_460EBY_N0110108SRLC07009_0000LMJ01	368	SHERLOC			SRLC07009		6.6b	
SIF_0545_0715335394_492EBY_N0265150SRLC07008_0000LMJ01	545	SHERLOC			SRLC07008		6.6c	
LRF_0080_0674037938_567EBY_N0032430SCAM03080_0390I6J01	80	SuperCam			SCAM03080		6.7a	
LRF_0080_0674038241_466EBY_N0032430SCAM03080_0380I6J01	80	SuperCam			SCAM03080		6.7b	
LRF_0541_0714960133_010EBY_N0263008SCAM01541_0370I6J01	541	SuperCam			SCAM01541		6.7c	
ZL0_0084_0674397938_318IOF_N0032430ZCAM03014_048085A03	84	Mastcam-Z	Left	L0 (Bayer RGB)	ZCAM03014	48	7.4a	R=[0.0241524, 1.04533], G=[0.0208030, 0.964634], B=[0.00855688, 0.977758]
ZL0_0130_0678477333_428IOF_N0042222ZCAM03014_048085A03	130	Mastcam-Z	Left	L0 (Bayer RGB)	ZCAM03014	48	7.4b	R=[0.0286324, 1.03245], G=[0.0307443, 0.938419], B=[0.0122007, 0.910590]
ZL0_0280_0691789725_081IOF_N0080064ZCAM03014_048085A02	280	Mastcam-Z	Left	L0 (Bayer RGB)	ZCAM03014	48	7.4c	R=[0.0154447, 1.02114], G=[0.0221612, 0.913167], B=[0.0111794, 0.852205]
ZL0_0318_0695174407_428IOF_N0090000ZCAM03014_048085A01	318	Mastcam-Z	Left	L0 (Bayer RGB)	ZCAM03014	48	7.4d	R=[0.0337273, 0.727339], G=[0.0313477, 0.654874], B=[0.0108279, 0.690909]
ZL0_0357_0698636542_223IOF_N0099314ZCAM03014_048085A02	357	Mastcam-Z	Left	L0 (Bayer RGB)	ZCAM03014	48	7.4e	R=[0.0248516, 0.853833], G=[0.0224211, 0.779965], B=[0.00432382, 0.750780]
ZL0_0473_0708929908_410IOF_N0260756ZCAM03014_048085A01	473	Mastcam-Z	Left	L0 (Bayer RGB)	ZCAM03014	48	7.4f	R=[0.0348209, 1.35683], G=[0.0299229, 1.05530], B=[0.00597129, 0.839913]
ZL0_0596_0719851262_285IOF_N0300000ZCAM03014_048085A01	596	Mastcam-Z	Left	L0 (Bayer RGB)	ZCAM03014	48	7.4g	R=[0.0363992, 0.846615], G=[0.0235048, 0.744481], B=[0.00533550, 0.766824]
ZL0_0662_0725705245_928IOF_N0320378ZCAM03014_048085A01	662	Mastcam-Z	Left	L0 (Bayer RGB)	ZCAM03014	48	7.4h	R=[0.0323654, 0.833203], G=[0.0222974, 0.702266], B=[0.00668008, 0.627028]
ZL0_0608_0720918859_348IOF_N0301096ZCAM03022_100085A01	608	Mastcam-Z	Left	L0 (Bayer RGB)	ZCAM03022	100	7.5	R=[0.0482621, 0.826837], G=[0.0412697, 0.721468], B=[0.0235769, 0.737473]

ZL0_0023_0668983099_910IOF_N0030770ZCAM03003_1000LMA01	23	Mastcam-Z	Left	L0 (Bayer RGB)	ZCAM03003	100	7.6, 7.7	R=[0.0257723, 1.04884], G=[0.0244602, 0.999683], B=[0.0257723, 0.986472]
ZL0_0016_0668361623_818IOF_N0030386ZCAM03002_0480LMA01	16	Mastcam-Z	Left	L0 (Bayer RGB)	ZCAM03002	48	7.14a	R=[0.00235123, 1.01942], G=[0.00235123, 0.971491], B=[0.00235123, 0.941215]
ZL0_0157_0680877265_410IOF_N0052512ZCAM03014_048085A03	157	Mastcam-Z	Left	L0 (Bayer RGB)	ZCAM03014	48	7.14b	R=[0.0273084, 1.02947], G=[0.0280545, 0.923135], B=[0.00706991, 0.898831]
ZL0_0435_0705555022_785IOF_N0243290ZCAM03014_048085A01	435	Mastcam-Z	Left	L0 (Bayer RGB)	ZCAM03014	48	7.14c	R=[0.0279944, 0.869295], G=[0.0228704, 0.789007], B=[0.00789258, 0.736778]
ZL0_0669_0726335065_144IOF_N0320580ZCAM03014_048085A01	669	Mastcam-Z	Left	L0 (Bayer RGB)	ZCAM03014	48	7.14d	R=[0.0337000, 0.832936], G=[0.0216123, 0.751736], B=[0.00784025, 0.714574]
ZL0_0353_0698291918_069IOF_N0096884ZCAM03014_048085A01	353	Mastcam-Z	Left	L0 (Bayer RGB)	ZCAM03014	48	8.10	R=[0.00792418, 0.428131], G=[0.00768858, 0.428376], B=[0.000830057, 0.457352]
ZL0_0385_0701128893_318IOF_N0140000ZCAM03014_048085A01	385	Mastcam-Z	Left	L0 (Bayer RGB)	ZCAM03014	48	8.10	R=[0.0162608, 1.07682], G=[0.0141283, 0.878936], B=[0.000936258, 0.705129]
ZL0_0387_0701309988_598IOF_N0150000ZCAM03014_048085A01	387	Mastcam-Z	Left	L0 (Bayer RGB)	ZCAM03014	48	8.10	R=[0.00702525, 0.368936], G=[0.00652985, 0.377980], B=[0.00323547, 0.467861]
ZL0_0236_0687908158_488IOF_N0072050ZCAM03014_048085A02	236	Mastcam-Z	Left	L0 (Bayer RGB)	ZCAM03014	48	8.11	R=[0.00582893, 0.511640], G=[0.00773381, 0.498659], B=[0.00133214, 0.479914]

Appendices

Appendix A

The Radiometric Coefficient files

The Radiometric Coefficient files (or RC-files) are second-order products obtained from the elaboration of Mastcam-Z radiance-calibrated calibration target images (see section 6.3). In the following I provide a detailed legend of each line in a standard RC file, which includes the name of the line (starting with the character "#"), the type of data (in square brackets) and the description of the data contained in that line. Subsequently, an example of a RC file is shown for sol 669 in filter L1 (800 nm) on page 166. The words "calibration targets" are shortened as "cal-target".

`# responsivity constants file` [string]
Full-path filename of this file when it was created.

`# associated selection filename` [string]
Full-path filename of the selection file used to generate these responsivity constants.

`# dust correction` [string]
Dust correction model used when generating responsivity constants.

`# outliers excluded from selections` [string]
Are "outliers" excluded from selection regions when generating the responsivity constants? There is currently a very strict algorithm defining outliers to be excluded. It is designed to exclude hot pixels and the like that may be included in a selection. It is NOT meant to be used to ignore inadvertently selected shadows or otherwise bad selections. The algorithm operates as follows: exclusion is determined on a per-channel basis. Histogram the pixel values into 11 bins of equal value range from the minimum value to the maximum value. Find any outlier bins (bins that are separated from the main cluster of values by one or more empty bins). Any values in these outlier bins are considered to be outlier values. If the total number of outlier values is ≤ 10, the mean selection value will be computed excluding these outlier values. NOTE: If the number of outlier values is > 10, the values will not be excluded, instead the user will be warned of this condition (which usually indicates a faulty selection), and prompted to correct it before saving the responsivity constants.

`# force fit to intercept origin` [string]
Fit line is forced to go through the point [0,0].

`# RC file creation time` [string]
Timestamp of when this file was created.

`# RC file format version` [string]
File format version.

#
`cal-target file` [string] Full-path or relative-path filename of the RAD-calibrated cal-target file used to generate these responsivity constants.
`unique sequence identifier` [string] Unique identifier of the cal-target sequence from which these responsivity constants were generated.
`local true solar time` [string] LTST of the cal-target image.
`solar azimuth (rover frame)` [float] Solar azimuth in rover frame at time of cal-target acquisition.
`solar elevation (rover frame)` [float] Solar elevation in rover frame at time of cal-target acquisition.
`fit method` [string] Method used to fit a line to the selection values. Possibilities are: - `use_only_chip_centers`; - `use_all_sunlit_regions`: chip centers + sunlit rings; - `use_only_sunlit_rings`; - `use_all_rings`: sunlit rings + ring shadows; - `use_all_regions`: chip centers + sunlit rings + ring shadows.
`ROI names` [string array] Names of all regions.
`ROI is selected` [boolean array] 1 if a selection exists for the corresponding named region, else 0.
`ROI marked bad` [boolean array] 1 if a selection for the corresponding named region has been marked bad and is not used in the fit, else 0: the selection is allowed to be used in the fit.
`ROI used in fit` [boolean array] 1 if a selection for the corresponding named region IS used in the fit, else 0: the selection for this region is not used in the fit. Will be 0 if there is no selection for the corresponding region.
`ROI radiances` [float array] Mean of USED values in each selected region - regions with no selection will have NaN.
`ROI uncertainty` [float array] Standard deviation of USED values in each selected region - will be NaN if no selection.
`ROI count` [integer array] Number of USED pixels in each selected region.
`ROI incidence angle` [float array] Angle between the vector from the region to the Sun and region surface normal for each region.
`ROI emission angle` [float array] Angle between the vector from the region to the detector and the region surface normal for each region.
`ROI azimuth angle` [float array] Angle in the plane of the region surface between the vector from the region to the Sun and the vector from the region to the detector.
`reflectances` [float array]

Calculated reflectance for each region. NaN if there is no selection or no lab reflectance model for the region.
`# camera id, filter number, rad-to-iof scaling factor, uncertainty` [four float values] Camera ID, filter number, calculated rad-to-iof scaling factor, uncertainty in the scaling factor.

Example of RC file - sol 669, filter L1 (800 nm)

```
# responsivity constants file: /scratch/cal_wg/flight/products/0669/rc_files/rc_ZL1__0726335056_0320580ZCAM03014_1.txt
# associated selection filename: /scratch/cal_wg/flight/products/0669/rc_files/Z00669_0320580ZCAM03014_048035571_FO1.sel
# dust correction: none
# outliers excluded from selections: Yes
# force fit to intercept origin: Yes
# RC file creation time: 2023-01-09T15:43:50Z
# RC file format version: 1.2 2022-05-31
#
# cal-target file: /scratch/cal_wg/flight/products/0669/rad/ZL1_0669_0726335056_144RAD_N0320580ZCAM03014_048085A01.IMG
# unique sequence identifier: 00669_zcam03014_03557_001
# local true solar time: 13:05:05
# solar azimuth (rover frame): 37.4871
# solar elevation (rover frame): 67.7393
# fit method:  use_only_chip_centers
# ROI names:  "Blue Chip Center"  "Green Chip Center"  "Yellow Chip Center"  "Red Chip Center"  "Black Chip Center"
"Dark Gray Chip Center"  "Light Gray Chip Center"  "White Chip Center"  "Black Ring"  "Dark Gray Ring"  "Light Gray Ring"
"White Ring"  "Black Ring Shadow"  "Dark Gray Ring Shadow"  "Light Gray Ring Shadow"  "White Ring Shadow"  "Black
Secondary Horizontal"  "Dark Gray Secondary Horizontal"  "Light Gray Secondary Horizontal"  "White Secondary Horizontal"
"Red Secondary Horizontal"  "Green Secondary Horizontal"  "Blue Secondary Horizontal"  "Black Secondary Vertical"  "Dark
Gray Secondary Vertical"  "Light Gray Secondary Vertical"  "White Secondary Vertical"  "Red Secondary Vertical"  "Green
Secondary Vertical"  "Blue Secondary Vertical"  "Blue Chip Outer"  "Green Chip Outer"  "Yellow Chip Outer"  "Red Chip
Outer"  "Black Chip Outer"  "Dark Gray Chip Outer"  "Light Gray Chip Outer"  "White Chip Outer"  "Gnomon"  "Gold"  "Deck"
# ROI is selected:  1  1  1  1  1  1  1  1  1  1  1  1  0  0  0  0  1  1  1  1  1  1  1  1  1  1  1  1  1  1  1  1  1  1
1  1  1  1  1  1  1
# ROI marked bad:   0  0  0  0  0  0  0  1  0  0  0  0  0  0  0  0  0  0  0  1  0  0  0  0  0  0  1  0  0  0  0  0  0  0
0  0  0  1  0  0  0
# ROI used in fit:  1  1  1  1  1  1  1  0  0  0  0  0  0  0  0  0  0  0  0  0  0  0  0  0  0  0  0  0  0  0  0  0  0  0
0  0  0  0  0  0  0
# ROI radiances:  0.031989332  0.036407288  0.091285534  0.091282636  0.022022225  0.050774548  0.080655284  0.10552662
0.031561576  0.051227223  0.070795760  0.099315345  NaN  NaN  NaN  NaN  0.028453734  0.052763894  0.081336990  0.10410106
0.091173448  0.041365623  0.038499620  0.012088150  0.031603854  0.053751044  0.072543986  0.060960762  0.021432867
0.019607559  0.043244924  0.044497933  0.043649755  0.044094864  0.044650659  0.044328745  0.044293959  0.044629496
0.011909686  0.060992837  0.087867759
# ROI uncertainty:  0.0010251829  0.00092458078  0.0018847070  0.0016933153  0.00097975636  0.0011039088  0.0017773096
0.0022193551  0.0012545585  0.0012506406  0.0028425378  0.0035026259  NaN  NaN  NaN  NaN  0.0010970038  0.0011636106
0.0026552086  0.0044806166  0.0032543806  0.0010242959  0.0012009761  0.00042607611  0.0010755071  0.0017130962
0.0027286065  0.0022689109  0.00059648530  0.00065979114  0.0022326323  0.0017271742  0.0018901474  0.0018942577
0.0021841403  0.0021148931  0.0020427989  0.0021763279  0.0032630546  0.0031546741  0.0032552586
# ROI count:  74  67  73  73  65  65  62  66  1432  3320  766  2262  0  0  0  0  934  911  911  914  874  873  865  1302
503  1270  1268  1262  442  1246  470  460  472  451  420  408  406  429  469  534  1745
# ROI incidence angle:  22.260748  22.260748  22.260748  22.260748  22.260748  22.260748  22.260748  22.260748  22.260748
22.260748  22.260748  22.260748  22.260748  22.260748  22.260748  22.260748  22.260748  22.260748  22.260748  22.260748
22.260748  22.260748  22.260748  72.506842  72.506842  72.506842  72.506842  72.506842  72.506842  72.506842  22.260748
22.260748  22.260748  22.260748  22.260748  22.260748  22.260748  22.260748  22.260748  22.260748  22.260748
# ROI emission angle:  58.309392  58.309392  58.309392  58.309392  58.309392  58.309392  58.309392  58.309392  58.309392
58.309392  58.309392  58.309392  58.309392  58.309392  58.309392  58.309392  55.257094  55.257094  55.257094  55.257094
55.257094  55.257094  55.257094  37.229692  37.229692  37.229692  37.229692  37.229692  37.229692  37.229692  58.309392
58.309392  58.309392  58.309392  58.309392  58.309392  58.309392  58.309392  58.309392  58.309392  58.309392
# ROI azimuth angle:  51.836590  51.836590  51.836590  51.836590  51.836590  51.836590  51.836590  51.836590  51.836590
51.836590  51.836590  51.836590  51.836590  51.836590  51.836590  51.836590  52.711009  52.711009  52.711009  52.711009
52.711009  52.711009  52.711009  34.920123  34.920123  34.920123  34.920123  34.920123  34.920123  34.920123  51.836590
51.836590  51.836590  51.836590  51.836590  51.836590  51.836590  51.836590  51.836590  51.836590  51.836590
# reflectances:  0.19865347  0.21245557  0.81136782  0.78961108  0.083866228  0.37057445  0.68153787  0.97493555
0.083866228  0.37057445  0.68153787  0.97493555  NaN  NaN  NaN  NaN  0.084091580  0.37078489  0.68171637  0.97454879
0.78955129  0.21265709  0.19881594  0.077894031  0.33452057  0.61867862  0.89473491  0.67630893  0.19671718  0.17893278
0.19865347  0.21245557  0.81136782  0.78961108  0.083866228  0.37057445  0.68153787  0.97493555  NaN  NaN  NaN
# camera id, filter number, rad-to-iof scaling factor, uncertainty
        4007  1  7.9310428  0.56726699
```

Appendix B

The model for diffuse illumination correction

In the linear fits employed for calibration on Mars, the reference laboratory reflectance is retrieved from a combination of the Bern data and the Copenhagen data, as described in section 5.3. In turn, the reflectance factor in the Bern data was obtained from the bidirectional reflectance through equation (4.12). As illustrated in section 4.1, the bidirectional reflectance considers either the light from the light source to the target and from the target to the observer as collimated beams, without any scattering or diffusion. This assumption might hold for a setting without diffusing agents (e.g., a planet without atmosphere), but the direct experience with the rover Perseverance showed that reality is quite different. As witnessed by figure 7.9, in the first 315 sols of the mission the diffuse illumination was rather unimportant, because the calibration targets were usually imaged around the martian noon, when the Sun was very close to the zenith, and the amount of airborne dust in the atmosphere was low. From sol 315 dust started to play a more and more influential role, especially after the autumn equinox (sol 360), when the minimum incidence angle at noon was larger. These two effects increased the diffuse illumination, which reduced the fraction of direct light. In the occurrence of this phenomenon, the reference laboratory reflectances computed by our model were likely not precise representative of the expected reality anymore, because they relied on the concept of bidirectional reflectance and did not consider diffuse illumination.

In order to pave the way for a solution to this problem, I developed a simple analytical model that could be further improved and implemented in the future, which makes use of the measured radiances from the sunlit and shadowed grayscale rings to correct the reference reflectances employed in the linear fits. In the following, I indicate the radiance with I, the irradiance with F, and the reflectance with R. The concept at the base of this model is a consequence of equation (4.10), but noticing that the solar irradiance that illuminates the clean spots is a sum of the direct light from the Sun and the diffuse light from the sky. It can be expressed as:

$$I_{tot} = (F_{dir} + F_{diff}) \cdot R_{ref} \; , \tag{B.1}$$

where I_{tot} is the measured radiance of the clean spots, R_{ref} is the reference reflectance from the Bern data, F_{dir} is the irradiance of the direct light and F_{diff} is the diffuse irradiance. The first step is the computation of F_{dir}, which, by definition, can be written as:

$$F_{dir} = \frac{I_{dir}}{R_{dir}} \; . \tag{B.2}$$

In equation (B.2), $Idir$ is the radiance of a region illuminated only by direct light from the Sun, and R_{dir} is the reflectance of that region. Given that R_{dir} is referred to the direct sunlight, we have that R_{dir} is precisely the reflectance of the clean spots from the Bern data. On the other hand, the radiance I_{dir} can be obtained as the difference between the radiance I_{tot} of a surface illuminated by direct+diffuse light (the clean spots), and the radiance I_{diff} of some region that only receives diffuse illumination (the ROIs in the shadowed grayscale rings):

$$I_{dir} = I_{tot} - I_{diff} \; . \tag{B.3}$$

The difference in equation (B.3) can only be computed between corresponding clean spots and shadowed grayscale rings of the same color, and then the differences can be averaged. Once I_{dir} and R_{dir} are known for the grayscale materials involved in equation (B.3), the ratio of equation (B.2) is computed in the form of a linear fit, from which the direct irradiance F_{dir} is retrieved as the slope.

The irradiance of diffuse light can be expressed similarly to equation (B.2):

$$F_{diff} = \frac{I_{diff}}{R_{diff}} \; , \tag{B.4}$$

where I_{diff} is again the radiance measured from the shadowed ROIs of the grayscale rings, and R_{diff} should be the relative reflectance of diffuse light. The latter is not known from measurements, but one way to model it is to use the reflectance from the Bern data corresponding to $i = 0°$, $e = 58°$ and $Az = 0°$. Therefore, the ratio of equation (B.4) can be computed again as a linear fit between the I_{diff} and R_{diff} of the same grayscales, for consistency, and the slope of the fit is F_{diff}.

At this point, the corrected values R_{corr} of the reference reflectance can be retrieved from equation (B.1):

$$R_{corr} = \frac{I_{tot}}{F_{dir} + F_{diff}} \; , \tag{B.5}$$

which only consists in dividing the radiances of the clean spots by the sum of direct and diffuse irradiance. R_{corr} are the new reference reflectances of the clean spots, that shall be used to compute the linear fits with the measured radiances I_{tot} as in the calibration procedure of section 6.5.

The model described above has the advantage of being rather simple, but it requires a couple of comments. Firstly, the whole model relies on the radiance measurements of (at least one of) the shadowed ROIs in the grayscale rings, which are necessary for equations (B.3) and (B.4). When the Sun is very close to the zenith, such as during the northern summer, the gnomon's shadow is barely or not visible at all, but the effects of diffuse illumination are usually negligible, and the model is not expected to be "switched on". Conversely, when the incidence angle is large enough to require the correction model, the resulting shadow might be hidden behind the gnomon upon a very narrow but unfortunate azimuth angle range, preventing the algorithm and the user to select even one ROI. This event could occur only for one of the eyes of Mastcam-Z, due to their angular separation. The intensity of diffuse illumination changes with time of sol and the optical depth of the atmosphere, and hence, picking the radiances of the shadowed ROIs from different moments of the same sol or from other sols would not be consistent and may likely affect systematically the determination of other parameters and the final result. In addition, even in the more common case in which some ROIs of the shadow are selected, we must keep into account that the grayscale rings are subject to the deposition of dust, with an expected increase from the outermost to the innermost, due to the increasing distance from the peripheral magnets. The measured radiance is perturbed by the presence of dust, as shown in section (7.2), and therefore it would not be consistent to compute the subtraction in equation (B.3) between clean spots and shadowed grayscale rings. A more consistent choice would be to compute the subtraction between the sunlit and shadowed grayscale rings because they experience the same piling of dust. However, in equation (B.4) the shadowed radiance is employed again to obtain the diffuse irradiance: if a significant layer of dust deposits on the grayscale rings, the diffuse reflectance R_{diff} should be modeled appropriately in order to ensure a fair consistency with I_{diff}.

In fact, the topic becomes more complex with the second discussion point, that is the modeling of the diffuse reflectance R_{diff}. The suggestion given in the model above, that is to use the reflectance from the Bern data corresponding to the incidence and azimuth angles equal to zero, implies that all the light scattered by the atmosphere is equivalent to a beam hitting the target from the zenith. This approximation should be tested in the future, in order to ensure an accurate correction, possibly by considering the estimates of the optical depth due to dust, which is a good indicator of the amount of suspended airborne dust, and hence, of the intensity of diffusion in the atmosphere.

Bibliography

AFSHAR-MOHAJER, N. et al. (2015). Review of dust transport and mitigation technologies in lunar and Martian atmospheres. *Advances in Space Research*, Vol. **56**, Issue 6, pp. 1222-1241. DOI: 10.1016/j.asr.2015.06.007

ALBEE, A. L. et al. (2001). Overview of the Mars Global Surveyor mission. *Journal of Geophysical research: Planets*. Vol. **106**, Issue E10. DOI: 10.1029/2000JE001306

ALLWOOD, A. C. et al. (2020). PIXL: Planetary Instrument for X-Ray Lithochemistry. *Space Science Reviews*, Vol. **216**, Issue 8. DOI: 10.1007/s11214-020-00767-7

AMIRI, H. E. S. et al. (2022). The Emirates Mars Mission. *Space Science Reviews*, Vol. **218**, Issue 4. DOI: 10.1007/s11214-021-00868-x

ARVIDSON, R. E. et al. (2006). Nature and origin of the hematite-bearing plains of Terra Meridiani based on analyses of orbital and Mars Exploration rover data sets. *Journal of Geophysical Research*, Vol. **111**, Issue E12. DOI: 10.1029/2006JE002728

BALARAM, J. et al. (2021). The Ingenuity Helicopter on the Perseverance Rover. *Space Science Reviews*, Vol. **217**, Issue 4. DOI: 10.1007/s11214-021-00815-w

BANERDT, W. B. et al. (2020). Initial results from the InSight mission on Mars. *Nature Geoscience*, Vol. **13**, pp. 183–189. DOI: 10.1038/s41561-020-0544-y

BHARTIA, R. et al. (2021). Perseverance's Scanning Habitable Environments with Raman and Luminescence for Organics and Chemicals (SHERLOC) Investigation. *Space Science Reviews*, Vol. **217**, Issue 4. DOI: 10.1007/s11214-021-00812-z

BELL, J. F. et al. (2003). Mars Exploration Rover Athena Panoramic Camera (Pancam) investigation. *Journal of Geophysical Research*, Vol. **108**, Issue E12. DOI: 10.1029/2003JE002070

BELL, J. F. et al. (2005). Solar eclipses of Phobos and Deimos observed from the surface of Mars. *Nature*, Vol. **436**, Issue 7047, pp. 55-57. DOI: 10.1038/nature03437

BELL, J. F. et al. (2017). The Mars Science Laboratory Curiosity rover Mastcam instruments: Preflight and in-flight calibration, validation, and data archiving. *Earth and Space Science*, Vol. **4**, Issue 7, pp. 396-452. DOI: 10.1002/2016EA000219

BELL, J. F. et al. (2021). The Mars 2020 Perseverance Rover Mast Camera Zoom (Mastcam-Z) Multispectral, Stereoscopic Imaging Investigation. *Space Science Reviews*, Vol. **217**, Issue 1. DOI: 10.1007/s11214-020-00755-x

BELL, J. F. III et al. (2022). Geological, Multispectral, and Meteorological Imaging Results from the Mars 2020 Perseverance Rover in Jezero Crater. *Science Advances*, Vol. **8**, Issue 47. DOI: doi.org/10.1126/sciadv.abo4856

BERTELSEN, P. et al. (2003). Magnetic Properties Experiments on the Mars Exploration Rover Spirit at Gusev Crater. *Science*, Vol. **305**, Issue 5685, pp. 827-829. DOI: 10.1126/science.1100112

BIBRING, J. P. et al. (2004). Perennial water ice identified in the south polar cap of Mars. *Nature*, Vol. **428**, pp. 627–630. DOI: 10.1038/nature02461

BLAKE, D. et al. (2012). Characterization and Calibration of the CheMin Mineralogical Instrument on Mars Science Laboratory. *Space Science Reviews*, Vol. **170**, Issue 1-4, pp. 341-399. DOI: 10.1007/s11214-012-9905-1

BROWN, A. J. et al. (2020). Olivine-Carbonate Mineralogy of the Jezero Crater Region. *Journal of Geophysical Research: Planets*, Vol. **125**. DOI: 10.1029/2019JE006011

BUZ, J. et al. (2019). Photometric characterization of Lucideon and Avian Technologies color standards including application for calibration of the Mastcam-Z instrument on the Mars 2020 rover. *Optical Engineering*, Vol. **58**, Issue 2. DOI: 10.1117/1.OE.58.2.027108

CABROL, N. A. et al. (2003). Exploring Gusev Crater with Spirit: Review of science objectives and testable hypotheses. *Journal of Geophysical Research*, Vol. **108**, Issue E12. DOI: 10.1029/2002JE002026

CARR, M. H. & HEAD, J. W. (2010). Geologic history of Mars. *Earth and Planetary Science Letters*, Vol. **294**, pp. 185–203. DOI: 10.1016/j.epsl.2009.06.042

CHENG, Y. et al. (2021). Making an Onboard Reference Map From MRO/CTX Imagery for Mars 2020 Lander Vision System. *Earth and Space Science*, Vol. **8**, Issue 8. DOI: 10.1029/2020EA001560

CHICARRO, A. et al. (2004). The Mars Express mission: an overview. Mars Express: the scientific payload. Ed. by Andrew Wilson, scientific coordination: Agustin Chicarro. ESA SP-1240, Noordwijk, Netherlands: ESA Publications Division, ISBN 92-9092-556-6, 2004, pp. 3 - 13.

CHIDE, B. et al. (2020). Recording laser-induced sparks on Mars with the SuperCam microphone. *Spectrochimica Acta Part B: Atomic Spectroscopy*, Vol. **174**. DOI: 10.1016/j.sab.2020.106000

CHRISTENSEN, P. R. et al. (2003). Miniature Thermal Emission Spectrometer for the Mars Exploration Rovers. *Journal of Geophysical Research*, Vol. **108**, Issue E12. DOI: 10.1029/2003JE002117

COUSIN, A. et al. (2022). SuperCam calibration targets on board the Perseverance rover: Fabrication and quantitative characterization. *Spectrochimica Acta Part B: Atomic Spectroscopy*, Vol. **188**. DOI: 10.1016/j.sab.2021.106341

CRISP, J. A. et al. (2003). Mars Exploration Rover mission. *Journal of Geophysical Research*, Vol. **108**, Issue E12. DOI: 10.1029/2002JE002038

EDGETT, K. S. et al. (2012). Curiosity's Mars Hand Lens Imager (MAHLI) Investigation. *Space Science Reviews*, Vol. **170**, Issue 1-4, pp. 259-317. DOI: 10.1007/s11214-012-9910-4

EHLMANN, B. L. & EDWARDS, C. S. (2014). Mineralogy of the martian surface. *Annual Review of Earth and Planetary Sciences*, Vol. **42**, pp. 291–315. DOI: 10.1146/annurev-earth-060313-055024

EHLMANN, B. L. et al. (2016). The sustainability of habitability on terrestrial planets: Insights, questions, and needed measurements from Mars for understanding the evolution of Earth-like worlds. *Journal of Geophysical Research: Planets*, Vol. **121**, pp. 1927–1961. DOI: 10.1002/2016JE005134

FARLEY, K. A. et al. (2020). Mars 2020 mission overview. *Space Science Reviews*, Vol. **216**, Issue 8. DOI: 10.1007/s11214-020-00762-y

FASSETT, C. I. & HEAD, J. W. (2005). Fluvial sedimentary deposits on Mars: Ancient deltas in a crater lake in the Nili Fossae region. *Geophysical Research Letters*, Vol. **32**, Issue L14201. DOI: 10.1029/2005GL023456

FASSETT, C. I. & HEAD, J. W. (2011). Sequence and timing conditions on early Mars. *Icarus*, Vol. **211**, pp. 1204-1214. DOI: 10.1016/j.icarus.2010.11.014

GARCZYNSKI, B. J. et al. (2022). Perseverance and the purple coating: A Mastcam-Z multispectral story. In *Paper presented at 53rd Lunar and Planetary Science Conference*, held 7–11 March, 2022 at The Woodlands, Texas. id. 2346.

GELLERT, R. et al. (2006). Alpha Particle X-Ray Spectrometer (APXS): Results from Gusev crater and calibration report. *Journal of Geophysical Research*, Vol. **111**, Issue E2. DOI: 10.1029/2005JE002555

GILLESPIE, A. R. et al. (1986). Color enhancement of highly correlated images. I. Decorrelation and HIS contrast stretches. *Remote Sensing of Environment*, Vol. **20**, Issue 3, pp. 209–235. 10.1016/0034-4257(86)90044-1

GOETZ, W. et al. (2005). Indication of drier periods on Mars from the chemistry and mineralogy of atmospheric dust. *Nature*, Vol. **436**, pp. 62–65. DOI: 10.1038/nature03807

GOLABEK, G. J. et al. (2011). Origin of the martian dichotomy and Tharsis from a giant impact causing massive magmatism. *Icarus*, Vol. **215**, Issue 1, pp. 346-357. DOI: 10.1016/j.icarus.2011.06.012

GOLOMBEK, M. P (1997). The Mars Pathfinder Mission. *Journal of Geophysical research: Planets*. Vol. **102**, Issue E2. DOI: 10.1029/96JE02805

GOLOMBEK, M. P. et al. (2003). Selection of the Mars Exploration Rover landing sites. *Journal of Geophysical Research*, Vol. **108**, Issue E12. DOI: 10.1029/2003JE002074

GÓMEZ-ELVIRA, J. et al. (2012). REMS: The Environmental Sensor Suite for the Mars Science Laboratory Rover. *Space Science Reviews*, Vol. **170**, Issue 1-4, pp. 583-640. DOI: 10.1007/s11214-012-9921-1

GOREVAN, S. P. et al. (2003). Rock Abrasion Tool: Mars Exploration Rover mission. *Journal of Geophysical Research*, Vol. **108**, Issue E12. DOI: 10.1029/2003JE002061

GOUDGE, T. A. et al. (2015). Assessing the mineralogy of the watershed and fan deposits of the Jezero crater paleolake system, Mars. *Journal of Geophysical Research: Planets*, Vol. **120**, Issue 4, pp. 775-808. DOI: 10.1002/2014JE004782

GRANT, J. A. et al. (2018). The science process for selecting the landing site for the 2020 Mars rover. *Planetary and Space Science*, Vol. **164**, pp. 106-126. DOI: 10.1016/j.pss.2018.07.001

GROTZINGER, J. P. et al. (2012). Mars Science Laboratory Mission and Science Investigation. *Space Science Reviews*, Vol. **170**, Issue 1-4, pp. 5-56. DOI: 10.1007/s11214-012-9892-2

GROTZINGER, J. P. et al. (2013). A Habitable Fluvio-Lacustrine Environment at Yellowknife Bay, Gale Crater, Mars. *Science*, Vol. **343**, Issue 6169. DOI: 10.1126/science.1242777

HABERLE, R. M. et al. (2017). The atmosphere and climate of Mars. *Cambridge University Press*, ISBN: 978-1-107-01618. DOI: 10.1017/9781139060172

HALLIDAY, A. et al. (2001). The Accretion, Composition and Early Differentiation of Mars. *Space Science Reviews*, Vol. **96**, pp. 197–230. DOI: 10.1023/A:1011997206080

HAMRAN, S. E. et al. (2020). Radar Imager for Mars' Subsurface Experiment—RIMFAX. *Space Science Reviews*, Vol. **216**, Issue 8. DOI: 10.1007/s11214-020-00740-4

HAPKE, B. (1993). Theory of Reflectance and Emittance Spectroscopy (Topics in Remote Sensing). *Cambridge: Cambridge University Press*. DOI: 10.1017/CBO9780511524998

HARTMANN, W. et al. (1999). Evidence for recent volcanism on Mars from crater counts. *Nature*, Vol. **397**, pp. 586–589. DOI: 10.1038/17545

HASSLER, D. M. et al. (2012). The Radiation Assessment Detector (RAD) Investigation. *Space Science Reviews*, Vol. **170**, Issue 1-4, pp. 503-558. DOI: 10.1007/s11214-012-9913-1

HASSLER, D.M. et al. (2013). Mars' Surface Radiation Environment Measured with the Mars Science Laboratory's Curiosity Rover. *Science*, Vol. **343**, Issue 6169. DOI: 10.1126/science.1244797

HAYES, A. G. et al. (2021). Pre-Flight Calibration of the Mars 2020 Rover Mastcam Zoom (Mastcam-Z) Multispectral, Stereoscopic Imager. *Space Science Reviews*, Vol. **217**, issue 29. DOI: 10.1007/s11214-021-00795-x

HECHT, M. et al. (2021). Mars Oxygen ISRU Experiment (MOXIE). *Space Science Reviews*, Vol. **217**, Issue 1. DOI: 10.1007/s11214-020-00782-8

HERKENOFF, K. E. et al. (2003). Athena Microscopic Imager investigation. *Journal of Geophysical Research*, Vol. **108**, Issue E12. DOI: 10.1029/2003JE002076

HORGAN, B. H. et al. (2020). The mineral diversity of Jezero crater: Evidence for possible lacustrine carbonates on Mars. *Icarus*, Vol. **339**. DOI: 10.1016/j.icarus.2019.113526

HORGAN, B. et al. (2022). Mineralogy, morphology, and geochronological significance of the Máaz formation and the Jezero crater floor. In *Paper presented at 53rd Lunar and Planetary Science Conference*, held 7–11 March, 2022 at The Woodlands, Texas. id. 1680.

JAKOSKY, B. & PHILLIPS, R. (2001). Mars' volatile and climate history. *Nature*, Vol. **412**, pp. 237–244. DOI: 10.1038/35084184

JAKOSKY, B. M. et al. (2015). The Mars Atmosphere and Volatile Evolution (MAVEN) Mission. *Space Science Reviews*, Vol. **195**, pp. 3–48. DOI: 10.1007/s11214-015-0139-x

JOHNSON, J. R. et al. (2022). Mastcam-Z Spectrophotometric Observations at the Van Zyl Overlook, Jezero Crater, Mars. In *Paper presented at 53rd Lunar and Planetary Science Conference*, held 7-11 March, 2022 at The Woodlands, Texas. id.1253.

KMINEK, G. et al. (2022). Mars Sample Return (MSR): Planning for Returned Sample Science. *Astrobiology*, Vol. **22**, Issue S1, pp. S-1-S-4. DOI: 10.1089/ast.2021.0198

KINCH, K. M. et al. (2006). Preliminary analysis of the MER magnetic properties experiment using a computational fluid dynamics model. *Planetary and Space Science*, Vol. **54**, Issue 1. DOI: 10.1016/j.pss.2005.07.008

KINCH, K. M. et al. (2007). Dust deposition on the Mars Exploration Rover Panoramic Camera (Pancam) calibration targets. *Journal of Geophysical Research*, Vol. **112**, Issue E06S03. DOI: 10.1029/2006JE002807

KINCH, K. M. et al. (2015). Dust deposition on the decks of the Mars Exploration Rovers: 10 years of dust dynamics on the Panoramic Camera calibration targets. *Earth and Space Science*, Vol. **2**, pp. 144–172. DOI: 10.1002/2014EA000073

KINCH, K. B. et al. (2020). Radiometric Calibration Targets for the Mastcam-Z Camera on the Mars 2020 Rover Mission. *Space Science Reviews*, Vol. **216**, Issue 8. DOI: 10.1007/s11214-020-00774-8

KLEIN, H. P. et al. (1976). The Viking Biological Investigation: Preliminary Results. *Science*, Vol. **194**, Issue 4260, pp. 99-105. DOI: 10.1126/science.194.4260.99

KLINGELHÕFER, G. et al. (2003). Athena MIMOS II Mössbauer spectrometer investigation. *Journal of Geophysical Research*, Vol. **108**, Issue E12. DOI: 10.1029/2003JE002138

KLIORE, A. et al. (1969). Mariners 6 and 7: Radio Occultation Measurements of the Atmosphere of Mars. *Science*, Vol. **166**, Issue 3911, pp. 1393-1397. DOI: 10.1126/science.166.3911.1393

KNAPMEYER-ENDRUN, B. et al. (2021). Thickness and structure of the martian crust from InSight seismic data. *Science*, Vol. **373**, Issue 6553, pp. 438-443. DOI: 10.1126/science.abf8966

LAMBERT, J. H. (1760). Photometria sive de mensura et gradibus luminis, colorum et umbrae. *Augustae Vindelicorum [Augsburg] : sumptibus vidvae Eberhardi Klett*. ETH-Bibliothek Zürich, Rar 1355. DOI: 10.3931/e-rara-9488

LANGE, R. et al. (2022). Mars 2020 Perseverance Rover Surface Operations Commissioning Phase Overview. *2022 IEEE Aerospace Conference (AERO)*, Big Sky, MT, USA, 2022, pp. 1-20. DOI: 10.1109/AERO53065.2022.9843314

LANGLAIS, B. et al. (2010). Crustal Magnetic Fields of Terrestrial Planets. *Space Science Reviews*, Vol. **152**, pp. 223–249. DOI: 10.1007/s11214-009-9557-y

LEER, K. et al. (2008). Magnetic properties experiments and the Surface Stereo Imager calibration target onboard the Mars Phoenix 2007 Lander: Design, calibration, and science goals. *Journal of Geophysical Research*, Vol. **113**, Issue E12. DOI: 10.1029/2007JE003014

LEIGHTON, R. B. et al. (1965). Mariner IV Photography of Mars: Initial Results. *Science*, Vol. **149**, Issue 3684, pp. 627-630. DOI: 10.1126/science.149.3684.627

LEMMON, M. T. et al. (2008). The Phoenix Surface Stereo Imager (SSI) Investigation. *39th Lunar and Planetary Science Conference, (Lunar and Planetary Science XXXIX)*, held March 10-14, 2008, in League City, Texas. LPI Contribution No. 1391., p.2156.

LEMMON, M. T. et al. (2013). Astrometric Observations of Phobos and Deimos During Solar Transits Imaged by the Curiosity Mastcam. *44th Lunar and Planetary Science Conference*, held March 18-22, 2013 in The Woodlands, Texas. LPI Contribution No. 1719, p.1787.

LEMMON, M. T. et al. (2022). Dust, sand, and winds within an active Martian storm in Jezero crater. *Geophysical Research Letters*, Vol. **49**, Issue 17. DOI: 10.1029/2022GL100126

LEVIN, G. V. & STRAAT, P. A. (1976). Viking Labeled Release Biology Experiment: Interim Results. *Science*, Vol. **194**, Issue 4271, pp. 1322-1329. DOI: 10.1126/science.194.4271.1322

LI, C. et al. (2021). China's Mars Exploration Mission and Science Investigation. *Space Science Reviews*, Vol. **217**, Issue 57. DOI: 10.1007/s11214-021-00832-9

MADSEN, M. B. et al. (1999). The magnetic properties experiments on Mars Pathfinder. *Journal of Geophysical Research*, Vol. **104**, Issue E4, pp. 8761-8779. DOI: 0148-0227/99/1998JE900006509.00

MADSEN, M.B. et al. (2003). Magnetic Properties Experiments on the Mars Exploration Rover mission. *Journal of Geophysical Research*, Vol. **108**, Issue E12. DOI: 10.1029/2002JE002029

MADSEN, M. B. et al. (2009). Overview of the magnetic properties experiments on the Mars Exploration Rovers. *Journal of Geophysical Research*, Vol. **114**, Issue E06S90. DOI: 10.1029/2008JE003098

MAHAFFY, P. R. et al. (2012). The Sample Analysis at Mars Investigation and Instrument Suite. *Space Science Reviews*, Vol. **170**, Issue 1-4, pp. 401-478. DOI: 10.1007/s11214-012-9879-z

MAHAFFY, P.R. et al. (2014). The imprint of atmospheric evolution in the D/H of Hesperian clay minerals on Mars. *Science*, Vol. **347**, Issue 6220, pp. 412-414. DOI: 10.1126/science.1260291

MAKI, J. N. et al. (2003). Mars Exploration Rover Engineering Cameras. *Journal of Geophysical Research*, Vol. **108**, Issue E12. DOI: 10.1029/2003JE002077

MAKI, J. N. et al. (2012). The Mars Science Laboratory Engineering Cameras. *Space Science Reviews*, Vol. **170**, Issue 1-4, pp. 77-93. DOI: 10.1007/s11214-012-9882-4

MAKI, J. N. et al. (2020). The Mars 2020 Engineering Cameras and Microphone on the Perseverance Rover: A Next-Generation Imaging System for Mars Exploration. *Space Science Reviews*, Vol. **216**, Issue 8. DOI: 10.1007/s11214-020-00765-9

MALIN, M. C. et al. (2017). The Mars Science Laboratory (MSL) Mast cameras and Descent imager: Investigation and instrument descriptions. *Earth and Space Science*, Vol. **4**, Issue 8, pp. 506-539. DOI: 10.1002/2016EA000252

MANGOLD, N. et al. (2020). Fluvial Regimes, Morphometry, and Age of Jezero Crater Paleolake Inlet Valleys and Their Exobiological Significance for the 2020 Rover Mission Landing Site. *Astrobiology*, Vol. **20**, Issue 8, p.994-1013. DOI: 10.1089/ast.2019.2132

MARTÍNEZ, G. M. et al. (2017). The Modern Near-Surface Martian Climate: A Review of In-situ Meteorological Data from Viking to Curiosity. *Space Science Reviews*, Vol. **212**, pp. 295–338. DOI: 10.1007/s11214-017-0360-x

MAURICE, S. et al. (2012). The ChemCam Instrument Suite on the Mars Science Laboratory (MSL) Rover: Science Objectives and Mast Unit Description. *Space Science Reviews*, Vol. **170**, Issue 1-4, pp. 95-166. DOI: 10.1007/s11214-012-9912-2

MAURICE, S. et al. (2021). The SuperCam Instrument Suite on the Mars 2020 Rover: Science Objectives and Mast-Unit Description. *Space Science Reviews*, Vol. **217**, Issue 3. DOI: 10.1007/s11214-021-00807-w

MAZUR, P. et al. (1978). Biological implications of the Viking mission to Mars. *Space Science Reviews*, Vol. **22**, pp. 3–34. DOI: 10.1007/BF00215812

MCEWEN, S. A. et al. (2007). Mars Reconnaissance Orbiter's High Resolution Imaging Science Experiment (HiRISE). *Journal of Geophysical research: Planets*, Vol. **112**, Issue E5. DOI: 10.1029/2005JE002605

MCSWEEN, H. et al. (2004). Basaltic rocks analyzed by the Spirit Rover in Gusev Crater. *Science*, Vol. **305**, Issue 5685, pp. 842-845. DOI: 10.1126/science.1099851

MERUSI, M. et al. (2022). The Mastcam-Z radiometric calibration targets on NASA's Perseverance rover: Derived irradiance time-series, dust deposition, and performance over the first 350 sols on Mars. *Earth and Space Science*, Vol. **9**. DOI: 10.1029/2022EA002552

MING, D. W. et al. (2006). Geochemical and mineralogical indicators for aqueous processes in the Columbia Hills of Gusev crater, Mars. *Journal of Geophysical Research: Planets*, Vol. **111**, Issue E2. DOI: 10.1029/2005JE002560

MITROFANOV, I. G. et al. (2012). Dynamic Albedo of Neutrons (DAN) Experiment Onboard NASA's Mars Science Laboratory. *Space Science Reviews*, Vol. **170**, Issue 1-4, pp. 559-582. DOI: 10.1007/s11214-012-9924-y

MOELLER, R. C. et al. (2021). The Sampling and Caching Subsystem (SCS) for the Scientific Exploration of Jezero Crater by the Mars 2020 Perseverance Rover. *Space Science Reviews*, Vol. **217**, Issue 1. DOI: 10.1007/s11214-020-00783-7

MORGAN, G. A. et al. (2021). Availability of subsurface water-ice resources in the northern mid-latitudes of Mars. *Nature Astronomy*, Vol. **5**, pp. 230–236. DOI: 10.1038/s41550-020-01290-z

MORRIS, R. V. et al. (2006a). Mössbauer mineralogy of rock, soil, and dust at Gusev crater, Mars: Spirit's journey through weakly altered olivine basalt on the plains and pervasively altered basalt in the Columbia Hills. *Journal of Geophysical Research*, Vol. **111**, Issue E02S13. DOI: 10.1029/2005JE002584

MORRIS, R. V. et al. (2006b). Mössbauer mineralogy of rock, soil, and dust at Meridiani Planum, Mars: Opportunity's journey across sulfate-rich outcrop, basaltic sand and dust, and hematite lag deposits. *Journal of Geophysical Research*, Vol. **111**, Issue E12S15. DOI: 10.1029/2006JE002791

MORRIS, R. V. et al. (2010). Identification of Carbonate-Rich Outcrops on Mars by the Spirit Rover. *Science*, Vol. **329**, Issue 5990, pp. 421-424. DOI: 10.1126/science.1189667

MUIRHEAD, B. K. et al. (2020). Mars sample return campaign concept status. *Acta Astronautica*, Vol. **176**, pp. 131-138. DOI: 10.1016/j.actaastro.2020.06.026

MURCHIE, S. et al. (2007). Compact Reconnaissance Imaging Spectrometer for Mars (CRISM) on Mars Reconnaissance Orbiter (MRO). *Journal of Geophysical Research*, Vol. **112**, Issue E5. DOI: 10.1029/2006JE002682

MURPHY, J. et al. (2016). Field Measurements of Terrestrial and Martian Dust Devils. *Space Science Reviews*, Vol. **203**, pp. 39–87. DOI: 10.1007/s11214-016-0283-y

NÚÑEZ, J. I. et al. (2022). Stratigraphy and mineralogy of the deposits within Séítah region on the floor of Jezero crater, Mars as seen with Mastcam-Z. In *Paper presented at 53rd Lunar and Planetary Science Conference*, held 7–11 March, 2022 at The Woodlands, Texas. id. 2937.

PEULVAST, J.-P. et al. (2001). Morphology, evolution and tectonics of Valles Marineris wallslopes (Mars). *Geomorphology*, Vol. **37**, Issues 3–4, pp. 329-352. DOI: 10.1016/S0169-555X(00)00085-4

POMMEROL, A. et al. (2011). Photometry and bulk physical properties of Solar System surfaces icy analogs: The Planetary Ice Laboratory at University of Bern. *Planetary and Space Science*, Vol. **59**, pp. 1601-1612. DOI: 10.1016/j.pss.2011.07.009

RAMPE, E. B. et al. (2020). Mineralogy and geochemistry of sedimentary rocks and eolian sediments in Gale crater, Mars: A review after six Earth years of exploration with Curiosity. *Geochemistry*, Vol. **80**, Issue 2. DOI: 10.1016/j.chemer.2020.125605

RICE, M. S. et al. (2022). Spectral diversity of rocks and soils in Mastcam observations along the Curiosity rover's traverse in Gale crater, Mars. *Journal of Geophysical Research: Planets*, Vol. **127**, Issue e2021JE007134. DOI: 10.1029/2021JE007134

RIEDER, R. et al. (2003). The new Athena alpha particle X-ray spectrometer for the Mars Exploration Rovers. *Journal of Geophysical Research*, Vol. **108**, Issue E12. DOI: 10.1029/2003JE002150

RIVOLDINI, A. et al. (2011). Geodesy constraints on the interior structure and composition of Mars. *Icarus*, Vol. **213**, Issue 2, pp. 451-472. DOI: 10.1016/j.icarus.2011.03.024

RODRIGUEZ-MANFREDI, J.A. et al. (2021). The Mars Environmental Dynamics Analyzer, MEDA. A Suite of Environmental Sensors for the Mars 2020 Mission. *Space Science Reviews*, Vol. **217**, Issue 3. DOI: 10.1007/s11214-021-00816-9

SÁNCHEZ-LAVEGA, A. et al. (2019). The onset and growth of the 2018 Martian Global Dust Storm. *Geophysical Research Letters*, Vol. **46**, pp. 6101– 6108. DOI: 10.1029/2019GL083207

SAUNDERS, R. et al. (2004). 2001 Mars Odyssey Mission Summary. *Space Science Reviews*, Vol. **110**, pp. 1–36. DOI: 10.1023/B:SPAC.0000021006.84299.18

SHAHRZAD, S. et al. (2019). Crater Statistics on the Dark-Toned, Mafic Floor Unit in Jezero Crater, Mars. *Geophysical Research Letters*, Vol. **46**, Issue 5, pp. 2408-2416. DOI: 10.1029/2018GL081402

SHEPARD, M. (2017). Introduction to Planetary Photometry. *Cambridge: Cambridge University Press*. DOI: 10.1017/9781316443545

SHOTWELL, R. (2005). Phoenix - the first Mars Scout mission. *Acta Astronautica*, Vol. **57**, Issues 2–8, pp. 121-134. DOI: 10.1016/j.actaastro.2005.03.038

SMITH, M. et al. (2017). Thermal Structure and Composition. In R. Haberle, R. Clancy, F. Forget, M. Smith, & R. Zurek (Eds.), The Atmosphere and Climate of Mars (Cambridge Planetary Science, pp. 42-75). *Cambridge: Cambridge University Press*. DOI: 10.1017/9781139060172.004

SOFFEN, G. A. & YOUNG, T. (1972). The Viking missions to Mars. *Icarus*, Vol. **16**, Issue 1, pp. 1-16. DOI: 10.1016/0019-1035(72)90133-9

SOUNESS, C. & HUBBARD, B. (2012). Mid-latitude glaciation on Mars. *Progress in Physical Geography: Earth and Environment*, Vol. **36**, Issue 2, pp. 238–261. DOI: 10.1177/0309133312436570

SQUYRES, S. W. et al. (2003). Athena Mars rover science investigation. *Journal of Geophysical Research*, Vol. **108**, Issue E12. DOI: 10.1029/2003JE002121

SQUYRES, S. W. et al. (2004a). The Spirit Rover's Athena Science Investigation at Gusev Crater, Mars. *Science*, Vol. **305**, Issue 5685, pp. 794-800. DOI: 10.1126/science.1100194

SQUYRES, S. W. et al. (2004b). The Opportunity Rover's Athena Science Investigation at Meridiani Planum, Mars. *Science*, Vol. **306**, Issue 5702, pp. 1698-1703. DOI: 10.1126/science.1106171

SQUYRES, S. W. et al. (2006). Rocks of the Columbia Hills. *Journal of Geophysical Research*, Vol. **111**, Issue E2. DOI: 10.1029/2005JE002562

SQUYRES, S. W. et al. (2012). Ancient Impact and Aqueous Processes at Endeavour Crater, Mars. *Science*, Vol. **336**, Issue 6081. DOI: 10.1126/science.1220476

STACK, K. M. et al. (2020). Photogeologic Map of the Perseverance Rover Field Site in Jezero Crater Constructed by the Mars 2020 Science Team. *Space Science Reviews*, Vol. **216**, Issue 127. DOI: 10.1007/s11214-020-00739-x

STÄHLER, S. C. et al. (2021). Seismic detection of the martian core. *Science*, Vol. **373**, Issue 6553, pp. 443-448. DOI: 10.1126/science.abi7730

SUNDARAJAN, V. (2013). Mangalyaan - Overview and Technical Architecture of India's First Interplanetary Mission to Mars. AIAA 2013-5503. *AIAA SPACE 2013 Conference and Exposition*. September 2013. DOI: 10.2514/6.2013-5503

VAGO, J. et al. (2015). ESA ExoMars program: The next step in exploring Mars. *Solar System Research*, Vol. **49**, pp. 518–528. DOI: 10.1134/S0038094615070199

VANIMAN, D. T. et al. (2014). Mineralogy of a Mudstone at Yellowknife Bay, Gale Crater, Mars. *Science*, Vol. **343**, Issue 6169. DOI: 10.1126/science.1243480

WEBSTER, C. R. et al. (2014). Mars methane detection and variability at Gale crater. *Science*, Vol. **347**, Issue 6220, pp 415-417. DOI: 10.1126/science.1261713

WIENS, R. C. et al. (2012). The ChemCam Instrument Suite on the Mars Science Laboratory (MSL) Rover: Body Unit and Combined System Tests. *Space Science Reviews*, Vol. **170**, Issue 1-4, pp. 167-227. DOI: 10.1007/s11214-012-9902-4

WIENS, R. C. et al. (2021). The SuperCam Instrument Suite on the NASA Mars 2020 Rover: Body Unit and Combined System Tests. *Space Science Reviews*, Vol. **217**, Issue 1. DOI: 10.1007/s11214-020-00777-5

WILHELMS, D. E. & SQUYRES, S. W. (1984). The martian dichotomy may be due to a giant impact. *Nature*, Vol. **309**, pp. 138-140. DOI: 10.1038/309138a0

WILLIAMS, R. M. E. et al. (2013). Martian Fluvial Conglomerates at Gale Crater. *Science*, Vol. **340**, Issue 6136, pp. 1068-1072. DOI: 10.1126/science.1237317

YOSHIZAKI, T. & MCDONOUGH, W. F. (2020). The composition of Mars. *Geochimica et Cosmochimica Acta*, Vol. **273**, pp. 137-162. DOI: 10.1016/j.gca.2020.01.011

ZHONG, S. & ZUBER, M. T. (2001). Degree-1 mantle convection and the crustal dichotomy on Mars. *Earth Planetary Science Letters*, Vol. **189**, pp. 75-84. DOI: 10.1016/S0012-821X(01)00345-4

ZUREK, R. W. & SMREKAR, S. E. (2007). An overview of the Mars Reconnaissance Orbiter (MRO) science mission. *Journal of Geophysical research: Planets*. Vol. **112**, Issue E5. DOI: 10.1029/2006JE002701